

Search for Charged Higgs Bosons with the ATLAS Detector at the LHC

DISSERTATION

zur Erlangung des akademischen Grades

**Doctor rerum naturalium
(Dr. rer. nat.)**

vorgelegt

**der Fakultät Mathematik und Naturwissenschaften der
Technischen Universität Dresden**

von

Dipl.-Phys. Patrick Czodrowski

geboren am 23.10.1982 in Mohrungen (Polen)

Eingereicht am 16.05.2013

1. Gutachter: Jun.-Prof. Dr. Arno Straessner
2. Gutachter: Prof. Dr. Michael Kobel

Kurzfassung

Die Entdeckung eines geladenen Higgs-Bosons, H^+ , wäre ein unbestreitbarer Nachweis von Physik jenseits des Standardmodells. In der vorliegenden Arbeit wird die Suche nach dem H^+ mit Hilfe von Proton-Proton-Kollisionen, welche im Jahr 2011 mit dem ATLAS Experiment am Large Hadron Collider, LHC, des CERN aufgenommen wurden, beschrieben. Im Rahmen dieser Arbeit wurde eine überarbeitete Analyse der Suche nach geladenen Higgs-Bosonen, die eine Verhältnismethode anwendet und damit die Sensitivität des traditionell direkten Suchansatzes stark verbessert, durchgeführt.

Leichte geladene Higgs-Bosonen, welche eine Masse geringer als die des Top-Quarks aufweisen, können aus einem Top-Quark-Zerfall hervorgehen. Im Gegensatz zu den schweren geladenen Higgs-Bosonen sind die leichten aufgrund des hohen Produktionswirkungsquerschnitts von Top-Quark-Paaren am LHC potenziell mit den ersten Daten des Experiments beobachtbar.

In den meisten Theorien und Szenarien sowie dem größten Bereich ihres Phasenraumes zerfallen leichte geladene Higgs-Bosonen meist im $H^\pm \rightarrow \tau^\pm \nu$ Kanal. Demzufolge spielen sowohl die τ -Identifikation als auch die τ -Fehlidentifikation eine besondere Rolle für die Suche nach geladenen Higgs-Bosonen. Eigens für die Ermittlung der Fehlidentifikationswahrscheinlichkeiten von Elektronen als hadronisch zerfallende τ -Leptonen wurde eine “tag-and-probe”-Methode, basierend auf $Z \rightarrow ee$ Ereignissen, entwickelt. Diese Messungen sind mit den allerersten Daten durchgeführt worden. Dabei haben diese einerseits für alle Analysen, welche die Elektronenveto-Algorithmen der τ -Identifikation nutzen, essenzielle Skalenfaktoren hervorgebracht. Andererseits wurde, beruhend auf diesen Ergebnissen, eine datenbasierte Abschätzungsmethode entwickelt und für die Untergründe der geladenen Higgs-Boson-Suche, die von der Fehlidentifikation von Elektronen als hadronisch zerfallende τ -Leptonen stammen, erfolgreich implementiert.

Im Rahmen dieser Arbeit wurden Triggerstudien, mit dem Ziel höchstmögliche Signaleffizienzen zu gewährleisten, durchgeführt. Neuartige Triggerobjekte, basierend auf einer Kombination aus τ -Trigger und fehlender transversaler Energie-Trigger, wurden entworfen, überprüft und in das Triggermenü für die Datennahme im Jahr 2012 aufgenommen.

Eine direkte Suche nach dem geladenen Higgs-Boson wurde in drei Kanälen mit einem τ -Lepton im Endzustand unter Berücksichtigung des gesamten Datensatzes des Jahres 2011 durchgeführt. Da kein signifikanter Überschuss, der von den Vorhersagen des Standardmodells abweicht, in den Daten beobachtet wurde, sind obere Ausschlussgrenzen auf $\mathcal{B}(t \rightarrow bH^+)$ gesetzt worden.

Letztlich ist die Analyse des Kanals mit einem hadronisch zerfallenden τ -Lepton und einem Myon oder Elektron im Endzustand des $t\bar{t}$ -Zerfalls, unter Anwendung der sogenannten Verhältnismethode, wiederholt worden. Diese Methode misst Verhältnisse von Ereignisausbeuten, anstatt die Verteilungen diskriminierender Variablen zu evaluieren. Folglich kürzen sich die meisten dominant beitragenden systematischen Unsicherheiten intrinsisch heraus. Die Daten stimmen mit den Vorhersagen des Standardmodells überein. Durch Zuhilfenahme der Verhältnismethode wurden die oberen Ausschlussgrenzen, im Vergleich zur direkten Suche, signifikant verbessert. Die Resultate der Verhältnismethode sind mit denen der direkten Suche, welche ein hadronisch zerfallendes τ -Lepton und zwei Jets im Endzustand des $t\bar{t}$ -Zerfalls nutzt, kombiniert worden. Auf diese Art und Weise konnten obere Ausschlussgrenzen auf $\mathcal{B}(t \rightarrow bH^+)$ in einem Bereich von 0,8 %–3,4 % für geladene Higgs-Bosonen in einem Massenbereich

für m_{H^+} zwischen 90 GeV und 160 GeV gesetzt werden.

Sollte das Minimal Supersymmetrische Standardmodell (MSSM) in der Natur realisiert sein, so haben die hier ermittelten oberen Ausschlussgrenzen auf $\mathcal{B}(t \rightarrow bH^+)$ direkte Konsequenzen für die Identität des Higgs-Boson-ähnlichen Teilchens, welches im Jahr 2012 am LHC entdeckt wurde.

Abstract

The discovery of a charged Higgs boson, H^+ , would be an unambiguous evidence for physics beyond the Standard Model. In this thesis a search for the H^+ , with the ATLAS experiment at the Large Hadron Collider, LHC, at CERN based on data taken in 2011, are described. A re-analysis of the charged Higgs boson search, utilising the ratio-method, was performed, which greatly enhanced the sensitivity compared to the traditional direct search approach.

Light charged Higgs bosons, with a mass lower than the top quark mass, can be produced in top quark decays. Due to the large production cross-section of top quark pairs the light charged Higgs bosons are accessible with early LHC data, in contrast to charged Higgs bosons heavier than the top quark mass. For light charged Higgs bosons the decay via $H^\pm \rightarrow \tau^\pm \nu$ is predominant in most theories and scenarios, in the most parts of their phase space. Therefore the τ identification and the τ mis-identification probabilities play an important role in the charged Higgs boson search. A tag-and-probe selection of $Z \rightarrow ee$ events was developed in order to asses the mis-identification probability of electrons as hadronically decaying τ leptons, utilising the very first data taken in 2010. The results of this analysis on the one hand provided scale factors crucial for all analyses utilising the electron veto algorithms of the τ identification. On the other hand a data-driven estimation technique for backgrounds stemming from electrons mis-identified as hadronically decaying τ leptons, dedicated for the charged Higgs boson search, was developed and successfully implemented, based upon the results of the tag-and-probe mis-identification results.

Trigger studies for the charged Higgs boson search aiming at the highest feasible signal efficiencies with the utilised combination of τ trigger and missing transverse energy trigger, during the 2012 data taking at a centre of mass energy of 8 TeV, were performed. Novel trigger items were designed, thoroughly tested and finally implemented into the trigger menu of the ATLAS experiment for data taking in 2012.

A direct charged Higgs boson search in three channels with τ leptons in the final state, was performed on the full dataset, with an integrated luminosity of 4.6 fb^{-1} , taken in 2011 at a centre of mass energy of 7 TeV. No significant excess over the Standard Model expectation was observed in data, thus limits on $\mathcal{B}(t \rightarrow bH^+)$ were set.

Finally the channel with a hadronically decaying τ lepton and an additional electron or muon in the final state from the $t\bar{t}$ decay was re-analysed with the so-called ratio-method. This method measures ratios of event yields instead of evaluating distributions of discriminating variables, thus most of the dominating systematic uncertainties intrinsically cancel to first order. The observed data are found to be in agreement with the Standard Model predictions. Utilising the ratio-method the limits obtained on $\mathcal{B}(t \rightarrow bH^+)$ were significantly improved, compared to the direct search in this channel. When the results of the ratio-method analysis are combined with the results of the direct search for charged Higgs bosons in $t\bar{t}$ decays, with a hadronically decaying τ lepton and jets in the final state, upper limits on $\mathcal{B}(t \rightarrow bH^+)$ are set in the range of 0.8 %–3.4 %, for m_{H^+} between 90 GeV and 160 GeV.

The limits set on $\mathcal{B}(t \rightarrow bH^+)$ have direct implications on the identity of the Higgs-like particle, with a mass of approximately 126 GeV discovered in 2012 at the LHC, if the Minimal Supersymmetric extension of the Standard Model (MSSM) is realised in nature.

Contents

Kurzfassung	v
Abstract	vii
Contents	ix
1 Introduction	1
2 Theoretical Framework	3
2.1 The Standard Model of Particle Physics	3
2.1.1 Particles, Fields and Interactions	3
2.1.2 Gauge Theory in a Nutshell	6
2.1.3 Brout-Englert-Higgs Mechanism	9
2.2 Supersymmetry	11
2.2.1 Sources of Supersymmetry Breaking	20
2.2.2 Two Higgs Doublet Model	21
2.2.3 Charged Higgs Boson Production and Decay	22
2.3 Current Status of charged Higgs Boson Searches	24
3 Monte Carlo Simulation	33
3.1 Methodology of Monte Carlo Simulation	33
3.2 Monte Carlo Simulation for Electron to τ Mis-identification Analysis	35
3.3 Monte Carlo Simulation for H^\pm Analysis with Data taken 2010	35
3.4 Monte Carlo Simulation for H^\pm Analyses with Data taken 2011	37
4 LHC and the ATLAS Detector	41
4.1 The Large Hadron Collider	41
4.2 The ATLAS Detector	42
4.2.1 Magnet Systems	46
4.2.2 Inner Detector	47
4.2.3 Calorimeter Systems	50
4.2.4 Muon Spectrometer	60

4.2.5	Forward Detectors	61
4.2.6	Trigger and Data Acquisition	63
4.3	Data Taking	67
5	Event Selection and Data-Driven Background Estimation Techniques	73
5.1	Event Cleaning	74
5.2	Trigger for the Charged Higgs Boson Analyses	74
5.2.1	Trigger for the $\tau_{\text{had}} + \text{Lepton}$ and $\tau_{\text{lep}} + \text{Jets}$ Channels	75
5.2.2	Trigger for the $\tau_{\text{had}} + \text{Jets}$ Channel	77
5.3	Physics Object Reconstruction	77
5.3.1	Muons	77
5.3.2	Electrons	77
5.3.3	Jets	78
5.3.4	b -Tagging	79
5.3.5	Hadronically decaying τ Leptons	79
5.3.6	Missing Transverse Momentum	79
5.3.7	Removal of Geometric Overlaps between Objects	80
5.4	Selection and Cut Optimisation	80
5.4.1	$\tau_{\text{had}} + \text{Lepton}$ Analysis Selection	80
5.4.2	$\tau_{\text{lep}} + \text{Jets}$ Analysis Selection	82
5.4.3	$\tau_{\text{had}} + \text{Jets}$ Analysis Selection	83
5.5	Background Estimations	84
5.5.1	Measurement of the τ Lepton Mis-identification Probability from Electrons	84
5.5.2	Backgrounds with Electrons and Jets Mis-identified as τ Leptons	88
5.5.3	Embedding Method	92
5.5.4	Multi-Jet Background	92
5.5.5	Backgrounds with Mis-identified Leptons	93
6	Direct Searches for the Charged Higgs Boson	95
6.1	Analysis of the $\tau_{\text{had}} + \text{Lepton}$ Channel	95
6.2	Analysis of the $\tau_{\text{lep}} + \text{Jets}$ Channel	95
6.3	Analysis of the $\tau_{\text{had}} + \text{Jets}$ Channel	98
6.4	Systematic Uncertainties	101
6.4.1	Systematic Uncertainties of Detector Simulation	101
6.4.2	Systematic Uncertainties of Generation of $t\bar{t}$ Events	103
6.4.3	Systematic Uncertainties of Data-Driven Background Estimates	103
6.5	Results	107

7 Indirect Search for the Charged Higgs Boson – The Ratio-Method	111
7.1 Ratio-Method:	
A Re-Analysis of the $\tau_{\text{had}} + \text{Lepton}$ Channel	111
7.2 Event Selection	112
7.3 Measured Event Yield Ratios	115
7.4 Systematic Uncertainties	115
7.4.1 Systematic Uncertainties of Detector Simulation	115
7.4.2 Systematic Uncertainties of Generation of $t\bar{t}$ Events	115
7.4.3 Systematic Uncertainties of Data-Driven Background Estimates	118
7.5 Results	119
7.5.1 Upper Limits obtained from Results of the Ratio-Method	119
7.5.2 Combination of Upper Limits obtained from Direct Searches for Charged Higgs Bosons in the $\tau_{\text{had}} + \text{jets}$ final state and the Ratio-Method Results	124
8 Comparison and Discussion of the Results	131
9 Summary and Outlook	137
A Monte Carlo Simulation Samples	141
A.1 Monte Carlo Simulation Samples for 2010 Analyses	141
A.1.1 Monte Carlo Simulation Samples for the Electron to τ Lepton Mis-identification Analysis	141
A.1.2 Monte Carlo Simulation Samples for the H^\pm Analysis	143
A.2 Monte Carlo Simulation Samples for 2011 Analyses	147
A.2.1 Monte Carlo Samples for H^\pm Ratio-Method Search Analysis	147
List of Figures	149
List of Tables	153
Bibliography	155
Acknowledgements	179

Chapter 1

Introduction

A famous physicist once stated: “It can scarcely be denied that the supreme goal of all theory is to make the irreducible basic elements as simple and as few as possible without having to surrender the adequate representation of a single datum of experience.” [1] or simplified: “Everything should be made as simple as possible, but no simpler.” The Standard Model of particle physics (SM) [2–4], introduced in the sixties of the 20th century, is consistent with all data gathered by high energy physics experiments, hitherto. Based on a set of symmetries it presents an axiomatic and potent model. Nevertheless, shortcomings to answer fundamentally important questions may indicate that it is indeed too simple. For example in the SM, dark matter and dark energy cannot be explained, the force of gravity is not incorporated, and a seemingly unnatural fine tuning of the Higgs Boson mass is necessary [5]. There are many candidates for extensions of the SM [6]. The simplest one for the Higgs sector is the Two Higgs Doublet Model (2HDM), achieved by adding a second Higgs doublet. It is compatible with the gauge invariance and contains in total five Higgs bosons, two charged, H^\pm , and three neutral, h^0 , H^0 and A^0 . A further possible and in terms of symmetry appealing extension is Supersymmetry [7, 8], which doubles the particle content of the SM. The Minimal Supersymmetric extension of the SM (MSSM) [9–12] is, due to its simplicity, one of the most studied and tested scenarios at the Large Hadron Collider (LHC) [13, 14]. The MSSM Higgs sector, if the supersymmetric particles are heavy enough, is a constrained 2HDM (type-II) [15–17] at low energies. The discovery of a charged scalar particle would thus clearly indicate the existence of physics beyond the SM, as H^\pm are also featured in many other extensions of the SM [18–20]. This thesis will focus on the search for light charged Higgs bosons, with a mass lower than the top quark mass. Subsequently the main production mechanism for light charged Higgs bosons is top quark decays, $t \rightarrow bH^+$.¹ The greatest source for top quarks at the LHC is the production of top pairs.

2012 was the year of the discovery of the Higgs-like particle [21, 22], with a mass of ap-

¹ In the following, charged Higgs bosons are denoted H^+ , with the charge-conjugate H^- always implied.

proximately 126 GeV² at the LHC at CERN³. Assuming this boson is one of the neutral MSSM Higgs bosons, only certain values of the MSSM parameters m_{H^+} and $\tan\beta$ are allowed for a given scenario. If the discovered boson is the lightest neutral MSSM Higgs boson (h^0), this would imply $\tan\beta > 3$ and $m_{H^+} > 155$ GeV [23]. On the one hand, the allowed region depends strongly on MSSM parameters, which on the other hand do not affect the charged Higgs boson production and decay significantly. Thus, by adjusting these MSSM parameters, the region in which the light neutral Higgs boson mass can take a value of about 126 GeV can change significantly. Should the recently discovered boson instead be the heavier CP-even Higgs boson (H^0), the additional constraint from $m_{H^0} \simeq 126$ GeV leads to an upper limit of roughly $m_{H^+} < 150$ GeV with suppressed couplings for h^0 [23]. If the recently discovered particle is a MSSM Higgs boson, excluding a low-mass charged Higgs boson would thus imply that it is the lightest neutral state, h^0 .

This thesis will guide through the searches for the light charged Higgs boson with τ leptons in the final state. The searches are performed with 4.6 fb^{-1} of data taken in 2011 at a centre of mass energy of 7 TeV by the ATLAS experiment [24] at the LHC.

Chapter 2 gives an overview of the Standard Model of particle physics, its problems, and possible extensions, with an emphasis on the Two Higgs Doublet Model (2HDM) and the charged Higgs boson production at the LHC, as well as the current status of charged Higgs boson searches.

Chapter 3 will introduce Monte Carlo simulation techniques, which are utilised for the prediction of physics processes at particle colliders.

Chapter 4 describes the LHC and the ATLAS detector.

Chapter 5 outlines the basic event selection and introduces the reconstructed entities, as well as describes the developed and utilised data-driven background estimation techniques.

Chapter 6 summarises the direct searches, conducted with data gathered in 2011 by the ATLAS detector, for the light charged Higgs boson and their results.

Chapter 7 re-analyses the τ +lepton channel with a novel approach, the ratio-method, which due to cancellation of most systematic uncertainties significantly enhances the sensitivity and improves the results of the direct searches.

Chapter 8 compares the results of the analyses described in this work with further charged Higgs boson searches conducted at the LHC.

Chapter 9 closes with a short summary and an outlook into the future of charged Higgs boson searches at the LHC.

² A system of units with $\hbar=c=1$ is used in this work.

³ “Organisation Européenne pour la Recherche Nucléaire” (European Organisation for Nuclear Research), the acronym CERN stems from the former name “Conseil Européen pour la Recherche Nucléaire” (European Council for Nuclear Research).

Chapter 2

Theoretical Framework

2.1 The Standard Model of Particle Physics

2.1.1 Particles, Fields and Interactions

The Standard Model (SM) of particle physics [2–4, 25–35] is a Quantum Field Theory (QFT) which describes the known particles and their couplings. Based on the gauge symmetry $SU(3)_C \times SU(2)_L \times U(1)_Y$ it is consistent with available electroweak precision data gathered at high energy physics experiments [36].

Its fundamental particles are fermions carrying a spin of $|s| = \frac{1}{2}$, the leptons and quarks, for which an overview is given in Table 2.1. Both carry electric, Q , except for the neutrinos, as well as weak charge, \vec{I} , a formalisation of the spin. The quarks have one additional quantum number of the strong force called colour (C). The single colour charges are named red, green, blue, with corresponding anti-colours. As a result of the required local gauge symmetry, forces are mediated by exchange of particles carrying an integer spin, which are called gauge bosons. An overview is given in Table 2.2. The photon, γ , is the exchange particle of the electromagnetic force. The photon mass is zero and the electromagnetic force has infinite range. Weak forces are mediated via W^\pm and Z bosons. The weak charge was introduced similarly to the strong isospin, mathematically described as a $SU(2)$ symmetry, to correctly describe this interaction. Charged and neutral weak interactions exist. The names were given historically depending whether the electric charge of a particles changed by one unit during the interaction. Mediators of the charged weak force, W^\pm , couple to left chiral particles and right chiral antiparticles only. A useful tool to connect the third component of the weak charge with the electrical charge is the Gell-Mann-Nishijima Equation 2.1, introducing the hypercharge, Y , conserved under weak interaction, important for the Glashow-Weinberg-Salam theory.

$$Q = \frac{Y}{2} + I_3^W \quad (2.1)$$

The weak interaction owns its name to its relative weakness, with respect to the electromagnetic interaction at low momentum transfers. Values of the coupling “constants” change with

family or generation			quantum numbers		
I	II	III	I_3^W	Q	Y^W
$\begin{pmatrix} \nu_e \\ e^- \end{pmatrix}_L$	$\begin{pmatrix} \nu_\mu \\ \mu^- \end{pmatrix}_L$	$\begin{pmatrix} \nu_\tau \\ \tau^- \end{pmatrix}_L$	$\begin{pmatrix} +\frac{1}{2} \\ -\frac{1}{2} \end{pmatrix}$	0 -1	-1 -1
$\begin{pmatrix} u \\ d' \end{pmatrix}_L$	$\begin{pmatrix} c \\ s' \end{pmatrix}_L$	$\begin{pmatrix} t \\ b' \end{pmatrix}_L$	$\begin{pmatrix} +\frac{1}{2} \\ -\frac{1}{2} \end{pmatrix}$	$+\frac{2}{3}$ $-\frac{1}{3}$	$+\frac{1}{3}$ $+\frac{1}{3}$
ν_{e_R}	ν_{μ_R}	ν_{τ_R}	0	0	0
e_R^-	μ_R^-	τ_R^-	0	-1	-2
u_R	c_R	t_R	0	$+\frac{2}{3}$	$+\frac{4}{3}$
d'_R	s'_R	b'_R	0	$-\frac{1}{3}$	$-\frac{2}{3}$

Table 2.1: Fermions ordered in electroweak multiplets, with selected quantum numbers. [36]

the scale of interaction energy, as depicted in Figure 2.1. This effect is called the running of coupling constants. The range of a force can be approximated with the Yukawa hypothesis [38], which makes use of Heisenberg's uncertainty principle, $\Delta E \cdot \Delta t \geq \frac{\hbar}{2}$. Therefore a force range, R_f , can be estimated by $R_f = c \cdot \Delta t$. Using the W^\pm mass, listed in Table 2.2, as energy scale, the range of the weak force can be approximated in the order of 10^{-18} m. Quantum Chromo Dynamics (QCD) is the field theory describing interactions of the coloured particles, a non-Abelian gauge theory. Self-coupling occurs between gluons, the massless mediators of the strong force. The potential energy of the QCD field rises with the distance of the interacting particles, which results in the so called confinement, meaning that no free colour charge has been observed yet.

interaction	boson	mass
electromagnetic	γ	$< 10^{-18}$ eV
neutral weak	Z	91.19 GeV
charged weak	W^\pm	80.40 GeV
strong	g	< 20 MeV

Table 2.2: List of the gauge bosons of the Standard Model of particle physics, with masses or their upper limits as determined by experimental data. [36, 39, 40]

Colour neutral mesons are made of a quark pair, one carrying a colour and the other the corresponding anti-colour. Baryons consist of three quarks each having one of the three different colours or anti-colours. Confinement is also the reason for hadronisation of quarks and gluons

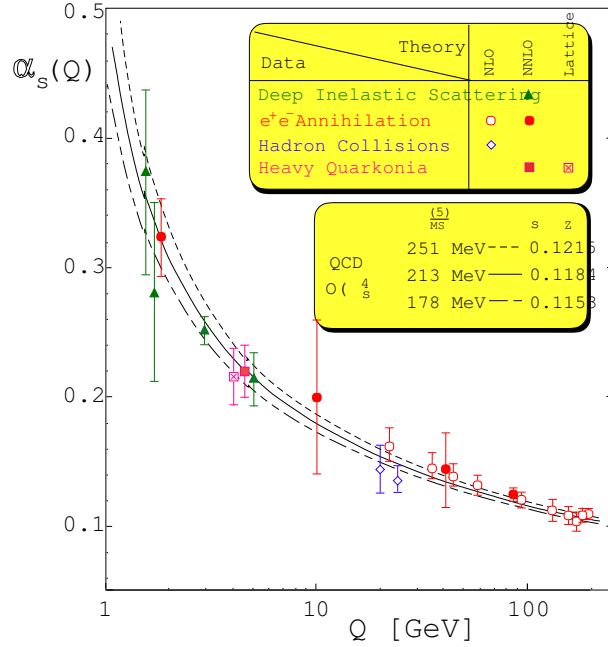


Figure 2.1: Summary of the running of the strong coupling, α_s , as a function of the respective energy scale, Q . [37]

in high energy interactions, which leads to jets of hadronic particles.

Leptons and quarks are grouped into weak iso-spin-duplets and iso-spin-singlets. These are arranged in three families or generations according to their mass. The leptons are paired up in one carrying electric charge, as the electron, e^- , the muon, μ^- , the tau lepton, τ^- , and their weak interacting partners, the electron neutrino, muon neutrino and tau neutrino, ν_e , ν_μ , ν_τ . As the left chiral fermions and their partners have the same weak quantum number they are ordered into electroweak multiplets, as listed in Table 2.1. The quark pairs consist of one up-type and one down-type quark, named after the first generation quarks, and carry an electric charge of $+\frac{2}{3}$ and $-\frac{1}{3}$, respectively. Charm and strange are the names given to the second generation quarks. Top and bottom, sometimes called truth and beauty, are the quarks of the third generation. The top quark stands out, as it is heavier than the weak gauge bosons ($m_t > m_{W^\pm}, m_Z$). It decays faster than a $t\bar{t}$ bound state can form. Top quark studies could therefore reveal the nature of “free” quarks.

Most of the directly observable matter in the universe is made up of the first fermion generation. All fermions of the 2nd and 3rd generations have higher masses, as listed in Table 2.3 and decay to the lightest stable quark or lepton. Solar, atmospheric, reactor and accelerator neutrino experiments, indirectly via the measurement of neutrino oscillations, confirm that neutrinos have nonzero masses [36]. The neutrino mass eigenstates are not equal to their electroweak ones, similar to the quarks. A consequence is neutrino oscillation as predicted by Pontecorvo [41–44]. The Pontecorvo-Maki-Nakagawa-Sakata (PMNS) matrix provides a relation between the mass eigenstates and electroweak eigenstates of the neutrinos. The Cabibbo-

family	lepton	mass (MeV)	generation	quark	mass (MeV)
I	e^-	0.5110	I	u	$2.3^{+0.7}_{-0.5}$
	ν_e	< 0.0022		d	$4.8^{+0.7}_{-0.3}$
II	μ^-	105.7	II	c	1 275
	ν_μ	< 0.008		s	95
III	τ^-	1 777	III	t	173 500
	ν_τ	< 18.2		b	4 650

Table 2.3: Fermions of the Standard Model of particle physics. [36]

Kobayashi-Maskawa (CKM) matrix provides this relation for the quarks [45]. Oscillations are observed in $K^0 - \bar{K}^0$ [46], $B^0 - \bar{B}^0$ [47] and $B_s^0 - \bar{B}_s^0$ [48] systems. Evidence of $D^0 - \bar{D}^0$ oscillations have been reported by three experiments using different D^0 decay channels [49–53]; an observation was claimed by the LHCb collaboration [54]. The imaginary phase in the CKM-matrix is very important, because it is the source of CP-violation and a contribution to the observed imbalance between matter and anti-matter in the universe.

2.1.2 Gauge Theory in a Nutshell

The unification of the electromagnetic and weak force was accomplished by S.L. Glashow, A. Salam and S. Weinberg (GSW) [2–4]. An important step in this direction was the idea that weak neutral and charged currents together form the symmetry group $SU(2)_L \times U(1)_Y$. The subscript “ L ” indicates that the weak isospin current couples to left-handed fermions and right-handed anti-fermions only. Introducing helicity in the Lagrangian a calculation results in the so-called “vector minus axial” (V-A) nature of the charged currents [55]. The symmetry group $SU(2)_L \times U(1)_Y$, with the hypercharge, Y , as defined by the Gell-Mann-Nishijima Equation 2.1, contains the electromagnetic interaction and the weak interaction. The GSW-theory was very successful in relating masses of weak gauge bosons to the gauge couplings. Invariance under local gauge transformations of the Lagrangian, which describes particle states, is considered a fundamental principle to describe their interactions. The Lagrangian density, \mathcal{L} , itself cannot be derived from underlying principles, but has to be found and validated using the basic principle of physics and nature: the principle of least action, given in Equation 2.2. It states that the action, S , during the transition of a physical system between two states is minimal. In case of quantum field theories S is a functional of the Lagrangian density, \mathcal{L} .

$$S = \int_{state_1}^{state_2} d^4x \mathcal{L}(\partial_\mu \psi(x), \partial_\mu \bar{\psi}(x), \psi(x), \bar{\psi}(x)) \quad (2.2)$$

With help of the Euler-Lagrange formalism (2.3) and the Lagrangian of a relativistic massive fermion (2.4) the Dirac Equation 2.5 can be derived. It describes the propagation of a fermion through space-time.

$$\frac{\partial \mathcal{L}}{\partial \bar{\psi}(x)} - \partial_\mu \frac{\partial \mathcal{L}}{\partial (\partial_\mu \bar{\psi}(x))} = 0 \quad (2.3)$$

$$\mathcal{L} = \bar{\psi}(x)(i\partial_\mu \gamma^\mu - m)\psi(x) \quad (2.4)$$

$$(i\partial_\mu \gamma^\mu - m)\psi(x) = 0 \quad (2.5)$$

In Equations 2.4, 2.3 and 2.5 $\psi(x)$ represents a Dirac field. It should be noted that the field itself is not an observable, only $|\psi(x)|^2$ is. Applying a global phase, α , in all space-time points, x , the gauge transformation on $\psi(x) \rightarrow e^{i\alpha}\psi(x)$ does not change the associated Lagrangian, \mathcal{L} , (2.4). As a global gauge symmetry can not be utilised to make predictions a local gauge symmetry is imposed. Applying a local gauge transformation, with $\alpha(x)$ varying at each point of space-time, the transformation $\psi(x) \rightarrow e^{i\alpha(x)}\psi(x)$ does change the equation of motion, which is not desired. To restore the invariance, also under local gauge transformation, a method called minimal coupling is applied. The derivative ∂_μ is replaced by the covariant derivative D_μ , defined in Equation 2.6. It requires the introduction of a new field, in this case a vector field, $A_\mu(x)$.

$$\partial_\mu \rightarrow D_\mu = \partial_\mu + iQeA_\mu, \quad (2.6)$$

where A_μ at the same time transforms as followed:

$$A_\mu \rightarrow A'_\mu = A_\mu + \frac{1}{Qe}\partial_\mu\alpha. \quad (2.7)$$

The thus modified Lagrangian, \mathcal{L}' , is invariant under the local gauge transformation, as terms stemming from the covariant derivative, compensate the before troublesome terms. The $A_\mu(x)$ field can be interpreted as the field of the photon, γ . A mass term, $\frac{1}{2}M_\gamma^2 A_\mu(x)A^\mu(x)$, would however destroy the just restored local gauge symmetry. The Lagrangian of quantum electrodynamics (QED) for fermions and massless photons is thus given by:

$$\mathcal{L}_{QED} = \bar{\psi}(x)(i\gamma_\mu \partial^\mu - m)\psi(x) - \frac{1}{4}F_{\mu\nu}(x)F^{\mu\nu}(x) + Qe\bar{\psi}(x)\gamma_\mu A^\mu(x)\psi(x), \quad (2.8)$$

with $F_{\mu\nu}$ the the “field strength tensor” defined as [56]:

$$F_{\mu\nu}(x) = \partial_\mu A_\nu(x) - \partial_\nu A_\mu(x). \quad (2.9)$$

Fermion masses are added “by hand” to \mathcal{L}_{QED} . The electroweak Lagrangian, \mathcal{L}_{EW} , must be extended by the gauge fields \vec{W}_μ and B_μ of the $SU(2)_L \times U(1)_Y$ group. It is rather troublesome that the requirement for local gauge invariance of \mathcal{L}_{EW} does again not allow for mass terms,

neither for the \vec{W}_μ -field and B_μ -field nor the fermions, as the weak interaction couples differently to left and right chiral particles.

$$\mathcal{L}_{EW} = \bar{\chi}_L \gamma^\mu D_\mu \chi_L + \bar{\nu}_R \gamma^\mu D_\mu \nu_R + \bar{e}_R \gamma^\mu D_\mu e_R - \frac{1}{4} \vec{W}_{\mu\nu} \vec{W}^{\mu\nu} - \frac{1}{4} B_{\mu\nu} B^{\mu\nu} \quad (2.10)$$

where

$$D_\mu = \partial_\mu - ig \frac{1}{2} \vec{\tau} \cdot \vec{W}_\mu - ig' \frac{Y}{2} B_\mu, \quad (2.11)$$

$$\chi_L = \begin{pmatrix} \nu \\ e \end{pmatrix}_L$$

and

$$\vec{W}_{\mu\nu} = \partial_\mu \vec{W}_\nu - \partial_\nu \vec{W}_\mu - g W_\mu \times W_\nu, \quad (2.12)$$

$$B_{\mu\nu}(x) = \partial_\mu B_\nu - \partial_\nu B_\mu. \quad (2.13)$$

These gauge fields cannot be associated directly with physical fields or particles. The physical neutral current fields, A_μ and Z_μ , identified with the gauge bosons γ and Z , can be interpreted as linear combinations of the third component of the \vec{W}_μ -field and the B_μ -field [57]. This mixing of fields can be parametrised by the weak mixing angle, θ_W . It provides the connection between the gauge fields and the physical measurable gauge particles.

$$\begin{pmatrix} A_\mu \\ Z_\mu \end{pmatrix} = \begin{pmatrix} \cos \theta_W & \sin \theta_W \\ -\sin \theta_W & \cos \theta_W \end{pmatrix} \begin{pmatrix} B_\mu \\ W_\mu^3 \end{pmatrix} \quad (2.14)$$

θ_W is not predictable, but can only be measured by experiment. The weak mixing angle has an experimentally determined value of $\sin^2(\theta_W) \approx 0.231$ [36]. The physical W^\pm bosons can be interpreted as a linear combination of the remaining first and second component of the W_μ -field:

$$W^\pm = \frac{1}{\sqrt{2}} (W_\mu^1 \mp i W_\mu^2). \quad (2.15)$$

The masses of the gauge bosons Z and W^\pm , as well as the fermions are required to be zero according the GSW-theory, as in any gauge theory, a clear contradiction to experimental observations. The GSW-theory is nevertheless very successful in describing the electroweak interactions of particles. For instance, interference of the Z and γ in the process $e^- e^+ \rightarrow \mu^- \mu^+$ introduces a forward-backward-asymmetry, which do not occur when considering only quantum electrodynamic contributions. This asymmetry was first verified by the PETRA experiments [55]. The GSW-model thus should to be extended by a mechanism that is able to generate gauge boson masses and fermion masses and respects the local gauge symmetry.

2.1.3 Brout-Englert-Higgs Mechanism

A thin plastic strip between thumb and index finger will, once force is applied, either curve to the right or the left. These are the ground states of the new system, both break the left-right symmetry [55, 56]. Replacing the imagined strip with a thin rod takes the step from a discrete symmetry to a continuous symmetry, as a rod can take any bent position as ground state, a simple analogon to illustrate the principle of spontaneous symmetry breaking. It is the fundament of the Brout-Englert-Higgs mechanism [58–63]. Breaking the global gauge invariance of a system would, according to the Goldstone theorem [64], result in one or more massless bosons. There is no experimental evidence for Brout-Englert-Higgs Goldstone bosons. However by breaking the local gauge symmetry Goldstone ghost fields can be absorbed by gauge bosons, which gain an additional degree of freedom. The longitudinal polarisation, additionally to the two transverse polarisations, is just what was needed for the bosons to acquire mass [62]. By adding \mathcal{L}_{Higgs} (2.17), invariant under local $SU(2)$ gauge transformations and containing four scalar fields ϕ_i , to \mathcal{L}_{EW} massive gauge bosons can be generated. These fields can then be arranged in an isospin doublet Φ with weak hypercharge $Y^W = 1$:

$$\Phi = \begin{pmatrix} \Phi^+ \\ \Phi^0 \end{pmatrix} = \frac{1}{\sqrt{2}} \begin{pmatrix} \phi_1 + i\phi_2 \\ \phi_3 + i\phi_4 \end{pmatrix}. \quad (2.16)$$

$$\mathcal{L}_{Higgs} = (D_\mu \Phi)^\dagger (D^\mu \Phi) - V(\Phi), \quad (2.17)$$

with

$$V(\Phi) = \mu^2 \Phi^\dagger \Phi + \lambda (\Phi^\dagger \Phi)^2, \quad (2.18)$$

with D_μ as given in Equation 2.11. The Higgs potential, $V(\Phi)$, is relevant for mass generation only if $\mu^2 < 0$ and $\lambda > 0$ as illustrated in Figure 2.2. Only in this parameter space it acquires a non-trivial minimum with a finite value for $\langle \Phi^\dagger \Phi \rangle = -\frac{\mu^2}{2\lambda}$. Without loss of generality the field can be expanded pertubatively around the minimum:

$$\Phi_0 = \frac{1}{\sqrt{2}} \begin{pmatrix} 0 \\ v \end{pmatrix}, \quad (2.19)$$

with

$$\langle |\phi_3|^2 \rangle = -\frac{\mu^2}{2\lambda} \equiv \frac{v^2}{2}. \quad (2.20)$$

Relation 2.19 defines the Vacuum Expectation Value (VEV), v . Expanding $\Phi(x)$ around the chosen minimum, Φ_0 , yields:

$$\Phi_0 = \frac{1}{\sqrt{2}} \begin{pmatrix} 0 \\ v + h(x) \end{pmatrix}. \quad (2.21)$$

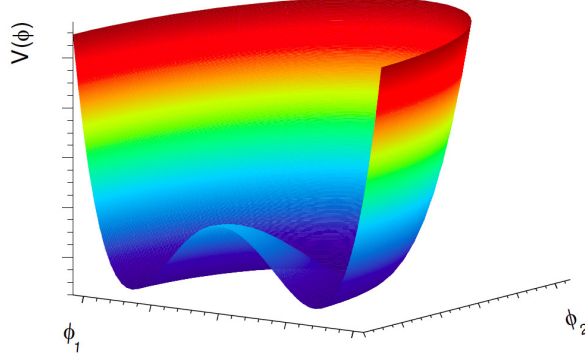


Figure 2.2: The Higgs potential, $V(\Phi)$, as function of two, out of four ϕ - fields. [65]

Where $h(x)$ is the field of the scalar Higgs boson, H [66]. Introducing Φ_0 in Equation 2.17 reveals the masses of the boson field to have the following form: $\frac{g^2 v^2}{8} [(W_\mu^2)^2 + (W_\mu^1)^2 + (W_\mu^3)^2]$.

The masses of bosons can be extracted from the complete Lagrangian as followed [55]:

$$\begin{aligned} m_{W^\pm} &= \frac{v}{2} g, \\ m_Z &= \frac{v}{2} \sqrt{g^2 + g'^2}, \\ m_H &= v \sqrt{2\lambda}. \end{aligned}$$

The charged lepton is still massless, as

$$M_\ell \bar{\ell} \ell = M_\ell (\bar{\ell}_R \ell_L + \bar{\ell}_L \ell_R),$$

mixes L and R lepton field, ℓ , components and would break the gauge invariance [67]. A way to give mass in a gauge invariant way is via the Yukawa coupling, G_ℓ , of the leptons with the Higgs field, by adding the Yukawa interaction terms:

$$\mathcal{L}_{\text{yuk}}^\ell = -\frac{G_\ell v}{\sqrt{2}} \bar{\ell} \ell - \frac{G_\ell}{\sqrt{2}} \bar{\ell} \ell H. \quad (2.22)$$

The charged lepton mass can be identified as:

$$M_\ell = \frac{G_\ell v}{\sqrt{2}}. \quad (2.23)$$

This procedure is able to generate a mass term for the fermion in a gauge invariant way. It does not specify the value of the mass as the introduced Yukawa constant, G_ℓ , is arbitrary [67]. The Higgs to lepton coupling strength,

$$C_{\bar{\ell} \ell H} = \frac{M_\ell}{v}, \quad (2.24)$$

is obtained. This is a precise prediction of the Standard Model that the LHC experiments should soon be able to verify experimentally.

Down-type fermions need an additional Higgs doublet for mass generation, which is the charge conjugated of Φ . Values of g and g' are related to the weak mixing angle, θ_W , via the relation $g' = g \cdot \tan \theta_W$. The tree level relation of the weak boson masses follows: $M_W = M_Z \cdot \cos \theta_W$. Eventually θ_W and v are related to the Fermi coupling, G_F , via:

$$\frac{1}{2v^2} = \frac{G_F}{\sqrt{2}}. \quad (2.25)$$

Its value is experimentally determined to $v = 246 \text{ GeV}$, fixed by the high precision muon decay measurements of G_F [68–70]. The masses of the weak bosons were predicted, by measurements of related physical constants [2–4] 15 years before their direct discovery, by the UA1 and UA2 (Underground Area 1&2) experiments at the Super Proton Synchrotron (SPS) at CERN in 1983 [71–74]. To have physical relevance the QFT of the SM has to be renormalisable. This nontrivial proof for the Brout-Englert-Higgs mechanism extended GSW-model was achieved by 't Hooft in 1971, four years after the theory was introduced.

In 2012, over 40 years after its postulation, the discovery of the Higgs-like particle [21, 22], with a mass around 126 GeV , within the mass range preferred by the SM, was announced by two LHC experiments. This is a great achievement considering the low rate at which Higgs bosons are produced at the LHC, compared to other SM processes, as illustrated in Figure 2.3. Latest measurements show that the newly discovered particle very probably has no spin and a positive parity, just as expected of SM Higgs bosons [75–79]. The missing piece is a precision measurement of the Higgs to fermion couplings, κ_F , first measurements were already conducted [78, 80, 81], more data however is necessary to reduce the uncertainties on the measured κ_F .

2.2 Supersymmetry

The SM describes matter particles and interactions down to quantum corrections and at per mill level. Still some problems remain unresolved. For example, dark matter is not explained in the SM, unnatural precise fine tuning of the Higgs mass at Born level, also known as the hierarchy problem, is necessary and gravity is not included. The unification of the three forces, electromagnetic, weak and strong, can not occur in the SM. The theory describing such a force unification scenario is called the Grand Unified Theory (GUT). The Haag-Łopuszański-Sohnius-theorem [83], an extension of the Coleman-Mandula theorem [84], states, that possible extensions of the Standard Model, which provide mass gaps, do not necessarily have to be members of the Poincaré group or an internal symmetry. As a nontrivial extension of the Poincaré algebra supersymmetry (SUSY) [7, 8] is a valid possibility. In the following the Minimal Supersymmetric Standard Model (MSSM) [9–12], as a special SUSY model is considered. A new

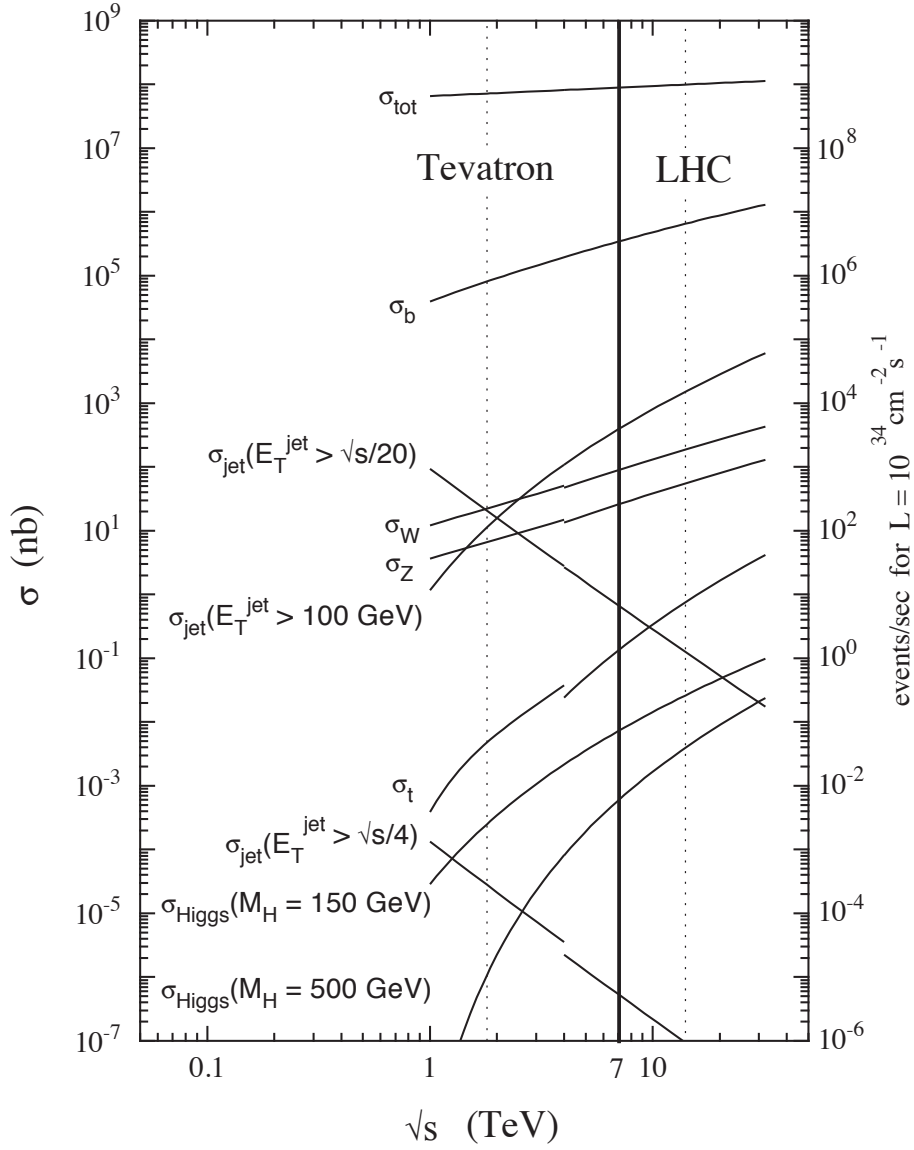


Figure 2.3: The SM production cross-sections (left axis) and events per second for a luminosity of $10^{34} \text{ cm}^{-2} \text{ s}^{-1}$ (right axis), as a function of the centre of mass energy, \sqrt{s} . On the left half of the plot ($\sqrt{s} < 5 \text{ TeV}$) the $p\bar{p}$ cross-sections, denoted by “Tevatron”, are given and on the right side ($\sqrt{s} > 5 \text{ TeV}$) pp cross-sections are given, denoted by “LHC”, thus a discontinuity in the cross-sections is observable in the plot. [82] (the image was modified to better visualise the $\sqrt{s} = 7 \text{ TeV}$ working point)

discrete symmetry, the R-parity, is introduced [85]:

$$P_R = (-1)^{(2s+3B+L)}, \quad (2.26)$$

with “ L ” the lepton number, “ B ” the baryon number and s the spin. With this definition SM particles have a R -parity value of 1 and therefore a R -parity value of -1 follows for SUSY particles. The generators of SUSY have to satisfy an algebra of anti-commutation and commutation relations, with P^μ , the four-momentum generator of space-time translations, of the form [86]:

$$\{Q, Q^\dagger\} = P^\mu, \quad (2.27)$$

$$\{Q, Q\} = \{Q^\dagger, Q^\dagger\} = 0, \quad (2.28)$$

$$[P^\mu, Q] = [P^\mu, Q^\dagger] = 0. \quad (2.29)$$

This symmetry introduces a superpartner for each SM particle. Applying the Q operator on a fermionic state creates a bosonic state and vice versa.

$$Q |\text{boson}\rangle = |\text{fermion}\rangle \quad Q |\text{fermion}\rangle = |\text{boson}\rangle \quad (2.30)$$

The SM field and superpartners created by applying Q belong to a supermultiplet. They have a spin of $s_{\text{SUSY}} = s_{\text{SM}} - \frac{1}{2}$, except the Higgs bosons, where $\frac{1}{2}$ is added. All quantum numbers, these are listed in Table 2.4, except for s and all couplings are equal. The nomenclature for SUSY-particles states that SUSY-bosons or “scalar” fermions get a “s-” prefix. SUSY-fermions, the gauginos, are indicated via the appendix “-ino”. This results in sparticle names as for example the selectron, \tilde{e} , the winos, \tilde{W}^\pm and the stop, \tilde{t} . The SUSY-particles are marked with a tilde ($\tilde{}$). Due to effects of electroweak symmetry breaking a mixing of higgsinos and electroweak gauginos occurs. The charged higgsinos (\tilde{h}_u^+ and \tilde{h}_d^-) and winos (\tilde{W}^\pm) form two mass eigenstates with an electric charge of ± 1 , the charginos ($\tilde{\chi}_i^\pm$). Following this pattern neutral higgsinos (\tilde{h}_u^0 and \tilde{h}_d^0) and neutral gauginos (\tilde{W}^0 and \tilde{B}^0) form four mass eigenstates, the neutralinos ($\tilde{\chi}_i^0$), as listed in Table 2.5. In most SUSY models the lightest neutralino, $\tilde{\chi}_1^0$, is found to be the lightest SUSY-particle. Commonly the indices i are increased the higher the sparticle masses are. The MSSM states that Higgs doublets mix, yielding five mass eigenstates, as three of the eight possible Goldstone bosons are absorbed by Z and W^\pm to produce their masses. The five massive scalar Higgs bosons of the MSSM are therefore:

h^0 light CP-even,

H^0 heavy CP-even,

A^0 CP-odd,

H^\pm charged Higgs bosons.

(s)particles	$s = 0$	$s = \frac{1}{2}$	$(SU(3)_C, SU(2)_L, U(1)_Y)$
sleptons,	$(\tilde{\nu} \tilde{e}_L)$	(νe_L)	$(1, 2, -\frac{1}{2})$
leptons	\tilde{e}_R	e_R	$(1, 1, 1)$
($\times 3$ families)			
squarks,	$(\tilde{u}_L \tilde{d}_L)$	$(u_L d_L)$	$(3, 2, \frac{1}{6})$
quarks	\tilde{u}_R	u_R	$(\bar{3}, 1, -\frac{2}{3})$
($\times 3$ families)	\tilde{d}_R	d_R	$(\bar{3}, 1, \frac{1}{3})$
Higgs,	$(h_u^+ h_u^0)$	$(\tilde{h}_u^+ \tilde{h}_u^0)$	$(1, 2, +\frac{1}{2})$
Higgsinos	$(h_d^0 h_d^-)$	$(\tilde{h}_d^0 \tilde{h}_d^-)$	$(1, 2, -\frac{1}{2})$
(s)particles	$s = \frac{1}{2}$	$s = 1$	$(SU(3)_C, SU(2)_L, U(1)_Y)$
gluino, gluon	\tilde{g}	g	$(8, 1, 0)$
winos, W bosons	$\tilde{W}^\pm \tilde{W}^0$	$W^\pm W^0$	$(1, 3, 0)$
bino, B boson	\tilde{B}^0	B^0	$(1, 1, 0)$

Table 2.4: The MSSM super-multiplets. [86]

The value of $\tan\beta$ is defined as the ratio of VEVs of the two Higgs doublets v_u and v_d :

$$\tan\beta = \frac{v_u}{v_d}. \quad (2.31)$$

Fixing $\tan\beta$ and one Higgs boson mass, preferred by literature are m_{A^0} or m_{H^\pm} , at the tree level is common practise to define a certain scenario.

The decay fractions of the different Higgs bosons are not determined by their mass alone. A small selection of the best studied MSSM scenarios is given in the following:

- Decoupling regime: $m_A \geq 150$ GeV for $\tan\beta = 30$ and $m_A \geq 400 - 500$ GeV for $\tan\beta = 3$. The last region results in the highest h^0 -mass. It then follows closely the decay schema drawn for the SM Higgs [87], shown in Figure 2.4. The heavier Higgs bosons decay channels are very sensible to the $\tan\beta$ value. An interesting issue is the strong enhancement of the couplings to the down-type fermions for $\tan\beta \gg 1$, leading to the decay of A^0 and H^0 into almost exclusively $b\bar{b}$ ($\sim 90\%$) and $\tau^+\tau^-$ ($\sim 10\%$).
- Anti-decoupling regime: $\tan\beta \geq 10$ and $m_A \leq m_{h^0}^{max}$. h^0 and A^0 decay via fermions $b\bar{b}$ ($\sim 90\%$) and $\tau^+\tau^-$ ($\sim 10\%$). H^\pm almost always decays into $\tau^\pm\nu_\tau$.
- Intense-coupling regime: $\tan\beta \geq 10$ and $m_A \sim 100 - 140$ GeV, stands out due to a strong suppression of the neutral Higgs into $\gamma\gamma$ decay, compared to the SM.

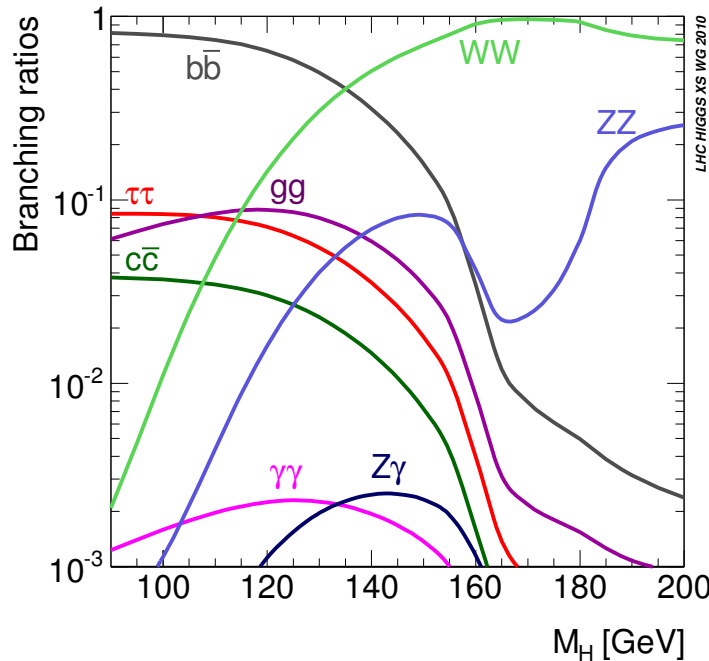


Figure 2.4: SM Higgs boson branching ratios as a function of the Higgs boson mass. [88]

Names	Spin	P_R	Gauge Eigenstates	Mass Eigenstates
Higgs bosons	0	+1	$h_u^0 \ h_d^0 \ h_u^+ \ h_d^-$	$h^0 \ H^0 \ A^0 \ H^\pm$
squarks	0	-1	$\tilde{u}_L \ \tilde{u}_R \ \tilde{d}_L \ \tilde{d}_R$	(same)
			$\tilde{s}_L \ \tilde{s}_R \ \tilde{c}_L \ \tilde{c}_R$ $\tilde{t}_L \ \tilde{t}_R \ \tilde{b}_L \ \tilde{b}_R$	(same) $\tilde{t}_1 \ \tilde{t}_2 \ \tilde{b}_1 \ \tilde{b}_2$
sleptons	0	-1	$\tilde{e}_L \ \tilde{e}_R \ \tilde{\nu}_e$	(same)
			$\tilde{\mu}_L \ \tilde{\mu}_R \ \tilde{\nu}_\mu$ $\tilde{\tau}_L \ \tilde{\tau}_R \ \tilde{\nu}_\tau$	(same) $\tilde{\tau}_1 \ \tilde{\tau}_2 \ \tilde{\nu}_\tau$
Neutralinos	$\frac{1}{2}$	-1	$\tilde{B}^0 \ \tilde{W}^0 \ \tilde{h}_u^0 \ \tilde{h}_d^0$	$\tilde{\chi}_1^0 \ \tilde{\chi}_2^0 \ \tilde{\chi}_3^0 \ \tilde{\chi}_4^0$
Charginos	$\frac{1}{2}$	-1	$\tilde{W}^\pm \ \tilde{h}_u^\pm \ \tilde{h}_d^-$	$\tilde{\chi}_1^\pm \ \tilde{\chi}_2^\pm$
gluino	$\frac{1}{2}$	-1	\tilde{g}	(same)
goldstino (gravitino)	$\frac{1}{2}$ $\left(\frac{3}{2}\right)$	-1	\tilde{G}	(same)

Table 2.5: Undiscovered (except for either h^0 or H^0 [21, 22], if SUSY is realised in nature) particles of the MSSM (with sfermion mixing of the first two families assumed as negligible). [86]

Grand Unified Theory (GUT)

The intersection of the three coupling constants, α_i , at the energy scale of new physics and below the Planck scale ($M_P = (8\pi G_{Newton})^{-\frac{1}{2}} = 2.4 \times 10^{18} \text{ GeV}$), would be the first step towards the GUT. M_P is the energy scale where quantum gravitational effects become important for particle interactions. Unfortunately the anticipated α_i crossing can not occur in the SM, as the interpolations towards higher interaction energies in Figure 2.5 show. Due to the additional particle content of SUSY-models the evolution of the coupling constants is modified such that an intersection of all three forces at interaction energies in the order of $O(10^{15} \text{ GeV})$, therefore named the GUT scale, is possible.

After the precise measurement of the $SU(3) \times SU(2) \times U(1)$ coupling constants, it has become possible to test the unification scenarios numerically.

In QFT the vacuum act as the medium. The vacuum, due to the presence of virtual pairs of particles, is polarised in the presence of a charge. The matter fields and transverse quanta of vector fields in this case behave like dipoles in a dielectric medium and cause screening, while the longitudinal quanta of vector fields behave like currents and induce anti-screening. Thus, the couplings become the functions of a distance or an energy scale,

$$\alpha_i = \alpha_i \left(\frac{Q^2}{\Lambda^2} \right) = \alpha_i(\text{distance}), \quad \alpha_i \equiv g_i^2 / 4\pi.$$

This dependence is described by the renormalisation group equations and is confirmed experimentally, as demonstrated in Figure 2.1. The three coupling constants to be compared are:

$$\begin{aligned} \alpha_1 &= (5/3)g'^2/(4\pi) = 5\alpha/(3 \cos^2 \theta_W), \\ \alpha_2 &= g^2/(4\pi) = \alpha/\sin^2 \theta_W, \\ \alpha_3 &= g_s^2/(4\pi), \end{aligned} \tag{2.32}$$

where g' , g and g_s are the $U(1)$, $SU(2)$ and $SU(3)$ coupling constants and α is the fine structure constant [89]. The factor of $5/3$ in the definition of α_1 has been included for proper normalisation of the generators. Assuming that the SM is valid up to the GUT scale, one can use the renormalisation group (RG) equations for the three couplings. The result of this interpolations is given in Figure 2.5, as an evolution of the inverse of the couplings as a function of the logarithm of the respective energy scale. In this presentation, the evolution becomes a straight line in first order. The second order corrections are small and do not cause any visible deviation from a straight line. Figure 2.5 clearly demonstrates that within the SM the coupling constant unification at a single point is impossible. It is excluded by more than 8 standard deviations [89, 90]. The unification can thus only be achieved if new physics enters between the electroweak scale and the Planck scale.

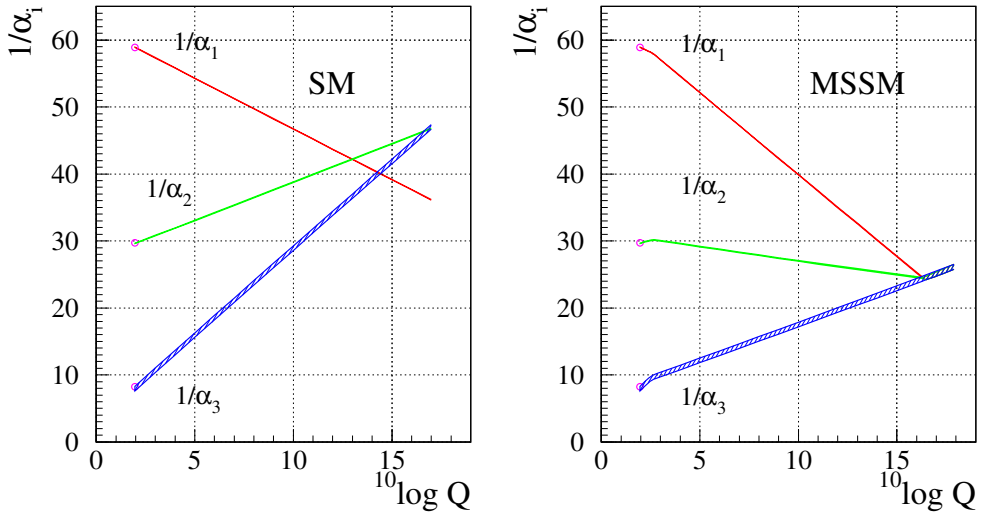


Figure 2.5: Evolution of the inverse of the three coupling constants as a function of the respective energy scale, Q , in the Standard Model (left) and in the MSSM (right). Only in the latter case unification is obtained. The SUSY particles are assumed to contribute only above the effective SUSY scale M_{SUSY} of about 1 TeV, which causes a change in the slope in the evolution of couplings. The thickness of the lines represents the error in the coupling constants. [89, 90] (picture edited)

Gravity

A globally broken supersymmetry implies the existence of a massless Weyl fermion called the goldstino. With supersymmetry as local symmetry it forms a new theory called supergravity [86]. It contains the superpartner of the graviton, the gravitino with a spin of $s = \frac{3}{2}$. This sparticle absorbs the goldstino and thereby acquires mass. This, due to its analogy, is called the super-Higgs mechanism. The interactions of the gravitino are suspected to be in the order of gravitational strength, thus will not play a role in present day collider physics. The gravitino mass is expected to be in the order of some 100 GeV, in a ‘‘Planck-scale-Mediated Supersymmetry Breaking’’ (PMSB) scenario, where the gravitino should be in the mass range of the other sparticles. Supergravity and certain MSSM scenarios raise hope for an unification of all four forces even below M_P .

Dark Matter

Only a few percent of the matter in the universe are made up of SM particles [91]. This result is obtained from astronomical observations and calculations concerning the movement of matter, which at these scales should be dominated by the gravitational force only. Models show that mass not directly observable has to drive the outer part of galaxies rotation velocity

(for a detailed description see chapter “23. Cosmological Parameters” in Reference [36]). As stated in Section 2.1.1 neutrinos do have mass. Calculations using the measured upper limits, as given in Table 2.3 reveal that neutrinos can not account for the expected dark matter exclusively [36]. They rather are a small piece of the puzzle. SUSY provides the lightest SUSY particle (LSP) [92, 93], the $\tilde{\chi}_1^0$ in Table 2.5. In most models and parameter spaces it is predicted to be heavier than the neutrinos, the reason for the mass difference will be provided in the following. As this sparticle neither carries strong nor electric charge it can only interact weakly or gravitationally, thereby making it a promising candidate for cold or cool dark matter, if stable. “Cold” describes the property of being non-relativistic at the beginning of galaxy formation. The decay of the LSP is prohibited, if R -parity conservation is assumed. Further consequence of P_R -conservation is the exclusive SUSY particle production in pairs. The motivation for this parity is the superpotential W_{MSSM} , which describes the Yukawa interactions of the MSSM. In its most common form it leads to a renormalisable Lagrangian density which contains lepton and baryon number violating terms, which would lead to a fast decay of the proton. Experimentally, with stored anti-protons, the proton was found to have a lifetime greater than 7×10^7 years, the theoretical lower bound ranges between $10^{31} - 10^{33}$ years, depending on the model assumed [36]. The R -parity conservation suppresses the proton decay. Another possible scenario is R -parity non-conservation, which results in a stable proton only if the Yukawa couplings are small.

Hierarchy Problem

Measuring the properties of weak interactions provides a vacuum expectation value of $\langle \Phi \rangle = m_H \sqrt{\frac{2}{\lambda}} \approx 174 \text{ GeV}$, where λ is the Higgs self-coupling parameter [36]. The m_H^2 receives quantum corrections from all particles interacting with the Higgs field directly and indirectly [94]. Two examples are shown in Figure 2.6. Here f is a massive fermion and couples with a term $\lambda_f H \bar{f} f$ in the Lagrangian and a heavy scalar particle S with mass m_S couples with the term $\lambda_S |H|^2 |S|^2$. This would lead to the following corrections of m_H^2 :

$$\Delta m_H^2 = -\frac{|\lambda_f|^2}{8\pi^2} \Lambda_{UV}^2 + \dots \quad (2.33)$$

$$\Delta m_H^2 = -\frac{|\lambda_S|^2}{16\pi^2} \left[\Lambda_{UV}^2 - 2m_S \ln\left(\frac{\Lambda_{UV}}{m_S}\right) + \dots \right]. \quad (2.34)$$

Λ_{UV} , the ultraviolet momentum cutoff, is used in QFT to regulate the loop integral. It seems reasonable to replace Λ_{UV} with a scale where new physics should appear, for example the GUT scale. Choosing dimensional regularisation on the loop integral instead of momentum cutoff, the Λ_{UV} terms vanish. The term containing m_S^2 cannot be eliminated without a counter term introduced for this sole purpose. In the momentum cutoff procedure counter terms performing mass tuning at Born level would have to reach a precision within the order of $\frac{m_H^2}{\Lambda^2} \approx 10^{-26}$. SUSY solves this fine tuning problem with its additional particle content, as sparticle mass corrections

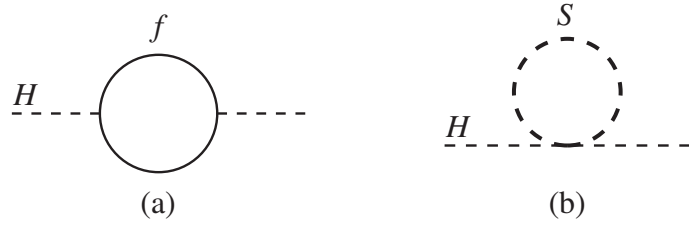


Figure 2.6: One-loop quantum corrections to the Higgs squared mass parameter, m_H^2 , due to (a) a Dirac fermion f , and (b) a scalar S . [86]

do have an opposite sign with respect to the fermion loop contributions. The same is true for the boson loops and their SUSY partners. Therefore physically motivated and exact counter terms for the hierarchy problem are generated. The downside of this argument is that there is no experimental evidence for a for example selectron with a mass of 511 keV. This implies that supersymmetry would have to be broken in the vacuum state, if realised in nature.

2.2.1 Sources of Supersymmetry Breaking

The hierarchy problem shows that supersymmetry has to be broken, otherwise it would have already been discovered. A beautiful aspect of the MSSM is that no new parameters except the Yukawa couplings are introduced. This property however is lost after the SUSY breaking. In the worst case scenario up to 105 free parameters would have to be introduced. “Soft” supersymmetry breaking describes breaking models that do not result in terms with quadratic divergences. Several models for supersymmetry breaking exist, some are shortly outlined in the following.

Supersymmetry Breaking by Non-Zero Term Vacuum Expectation Value

These non-soft breaking models build upon a vacuum state not invariant under supersymmetry caused by a non-vanishing term leading to a non-zero VEV. Such theories are separated into two groups, depending on the form of the non vanishing term. Fayet-Iliopoulos (D-term) breaking [9, 10, 95] introduces a term linear to the auxiliary field of the gauge supermultiplet. If this term drives the breaking, it would have to belong to a $U(1)$. Not the $U(1)_Y$, as this would only break colour and/or electromagnetism, but not SUSY. This ansatz only works if a hidden sector is assumed, in which a yet unknown $U(1)$ symmetry is realised and hardly couples to the visible world. A further problem is that in the D-term breaking scenario it is difficult to give the MSSM sparticles, especially the gauginos, appropriate masses. This downside brought this breaking theory on the brink of being ruled out.

The F-term or O’Raifeartaigh models [96] have brighter phenomenological prospects, as in detailed explained in the appendix of Reference [97]. These introduce a dimensional $([\text{mass}]^2)$ multiplicative parameter k of a linear chiral supermultiplet term in the superpotential. Although it seems unnatural that k needs to be tiny compared to the Planck scale [98], to create the correct

order of magnitude for a soft MSSM breaking, it fulfils most criteria of a physically relevant candidate [99].

Models with dynamical supersymmetry breaking make use of dimensional transmutation. A new non-Abelian gauge symmetry with gauge coupling, g , being perturbative at M_P is the main idea behind this breaking mechanism. Taking QCD as an analogy g gets stronger at scales smaller than the Planck scale.

Hidden Sector Supersymmetry Breaking

These theories assume that the source of symmetry breaking lies in an sector of particles which have no or only very small direct couplings to the “visible” sector. This sector is therefore called “hidden”. This category has famous members as the “gravity-mediated”, also called the Planck-scale-Mediated Supersymmetry Breaking scenario (PMSB), as it assumes that near M_P new physics, including gravity, enters. A special member of this group is the minimal SUperGRAvity, short mSUGRA [100–105] introducing only 5 additional parameters. The second competing theory family is the Gauge-Mediated Supersymmetry Breaking (GMSB). In this model the flavour-blind mediating interactions for SUSY are the ordinary electroweak and QCD gauge interactions, but introduce new chiral multiplets of messenger particles, which couple to a supersymmetry breaking vacuum expectation value.

Further hidden sector SUSY breaking theory members are hiding behind the acronyms XMSB (eXtra-dimensional-Mediated Supersymmetry Breaking) and AMSB (Anomaly-Mediated-Supersymmetry Breaking), Reference [86] provides a good overview and the References therein more details.

2.2.2 Two Higgs Doublet Model

The MSSM is the most studied and tested scenario at the LHC, therefore the Two Higgs Doublet Model (2HDM) [106] will be introduced shortly. The MSSM Higgs sector, if the supersymmetric particles are heavy enough, is described by a constrained 2HDM (type-II) [15–17] at low energies. A more general description of the Higgs sector and its interaction with fermions is provided by the 2HDM. The general 2HDM extension of the SM features two scalar doublets of equal hypercharge $\Phi_{1,2} = (\phi_{1,2}^+, \phi_{1,2}^0)^T$, thereby giving rise to five massive scalar Higgs bosons.

Charged Higgs bosons are also featured in more exotic extensions of the SM, as for example the little Higgs model [107] and Higgs triplet models [108], but these lie beyond the scope of this work. Constraints for the Yukawa matrices are selected to categorise the specific models into different types. In the common 2HDM model types I, II, III [109–111], the Higgs doublets couple to all fermion families proportional to their masses (modulo additional parameters) [112]. Further types exist for the 2HDM all featuring different constraints and phenomenologies.

- **2HDM-I:** only one Higgs doublet generates all the masses, of gauge bosons and

fermions [17]. The second doublet only contributes via mixing. Therefore the Higgs phenomenology shows similarities to the SM, but the SM Higgs couplings are shared among the neutral scalar spectrum [112].

- **2HDM-II:** natural flavor conservation [113] is featured, its phenomenology is very similar to the 2HDM-I. Here the SM couplings are not exclusively shared via mixing, but also via the Yukawa structure.
- **2HDM-III:** distinguishes itself through the presence of flavor changing neutral scalar interactions, these need a special suppression mechanism [114]. For example a dedicated texture of the Yukawa couplings [115] can be imposed.

In the special case of the constrained MSSM [116] several mass relations can be derived from the Higgs potential. The most relevant concerning the charged Higgs boson is:

$$m_{H^+}^2 = m_{A^0}^2 + m_W^2, \quad (2.35)$$

which, by implying the tree level sum rule:

$$m_{H^0}^2 + m_{h^0}^2 = m_{A^0}^2 + m_Z^2, \quad (2.36)$$

and the mass product relation:

$$m_{H^0}^2 m_{h^0}^2 = m_{A^0}^2 m_Z^2 \cos^2 2\beta, \quad (2.37)$$

results in:

$$m_{H^+} \geq m_W, \quad (2.38)$$

$$m_{H^0} \geq m_Z, \quad (2.39)$$

$$m_{A^0} \geq m_{h^0}, \quad (2.40)$$

$$\text{and } m_{h^0} \leq m_Z |\cos 2\beta| \leq m_Z. \quad (2.41)$$

From these relations it follows that this model predicts (at least) one light Higgs boson, which due to its strong coupling to WW is able to preserve unitarity.

2.2.3 Charged Higgs Boson Production and Decay

In the type-II 2HDM, which corresponds to the Higgs sector of the Minimal Supersymmetric Standard Model (MSSM), the production and decay of the H^+ partially depend on the mass. For low masses ($m_{H^+} < m_t$), commonly called light charged Higgs bosons, the main production mechanism is from the decay of a top quark. The leading source of top quarks at the LHC is via $t\bar{t}$ production. For H^+ boson masses above the top quark mass ($m_{H^+} > m_t$), commonly called heavy charged Higgs bosons, the leading H^+ production mode at the LHC is expected

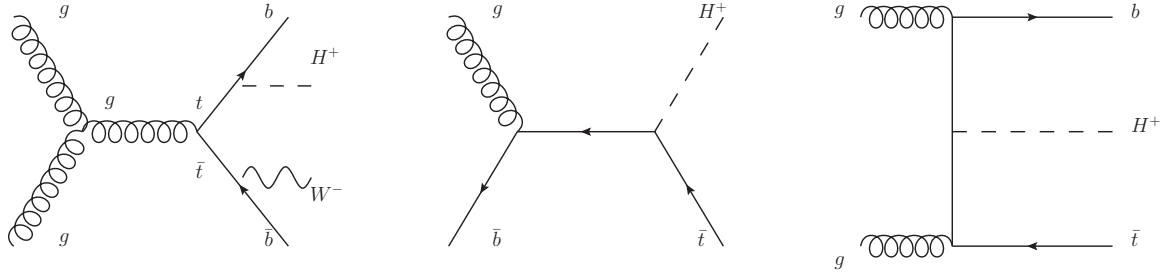


Figure 2.7: Example of leading-order Feynman diagrams for the production of light charged Higgs bosons, at masses below (the left diagram) and heavy charged Higgs bosons, above the top quark mass (the middle and right diagram, 4 – 5 flavor scheme).

to be top-associated production. Feynman diagrams illustrating the leading-order production mechanisms are shown in Figure 2.7.

The production and decay of H^+ is further controlled by $\tan\beta$, as depicted in Figure 2.8. The branching fractions of the H^+ as a function of mass (for $\tan\beta = 1$) are illustrated in Figure 2.9. Note that for the light charged Higgs Boson the dominant decay channel is $H^\pm \rightarrow \tau^\pm \nu$, thus this channel is the most promising for the charged Higgs searches and will be explored in this work.

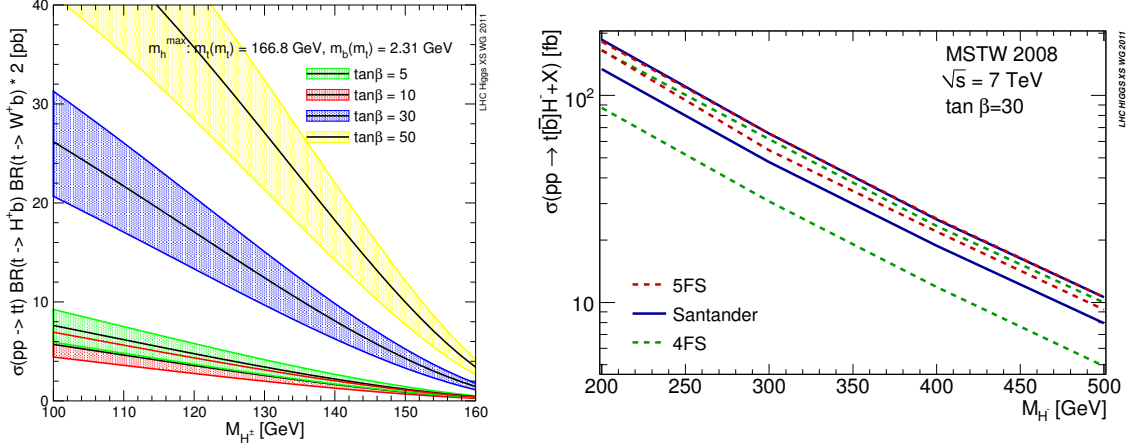


Figure 2.8: Production cross-section for the charged Higgs as a function of mass for the light charged Higgs (resulting from $t\bar{t}$ production and decay), predictions are given for a range of $\tan\beta$ values in the left plot, and in the right plot for the heavy charged Higgs (resulting from associated production with top), predictions are given for the different diagrams (4 – 5 flavor scheme). [88]

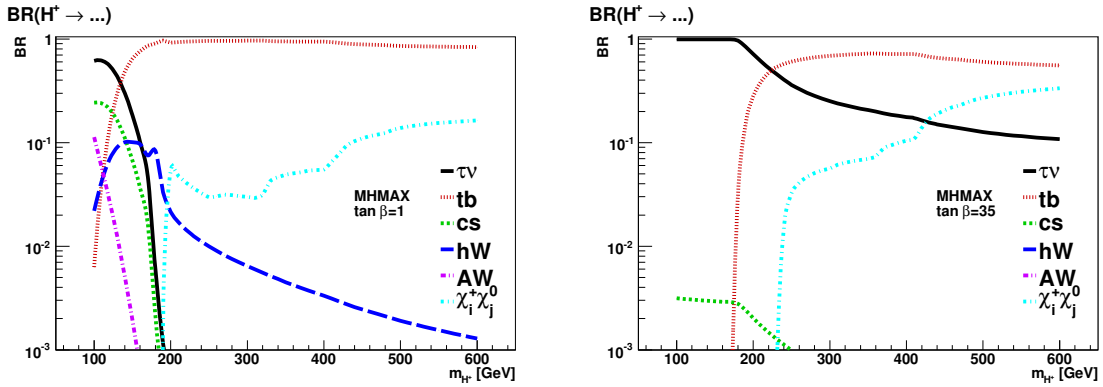


Figure 2.9: Branching fractions of the H^+ for a range of masses. A value of $\tan\beta = 1$ and $\tan\beta = 35$ is assumed in the left and right plot, respectively. For higher values of $\tan\beta$, the decays to hW and AW are negligible in the m_h^{\max} scenario. [117]

2.3 Current Status of charged Higgs Boson Searches

Searches for the charged Higgs boson were performed by experiments before the LHC. A short summary of the pre-LHC status is given in this section.

LEP

A combined LEP limit for charged Higgs bosons [118] in any type-II 2HDM is about 80 GeV [119–122] and does not depend on the branching ratios of the charged Higgs boson, as shown in Figure 2.10. The translation of this result into a production cross-section limit, under the assumption of $\mathcal{B}(H^+ \rightarrow \tau^+ \nu) = 1$ is given in Figure 2.11. In the MSSM, it can be indirectly strengthened to about 130 GeV by the experimental constraints on the mass m_A and the fact that $m_{H^+}^2 \simeq m_A^2 + m_W^2$. Charged Higgs bosons with mass below 72.5 GeV in the type-I scenario, with pseudo-scalar masses above 12 GeV are excluded at the 95 % (C.L.) by the combined LEP results [118].

Tevatron

At the Tevatron, the searches for MSSM Higgs bosons in $p\bar{p}$ collisions complement those performed at LEP, as they cover regions of the MSSM parameter space with either a small (below 1.5) or large (above 30) $\tan\beta$ values. No evidence for charged Higgs bosons has been found here either. The resulting limits on $\mathcal{B}(t \rightarrow bH^+)$ by the Tevatron experiments, CDF [123, 124] and DØ [125–127], for the light H^+ are given in Figure 2.12 and 2.13.

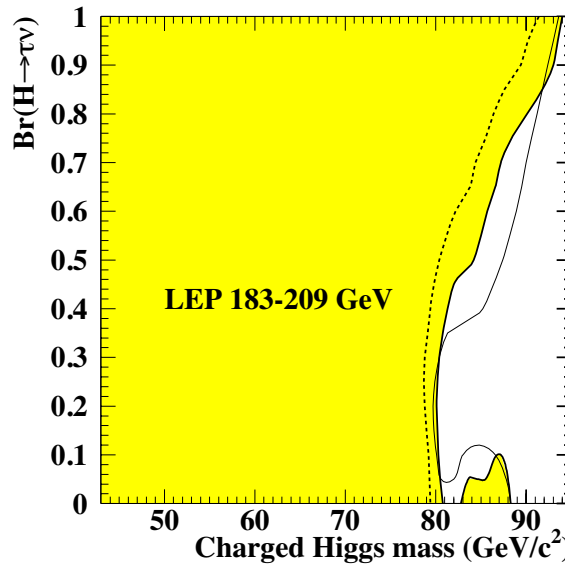


Figure 2.10: Type-II 2HDM: excluded regions in the $\mathcal{B}(H^+ \rightarrow \tau^+ \nu) - m_{H^\pm}$ plane, based on the combined data collected by the four LEP experiments at centre-of-mass energies from 183 to 209 GeV. The shaded area is excluded at the 95 % or higher C.L. The expected exclusion limit (at the 95 % C.L.) is indicated by the thin solid line and the thick dotted line inside the shaded area is the observed limit at the 99.7 % C.L. [118]

$H^+ \rightarrow c\bar{s}$ Searches

The charged Higgs boson can also decay hadronically via $H^+ \rightarrow c\bar{s}$. This decay mode is dominant in the MSSM, when considering the parameter space with $\tan\beta < 1$. For example at $\tan\beta < 1$ $\mathcal{B}(H^+ \rightarrow c\bar{s}) \approx 70\%$, at $m_{H^+} = 110$ GeV [128, 129], but for $\tan\beta > 3$ the tauonic decay mode with $\mathcal{B}(H^+ \rightarrow \tau\nu) \approx 90\%$ dominates for masses up to the top quark mass. Therefore this decay channel is complementary, considering the $\tan\beta$ parameter space, to the tauonic decays modes.

The Tevatron experiments, as well as the ATLAS experiment have performed searches for hadronically decaying charged Higgs bosons in this decay channel, the latest results and limits are given in plots in Figure 2.14.

Indirect Searches and Constraints

Indirect searches via the measurements of rare B meson decays have been carried out by the B factories BABAR and Belle. A very descriptive overview is given in Reference [131], which combines the results of flavor physics data that is sensitive to charged Higgs boson contributions. Reference [131] states a combined limit in a type-II 2HDM non-SUSY scenario on the charged Higgs boson mass of $m_{H^\pm} > 316$ GeV irrespective of the $\tan\beta$ value. Examples of the

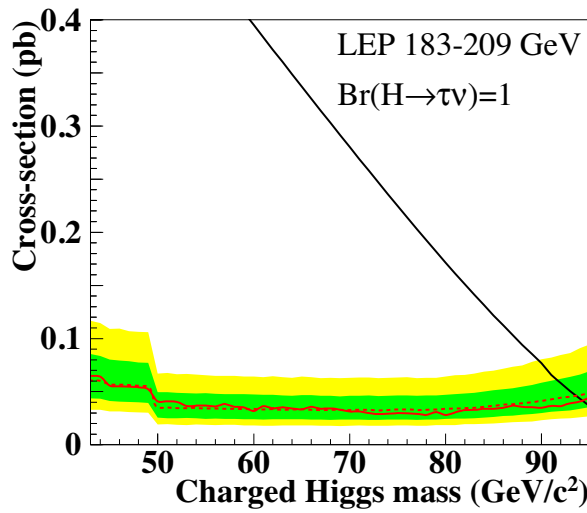


Figure 2.11: Type-II 2HDM: the 95 % C.L. upper limits on the production cross-section as a function of m_{H^\pm} for an assumed $\mathcal{B}(H^+ \rightarrow \tau^+ \nu) = 1$, combining the data collected by the four LEP experiments at centre-of-mass energies from 183 to 209 GeV. The solid lines represent the observed exclusion limits, while the expected exclusion limits are indicated by the dashed lines. The shaded bands represent the $\pm 1\sigma$ and $\pm 2\sigma$ excursions around the expected limits. The intersections of the curves (solid or dashed) with the thick line showing the theoretical (tree-level) charged Higgs cross-section represent the (observed or expected) 95 % C.L. lower limits on the charged Higgs boson mass. [118]

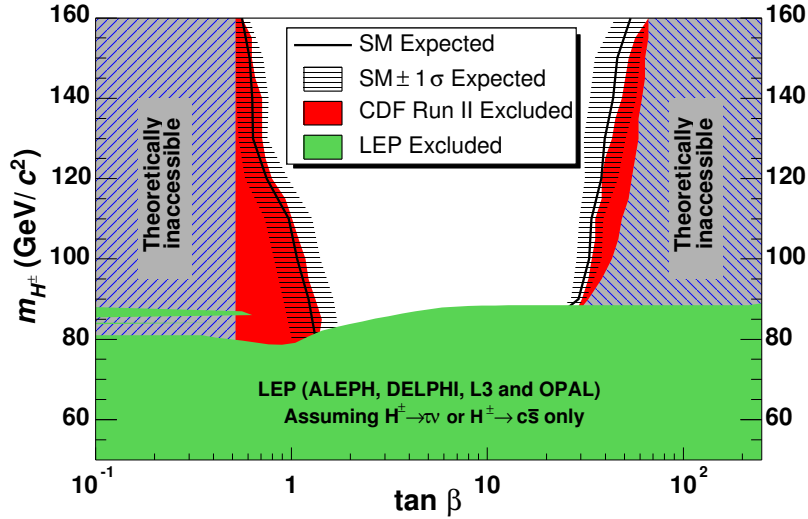


Figure 2.12: The MSSM results obtained with 193 pb^{-1} at CDF. The SM-expected exclusion limits are indicated by black solid lines and the $\pm 1\sigma$ confidence band around it is obtained by generating pseudo-experiments. The darkest solid region represents the area excluded at 95 % C.L. The solid lower region is the LEP combined results from direct searches [36](2004 edition). The MSSM parameters are defined in [19] and are set to $M_{SUSY} = 1000 \text{ GeV}$, $\mu = -500 \text{ GeV}$, $A_t = A_b = 2000 \text{ GeV}$, $A_\tau = 500 \text{ GeV}$, $M_2 = M_3 = M_Q = M_U = M_D = M_E = M_L = M_{SUSY}$, and $M_1 = 0.498 M_2$. [123]

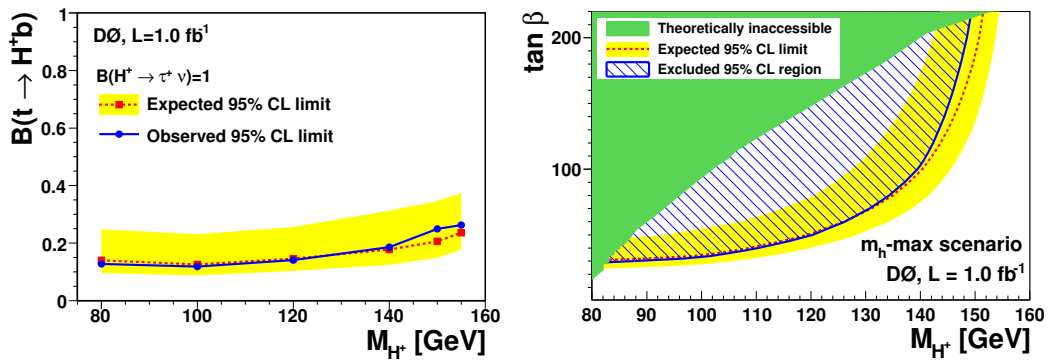


Figure 2.13: Upper limit on $\mathcal{B}(t \rightarrow H^+ b)$ for the simultaneous fit of $\mathcal{B}(t \rightarrow H^+ b)$ and $\sigma_{t\bar{t}}$ versus m_{H^+} is given in the left plot. The excluded region of the $\tan\beta - m_{H^+}$ parameter space in the MSSM for the m_h^{\max} scenario is shown in the right plot. Yellow bands illustrate the $\pm 1\sigma$ confidence band around the expected limits. [125]

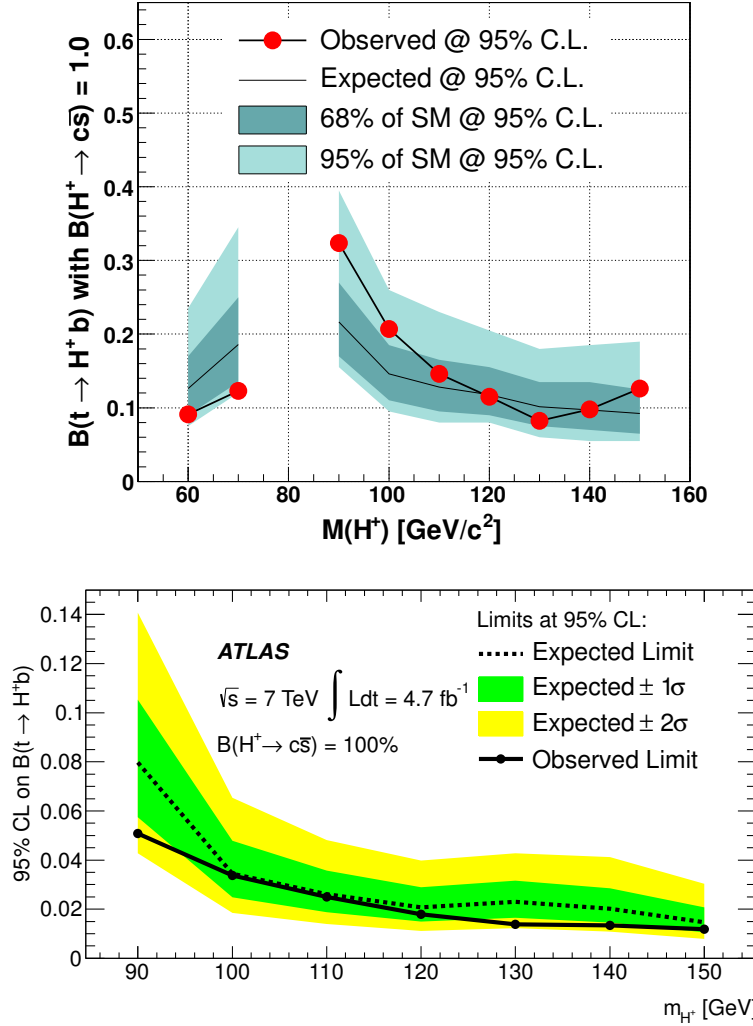


Figure 2.14: Top plot: Assuming $\mathcal{B}(H^+ \rightarrow c\bar{s}) = 100\%$ upper limits were set on $\mathcal{B}(t \rightarrow H^+ b)$, observed limits (points) from 2.2 fb^{-1} CDF II data are compared to the expected limits (solid line) with 68 % and 95 % uncertainty band, for charged Higgs masses of 60 GeV to 150 GeV, except for the region where $m_{H^+} \approx m_W$. [124]

Lower plot: The extracted 95 % C.L. upper limits on $\mathcal{B}(t \rightarrow H^+ b)$ are shown in the range of the charged Higgs mass from 90 GeV to 150 GeV, in the right plot by the ATLAS collaboration utilising 4.7 fb^{-1} pp data at $\sqrt{s} = 7 \text{ TeV}$ taken in 2011 at the LHC. The limits are calculated using the CL_s limit-setting procedure. [130]

exploited processes are:

- $B \rightarrow X_s \gamma$: As the transition at quark level ($b \rightarrow s\gamma$) is a flavour changing neutral process it is forbidden at the tree level in the SM. Thus these decays are only allowed through “penguin” processes [132] at one loop level of the perturbation theory. An enhancement of the rate predicted by the SM could be possible via additional contributions from H^\pm bosons, as shown in Figure 2.15. It should be noted that in some scenarios of the MSSM chargino contributions can partially cancel the H^\pm contribution and thereby would be harder accessible via this channel. Assuming no such destructive interferences in a generic type-II 2HDM a limit of $m_{H^\pm} > 295$ GeV was set on the charged Higgs mass [133, 134].
- $\bar{B} \rightarrow D^{(*)}\tau^-\bar{\nu}_\tau$: A recently improved study [135] of these channels (D^* and D in the final state) by the BABAR collaboration has found the measured excess over the SM expectation, illustrated in Figure 2.16, not explainable with the type-II 2HDM, for any values of $\tan\beta$ and m_{H^\pm} . The level of disagreement of the measured Ratios ($\mathcal{R}(D) = \frac{\mathcal{B}(\bar{B} \rightarrow D\tau^-\bar{\nu}_\tau)}{\mathcal{B}(\bar{B} \rightarrow D\ell^-\bar{\nu}_\ell)}$ and $\mathcal{R}(D^*) = \frac{\mathcal{B}(\bar{B} \rightarrow D^*\tau^-\bar{\nu}_\tau)}{\mathcal{B}(\bar{B} \rightarrow D^*\ell^-\bar{\nu}_\ell)}$) in the $\tan\beta - m_{H^\pm}$ plane is depicted in Figure 2.17. Further this analysis was able to exclude a significant portion of the type-III 2HDM.



Figure 2.15: An example of $b \rightarrow s\gamma$ transition through W boson exchange (left) and charged Higgs boson exchange (right). A second diagram can be drawn with the photon emitted from the charged boson. [131]

The anomalous magnetic moment of the muon, $a_\mu = \frac{g-2}{2}$, receives non-zero contributions from radiative corrections. It has been determined to high precision both theoretically and experimentally, thus can be utilised to probe effects of new physics, including the MSSM [136]. Comparing the precisely measured value for a_μ [137]

$$a_\mu^{\text{exp}} = (11\,659\,208.0 \pm 6.3) \times 10^{-10}$$

to a calculated SM prediction [138]

$$a_\mu^{\text{SM}} = (11\,659\,178.5 \pm 6.1) \times 10^{-10}$$

shows a discrepancy of:

$$\delta a_\mu = a_\mu^{\text{exp}} - a_\mu^{\text{SM}} = (29.5 \pm 8.8) \times 10^{-10},$$

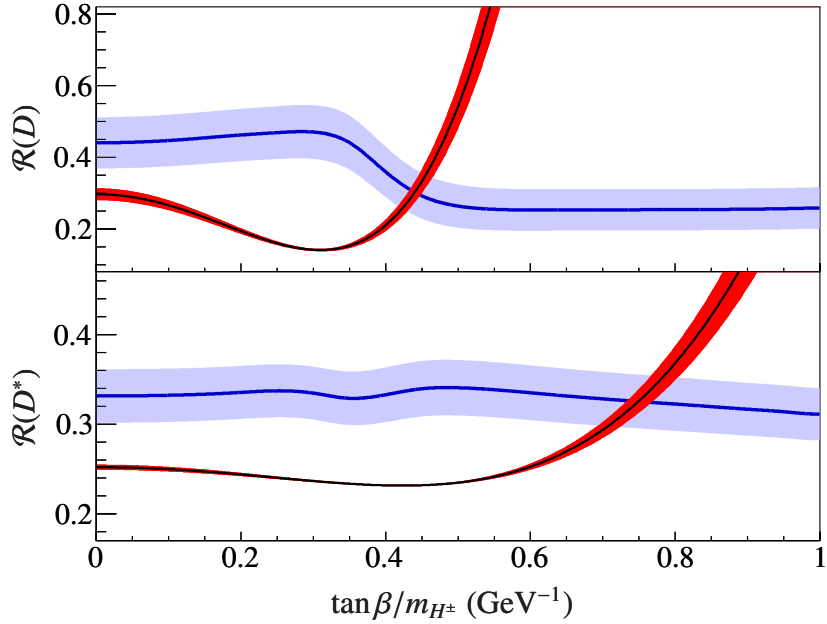


Figure 2.16: Comparison of the BABAR $B \rightarrow D^{(*)}\tau\nu$ results (light band, blue) with predictions that include a charged Higgs boson of type-II 2HDM (dark band, red). The widths of the two bands represent the uncertainties. The SM corresponds to $\tan\beta/m_{H^\pm} = 0$. [135]

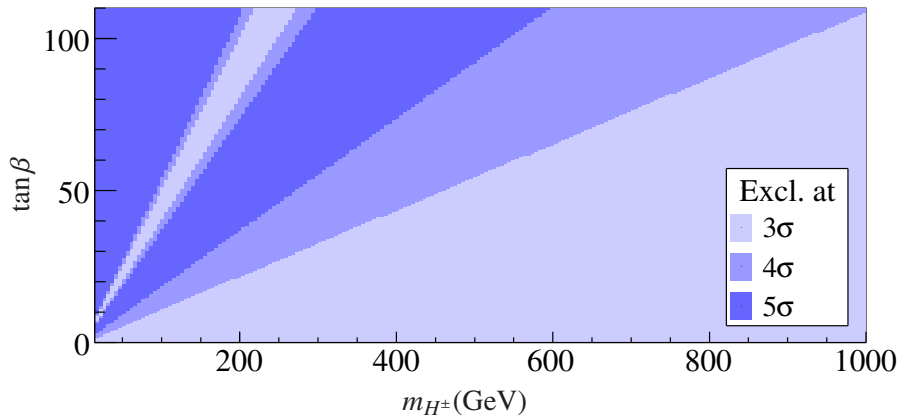


Figure 2.17: Level of disagreement between BABAR measurement of $\mathcal{R}(D^{(*)})$ and the type-II 2HDM predictions for all values in the $\tan\beta - m_{H^\pm}$ parameter space. [135]

this corresponds to a 3.4σ deviation of the measurement from the SM. The 95 % C.L. allowed range, including the uncertainties from two loop SUSY corrections which have not been included, is:

$$11.5 \times 10^{-10} < \delta a_\mu < 47.5 \times 10^{-10}.$$

a_μ and δa_μ can then be utilised to constrain MSSM models, as for example done in Reference [136].

Further the measured dark matter density, as can for example be determined from the WMAP data [139] or the Planck data [140], can be taken into account, by requiring and setting constraints on a neutral LSP. This however was shown to not create distinct constraint regions in the $\tan\beta - m_{H^\pm}$ plane [136].

Chapter 3

Monte Carlo Simulation

3.1 Methodology of Monte Carlo Simulation

For the prediction of physics processes in particle colliders Monte Carlo simulation (MC) is utilised. The MC chain is directly incorporated into the ATLAS software framework, Athena [141], as shown in the flow chart in Figure 3.1.

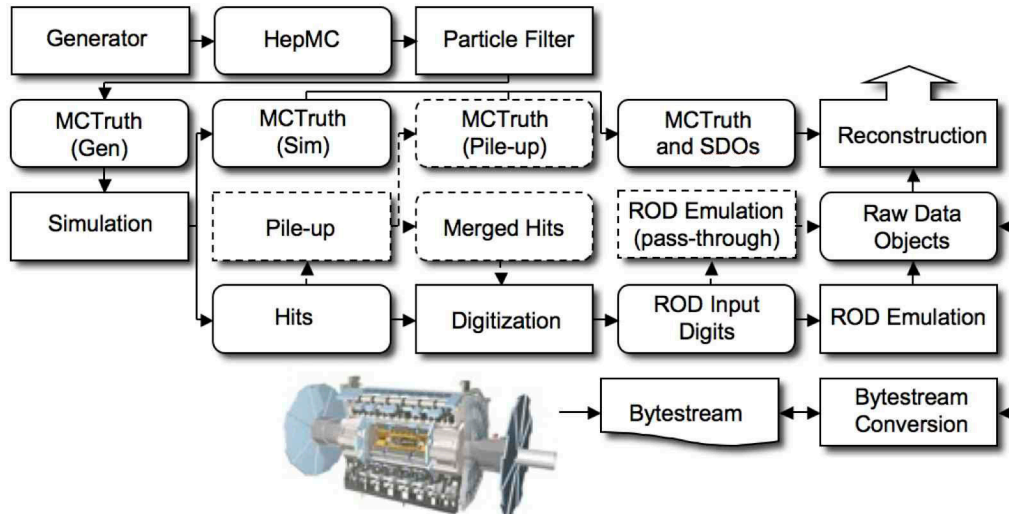


Figure 3.1: The flow of the ATLAS simulation software, from event generators (top left) through reconstruction (top right). Algorithms are placed in square-cornered boxes and persistent data objects are placed in rounded boxes. The optional pile-up portion of the chain, used only when events are overlaid, is dashed. Generators are used to produce data in HepMC format. Monte Carlo generation information is saved in addition to energy depositions in the detector (hits). This information is merged into Simulated Data Objects (SDOs) during the digitisation. Also, during the digitisation stage, Read Out Driver (ROD) electronics are simulated. [142]

A necessary input are the Parton Distribution Functions (PDFs) [143, 144], these are available from different groups, based on fits of the data of various scatter measurements over a wide range of energy. Matrix elements are calculated by integrating over all Feynman diagrams contributing to the process or final state that should be simulated. By integrating the Matrix element over the desired phase space the hard or partonic process is calculated. Depending on the order of α_s , rising due to virtual loops or radiation correction, of the Feynman diagrams taken into account the calculations are named: leading order (LO), next to leading order (NLO), next to next to leading order (NNLO) and next to next to leading logarithms (NNLL) etc. Examples of LO generators are PYTHIA [145], HERWIG [146] and ALPGEN [147]. Here initial state radiation and final state radiation corrections are performed by the parton shower simulation algorithms, as for example provided by HERWIG and PYTHIA. The parton showering, the second step of the Monte Carlos simulation process, describes the transition from the scale of the hard process down to the scale where the hadronisation takes place. For the underlying event, the not-hard process or soft process in an collision event, similar calculations are performed and overlaid with the hard process to better simulate the conditions of a LHC collision. The four-momentum vectors of the hard process and the underlying event are passed on to the hadronisation. Here quarks and gluons form hadrons, as they cannot exist as free particles. The τ lepton decays are performed by a dedicated package, TAUOLA [148]. PHOTOS [149] handles the simulation of electromagnetic radiation. It is utilised by TAUOLA, which therefore cannot be used without PHOTOS. PHOTOS is further improves the description of electromagnetic radiation in, for example, the decay $W \rightarrow e\nu$, where radiation distorts the electron energy distribution [142]. The resulting particles and their four-momentum vectors are then further passed on to the ATLAS detector simulation, which utilises the GEANT4 simulation toolkit [142, 150]. GEANT4 simulates the interaction of the particles with the detector material, including the formation of electromagnetic and hadronic showers. Further it is able to emulate the electronic response of the detectors, which are then passed on to the digitisation step. The ATLAS detector geometry used for simulation, digitisation, and reconstruction is built from databases with information describing the physical construction and conditions data. These databases contain all the information needed to emulate a single data-taking run of the real detector (as for example detector mis-alignments or detector component temperatures) [142]. The digitisation describes the step from the energy deposited in the sensitive regions of the detector into voltages and currents that are read out, the detector response. The output of the simulation chain is thus in a format identical to the output of the ATLAS data acquisition system. Both the simulated and real data from the detector are then run through the same ATLAS trigger and reconstruction algorithms. In the following sections a short overview of the different simulation software packages that were utilised for the different studies is given.

3.2 Monte Carlo Simulation for Electron to τ Mis-identification Analysis

The Monte Carlo simulation used in the analysis explained in Section 5.5.2 and documented in Reference [151, 152] utilises PYTHIA [145] to create $\sqrt{s} = 7$ TeV signal and background processes and GEANT4 [142, 150] is used to simulate the ATLAS detector [142]. Pileup has been included in the simulation for a mean number of interactions per event, $\langle n_{\text{vtx}} \rangle$, of 2.2, while the mean number in data taken in 2010 is $\langle n_{\text{vtx}} \rangle = 2.4$. The average number of primary vertices per event in data throughout the data taking period exceeded that in the Monte Carlo samples. The primary vertex distributions for the Monte Carlo samples are therefore re-weighted event by event to match the distribution of the number of interactions per event in data. Effects of the bunch-train pileup configuration have been included in all Monte Carlo samples. A full list of the Monte Carlo simulation samples used is given in the Appendix Section A.1.1 in Table A.1.

The signal Monte Carlo process is mainly $Z \rightarrow ee$, generated requiring $m_{ee} > 60$ GeV. The $\gamma^* \rightarrow ee$ sample, generated with $15 < m_{ee} < 60$ GeV is also included as a signal because it has the same di-electron final state. The main background Monte Carlo samples are $W \rightarrow \tau\nu$, $W \rightarrow e\nu$, $Z \rightarrow \tau\tau$ and QCD. For QCD production, the at generator level electron-filtered J1-J3 samples and the J0, J4, and J5 samples are used. The jet p_{T} range of the hard scatter for J0, J1, J2, J3, J4, J5 are less than 17, 17 – 35, 35 – 70, 70 – 140, 140 – 280 GeV, and more than 280 GeV, respectively. All filtered and non-filtered samples were directly summed-up. Table A.1 lists the samples with MC10 tune used, all were generated with PYTHIA. The W/Z cross-sections are calculated at NNLO order [153, 154] and the $\gamma^* \rightarrow ee$ cross-section is calculated at NLO [155–157]. Further information on the QCD samples is given in Reference [158].

3.3 Monte Carlo Simulation for H^\pm Analysis with Data taken 2010

The background estimation methods validation and search for the charged Higgs with data taken in 2010, as summarised in Section 5.5 and documented in References [159, 160], utilise a production of $t\bar{t}$ and single-top events with MC@NLO [161] with HERWIG [146] for hadronisation and JIMMY [162] for the underlying event. Overlap between $t\bar{t}$ and single-top final states is removed in these MC@NLO samples [163]. A $t\bar{t}$ production cross-section of 164.6 pb [164] obtained from approximate NNLO calculations [165] is used (both for SM-like $t\bar{t}$ and decays via H^\pm), for single-top production the the MC@NLO values are used.

ALPGEN [147] is utilised for the generation of W and Z events with up to five partons together with HERWIG/JIMMY. A so-called MLM matching scheme [166] is applied. The ALPGEN

cross-sections are rescaled by a factor 1.20 (W) and 1.25 (Z) to match cross-section calculated at NNLO [167]. QCD jet events, including $b\bar{b}$, and H^\pm signal events are generated with PYTHIA [145] (including a variant, PYTHIA B [168, 169], for production of events with B -hadrons), using TAUOLA [148] for τ lepton decays and PHOTOS [149] for photon radiation off charged leptons. Events hadronised by PYTHIA use the ATLAS Minimum Bias Tune 1 (AMBT1) [170], while HERWIG/JIMMY samples use the ATLAS Underlying Event Tune 1 (AUET1) [171]. The QCD jet events for the H^\pm in the τ +lepton channel study employs lepton filters, requiring either a generated muon in the event or an electron-like energy content in $\eta - \phi$ cell of size 0.12 by 0.12 (sensitive to both generated and fake reconstructed electrons).

Process	Generator	Cross-section [pb]
$t\bar{t}$ with $\geq 1\ell$	MC@NLO	89.7
single-top (s, t, Wt channel)	MC@NLO	21.4, 1.41, 14.6
$W \rightarrow \ell\nu + \text{jets}$	ALPGEN	$3.1 \cdot 10^4$
$Z \rightarrow \ell\nu + \text{jets}$	ALPGEN	$3.2 \cdot 10^3$
QCD jets (17–280 GeV)	PYTHIA	$7.2 \cdot 10^8$
$b\bar{b}$ with μ filter	PYTHIA B	$7.4 \cdot 10^4$
$t\bar{t} \rightarrow bH^\pm bW$ with $H^\pm \rightarrow \tau\nu$	PYTHIA	18.5

Table 3.1: Simulated events used for the 2010 H^\pm analyses. The $W/Z + \text{jets}$ as well as the s - and t -channel single-top events are only simulated for decays involving leptons (e , μ , or τ), and the cross-section given includes this branching ratio. NLO+NNLL calculations are used for $t\bar{t}$, NLO for single-top, NNLO for $W/Z + \text{jets}$, and LO for QCD multi-jet and $b\bar{b}$. The $b\bar{b}$ cross-section is given for the phase space with at least one muon in the decay chain with $p_T > 15$ GeV. The H^+ sample uses $m_{H^+} = 130$ GeV and $\tan\beta = 35$ as input. [159]

All events are propagated through a detailed ATLAS detector simulation using GEANT4 [142, 150] and reconstructed by the same algorithms as the data. cross-sections and simulated event samples are summarised in Table 3.1. Table A.2 in the Appendix Section A.1.2 gives a complete list of the datasets used, together with the number of events they each contain.

3.4 Monte Carlo Simulation for H^\pm Analyses with Data taken 2011

This section describes the Monte Carlo simulation samples utilised in the analyses with the data taken in 2011 as summarised in Section 6 and 7 and documented in References [172, 173], for even more details of the analyses please refer to the supporting documentation provided in References [174–177].

Monte Carlo samples intended for the analysis of the 2011 data are provided by the MC11 campaign of the ATLAS production group. The sample statistics of the MC11 production round are such that the statistical uncertainties obtained when working with the Monte Carlo simulated samples remain smaller than those of the 2011 data sample. In this study, the estimation of the multi-jet background is only performed with data-driven techniques, therefore none of the QCD Monte Carlo samples are used.

The modelling of the $t\bar{t}$ and single top quark events is performed with MC@NLO [161], except for the t -channel of the single quark production, in which case ACERMC [178] is used. The top quark mass is set to 172.5 GeV and the parton density function is CT10 [143]. The parton shower and the underlying event are added using HERWIG [146] and JIMMY [162] for events generated with MC@NLO. PYTHIA [145] is instead used for events generated with ACERMC. The inclusive $t\bar{t}$ production cross section is normalised to the approximate NNLO prediction of 167 pb [179]. For the single top quark production, approximate NNLO calculations are used for the inclusive cross-sections, 64.6 pb, 4.6 pb and 15.7 pb for the t -, s - and Wt -production channels, respectively [180–182]. Single top quark events are available for each of the leptonic, e , μ and τ , t - and s -channels and for the inclusive Wt -channel. Overlaps between single top quark and $t\bar{t}$ final states are removed [163].

Various $t\bar{t}$ samples using other generators and parameter setups are also available. For instance, $t\bar{t}$ samples simulated using POWHEG [183], interfaced with PYTHIA or HERWIG/JIMMY, allow the comparison of two different parton shower and hadronisation models. For initial state radiation and final state radiation studies, a set of $t\bar{t}$ samples, generated with ACERMC and PYTHIA, is available. The initial and final state parameters and their combinations are set to a range of values not excluded by current data.

Single vector boson production is simulated using ALPGEN interfaced to HERWIG/JIMMY for the underlying event model. The parton density function CTEQ6.1 [144] is used for both matrix element calculations and parton shower evolution. The additional partons produced in the matrix element part of the event generation can be light partons or heavy quarks. The MLM matching [166] is applied inclusively for the production of $W+5$ partons and exclusively for lower multiplicity sub-samples. The production cross-sections of all samples are rescaled by 1.20 and 1.25, respectively, to match NNLO cross-section calculations [184, 185].

Diboson events (WW , WZ and ZZ) are generated and hadronised using HERWIG. For these

events, inclusive decays are used for both gauge bosons, and a filter, requiring at least one electron or muon with $p_T > 10$ GeV and a pseudorapidity $|\eta| < 2.8$, is applied at the generator level. Similarly to the single vector boson production, the cross-sections are rescaled, by 1.48 for WW , 1.60 for WZ , and 1.30 for ZZ , to match the NLO predictions [186].

In addition to the SM background samples, three types of signal samples are produced with PYTHIA 6.425 [145] for $90 \text{ GeV} < m_{H^\pm} < 160 \text{ GeV}$: $t\bar{t} \rightarrow b\bar{b}H^+W^-$, $t\bar{t} \rightarrow b\bar{b}H^-W^+$ and $t\bar{t} \rightarrow b\bar{b}H^+H^-$, where charged Higgs bosons decay as $H^\pm \rightarrow \tau^\pm\nu$. TAUOLA 1.20 [148] is used for simulation of τ decays, and PHOTOS 2.15 [149] is used for photon radiation from charged leptons.

Event generators are tuned to describe the ATLAS data. The parameter sets AUET2B [170] and AUET2 [171] are used for events hadronised with PYTHIA and HERWIG/JIMMY, respectively. The SM background and signal samples used in this study are summarised in Tables 3.2 and A.4, respectively. All Monte Carlo events are propagated through a detailed GEANT4 simulation [142, 150] of the ATLAS detector, and they are reconstructed with the same algorithms as the data. Only events recorded with all ATLAS sub-systems fully operational are used for this analysis. Together with the requirement of having $\sqrt{s} = 7$ TeV pp collisions with stable beams, this results in a 2011 data sample of $4.6 \pm 0.2 \text{ fb}^{-1}$, with an uncertainty of 3.9 % [187].

Process	Generator	Cross-section [pb]	
SM $t\bar{t}$ with at least one lepton, $\ell = e, \mu, \tau$	MC@NLO 4.01 [161]	91	[179]
Single top quark t -channel (with ℓ)	ACERMC 3.8 [178]	21	[180]
Single top quark s -channel (with ℓ)	MC@NLO 4.01 [161]	1.5	[181]
Single top quark Wt -channel (inclusive)	MC@NLO 4.01 [161]	16	[182]
$W \rightarrow \ell\nu$	ALPGEN 2.13 [147]	$3.1 \cdot 10^4$	[184]
$Z/\gamma^* \rightarrow \ell\ell$ with $m(\ell\ell) > 10$ GeV	ALPGEN 2.13 [147]	$1.5 \cdot 10^4$	[185]
WW	HERWIG 6.520 [146]	17	[186]
ZZ	HERWIG 6.520 [146]	1.3	[186]
WZ	HERWIG 6.520 [146]	5.5	[186]
H^+ signal with $\mathcal{B}(t \rightarrow bH^+) = 3\%$	PYTHIA 6.425 [145]	9.9	

Table 3.2: Cross-sections for the simulated processes and the generators used to model them.

All background cross-sections are normalised to NNLO predictions, except for diboson event production where the NLO prediction is used. For the diboson events, a filter is applied at the generator level, by requiring at least one electron or muon with $p_T > 10$ GeV and $|\eta| < 2.8$. [174]

The LHC peak luminosity exceeded $10^{33} \text{ cm}^{-2}\text{s}^{-1}$ for most of the 2011 data-taking period, a level at which more than one interaction per bunch crossing occurs (on average, 6.3 and 11.6, respectively before and after the September 2011 technical stop, during which the β^* -value was reduced from 1.5 to 1.0 m). In addition, the LHC ran with an in-train bunch separation of 50 ns. Thus, the out-of-time pile-up (overlapping signals in the detector from other neighbouring bunch crossings) is very important. For the pile-up simulation, minimum bias events are generated with PYTHIA, assuming variable pile-up rates, and added to the hard process in each Monte Carlo event. Prior to the analysis, the simulated events are reweighted to match the distribution of the average number of pile-up interactions $\langle \mu \rangle$ in the data [188]. As an illustration of the “pile-up reweighting procedure”, Figure 3.2 shows the normalised distribution of the number of reconstructed vertices with five or more tracks, in data and in a $t\bar{t}$ Monte Carlo sample, before and after performing the pile-up reweighting.

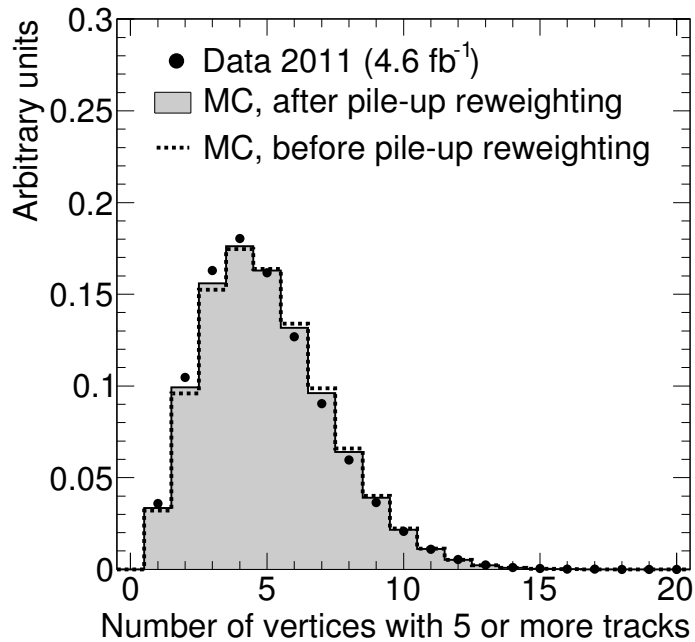


Figure 3.2: Normalised distribution of the number of vertices with five or more tracks, in data taken 2011 with $\sqrt{s} = 7$ TeV and in a $t\bar{t}$ Monte Carlo sample, before and after pile-up reweighting of the simulated events. [175]

Chapter 4

LHC and the ATLAS Detector

4.1 The Large Hadron Collider

The Large Hadron Collider (LHC) [14] is situated at the European Organisation for Nuclear Research (CERN), located in a tunnel 50 m to 175 m beneath the surface at the Swiss-French border close to Geneva. Prime motivation to design and construct this enormous object was to find the source of electroweak symmetry breaking, presumably the Brout-Englert-Higgs mechanism [58–63] and the predicted Higgs boson. Large Electron Positron collider (LEP) [189], LHC’s predecessor, was abandoned end of the year 2000 with a peak centre of mass energy, (\sqrt{s}), of 209 GeV to free its approximately 26.7 km long tunnel for the terascale proton-proton collider. The magnet system of the LHC machine consists of 1232 dipoles and around 8000 correction magnets, as well the worlds largest cryogenic system at liquid helium temperature. A working temperature of 1.9 K created by the super fluid helium is necessary for superconducting magnets, which provide the magnetic field of 8.33 T to hold the proton beam on a circular path. At design energy of 7 TeV per proton beam the centre of mass energy, \sqrt{s} , of 14 TeV is anticipated. This is greater than the centre of mass energy of the Tevatron [190], a proton-antiproton machine situated at the Fermilab, USA, which provided more than 12 fb^{-1} of data [191] at $\sqrt{s} = 1.96 \text{ TeV}$ until its shutdown on September 30th, 2011.

The acceleration of the proton bunches is not achieved by the LHC alone. A chain of pre-accelerators is involved, illustrated in Figure 4.1. The LINAC (LINEar ACcelerator) provides 50 MeV beam energy as the first step. The following PSB (Proton Synchrotron Booster) passes the beam with 1.4 GeV on to the PS (Proton Synchrotron) which injects it with 26 GeV into the SPS (Super Proton Synchrotron). In 1983 the W^\pm and Z^0 boson were discovered at this storage ring [71–74]. As the last pre-accelerator the SPS injects the proton beams into the LHC with an energy of 450 GeV. The dimensional differences of the SPS, measuring 7 km in circumference, to the LHC, with around 27 km in circumference, are visualised in Figure 4.2.

Collisions or bunch-crossings occur, if the LHC is nominally filled with a bunch spacing of 25 ns, at a frequency of 40.08 MHz where the four major experiments ATLAS (A Toroidal

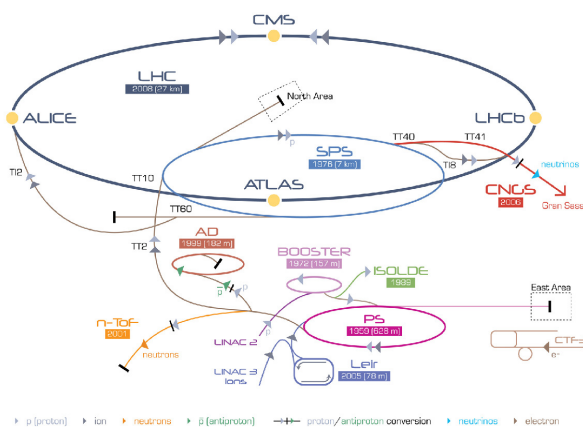


Figure 4.1: The CERN accelerator complex. [192]

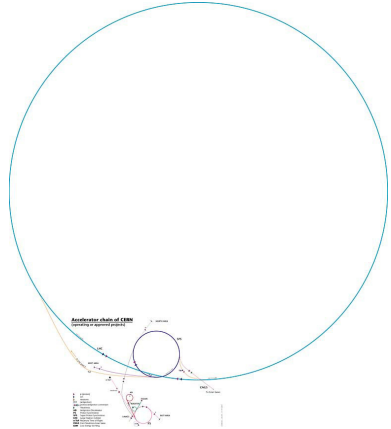


Figure 4.2: The LHC and its pre-accelerator system unscaled. [193]

LHC ApparatuS) [24], CMS (Compact Muon Solenoid) [194], ALICE (A Large Ion Collider Experiment) [195] and LHCb (Large Hadron Collider beauty) [196] are located, as illustrated in Figure 4.3. Further two forward particle experiments are hosted by the LHC. LHCf (Large Hadron Collider forward) [197], consists of two small detectors each placed a at distance 149 m from the ATLAS interaction point. TOTEM (TOTal Elastic and diffractive cross-section Measurement) [198], with a total length of 440 m set up close to the CMS detector. Additionally to the six already existing a seventh experiment was approved for the installation at the LHC, the MoEDAL (Monopole and Exotics Detector At the LHC) [199] is planned to share the experimental cavern with LHCb following the 2013–2014 shutdown. After this first long break for maintenance and upgrades for the LHC and the experiments, collisions close to the nominal $\sqrt{s} = 14$ TeV are anticipated for physics analysis during 2015. Further in future an upgrade of the LHC to HL-LHC (High Luminosity - Large Hadron Collider), which amongst other machine parameters should increase the luminosity, is planned [200–206].

4.2 The ATLAS Detector

The design of the ATLAS detector, as most of the latest multipurpose detectors, follows an overall cylindrical shape with a layered layout, as depicted in the cut-away view of the detector in Figure 4.4. It is separated in a central part, the “barrel” and the “end-caps”, to cover the forward and backward regions. This modularity allows for a good overall detector serviceability. The barrel components are shaped cylindrically, whereas the end-cap systems are arranged as discs in the x - y -plane. This separation is followed in each system of the ATLAS detector. A schematic overview of the subsystems and particles which they are designed to detect, is given in Figure 4.5. The innermost layer, called Inner Detector (ID) or tracker, consists of three subsystems and measures the momenta and charge of electrically charged particles, as well as primary and secondary vertices. The surrounding central solenoid provides a magnetic field

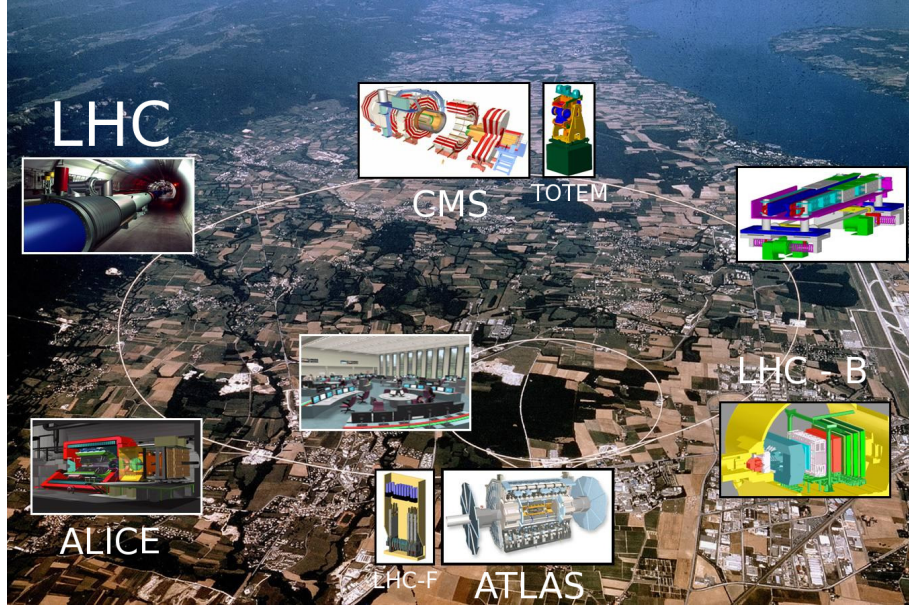


Figure 4.3: The LHC and its experiments. [207] (image modified)

with a mean value of 2 T. Energy measurement with high resolution is the main purpose of the electromagnetic calorimeters (ECAL) and hadronic calorimeters (HCAL). Both are designed to fully absorb the respective particles and their showers. Muons, passing all these layers with only a small energy and momentum loss, are precisely measured by the Muon Spectrometer (MS). Together with the ID and the air-core toroid magnets, providing a toroidal shaped magnetic field, the MS is responsible for a precise muon momentum measurement.

Particles of interest, except neutrinos, should not escape undetected. Major crack regions pointing back towards the interaction point (IP) were successfully obviated in the design. A short description of the sub-detectors and the magnet systems is given in the following sections.

The origin of the ATLAS detectors coordinate system is the nominal IP. A right-handed Cartesian coordinate system was specified as followed: the positive x -axis is defined pointing towards the centre of the LHC ring, the positive y -axis points towards the surface, therefore the z -axis follows the direction of the beam pipe. Protons consist of sub-particles, called partons, shorthand for gluons and quarks. These partons, the interacting particles during a pp collision, carry an unknown fraction of the longitudinal proton momentum. The fraction of the transverse momentum component is negligibly small compared to the longitudinal component, therefore an approximate conservation of momentum in the transverse plane is assumed:

$$\sum p_T \approx 0.$$

This assumption motivates the usage of transverse momentum, p_T , defined as:

$$p_T = \sqrt{p_x^2 + p_y^2}.$$

Cylindrical coordinates are commonly used to describe the position of a particle, as this reflects the detector geometry. The value of the polar angle reveals whether the object in question

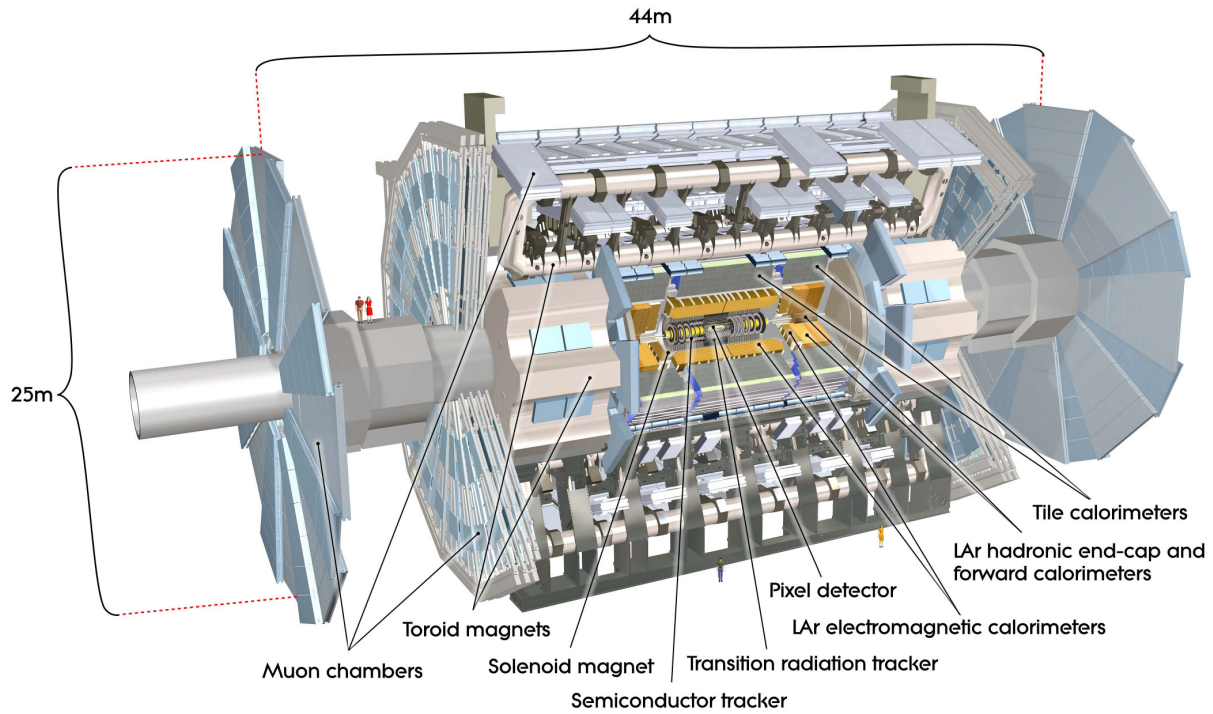


Figure 4.4: Cut-away view of the ATLAS detector, with all subsystems. [208]

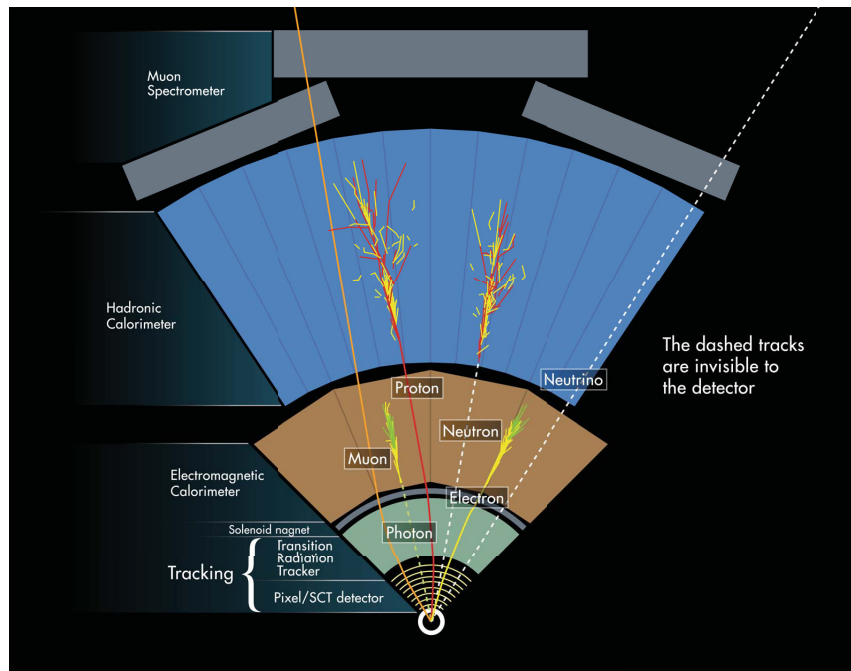


Figure 4.5: Schematic view of the layers of the ATLAS detector, also showing a selection of particles and in which parts they are measured. [209]

was reconstructed in the barrel or in the end-cap part of the detector. The polar angle, θ , measured from the positive z -axis to the particle, helps to define the pseudorapidity η , illustrated in Figure 4.6:

$$\eta = -\ln \left[\tan \left(\frac{\theta}{2} \right) \right].$$

One reason to prefer η over θ is the feature that the number of charged particles produced in inelastic pp collision events, as a function of η is approximately constant. The azimuthal angle $\phi = 0$ corresponds to the positive x -axis. ϕ increases clock-wise looking in the positive z -direction and is measured in a range from $-\pi$ to $+\pi$.

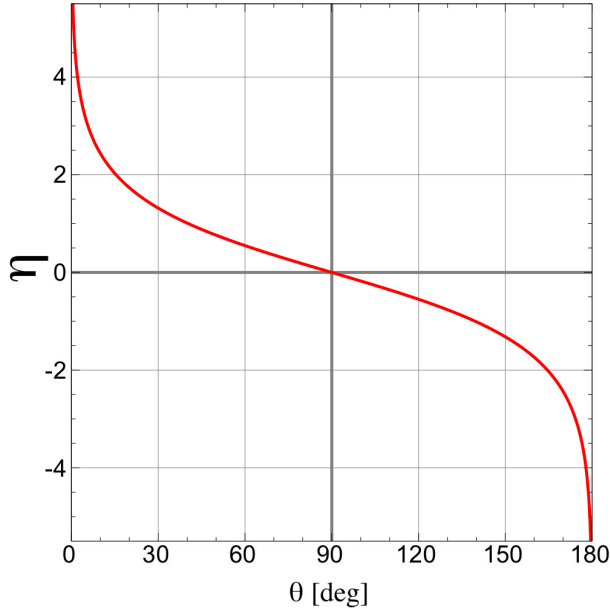


Figure 4.6: Pseudorapidity, η , as a function of the polar angle, θ . [210]

Further a distance measurement in the $\eta - \phi$ plane is introduced:

$$\Delta R = \sqrt{(\Delta\eta)^2 + (\Delta\phi)^2},$$

where $\Delta\eta$ is the difference in pseudorapidity of the two objects in question, and $\Delta\phi$ the difference between their azimuthal angles. This quantity is often utilised to define a cone around a reconstructed object in order to measure its isolation. ΔR is also utilised for the so-called overlap removal, if two reconstructed objects are geometrically very close, one, commonly the object with higher reconstruction efficiency, is preferred over the other, the latter is thus discarded.

4.2.1 Magnet Systems

The conceptual design of the magnet system was one prime issue of the detector, as all sub detectors had to be planned to function within its environment. Limits imposed by the experimental cavern size, combined with the requirement to measure the momentum of muons up to 1 TeV with a relative precision of at least 10 %, led to the choice of superconducting technology. The magnet system consists of one small radius, thin walled solenoid and three air-core toroids. This system creates a magnetic field in a volume of approximately 12 000 m³ (defined as the volume where the magnetic field exceeds 50 mT). Situated at smaller radii than the barrel ECAL, integrated in its cryostat, the solenoids material budget was minimised to reduce the impact on the calorimeters performance. A thickness of about 0.66 electromagnetic radiation lengths (X_0) in radial direction was achieved. This impairs the ECAL barrel resolution in the region of $1.2 < |\eta| < 1.4$ to some extent. With an inner diameter of 2.4 m and an axial length of 5.8 m the central solenoid does not cover the complete ID. This results in a magnetic field non-uniformity at the end regions of the tracker volume. The solenoid provides an axial magnetic field of around 2 T. The three superconducting air-core toroids, one located in the barrel region, the other two installed as end-caps, consist of eight independent coils each. With an axial length of 25.3 m, an inner diameter of 9.4 m and an outer diameter of 20.1 m, weighting 830 t, the barrel toroid provides a toroidally field of approximately 0.5 T for the muon detectors. The end-cap toroids contribute approximately 1 T, weighting 239 t each, spanning from 1.7 m up to 10.7 m in radius [211]. The solenoid magnetic field was mapped with Hall probes [212]. Discrepancies between the modelled and the measured magnetic field were in the order of 0.5 mT, only some locations at the edges of the ID volume differed up to 5 mT.

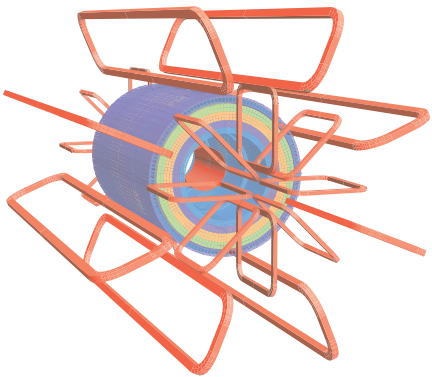


Figure 4.7: Shown is the layout of the magnet systems (in red) of the ATLAS detector, together with a model of the calorimeter systems magnetic properties, represented colour coded. [24]

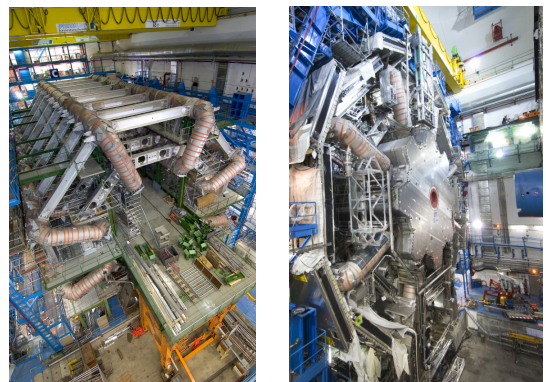


Figure 4.8: The barrel toroid system with support structure (left) and one installed end-cap toroid (right). [213, 214]

4.2.2 Inner Detector

The ATLAS Inner Detector (ID) was designed to provide charge and momentum measurement, robust and redundant pattern recognition, as well as vertex measurements for charged tracks with a p_T above 0.5 GeV within $|\eta| < 2.5$. Precise measurements of secondary decay vertices are crucial for b -tagging and the identification of hadronically decaying τ leptons. A very high granularity is needed to separate particle tracks this close to the interaction point (IP). The ID consists of three independent supplementary sub-detectors, a pixel detector [215], the silicon micro-strip sensors, also called SemiConductor Tracker (SCT) [216, 217] and a Transition Radiation Tracker (TRT) [218]. A cut away view of the ID and its components is given in Figure 4.9. These components are installed very closely around the beam pipe, which in the ID region is manufactured of beryllium to reduce material budget and reduce the probability of multiple scattering. The TRT provides a very efficient electron identification for $|\eta| < 2.0$, this will be explained in detail in the respective section. Meeting the physics requirements, while at the same time providing a robust and stable operation over years was the greatest challenge of the ID systems design. Withstanding the harsh radiation conditions near the IP stood in conflict with the requirement for a low material budget. The material budget of the trackers was greater than anticipated, reaching up to $1.2 X_0$ at $\eta \approx 1.7$ [219]. Cooling the pixel detector and SCT to approximately -10 to -5 °C degrees Celsius, decelerates the radiation induced doping concentration changes of the silicon pn-diodes. The ID, including its envelope, measures 7 m in length and 1.15 m in radius.

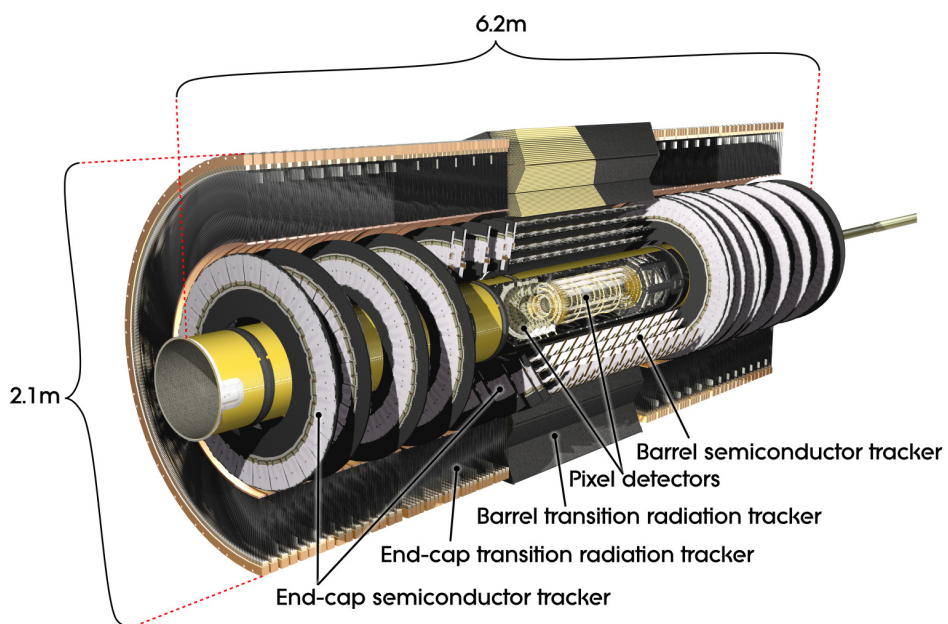


Figure 4.9: Full inner detector overview with labelled barrel and end-cap components. [24]

Pixel Detector

The pixel detector sensors are $250\text{ }\mu\text{m}$ thick and made of double sided processed, oxygenated n-type wafers. This design allows for a good charge collection efficiency, even after radiation-invoked type inversion. In long term studies highly oxygenated material proved a high tolerance for charged hadron radiation [215]. The operation voltage is expected to be raised from initially approximately 150 V to 600 V after ten years of operation. The pixel detector consists of three layers in the central region, situated at the following given radii measured from the IP, 50.5 mm, directly on the beam pipe of the LHC, 88.5 mm and 121.2 mm. Three discs at distances of $z = \pm 495\text{ mm}$, $z = \pm 580\text{ mm}$ and $z = \pm 650\text{ mm}$ cover the higher η -regions. The spacial resolution of the pixel detector is designed to achieve $10\text{ }\mu\text{m}$ in the $R - \phi$ plane and $115\text{ }\mu\text{m}$ in z -direction in the barrel and R -direction in the end-caps.

SCT

The SCT utilises a classical single-sided p-in-n technology with AC-coupled readout strips. A small angle (40 mrad) stereo strip technology enables for a reconstruction of the tracks z -coordinate, by the measurement of R and ϕ . This technique allows for a separation of two charged tracks, if their inter-space, while passing the SCT, is greater than $200\text{ }\mu\text{m}$. The four double layers of strips in the barrel provide up to eight measurements per traversing track. Nine discs in each end-cap, consisting of double layer strips, complete the SCT. Figure 4.10 and Figure 4.11 provide the radii of the SCT layers. The designed resolution of the SCT is $17\text{ }\mu\text{m}$ in the $R - \phi$ plane and $580\text{ }\mu\text{m}$ in z -direction in the barrel and in R -direction in the end-caps.

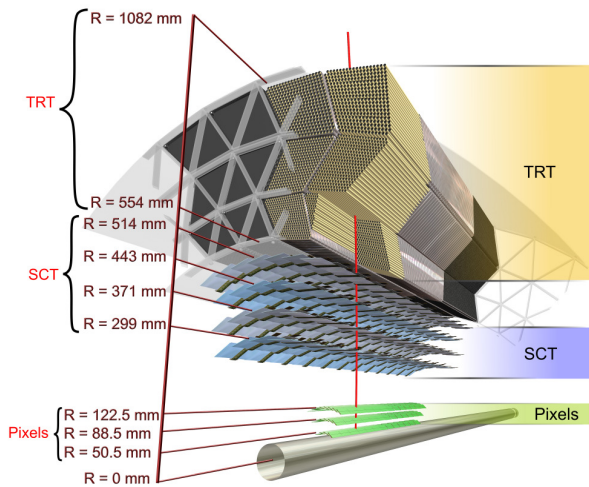


Figure 4.10: ID barrel with its systems in detail. The red line indicates a charged track with $p_T = 10\text{ GeV}$ at $\eta = 0.3$. [24]

TRT

The basic detector elements of the TRT are polyimide drift tubes, called straw tubes. Their diameter measures 4 mm. Each tube is filled with a gas mixture of 70 % Xe, 27 % CO₂ and 3 % O₂. The gas mixture is filled with 5–10 mbar over-pressure. Tubes are build in as multi-layer system of aluminium, graphite, and polyimide layers. The straw resistance is below $300 \frac{\Omega}{m}$. A 31 μ m diameter thin, very pure, gold plated tungsten wire is used as the anode of the system. It is kept at ground-potential and directly connected to the front-end electronics. The nominal operational voltage of the cathodes is given with 1530 V and the thus achieved gain factor is in the order of 2.5×10^4 . Charged particles traversing the straws ionise the gas and by secondary ionisation the measurable current is created.

The special feature of the TRT are the different dielectric constants of the straws multi-layer system. While traversing the straw this variation invokes transition radiation, with a higher probability for electrons in contrast to the heavier hadrons, like charged pions. Straws are arranged in three layers of bundles of 144 cm length in the barrel, covering the radial range of 554–1082 mm, as can be evinced in Figure 4.10. The barrel straw anodes are electrically split and mechanically supported in the centre of the detector. Radially arranged straws with a length of 37 cm cover charged tracks up to $|\eta| = 2.0$. Merely a $R - \phi$ -measurement in the barrel and a $z - \phi$ -measurement in the end-caps, with an intrinsic accuracy of 130 μ m is provided. The example track indicated in Figure 4.10 traverses 36 straws, which is close to the estimated average for $\eta < 2.0$ of 35 straw hits per charged track.

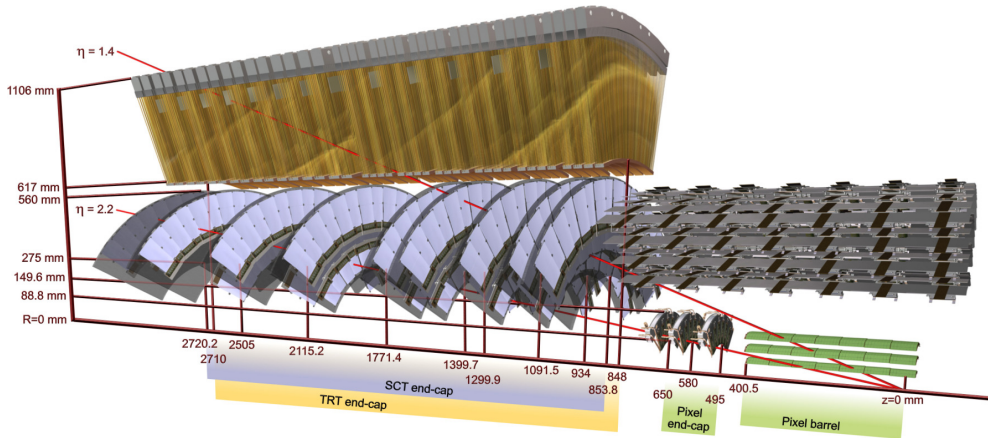


Figure 4.11: Full inner detector overview with red lines indicating charged tracks with a $p_T = 10 \text{ GeV}$ transversing the ID at $\eta = 1.4$ and $\eta = 2.2$. The barrel part of the TRT is not depicted. [24]

4.2.3 Calorimeter Systems

The calorimeter technology and design of the ATLAS detector features a lead Liquid Argon (LAr) sampling calorimeter and a system with scintillating plastic tiles. In contrast to the systems described so far the intrinsic energy resolution of the calorimeters improves with higher particle energies. The ATLAS calorimeter system consists of an electromagnetic and a hadronic calorimeter. It was constructed to precisely measure energies and positions of electromagnetically and strongly interacting particles, electrons and photons, and hadrons, respectively. Furthermore it provides input for the Level-1 trigger. The overall calorimeter layout is depicted in Figure 4.12. The calorimeter was designed for complete coverage of the region $|\eta| < 4.9$. This hermeticity makes missing transverse energy determination [220] possible⁴, which is an important indicator for neutrinos or new physics. Both sampling calorimeters posses full ϕ -symmetry and ϕ -coverage, though with different materials and geometries. In the passive absorber material secondary particle showers are initiated. Measurement of their quantity and therefore the deposited energy is the purpose of the active detector material. The design ensures enough electromagnetic radiation lengths (X_0) or interaction lengths (λ) to capture the greatest part of the showers initiated by incident particles with energies of up to several TeV. X_0 is defined as the mean distance during which a high energy electron loses energy to $\frac{1}{e}$ of its initial value by bremsstrahlung. For a high energetic photon it is $\frac{7}{9}$ th of the mean free path for pair production. The nuclear interaction length, λ , is defined as the mean free distance a relativistic particle passes through matter, before its energy decreases to $\frac{1}{e}$ of the initial value. Several layers, typically three, in longitudinal or η -direction of the calorimeters enhance the of the shower reconstruction accuracy.

Electromagnetic Calorimetry

The precision electromagnetic (EM) calorimeter system consists of a barrel (EMB) and two end-cap calorimeters (EMEC). The barrel is built of two identical halves, each with an axial length of 320 cm, spanning over the radial range from 140 cm to 200 cm. These are divided by a gap of 0.6 cm at $z = 0$ cm. The wheels of the EMECs are 63 cm thick, with inner and outer radii of 33.0 cm and 209.8 cm, positioned at $|z| = 374.4$ cm. One wheel is mechanically subdivided into two wheels, the outer and inner covering $1.375 < |\eta| < 2.5$ and $2.5 < |\eta| < 3.2$, respectively. The z -position of the wheels was changed by $|z| = +4$ cm, from the nominal position, yielding inner detector services. This shift degenerates the designed projectivity of the geometry slightly. An overlap region between the barrel $|\eta| < 1.475$ and the EMEC $1.375 < |\eta| < 3.2$ was designed for a smooth transition and thus to avoid crack regions. The accordion geometry of the absorbers and kapton electrodes of the electromagnetic calorimeters provides a full ϕ -coverage.

⁴ The resolution follows a function $\sigma = k \cdot \sqrt{\sum E_T}$, where the value of the parameter k is, before pile-up mitigation, about $0.7 \text{ GeV}^{0.5}$, much larger than the resolution observed in 2010 ATLAS data [221], due to the increased pile-up conditions. [220]

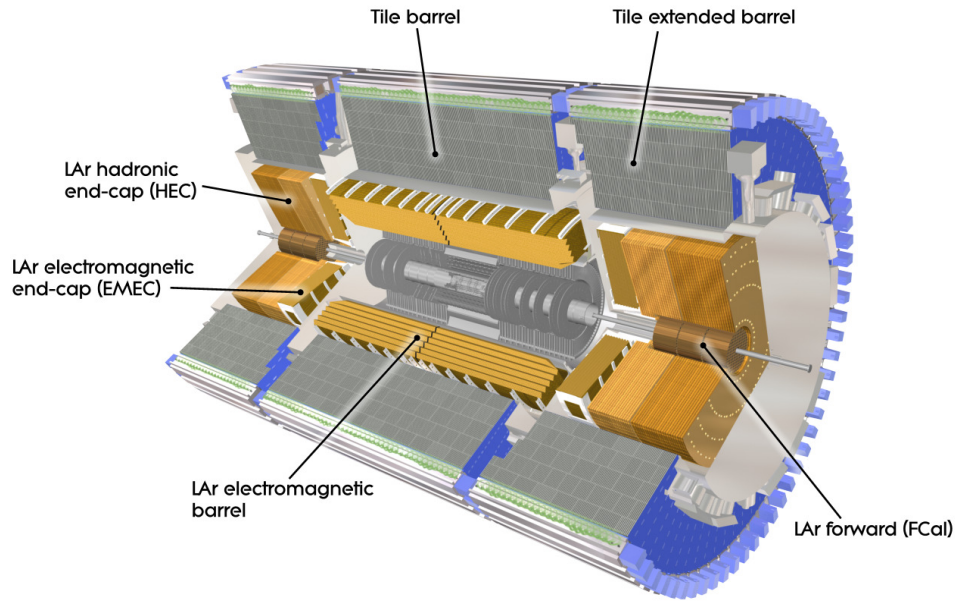


Figure 4.12: The ATLAS calorimeter systems cut-away view exposing all sub-components. [24]

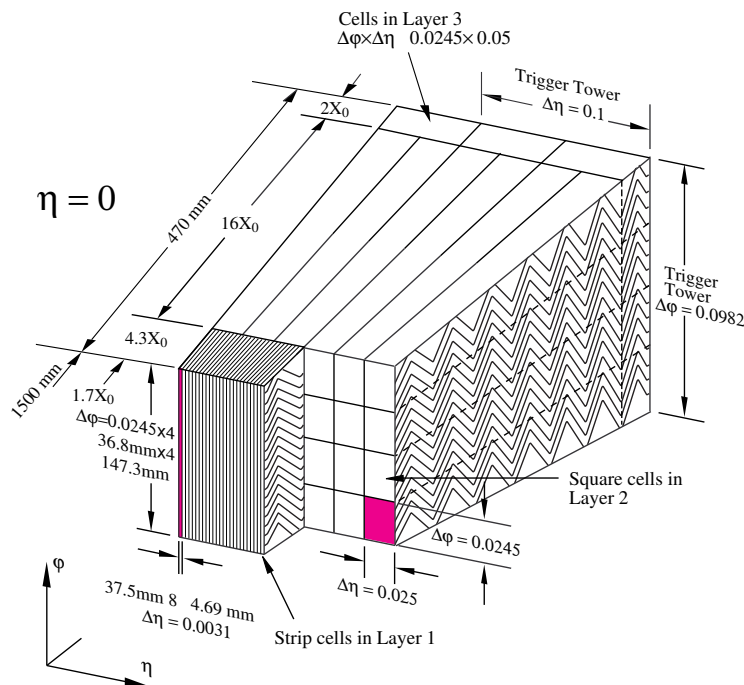


Figure 4.13: Layers, cells and spacial dimensions of the electromagnetic calorimeter at $\eta = 0$, with the samplings different granularity and visualising the Trigger Tower cell grouping. [24]

The folding angles of the accordion waves were optimised, depending on the radius, to keep the traversed LAr gap width constant, as can be evinced in Figure 4.13. To limit the decrease of the sampling fraction as $|\eta|$ increases, the absorber lead plates thickness changes from 1.53 mm for $|\eta| < 0.8$ to 1.13 mm for $|\eta| > 0.8$ in the barrel. In the end-cap calorimeters the plates have a thickness of 1.7 mm for $|\eta| < 2.5$ and 2.2 mm for $|\eta| > 2.5$. To provide mechanical stability these are glued in between two 0.2 mm thick stainless-steel sheets. The electrodes consist of three conductive copper layers separated by insulating polyimide sheets, located between the absorber plates.

		granularity $[\Delta\eta \times \Delta\phi]$ versus $ \eta $			
		barrel		end-cap	
Presampler		0.025×0.1	$ \eta < 1.52$	0.025×0.1	$1.5 < \eta < 1.8$
Layer 1	$0.025/8 \times 0.1$		$ \eta < 1.40$	0.050×0.1	$1.375 < \eta < 1.425$
		0.025×0.025	$1.40 < \eta < 1.475$	0.025×0.1	$1.425 < \eta < 1.5$
				$0.025/8 \times 0.1$	$1.5 < \eta < 1.8$
				$0.025/6 \times 0.1$	$1.8 < \eta < 2.0$
				$0.025/4 \times 0.1$	$2.0 < \eta < 2.4$
				0.025×0.1	$2.4 < \eta < 2.5$
				0.1×0.1	$2.5 < \eta < 3.2$
Layer 2	0.025×0.025		$ \eta < 1.40$	0.050×0.025	$1.375 < \eta < 1.425$
		0.075×0.025	$1.40 < \eta < 1.475$	0.025×0.025	$1.425 < \eta < 2.5$
				0.1×0.1	$2.5 < \eta < 3.2$
Layer 3	0.050×0.025		$ \eta < 1.35$	0.050×0.025	$1.5 < \eta < 2.5$

Table 4.1: Granularity of the electromagnetic calorimeter for the different $|\eta|$ -regions. [24]

The η -segmentation was realised by etching patterns onto the different layers. Ganging together an appropriate number of electrodes, as shown in Figure 4.13, results in ϕ -separation. Segments of the ECAL that are read out together are called cells. The granularity of the EMB and EMEC cells as a function of $|\eta|$ is given in Table 4.1.

High energy electrons predominately lose their energy by bremsstrahlung in matter [36]. High energetic photons, γ , traversing matter preferably perform electron-positron pair production. The e^- and e^+ emit bremsstrahlung again, thus an electromagnetic shower is formed. In the electromagnetic calorimeter the charged shower particles ionise the liquid-argon. The produced charges travel, due to the electrical field, to the electrodes where the current is read out. The nominal voltage applied is about 2000 V for the EMB.

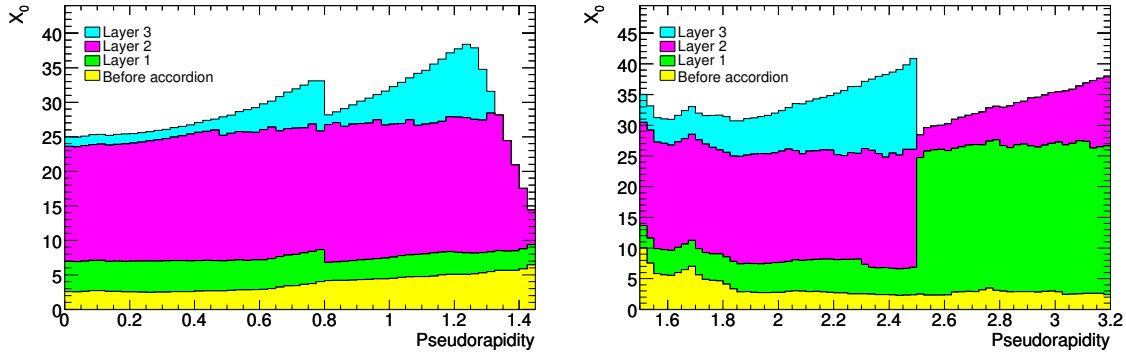


Figure 4.14: Cumulative material before and of the electromagnetic calorimeter given in X_0 as a function of $|\eta|$, showing the different layers colour coded for the barrel (left) and the end-caps (right). [24]

An additional separate layer, the pre-sampler, consisting of a single active layer of liquid-argon, with a thickness of 11 mm for the barrel up to $|\eta| = 1.52$ and 2 mm for the EMEC $1.5 < |\eta| < 1.8$, was installed. The reason for the introduction of this coarsely granulated layer is the large amount of material accumulated before of the electromagnetic calorimeter. In the region $|\eta| < 1.8$ it can reach several radiation lengths, X_0 , as can be seen in Figure 4.14. An electromagnetic shower therefore starts before the incident particle reaches the calorimeter. Corrections for upstream energy losses, using the pre-sampler information, improve the resolution of the reconstructed energy.

The region of $|\eta| < 2.5$ is also called the precision-measurement-region, as the granularity is very fine and the longitudinal direction is covered by at least three sampling layers. Energy resolution is degenerated in the overlap region $1.375 < |\eta| < 1.5$, as the cells are coarser and only two samplings per calorimeter are provided, as detailed listed in Table 4.1. This region is often misleadingly referred to as crack-region due to its non-optimal energy resolution. The ECAL inner wheel $2.5 < |\eta| < 3.2$ is equipped with only two layers in the η -direction.

The granularity of the cells in the first or strip layer is finely segmented in η , optimised for electron and jet separation. By providing an equally fine granularity in ϕ and η , the second layer allows for reconstruction of the electron or photon shower position and direction. In this way allows for separation of primary photons from the IP and photons from π^0 -decays [222], with a rejection factor⁵ of about 5000 [224]. With its depth of approximately $16 X_0$ the second layer is designed to absorb the largest part of the electromagnetic showers induced by electromagnetic interacting particles with energies up to several TeV. The coarser third sampling allows for rejection of early starting hadronic showers, which occur at low rates.

⁵ The identification is separately optimised for unconverted and converted photons to provide a photon identification efficiency of about 85 % for photon candidates with $E_T > 40 \text{ GeV}$, and a corresponding background rejection factor of about 5000 [223].

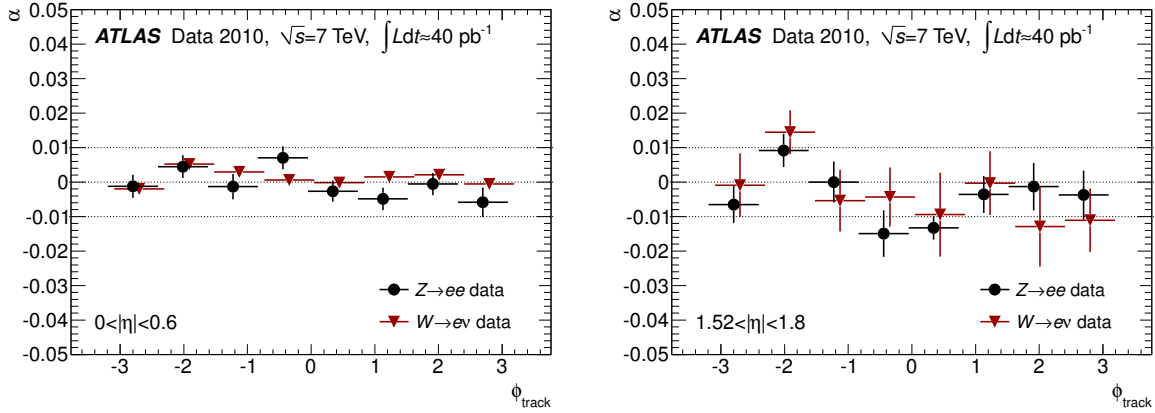


Figure 4.15: The α energy-scale correction factor as a function of the electron track ϕ for (left) $|\eta| < 0.6$ and (right) $1.52 < |\eta| < 1.8$ determined by the baseline calibration using $Z \rightarrow ee$ decays (circles) and by the E/p method using $W \rightarrow ev$ decays (triangles). Errors are statistical only. [228]

The strategy to calibrate the EM calorimeter was validated using test-beam data [225–227]. Energy calibration is performed in three steps [228]:

1. Raw signal is extracted from each cell in ADC counts and converted into a deposited energy, using the electronic calibration of the EM calorimeter [229–231].
2. Monte Carlo Simulation based calibration [167] corrections are applied at cluster level to account for energy loss due to absorption in the passive material and leakage outside the cluster. For $|\eta| < 2.47$. Further corrections depending on η and ϕ coordinates of the electron are made to compensate for the energy modulation as a function of the impact point.
3. The in-situ calibration with $Z \rightarrow ee$ decays determines the energy scale and inter-calibrates [228] different regions of the calorimeters with $|\eta| < 4.9$.

The ATLAS ECAL, due to its layout and construction, is uniform to a level of less than about 1 %. This was shown in test beam results [225–227] and with first collision data of 2010 [228], as shown in Figure 4.15.

The fractional energy resolution of the electromagnetic calorimeter is conventionally parametrised as follows:

$$\frac{\sigma_E}{E} = \frac{a}{E} \oplus \frac{b}{\sqrt{E}} \oplus c.$$

Here a is the noise term, b the sampling term and c is called the constant term, all are η -dependent parameters. Figure 4.16 shows the noise measured in randomly triggered events at the cell level as a function of η for all layers of the LAr calorimeters. In all layers, a good agreement with the expected noise [229] is observed [232].

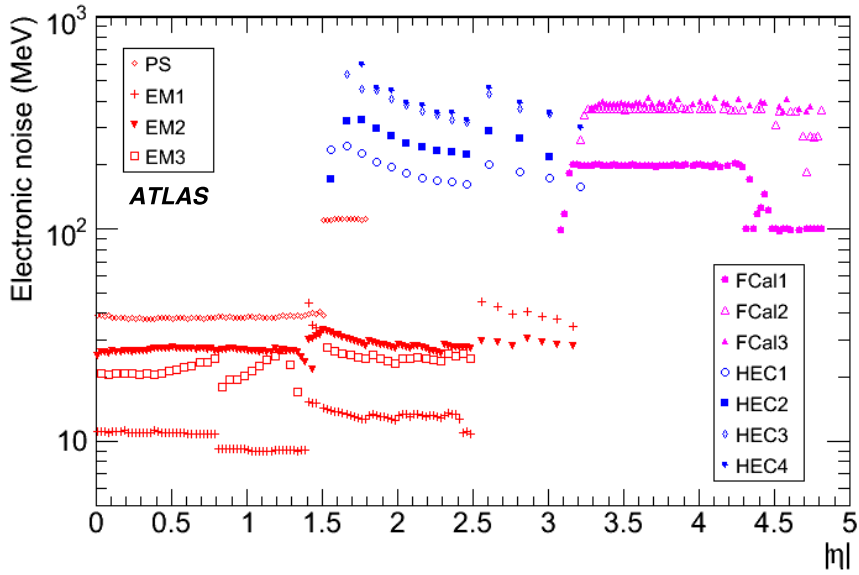


Figure 4.16: Electronic noise (σ_{noise}) in randomly triggered events at the EM scale in individual cells for each layer of the calorimeter as a function of $|\eta|$. The results are averaged over ϕ . [232]

During a combined test beam measurement in 2004 the sampling term and the constant terms were determined with a fit after subtracting the in advance measured noise term. Figure 4.17 shows the resolution values where the noise contribution and the beam spread have been subtracted in quadrature from the total resolution values. Two different fit functions were used, the data results are compatible with each other [227]:

$$b = (10.5 \pm 0.4)\% \cdot \sqrt{\text{GeV}} \quad \text{and} \quad c = (0.2 \pm 0.1)\%$$

and

$$b = (10.2 \pm 0.4)\% \cdot \sqrt{\text{GeV}} \quad \text{and} \quad c = (0.2 \pm 0.2)\%.$$

The constant term, c , was further derived using pp collision data for the different calorimeter regions, as given in Table 4.2 [228].

The calorimeter closest to the IP of the Forward Calorimeters (FCal), described in detail later, is also a part of the electromagnetic calorimeter system of ATLAS.

From end of April until early July of the data taking in 2011 a problem in reading out six Front End Boards (FEBs) and one calibration board of the LAr barrel persisted. The source was identified to be a burnt fuse on a controller board, which lead to the loss of the Timing Trigger and Control System (TTC) signal. The so-called “LAr hole” covered the area of $0 < \eta < 1.4$ and $-0.84 < \phi < -0.64$. Four of the FEBs and the calibration board were successfully recovered, thus restoring 90 % of the depth coverage over the whole η range. The two not recovered FEBs

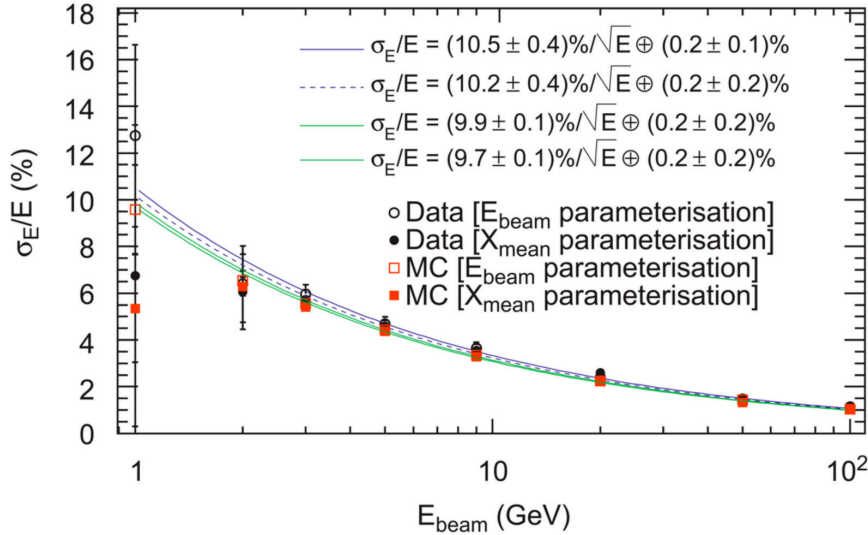


Figure 4.17: Resolution values, obtained from the MC simulation and data samples with the two different parametrisation of the calibration constants, and cluster noise contributions, after subtracting the noise contribution and the beam spread (data only). [227]

Sub-system	$ \eta $ -range	Effective constant term, c_{data}
EMB	$ \eta < 1.37$	$1.2\% \pm 0.1\% \text{ (stat)} \pm 0.5\% \text{ (syst)}$
EMEC (outer wheel)	$1.52 < \eta < 2.47$	$1.8\% \pm 0.4\% \text{ (stat)} \pm 0.4\% \text{ (syst)}$
EMEC (inner wheel)	$2.5 < \eta < 3.2$	$3.3\% \pm 0.2\% \text{ (stat)} \pm 1.1\% \text{ (syst)}$
FCal	$3.2 < \eta < 4.9$	$2.5\% \pm 0.4\% \text{ (stat)} \pm 1.0\% \text{ (syst)}$

Table 4.2: Measured effective constant term c_{data} from the observed width of the $Z \rightarrow ee$ peak for different calorimeter $|\eta|$ regions. [228]

controlled mostly cells of the third sampling. Detailed reports about planning, execution and a summary report of the recovery operation can be found in References [233–236].

Hadronic Calorimetry

The hadronic calorimeter system utilises different techniques. The barrel calorimeter covering $|\eta| < 1.0$ and the extended barrel tile calorimeter, covering $0.8 < |\eta| < 1.7$ consist of scintillating plastic tiles and steel plates, layout and segmentation of these calorimeters are depicted in Figure 4.18. The second component is the Hadronic end-cap Calorimeter (HEC) located in the wheels, covering $1.5 < |\eta| < 3.2$. It uses a copper-LAr technique similar to the lead-LAr of the EMEC and the FCals. The latter covers $3.1 < |\eta| < 4.9$ and also utilises the LAr technology. The cryostats are therefore shared by EMEC, HEC and FCals, as shown in Figure 4.20. With a radial range from 2.28 m to 4.25 m the barrel and extended tile provide approximately 7.4λ in this direction. The cumulative amount of the ATLAS detector material in units of λ as a function of the pseudorapidity is provided in Figure 4.21.

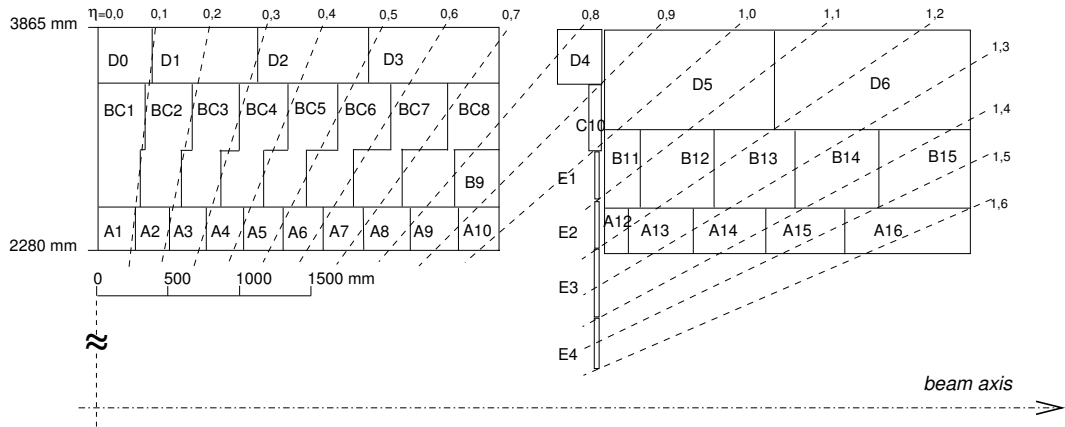


Figure 4.18: Segmentation of the hadronic tile calorimeter in η and radius, for the central barrel (left) and the extended barrel (right). [24]

Fundamental elements of the sampling tile calorimeters are scintillating plastic tiles and steel plates. Tiles provided in eleven sizes, all 3 mm thick, with radial lengths ranging from 97 mm to 187 mm and azimuthal lengths from 200 mm to 400 mm, constitute the active detector material. Thicker steel plates serve as passive absorber material, an approximate volume ratio of 4.7 : 1 is achieved. A schematic view of this stacking structure is given in Figure 4.19. Ionising secondary shower particles produce ultraviolet scintillation light in the polystyrene. Each tile is read out by two fluorine doped wavelength shifting fibres. By grouping and coupling of the fibres, a three dimensional cell structure is created, as depicted in Figure 4.18. The visible light from the fibre bunches creates an electrical signal in the photo-multipliers (PMTs) which is then read out. Three radial sampling layers with approximately 1.5λ , 4.1λ and 1.8λ at $|\eta| = 0$, possess a granularity in $\Delta\eta \times \Delta\phi$ of 0.1×0.1 for the first two layers and for the third layer

0.2×0.1 . Long term irradiation tests of tile-fibre-systems indicate, that a light loss of less than 10 % is expected after a ten year of operation. The tile calorimeters are equipped with three calibration systems, a charge injection, a laser and three ^{137}Cs radioactive sources. The latter ones are driven by a flowing liquid (water) through a in total 10 km long measuring tube system to reach all cells [237]. These test optical as well as digitised signals and help to set the PMT gains to an uniformity of $\pm 3\%$.

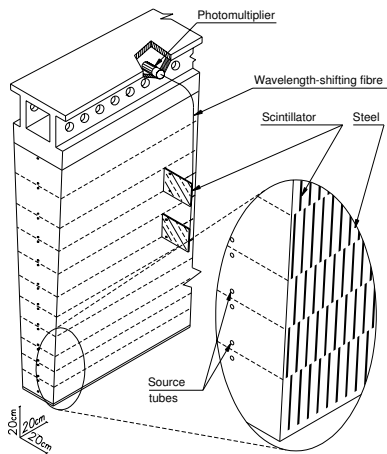


Figure 4.19: Schematic view of a hadronic calorimeter module including the read out components. [24]

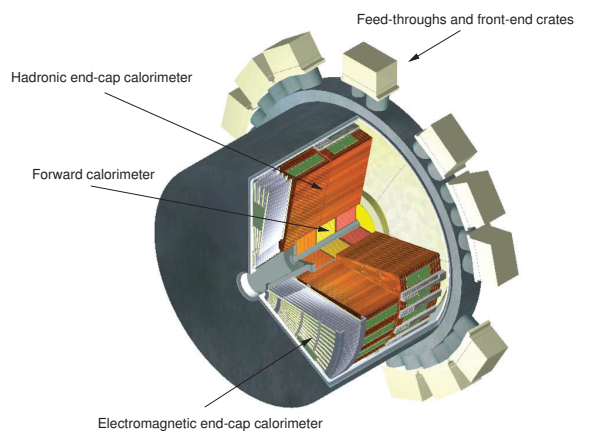


Figure 4.20: Cut-away view of the three end-cap calorimeters situated in the end-cap cryostat extending 3.17 m in length, with an outer radius of 2.25 m. [24]

The HEC is situated at larger distance to the IP than the EMEC, as shown in Figure 4.20. It consists of two wheels, the front wheel, HEC1, and rear wheel, HEC2, providing a total of four longitudinal layers. The modules of the HEC are build of copper plates. HEC1 begins with a 12.5 mm thick front plate, followed by 24 discs of 25 mm. HEC2 provides a coarser sampling fraction with 16 plates each 50 mm thick in addition to a 25 mm front plate. Corresponding thicknesses in interaction lengths along the η -axis of the HEC are depicted in Figure 4.21. Here HEC0 indicates the first sampling of HEC1. The inner radius changes from 372 mm for the first nine plates of HEC1 to 475 mm for the following HEC plates [238]. Gaps filled with LAr, the active material, are kept constant at 8.5 mm throughout the HEC. The cell structure, created by etching a pattern on the central foil in each gap, provides a semi-pointing geometry with cell sizes of 0.1×0.1 for $|\eta| < 2.5$ and 0.2×0.2 , in $\Delta\eta \times \Delta\phi$ for higher $|\eta|$ -values. A shielding plug made of 19.5 t copper is mounted behind the HEC2, to protect the most forward muon chambers [238].

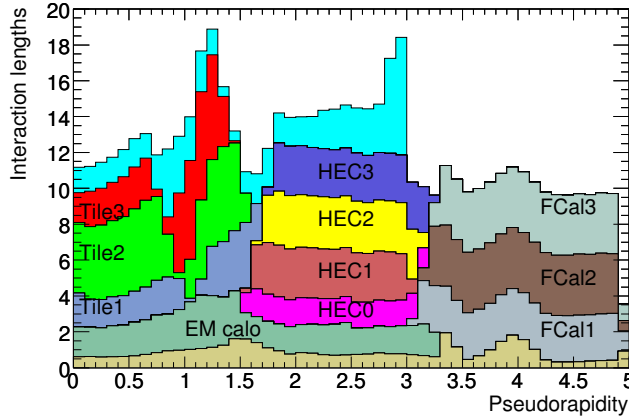


Figure 4.21: Cumulative amount of material measured in λ as a function of $|\eta|$ until the first layer of the MS (the material between hadronic calorimeters and MS is highlighted in cyan). [24]

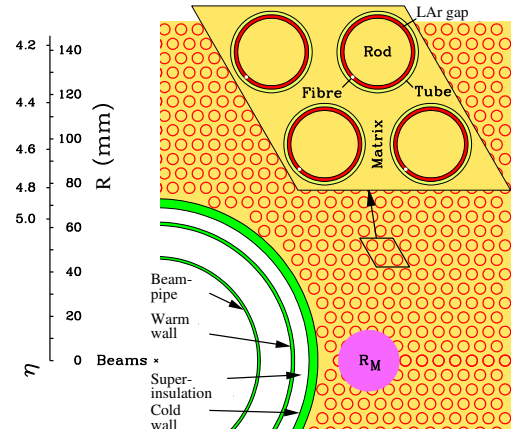


Figure 4.22: Schematic of the FCal electrode structure, with the Molière radius, R_M , represented by a solid disc. [24]

Forward Calorimeters

The FCals, which cover the highest $|\eta|$ -regions, $3.1 < |\eta| < 4.9$, are exposed to high particle fluxes. They are located at a distance of approximately 4.7 m from the interaction point. This resulted in a design of very small LAr gaps, smaller than the usual 2.1 mm of the barrel [238]. The FCal is divided into three 45 cm deep modules, adding up to a total depth of 9.94 λ or $208.1 X_0$. Electrodes are small diameter rods running in a matrix of high precision drilled holes parallel to the beam line. A radiation hard plastic fibre wound around the rod provides the LAr gap. A detailed view of FCal1 and its electrode structure is given in Figure 4.22. The first partition, FCal1, is made of copper plates. This material improves heat removal and optimises resolution for electromagnetic interacting particles. The FCal1 with 0.269 mm LAr gaps and a depth of $27.6 X_0$ is designed to fully absorb electromagnetic showers. For FCal2 and FCal3 tungsten is used as absorber material. This minimises the lateral spread of hadronic showers and with absorption lengths of 3.68λ and 3.60λ it is designed to provide full shower containment [238]. The LAr gap sizes are designed wider the further the distance from the IP is, 0.376 mm for FCal2 and 0.508 mm for FCal3. In this way higher readout currents and therefore better energy measurement resolutions are achieved.

4.2.4 Muon Spectrometer

The ATLAS muon system is designed to achieve a relative p_T -resolution for 1 TeV muon tracks in stand-alone mode of approximately 10 %. The lower boundary for muon identification is given with a muon momentum of approximately 3–4 GeV. Energy of this order is on average lost by muons traversing the detector material from the IP to the muon systems. Resistive Plate Chambers (RPCs) are situated in the barrel part $|\eta| < 1.05$. Thin Gap Chambers (TGCs) are used in the end-cap $1.05 < |\eta| < 2.4$, both provide Level-1 trigger signals [239].

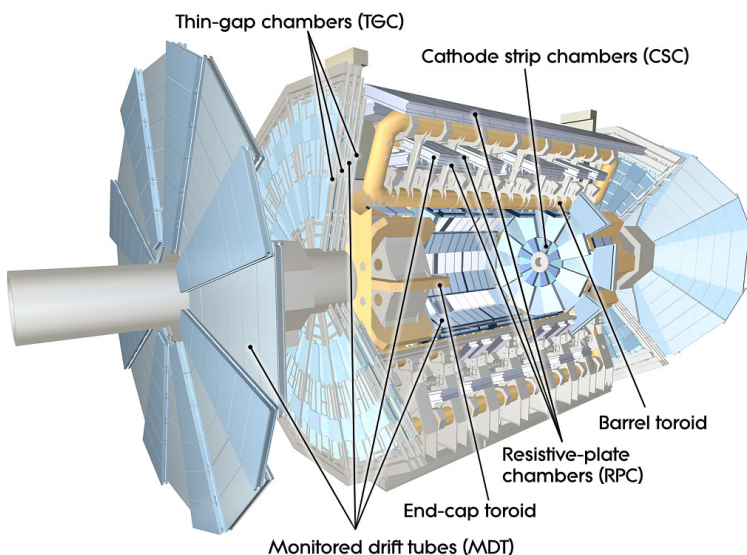


Figure 4.23: Muon spectrometer with its four chamber sub-systems. [24]

To achieve the design resolution, a strict alignment requirement of $\pm 30 \mu\text{m}$ is set. An optical system of around 5000 sensors permanently controls the placement of the muon system components. This allows potential offline data corrections in case of in situ displacements. Further, around 1700 three-dimensional Hall probes are arranged on the chambers providing precise information about position and shape of the conductors of each coil. These measure the magnetic field with high accuracy throughout the whole volume, a requirement for high precision muon measurements. In the region of $|\eta| < 1.0$ the barrel toroid and for the region $1.4 < |\eta| < 2.7$ the end-cap toroids provide the magnetic field. In the so called intermediate region $1.0 < |\eta| < 1.4$, where these fields overlap, field modelling calculations are non-trivial. Partial reduction of the bending power occurs in this region. Detectors are placed in concentric cylindrical shells around the barrel at radii of 5 m, 7.5 m and 10 m. Large wheels included in the end-cap spectrometer systems are situated at distances of $|z| \approx 7.4 \text{ m}, 10.8 \text{ m}, 14.0 \text{ m}$ and 21.5 m . In ϕ varying gap sizes, at $|\eta| \approx 0$ up to 2 m, are necessary for services of the inner detector, solenoid and calorimeters.

Highest precision momentum measurement is achieved by the Monitored Drift Tube chambers

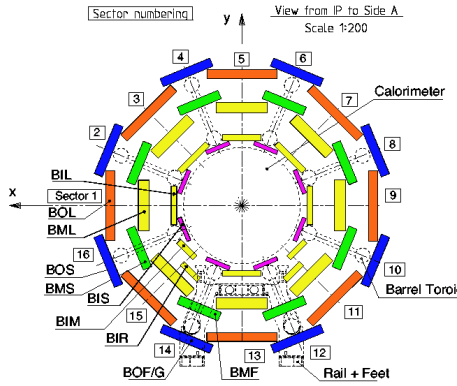


Figure 4.24: Barrel muon system cross-section, perpendicular to the beam axis or non bending plane, the outer diameter measures about 20 m. [24]

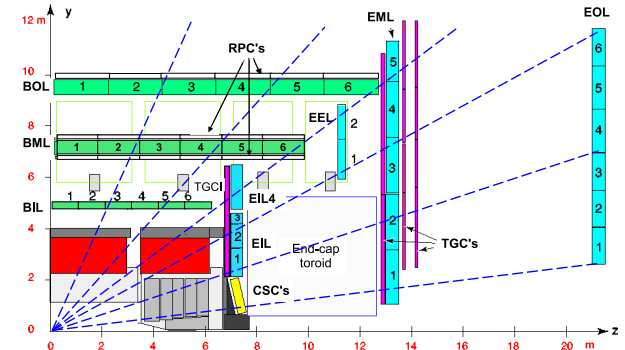


Figure 4.25: cross-section of the muon system in the bending plane, with dashed lines representing muons, demonstrating that typically three systems are transversed. [24]

(MDTs), covering the complete η -range of the MS. An average resolution of $80\text{ }\mu\text{m}$ per tube or about $35\text{ }\mu\text{m}$ per chamber, each containing three to eight layers of MDTs, is achieved. In the innermost layer of the end-cap Cathode-Strip Chambers (CSCs) instead of MDTs are installed, because of their higher rate capacity and better time resolution. CSCs are multi-wire proportional chambers with cathode plates segmented into orthogonal strips, allowing for a measurement of both coordinates. They have a resolution of $40\text{ }\mu\text{m}$ in the bending plane (η) and 5 mm in the transverse plane (ϕ). To safely identify a certain beam crossing, for higher level trigger decision, the system has to provide a good time resolution. The technology of the RPCs provides a time resolution of $\sigma \sim 1.5\text{ ns}$ [239], while at the same time measuring track coordinates in η and ϕ . As the MDTs are designed to perform as precision trackers for the η coordinate only, this measurement is then matched with trigger detector hits. In case of a successful match, the non-bending plane coordinate of the trigger is adopted as the second coordinate for the MDT.

4.2.5 Forward Detectors

Three smaller detector systems, depicted in Figure 4.26, dedicated to the coverage of the very forward region are installed in addition to the main ATLAS detector systems. They are named LUCID (LUminosity measurement using Cherenkov Integrating Detector), positioned at $\pm 17\text{ m}$ from the IP near the TAS (Target Absorber Secondaries), ZDC (Zero-Degree Calorimeter), embedded in the TAN (Target Absorber Neutral) at a distance $\pm 140\text{ m}$, and ALFA (Absolute Luminosity For ATLAS) situated at about $\pm 220\text{ m}$, as sketched in Figure 4.26.

LUCID a relative luminosity monitor for ATLAS. By detecting inelastic proton-proton scattering, it is dedicated to online luminosity monitoring. A usage as a rapidity-gap veto trigger

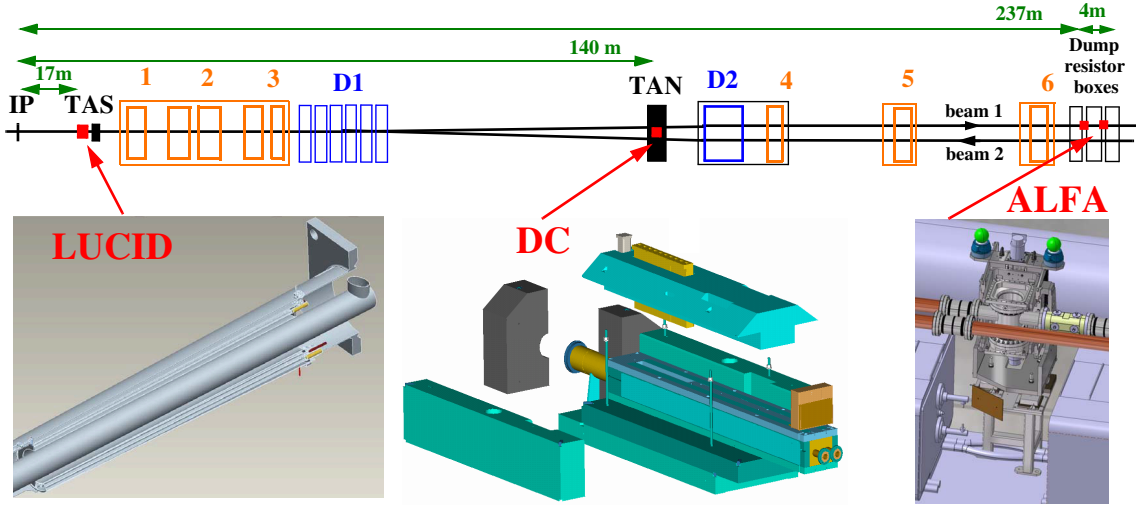


Figure 4.26: Position of the forward detectors along the beam line, with the distances measured from the ATLAS IP. [24]

for ATLAS is conceivable. LUCID is based on the principle that the number of interactions in a bunch-crossing is proportional to the number of particles detected in the forward region. It is build of an array of Cherenkov cones. A further detector dedicated for bunch-by-bunch luminosity measurements is the Beam Conditions Monitor (BCM) [240], it consists of four small diamond sensors on each side of the ATLAS IP arranged around the beampipe in a cross pattern [187].

The luminosity scale determined by the ATLAS for 2011 has been evaluated based on 2011 van der Meer scan data [241], because of various operational issues with the LUCID detector described in Reference [187]. The LUCID and BCM [242] results were used as a cross-check of the stability. Further independent cross checks were provided by utilising the ATLAS calorimeters. In the first method, the PMT current drawn in Tile Calorimeter modules is used [243], while in the second the current drawn across the liquid argon gaps in the Forward Calorimeter modules is used [244]. Since the currents drawn are related to the mean number of particles interacting in each calorimeter, the observed currents are sensitive to the luminosity. A review of the luminosity measurements for ATLAS is given in Reference [245].

The ZDCs are located between the beam-pipes just after the split. Primarily the calorimeters are designed to detect forward neutrons in $|\eta| > 8.3$ from heavy ion collisions. The neutron number in this very forward region is strongly correlated to the centrality of the collisions. Background neutrons, beam-gas and halo effects are reduced by a coincidence trigger, requiring a signal from both ZDCs. One detector consists of four modules, one electromagnetic with about $29 X_0$ and three hadronic calorimeters, each with a depth of about 1.16λ . Its time resolution of roughly 100 ps provides an ID-independent measurement of the vertex location with a precision of ± 3 cm along the beam axis.

ALFA follows the traditional approach for hadron colliders to measure the absolute lumi-

nosity via elastic scattering at small angles. Its detectors consist of scintillating-fibre trackers located inside Roman-pots. This technique, successfully used in the past, is based upon separation of the detector volume, called the pot, from the accelerators vacuum by a thin window. An interconnection with bellows to the beam-pipe allows for a proximity of the detector to the beam of 0.85 mm. The connection of the elastic-scattering amplitude in forward direction to the total cross-section is provided by the optical theorem, an overview given in Reference [246], which allows for an extraction of the luminosity. Measurements of extremely small scattering angles of around $3 \mu\text{rad}$ translate to a resolution requirement of $30 \mu\text{m}$. As this is less than the nominal beam divergence, remoteness from the IP and vicinity to the beam are necessary. Two Roman-pot stations are placed within 4 m on each side at a distance of 240 m from the IP. The anticipated spatial resolution of ALFA is $(25 \pm 3) \mu\text{m}$. ALFA already recorded three data runs, one in 2011 and two in 2012, the collaboration is close to finish the physics analysis of the 2011 data set [247].

4.2.6 Trigger and Data Acquisition

The trigger system plays a crucial role in the Large Hadron Collider experiments as the collision and data rates are significantly higher than the rates at which they can be stored. Therefore only the events with an interesting topologies should be selected by the trigger system and stored for analysis. Each bunch crossing produces about 1.5 MB of data in the read out system of the ATLAS detector. In 2011 installed systems for archival storage and data processing possessed a capability corresponding to a rate of 300 MB/s [248], this was upgraded to 600 MB/s [249] for the data taking in 2012. The necessary rejection power in the order of 10^7 can hardly be achieved in a single processing step. Large general purpose collider experiments currently use at least two entities for event selection before storing the data. The ATLAS trigger system consists of three levels, labelled as Level-1 (L1), Level-2 (L2) and event filter (EF). L2 and EF together form the High-Level Trigger (HLT). Data of an event passing these filters is transferred to the Data Acquisition system (DAQ). An overview of the information and data flow is given in Figure 4.27.

The hardware based L1 trigger uses reduced granularity information from the muon spectrometers, RPC and TGC, as well as all calorimeter subsystems. It searches for signatures of high- p_T muons, electrons/photons, jets, hadronically decaying τ leptons, large total and large missing transverse energy (E_T^{miss}). Detector readout systems, especially the limited pipeline memories, require a L1 decision within $2.5 \mu\text{s}$ after the bunch-crossing occurs. Subtraction of the cable-propagation delays, results in an actual required L1 processing time of less than $1.5 \mu\text{s}$. Commercially available computers and networking hardware, as used for the HLT, could not meet these needs. Therefore, the L1 trigger was assembled from custom made electronics. The L1 consists of three major components:

- L1Calo, a pipe-lined digital system works with about 7000 analog trigger towers with

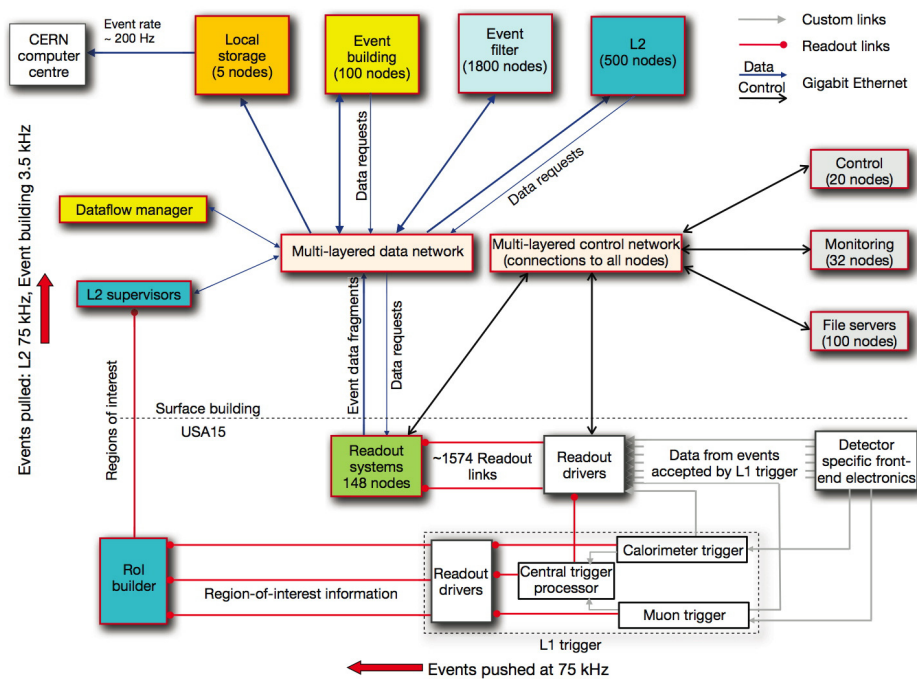


Figure 4.27: Block diagram depicting the interactions, connections, hardware and the data flow of the trigger and DAQ systems. [24]

a granularity of 0.1×0.1 in $\Delta\eta \times \Delta\phi$ and larger areas for higher $|\eta|$. It is located in a nearby service cavern, called USA15. Further details of this trigger architecture are given in Figure 4.28.

- The L1 muon trigger combines information of three triggers, one covering the barrel and two for the end-cap regions. Each trigger requires coincidence of hits in different trigger detector stations which have to be re-constructable, within a certain road to the IP.
- The Central Trigger Processor (CTP) receives the signals from L1Calo and the L1 muon trigger. Using look-up tables, it creates trigger decisions from the input, as visualised in Figure 4.29.

While the decision is processed by the trigger, all detector readout channels are stored in pipeline memories, placed on and around the detector. The muon time of flight to the spectrometer exceeds a bunch-crossing interval. The typical width of a calorimeter signal extends over 25 bunch-crossings. These effects are accounted for. Vicinity to the detector where radiation levels are high and therefore threaten the data reliability as well as technical aspects led to the shortest feasible pipeline length, preset by the the L1 processing time. Regions-of-Interest (RoIs), identified as possible trigger sources by the CTP, are passed on to the L2 with a maximal rate of 100 kHz. In 2011 the L1 rate was limited to approximately 50 kHz, as shown in Figure 4.30 [250].

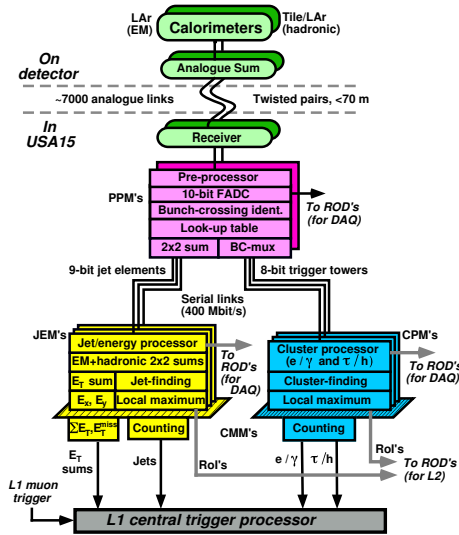


Figure 4.28: Architecture of the L1 calorimeter trigger listing the tasks performed by the three algorithmic processors. [24]

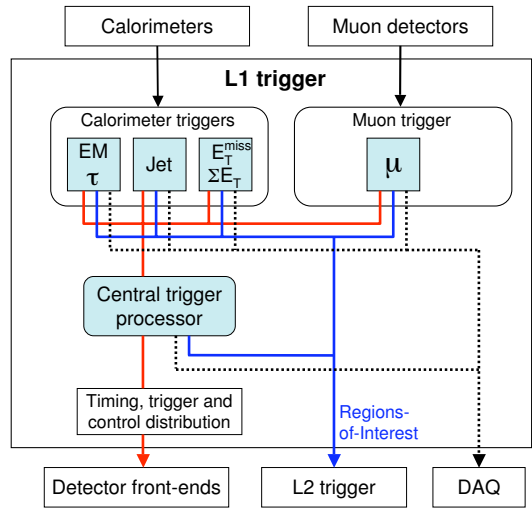


Figure 4.29: Block diagram of the L1 trigger with the data flow direction from left to right. [24]

The L2 trigger processes only the information within the RoIs in order to minimise the data transfer from the detector readout, evaluating only approximately only 2 % of the complete

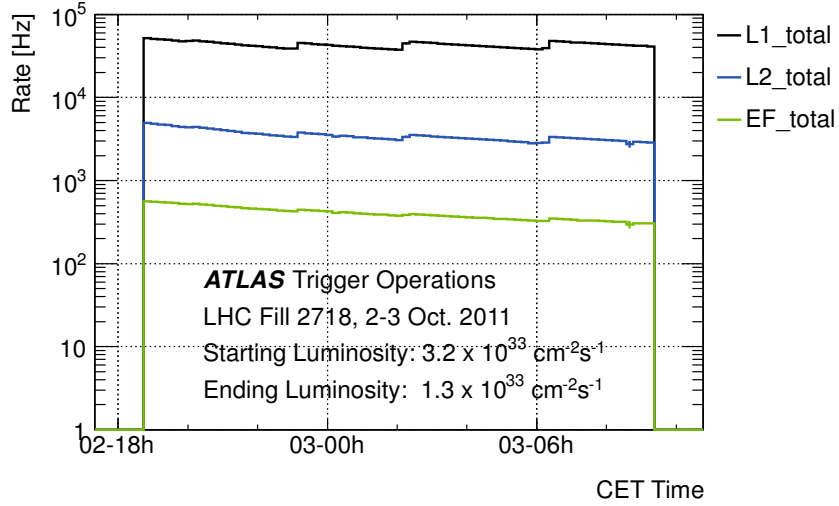


Figure 4.30: Data trigger output and recording rate of ATLAS at a luminosity of $3.2 \times 10^{33} \text{ cm}^{-2} \text{s}^{-1}$. [250]

available information. In several refining steps, each using data of additional detector subsystems, a hypothesis algorithm determines whether identified features meet the selection criteria. The L2 reduces the event rate below 5 kHz within an average processing time of less than 40 ms per event.

The EF, a processing farm, runs tasks with the standard ATLAS event reconstruction software. Event selection similar to L2 is repeated with full detector data access. A subset of tags, created during this decision process, is appended to the output event data structure. EF processing times per event were on average in the order of 4 s. An important task in this step is the classification of events according to ATLAS physics streams: “e/gamma”, “muon”, “jetTauEtmiss” and “minBias”. Event data passing this last filter, with an average rate of approximately 400 Hz in 2011 and approximately 600 Hz in 2011, is transmitted to the Subfarm Output Unit (SFO). The SFO, interface between HLT and CERN’s central data recording service, features an output bandwidth capable to handle peak event rate values up to 400 Hz. In case of prolonged transmission failure its capacity allows storage of full event data of about 24 h data-taking. In 2012 this system was upgraded and additional 200 Hz were written into the “delayed stream”, which will be reconstructed during the long shutdown [249].

In addition to the data streams mentioned, a subset of events is written to calibration and express streams. Only events usable for data quality or detector status monitoring are selected for these special streams. All triggers discussed above are fully configurable. Weights of selection tags, prescale factors, may be edited to control the event rate for chosen event signatures.

4.3 Data Taking

The LHC started up on September 10th, 2008. Nine days after the first beam passed the complete ring an accident occurred [251]. A faulty electric connection between two dipoles was determined as the source. This forced the LHC into a long repair and safety upgrade phase of about one year. Several dipoles and multipoles were brought to the surface for mending. Other similar faulty connections were detected and replaced. The re-startup occurred on November 20th, 2009, and it took a machine learning period until March 30th 2010 before an energy of $\sqrt{s} = 7$ TeV was successfully established and sustained until the end of 2011, while the instantaneous luminosity was constantly increases [252]. A further step towards nominal operation was taken in the beginning of 2012, when the centre of mass energy was raised to 8 TeV. The anticipated bunch spacing of 25 ns, thus roughly 7 m between each other, was achieved just before end of the proton-proton operation in December 2012. The ring was filled with 2748 bunches out of the possible 2808 [14]. The most common run setup during 2011 and 1012 *pp* collision operation was 1380 bunches with a spacing of 50 ns. The LHC delivered 48 pb⁻¹ in 2010 [253], 5.6 fb⁻¹ in 2011 [253] at $\sqrt{s} = 7$ TeV, and 23.3 fb⁻¹ [254] in 2012 at $\sqrt{s} = 8$ TeV, as shown in Figure 4.31, reaching a peak instantaneous luminosity of $7.73 \times 10^{33} \frac{1}{\text{cm}^2\text{s}}$, recorded by ATLAS, as illustrated in Figure 4.32. For an overview of the luminosities delivered to all experiments by the LHC refer to Reference [255]. In 2015 the design luminosity of $10^{34} \frac{1}{\text{cm}^2\text{s}}$ [14] is planned to be reached. At design luminosity, an average of 23 inelastic proton-proton interactions per bunch crossing was estimated [14], the value measured by ATLAS in 2012 during stable beam conditions was already close to 40, as visualised in Figure 4.33.

The data taking is divided in periods which usually mark similar data and detector conditions or have planned technical stops in between them. Further one fill of the LHC is labelled with a run-number. Table 4.3 and Table 4.4 provide an overview of the data taking in 2010 and 2011. The excellent data taking efficiency by ATLAS of 96 % and 98 %, relative to the LHC delivered luminosity, in the years 2010 and 2011, respectively, should be noted as a remarkable achievement.

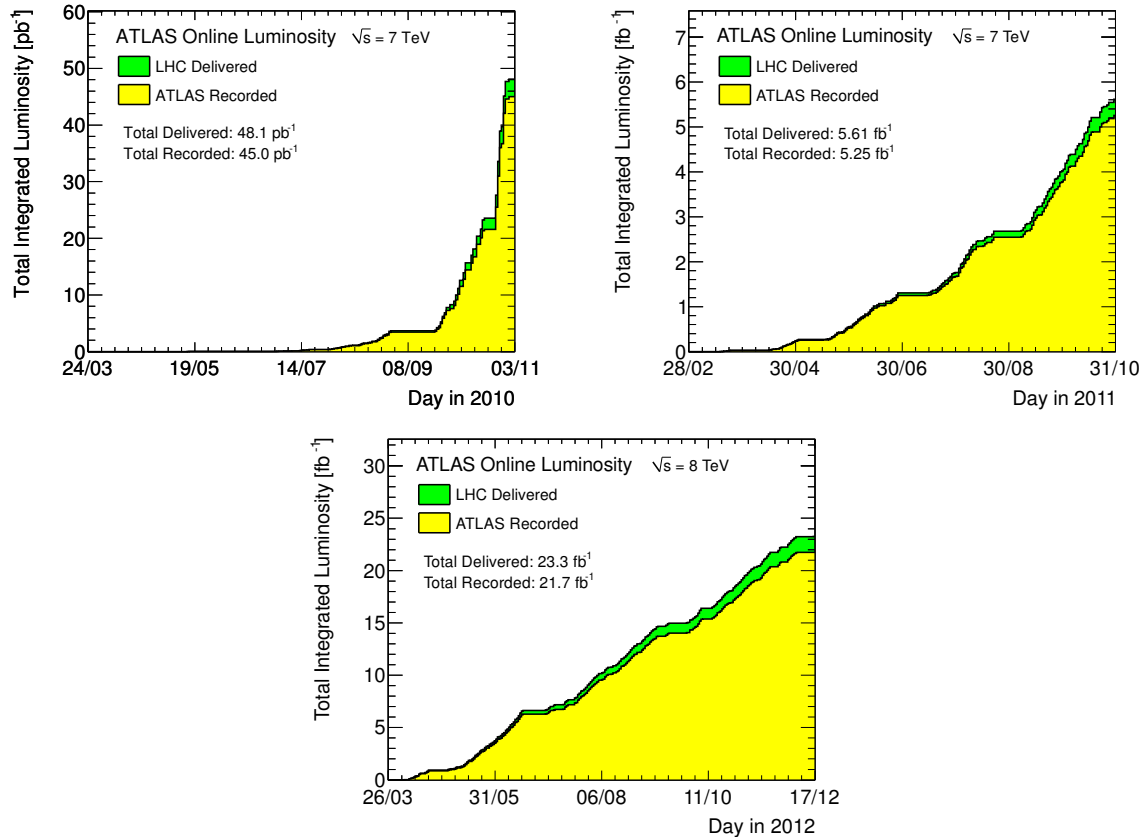


Figure 4.31: Total integrated luminosity in 2010 (top), 2011 (lower left), and 2012 (lower right). Cumulative luminosity versus day delivered to (green), and recorded by ATLAS (yellow) during stable beams and for pp collisions at 7 and 8 TeV centre of mass energy in 2010, 2011 and 2012. The delivered luminosity accounts for the luminosity delivered from the start of stable beams until the LHC requests ATLAS to turn the sensitive detector off to allow a beam dump or beam studies. Given is the luminosity as determined from counting rates measured by the luminosity detectors. These detectors have been calibrated with the use of the van-der-Meer beam-separation method, where the two beams are scanned against each other in the horizontal and vertical planes to measure their overlap function. [254]

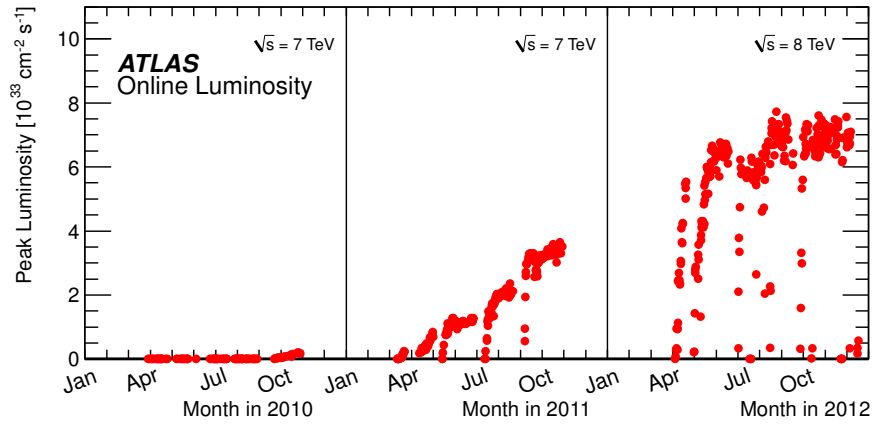


Figure 4.32: The peak instantaneous luminosity delivered to ATLAS per day as a function of time during the pp runs of 2010, 2011 and 2012. The online luminosity measurement is used for this plot. [254]

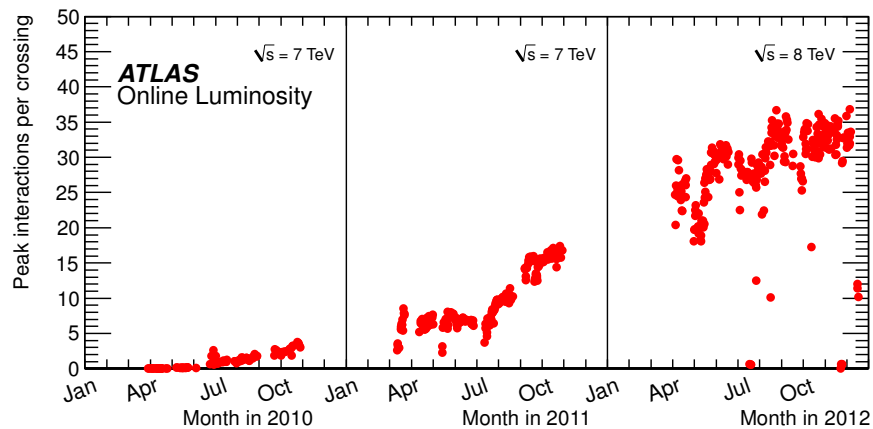


Figure 4.33: The maximum mean number of events per beam crossing as a function of time during the pp runs of 2010, 2011 and 2012. Only the values during stable beam periods are shown. [254]

Period	Date Range	Run-number Range	Stable Lumi (pb^{-1})	Rec. Lumi (pb^{-1})	Eff.	M.i.L. ($10^{30} \text{cm}^{-2} \text{s}^{-1}$)	μ_{max}
A	Mar-30 : Apr-19	152166 : 153200	4.3e-4	4.0e-4	92 %	2.5e-3	1.6e-2
B	Apr-23 : May-17	153565 : 155160	8.9e-3	8.7e-3	98 %	6.5e-2	1.4e-1
C	May-17; Jun-05	155228 : 156682	9.6e-3	8.8e-3	92 %	2.2e-1	1.8e-1
D	Jun-24 : Jul-19	158045 : 159224	3.2e-1	3.1e-1	97 %	1.5	2.1
E	Jul-29 : Aug-18	160387 : 161948	1.1	1.1	97 %	3.8	1.5
F	Aug-19; Aug-30	162347 : 162882	2.0	1.9	97 %	9.9	2
G	Sep-22 ; Oct-07	165591 : 166383	9.4	9.0	95 %	68	2.7
H	Oct-07 ; Oct-18	166466 : 166964	9.1	8.6	95 %	143	3.1
I	Oct-24 ; Oct-29	167575 : 167844	24	23	96 %	198	3.6
2010	Mar-30; Oct-29	152166 : 167844	46	44	96 %	198	3.6

Table 4.3: Periods of the pp data taken in 2010 by the ATLAS detector. (Maximal instantaneous Luminosity = M.i.L.) [256]

Period	Date Range	Run-number Range	Stable Lumi (pb ⁻¹)	Rec. Lumi (pb ⁻¹)	Eff.	M.i.L. (10 ³⁰ cm ⁻² s ⁻¹)	μ_{\max}
A	Mar-13 : Mar-21	177531 : 177965	9	8.7	97 %	154	7.1
B	Mar-21 : Mar-24	177986 : 178109	18	18	97 %	247	9.2
D	Apr-14 : Apr-29	179710 : 180481	186	182	98 %	659	7.3
E	Apr-30 : May-03	180614 : 180776	53	52	98 %	832	7.6
F	May-15; May-25	182013 : 182519	160	156	98 %	1 100	8
G	May-27; Jun-14	182726 : 183462	572	566	99 %	1 263	7.9
H	Jun-16 : Jun-28	183544 : 184169	287	283	99 %	1 264	6.8
I	Jul-13 : Jul-29	185353 : 186493	416	406	97 %	1 887	9.1
J	Jul-30 : Aug-04	186516 : 186755	240	237	98 %	1 995	9.6
K	Aug-04: Aug-22	186873 : 1877815	685	676	99 %	2 328	11
L	Sep-07 : Oct-05	188902 : 190343	1 625	1 599	98 %	3 252	16
M	Oct-06 : Oct-30	190503 : 191933	1 184	1 160	98 %	3 848	32
2011	Mar-13 : Oct-30	177531 : 191933	5 434	5 341	98 %	3 848	32

Table 4.4: Periods of the pp data taken in 2011 by the ATLAS detector. (Maximal instantaneous Luminosity = M.i.L.) [256]

Chapter 5

Event Selection and Data-Driven Background Estimation Techniques

In this chapter trigger and reconstructed physics objects utilised for the event selections, as well as the data-driven background and efficiency estimation techniques applied by the three different light charged Higgs boson analyses are discussed. All the studies presented in this work were performed with the help of ROOT – A Data Analysis Framework [257], utilising ROOT n-tuples produced by ATHENA [141]. In this context “light” charged Higgs boson refers to m_{H^\pm} smaller than the top quark mass, m_t . At the LHC the dominant production mode for H^\pm is through top quark decay via $t \rightarrow b H^\pm$. The dominant source of top quarks at the LHC is $t\bar{t}$ production, as shown by the example Feynman diagram in Figure 5.1.

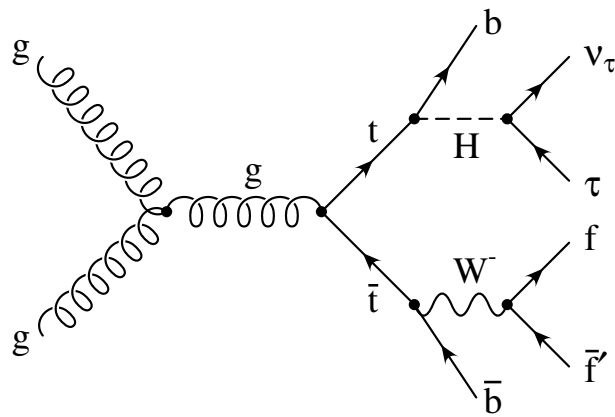


Figure 5.1: Example for a leading-order Feynman diagram for the production of a charged Higgs boson through gluon fusion in $t\bar{t}$ decays. [172]

The nomenclature for the different channels is best explained considering the diagram in Figure 5.1, where the first object in the name always denotes the identified particle stemming from the charged Higgs boson decay and the second object(s) name the reconstructed product(s) of the W boson decay. Note that “ τ_{had} ” stands in shorthand for hadronically decaying τ leptons, an approximate branching ratio of 65 %, and “ τ_{lep} ” for leptonically decaying τ leptons with a

branching ratio of approximately 35 %, as illustrated in Figure 5.2. Further note that leptons from τ_{lep} decays can not be distinguished from leptons stemming from other sources.

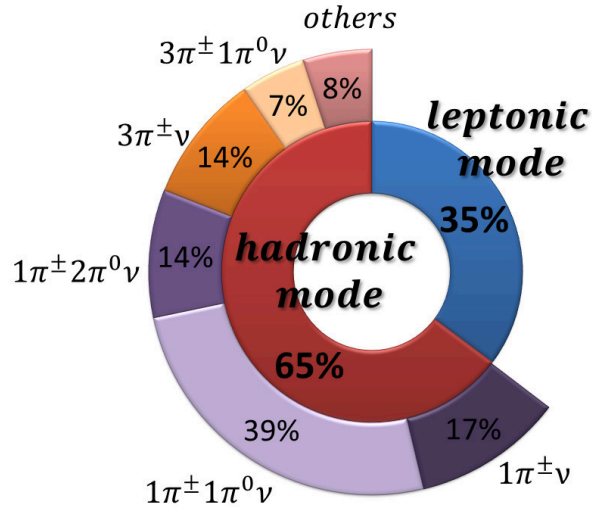


Figure 5.2: Pie chart illustrating the most common decay modes and their branching ratios of the τ lepton based on the data found in Reference [36]. [258]

5.1 Event Cleaning

The basic ATLAS data quality checks are applied. To ensure that no jet in the event is consistent with having originated from instrumental effects, such as spikes in the hadronic end-cap calorimeter, coherent noise in the electromagnetic calorimeter, or non-collision backgrounds a selection, the so-called “jet cleaning”, is performed by discarding events where any jet with $p_T > 20 \text{ GeV}$ fails the quality cuts discussed in Reference [259]. In addition, events are discarded if the primary vertex, the one with the largest sum of track momenta, has less than five associated tracks.

In periods E–H of 2011 data taking six front-end boards in the electromagnetic Liquid Argon barrel calorimeter could not be read out. Therefore events with a calorimeter jet in the vicinity of this “LAr hole” are discarded. If an electron or a jet with E_T greater than 15 or 20 GeV, respectively, is identified within $0.1 < \eta < 1.5$ and $-0.5 < \phi < -0.9$. This veto is applied in the same step as the jet cleaning.

5.2 Trigger for the Charged Higgs Boson Analyses

A trigger has to balance between maintaining the rate within the bandwidth limits and high signal selection efficiencies for analyses. Keeping the output rates under control is a crucial part

of efficient and stable data acquisition. The performance of the ATLAS trigger is described in Reference [248]. Dedicated studies were performed for the combined τ and missing transverse energy trigger.

Dedicated trigger studies, to ensure stable rates throughout the 2012 data taking, as well as highest possible signal efficiencies were carried out. Due to changes in the τ as well as the E_T^{miss} trigger algorithms in the beginning (period A) of the 2012 data taking these detailed studies ensured the highest amount feasible of data recorded for the charged Higgs $\tau_{\text{had}} + \text{jets}$ analysis. It is important to keep the E_T^{miss} threshold low, else the sensitivity for the low charged Higgs masses could be reduced, as Figure 5.3 demonstrates. A τ trigger isolation at Level 1 was tested in combination with non-isolated higher threshold trigger, to compensate for isolation inefficiencies for higher p_T τ leptons, as can be evinced in Figure 5.4. This setup however did not save as much trigger bandwidth as anticipated and after the trigger hardware upgrade was replaced by a non-isolated low p_T threshold (29 GeV) τ trigger, which required one or three tracks. In combination with a new E_T^{miss} trigger, utilising topological clusters of the calorimeters [260] at trigger level for improved E_T^{miss} calculation, with a E_T^{miss} threshold at 50 GeV was tested and approved for the 2012 data taking.

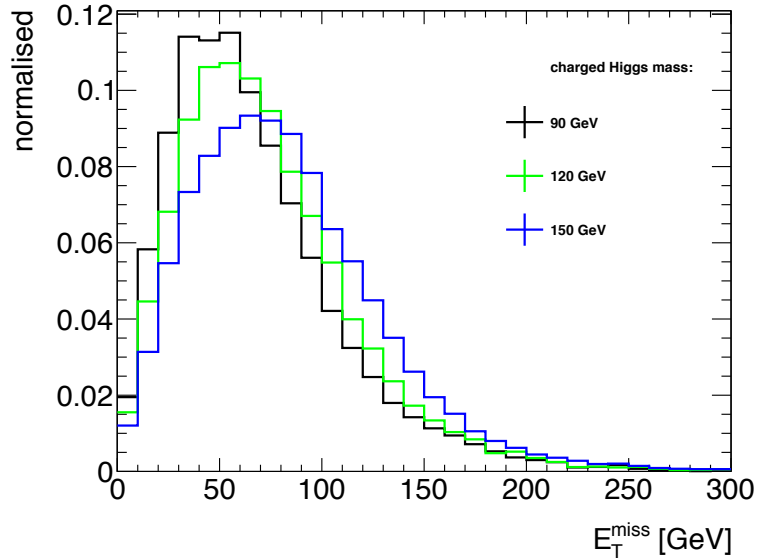


Figure 5.3: E_T^{miss} distributions for different light charged Higgs boson signal masses.

5.2.1 Trigger for the $\tau_{\text{had}} + \text{Lepton}$ and $\tau_{\text{lep}} + \text{Jets}$ Channels

The $\tau_{\text{had}} + \text{lepton}$ and the $\tau_{\text{lep}} + \text{jets}$ final state analysis rely on events passing a single-lepton trigger. Electron trigger with a p_T threshold of 20 or 22 GeV for periods B–H and for periods I–K respectively. Muon trigger at 18 GeV for the periods B–H and the same p_T threshold but tighter selection criteria for periods I–M. These thresholds are low enough to guarantee that electrons

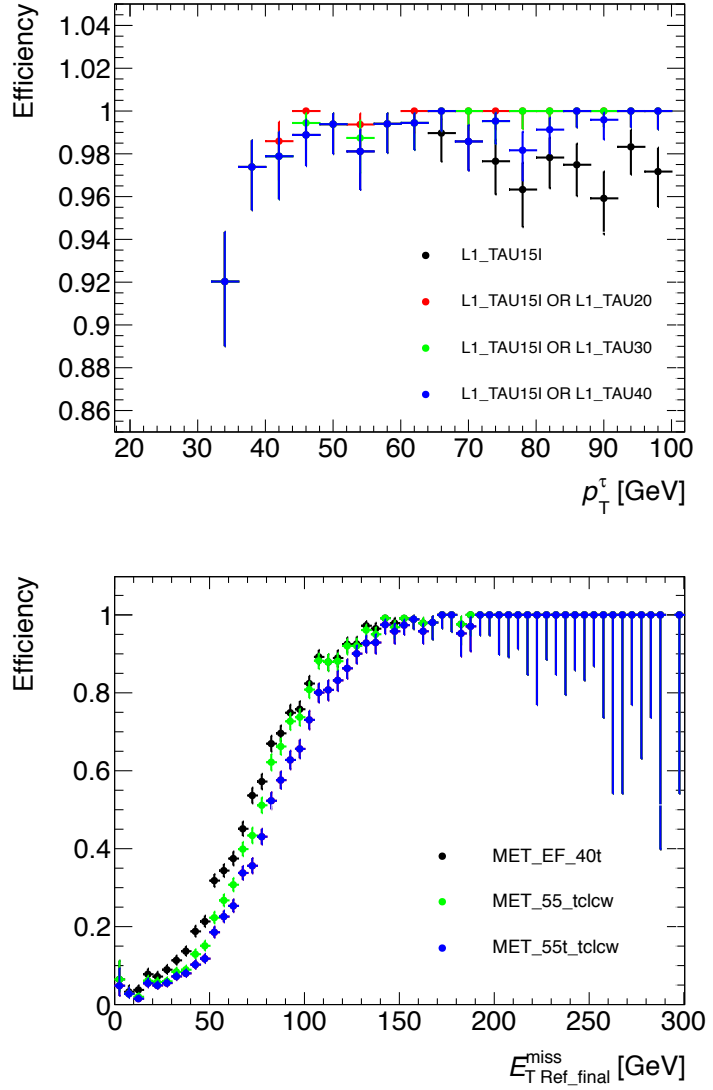


Figure 5.4: Trigger turn on curves of components of a possible $\tau_{\text{had}} + \text{jets}$ charged Higgs search analysis for the data taking in 2012. Level 1 isolation studies of the τ trigger with possible logical “OR” combinations with higher threshold non-isolated items to recover the inefficiency at higher p_T are shown in the top plot. The turn-on curve, shown in the lower plot, studies new E_T^{miss} trigger item options at Event Filter level, where a “t” after the threshold value denotes “tight” to denote the closeness of the threshold value to the Level 2 threshold, and “tclcw” denotes a E_T^{miss} calculated using “topological clusters” with the “local cluster weighting” calibration scheme. A signal sample with $m_{H^\pm} = 130$ GeV was used for these histograms.

with $E_T > 25 \text{ GeV}$ and muons with $p_T > 20 \text{ GeV}$ are situated in the plateau region of the trigger-efficiency curve.

5.2.2 Trigger for the $\tau_{\text{had}} + \text{Jets}$ Channel

The $\tau_{\text{had}} + \text{jets}$ final state analysis relies on events passing a combined τ and E_T^{miss} trigger. For periods B–K the trigger has a p_T threshold of 29 GeV for the τ object and a E_T^{miss} threshold of 35 GeV . For the periods L–M, the trigger has the same thresholds, but additionally requires three jets at Level-1 with a minimum p_T of 10 GeV . This was proven to have no influence on the signal efficiency, but reduced this trigger L1 rates by 50 %. In both cases no correction on the E_T^{miss} is applied for muon objects. The efficiency of these triggers, as measured in signal simulation, after all selection criteria, is 70 % [172].

5.3 Physics Object Reconstruction

This section provides details on the reconstructed physics objects used in the analyses. Note that some requirements, as for example the thresholds for the transverse energy, E_T , or the transverse momentum, p_T , of charged leptons and τ leptons amongst others, might be increased in steps in the different analyses selections.

5.3.1 Muons

Muon candidates are required to contain matching ID and MS tracks [261], a $p_T > 15 \text{ GeV}$ and to lie within $|\eta| < 2.5$. Further they have to fulfil tight identification selection criteria and good track quality is ensured by imposing criteria on the number of hits in the ID sub-detectors, taking known in-operational channels into account [262]. Only isolated muons are accepted by requiring that the transverse energy deposited in the calorimeters and the transverse momentum of the inner detector tracks in a cone of radius $\Delta R = 0.2$ and 0.3 around the muon amounts to less than 4 GeV and 2.5 GeV , respectively. The energy deposited in the calorimeter and the muon track momentum itself are excluded from the energy sum in the cone when applying these isolation requirements. Scale factors are applied to simulated events with muons to account for trigger and identification efficiency differences between the data and simulations.

5.3.2 Electrons

Electrons are reconstructed by matching clustered energy deposits in the electromagnetic calorimeter to tracks reconstructed in the ID. Candidates are required to meet quality requirements based on the expected shower shape, enclosed in the definition of the tight electron

identification requirements, which have an efficiency in the range of 70–80 % [228]. Electrons are additionally requested to have $E_T > 20$ GeV, where $E_T = E_{\text{clus}}/\cosh(\eta_{\text{track}})$ is computed using the calorimeter cluster energy, E_{clus} , and the direction of the electron track, η_{track} . The pseudorapidity range for the electromagnetic cluster covers the fiducial volume of the detector, $|\eta| < 2.47$. The transition region between the barrel and end-cap calorimeters, $1.37 < |\eta| < 1.52$, is excluded. In addition, E_T and η -dependent calorimeter and tracking isolation requirements are imposed in a cone with a radius $\Delta R = 0.2$ and 0.3, respectively, around the electron position, excluding the electron object itself. The isolation criteria applied have an efficiency of about 90 % [228, 263]. The efficiencies of the electron trigger, reconstruction and identification are measured using $Z \rightarrow ee$ and $W \rightarrow ev$ events, in both data and Monte Carlo simulation samples. The MC simulations are generally found to model the data well [228], considering the electron reconstruction, with a few exceptions mainly regarding the lateral development of showers and the TRT in the end-caps. Scale factors are derived to parametrise these efficiency differences between the data and simulations.

5.3.3 Jets

Jets are reconstructed using the anti- k_t algorithm [264, 265] with a size parameter value of $R = 0.4$. The jet finder uses three-dimensional, noise-suppressed clusters of calorimeter cells, topological clusters [260], that are reconstructed at the electromagnetic scale, appropriate for the energy deposited by electrons or photons. Jets are then calibrated to the hadronic energy scale with correction factors based on simulation [266, 267].

A method that allows identification and selection of jets originating from the hard-scatter interaction using tracking and vertex information is utilised [268]. It is referred to as the “Jet Vertex Fraction” (JVF), defined as the fraction of the total transverse momentum of the charged particle tracks associated to the jet that belongs to tracks which are also compatible with the primary vertex:

$$\text{JVF}(\text{jet}_i, \text{vtx}_j) = \frac{\sum_k p_T(\text{trk}_k^{\text{jet}_i}, \text{vtx}_j)}{\sum_n \sum_l p_T(\text{trk}_l^{\text{jet}_i}, \text{vtx}_n)}. \quad (5.1)$$

By convention, jets with no associated tracks are assigned a JVF value of -1 to keep a high efficiency for jets at large values of $|\eta|$, outside the range of the inner tracking detectors. The jet selection based on JVF is insensitive to pile-up. A requirement of $|\text{JVF}| > 0.75$ is set for all jets during event selection. Discrepancies between the simulated and measured JVF distributions are accounted for as a systematic uncertainty in the analyses [269, 270].

5.3.4 b -Tagging

To identify jets initiated by b -quarks, the MV1 algorithm [271] is utilised. The MV1 algorithm is a neural-network based algorithm that uses the output weights of IP3D, SV1 and JetFitterCombNN as inputs [271, 272], combining impact-parameter information with the explicit determination of a secondary vertex. A working point corresponding to an average efficiency of about 70 % for b -jets with $p_{\mathrm{T}} > 20 \, \mathrm{GeV}$ in $t\bar{t}$ events and a light-quark jet rejection factor of about 130 is chosen. As the b -tagging algorithm relies on information of the inner tracking detectors, the acceptance region for all jets is restricted to $|\eta| < 2.4$. Tagging and mis-tagging efficiency scale factors relate efficiencies, as determined in various data samples, to their counterparts in simulation [273–275]. These are applied to simulation, after the b -tagging algorithm was run to the jets.

5.3.5 Hadronically decaying τ Leptons

To reconstruct hadronically decaying τ leptons, anti- k_t jets with either one or three associated tracks reconstructed in the ID and depositing $E_{\mathrm{T}} > 10 \, \mathrm{GeV}$ in the calorimeter are considered as τ lepton candidates [276]. Dedicated veto algorithms are utilised to reject electrons and muons [277]. The τ lepton candidates are further required to have a visible transverse momentum of at least $20 \, \mathrm{GeV}$ and to be within $|\eta| < 2.3$. Hadronically decaying τ leptons are identified with a likelihood criterion designed to discriminate against quark and gluon initiated jets by using shower shape and tracking variables as inputs. A working point utilising a likelihood-based identification technique with an efficiency of about 30 % for hadronically decaying τ leptons with $p_{\mathrm{T}} > 20 \, \mathrm{GeV}$ in $Z \rightarrow \tau\tau$ events is chosen, leading to a rejection factor of about 100–1000 for jets [277]. The rejection factor depends on the p_{T} and η of the τ lepton candidate and on the number of associated tracks. Only τ lepton candidates which fulfil the likelihood-based identification criterion are hence referred to as “ τ leptons”.

5.3.6 Missing Transverse Momentum

The magnitude of the missing transverse momentum, $E_{\mathrm{T}}^{\mathrm{miss}}$, is reconstructed from noise-suppressed clusters of cells in the calorimeters, topological clusters [260] and from muon tracks reconstructed in the muon spectrometer and the inner tracking detectors [221]. Clusters of calorimeter cells belonging to jets, including τ lepton candidates, with $p_{\mathrm{T}} > 20 \, \mathrm{GeV}$ are calibrated to the hadronic energy scale. Calorimeter cells not associated to any object are also taken into account and calibrated at the electromagnetic energy scale. To deal appropriately with the energy deposited by muons in the calorimeters, the contributions of muons to $E_{\mathrm{T}}^{\mathrm{miss}}$ are calculated differently for isolated and non-isolated muons.

5.3.7 Removal of Geometric Overlaps between Objects

When selected lepton and jet candidates, satisfying the criteria above, overlap with $\Delta R < 0.4$ or 0.2 , the following procedures are applied in this respective order: muon candidates are rejected if they are found within $\Delta R < 0.4$ of any jet with $p_T > 25$ GeV; a τ lepton candidate is rejected if found within $\Delta R < 0.4$ of a b -tagged jet or within $\Delta R < 0.2$ of a selected muon or electron and jets are removed if they are within $\Delta R < 0.2$ of a selected τ lepton or electron.

5.4 Selection and Cut Optimisation

5.4.1 $\tau_{\text{had}} + \text{Lepton}$ Analysis Selection

This analysis relies on the detection of $\tau_{\text{had}} + \text{lepton}$ decays of $t\bar{t}$ decays, where the hadronically decaying τ lepton arises from $H^\pm \rightarrow \tau_{\text{had}}^\pm \nu$, while the lepton, ℓ , an electron or muon, stem from a leptonically decaying W boson, i.e. $t\bar{t} \rightarrow b\bar{b}WH^+ \rightarrow b\bar{b}(\ell\nu)(\tau_{\text{had}}\nu)$. In this analysis $E_{\text{T}}^{\text{miss}}$ is used as the discriminating variable for SM $t\bar{t}$ events and those where the top quark decays are mediated via a charged Higgs boson, in which case the neutrinos are likely to carry away more energy (also see Figure 5.3). In the lepton case the object p_T and E_{T} cuts were determined by the trigger thresholds. The lower thresholds of further reconstructed objects were set in accordance to the validity range for the applied MC to data scale factors.

In the charged Higgs search with data taken in 2010 [159] a scan of the $E_{\text{T}}^{\text{miss}}$ and the transverse energy sum in the calorimeters, $\sum E_{\text{T}}$, phase space was performed to determine a signal to background ratio optimised set of cuts. The distributions, for the analysis with the data taken in 2010, of selected events before the application of the $E_{\text{T}}^{\text{miss}} > 60$ GeV and $\sum E_{\text{T}} > 200$ GeV selection criteria are given in Figure 5.6 and Figure 5.5, respectively.

Due to increased pile-up conditions the $\sum E_{\text{T}}$ variable was not modelled well in the data taken in 2011. $\sum p_T$ is defined as the sum of the transverse momenta of all tracks associated with the primary vertex. Tracks entering the sum must pass quality cuts on the number of hits in the central tracking detector and a $p_T > 1$ GeV. As this variable is based on tracks from the primary vertex (as opposed to energy deposits in the calorimeter), it is robust against pile-up. The $E_{\text{T}}^{\text{miss}}$ contribution from QCD in the analyses with 2011 data was estimated utilising a data-driven background estimation method, therefore no cut was applied on this variable. The $\tau_{\text{had}} + \text{lepton}$ analysis relies in the single-lepton triggers, as described in Section 5.2.1. A matching of the selected lepton and the single-lepton trigger object is performed by requiring $\Delta R < 0.2$.

To efficiently select $\tau_{\text{had}} + \text{lepton}$ events, the following requirements are imposed:

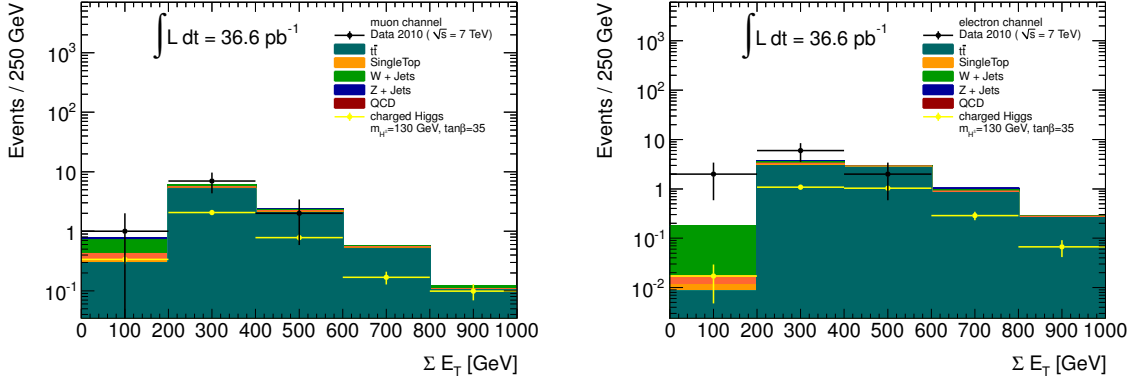


Figure 5.5: The sum over the transverse energy $\sum E_T$ distributions before applying the $\sum E_T > 200 \text{ GeV}$ cut for $\tau_{\text{had}} + \text{leptons}$ channel of the charged Higgs search, split in the muon (left) and electron (right) channels.

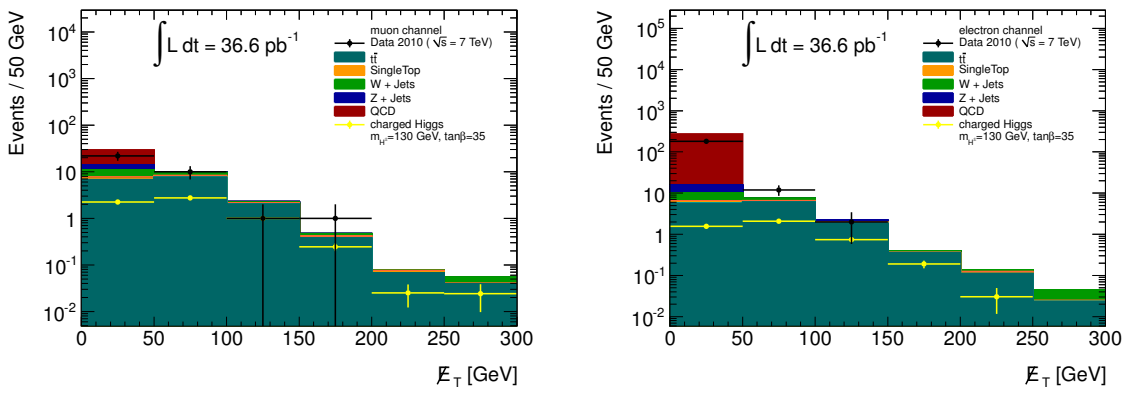


Figure 5.6: The missing transverse energy E_T^{miss} distributions before applying the $E_T^{\text{miss}} > 60 \text{ GeV}$ cut for $\tau_{\text{had}} + \text{leptons}$ channel of the charged Higgs search, split in the muon (left) and electron (right) channels.

- exactly one lepton with $E_T > 25$ GeV (electron) or $p_T > 20$ GeV (muon) and matched to the corresponding trigger object, no further electron or muon present in the event;
- exactly one τ lepton within $|\eta| < 2.3$ with $p_T > 20$ GeV and a reconstructed electric charge opposite to the selected lepton;
- at least two jets with $p_T > 20$ GeV, with at least one b -tagged jet among them;
- $\sum p_T > 100$ GeV to suppress multi-jet events.

After imposing the above listed event selection the total signal efficiency is determined from simulation and given, separately for the muon and electron triggered categories, in Table 5.1 for different charged Higgs boson mass hypotheses.

m_{H^\pm} (GeV)	μ -channel efficiency (%)	e -channel efficiency (%)
90	0.402	0.321
100	0.416	0.309
110	0.425	0.324
120	0.422	0.307
130	0.403	0.293
140	0.350	0.268
150	0.293	0.232
160	0.229	0.192

Table 5.1: Signal efficiency as a function of the charged Higgs boson mass determined from simulation.

5.4.2 $\tau_{\text{lep}} + \text{jets}$ Analysis Selection

This analysis relies on the detection of $\tau_{\text{lep}} + \text{jets}$ decays of $t\bar{t}$ events, where the charged lepton, ℓ an electron or muon, arises from the subsequent $H^\pm \rightarrow \tau_{\text{lep}}^\pm \nu$ decay, while the jets stem from a hadronically decaying W boson, i.e. $t\bar{t} \rightarrow b\bar{b}WH^+ \rightarrow b\bar{b}(q\bar{q}')(\tau_{\text{lep}}\nu)$.

The $\tau_{\text{lep}} + \text{jets}$ analysis uses events passing a single-lepton trigger with an E_T threshold of 20–22 GeV for electrons and a p_T threshold of 18 GeV for muons. In addition, to select a sample of $\tau_{\text{lep}} + \text{jets}$ events enriched in $t\bar{t}$ candidates, the following requirements are imposed:

- exactly one lepton with $E_T > 25$ GeV (electron) or $p_T > 20$ GeV (muon) and matched to the corresponding trigger object, neither a second lepton nor a hadronically decaying τ lepton in the event;

- at least four jets with $p_T > 20$ GeV, exactly two of these b -tagged;
- $E_T^{\text{miss}} > 40$ GeV and, to discriminate between E_T^{miss} arising from isolated neutrinos and from poorly reconstructed leptons, this requirement is tightened to $E_T^{\text{miss}} \times |\sin \Delta\phi_{\ell,\text{miss}}| > 20$ GeV if the azimuthal angle, $\Delta\phi_{\ell,\text{miss}}$, between the lepton and E_T^{miss} is smaller than $\pi/6$.

5.4.3 $\tau_{\text{had}}+\text{Jets}$ Analysis Selection

This analysis relies on the detection of $\tau_{\text{had}}+\text{jets}$ decays of $t\bar{t}$ events, where the hadronically decaying τ lepton arises from the $H^\pm \rightarrow \tau_{\text{had}}^\pm \nu$ decay, while the jets stem from a hadronically decaying W boson, i.e. $t\bar{t} \rightarrow b\bar{b}WH^+ \rightarrow b\bar{b}(q\bar{q}')(\tau_{\text{had}}\nu)$. For the selected events, the transverse mass, $m_T = \sqrt{2p_T^\tau E_T^{\text{miss}} (1 - \cos \Delta\phi_{\tau,\text{miss}})}$, with $\Delta\phi_{\tau,\text{miss}}$ defined as the azimuthal angle between the hadronically decaying τ lepton and the direction of the missing transverse momentum, is used as final discriminating variable. The m_T variable is usually utilised for the leptonically decaying W boson analyses. Therefore the discriminating power grows with the increasing mass difference of the charged Higgs boson signal and the W bosons from $t\bar{t}$ background decays.

The $\tau_{\text{had}}+\text{jets}$ analysis uses events passing a $\tau + E_T^{\text{miss}}$ trigger described in Section 5.2.2 with a threshold of 29 GeV for the τ trigger object and 35 GeV for the E_T^{miss} . The following requirements to select a sample $\tau_{\text{had}}+\text{jets}$ events are imposed:

- at least four jets with $p_T > 20$ GeV, excluding hadronically decaying τ leptons, among them at least one b -tagged jet;
- exactly one hadronically decaying τ lepton with $p_T > 40$ GeV within $|\eta| < 2.3$ and matching the corresponding τ trigger object;
- neither a second hadronically decaying τ lepton with $p_T > 20$ GeV, nor any electrons with $E_T > 20$ GeV, nor any muons with $p_T > 15$ GeV;
- $E_T^{\text{miss}} > 65$ GeV;
- to reject events in which a large reconstructed E_T^{miss} is present due to the limited resolution of the energy measurement the ratio, based on the $\sum p_T$, must satisfy:

$$\frac{E_T^{\text{miss}}}{0.5 \text{ GeV}^{1/2} \cdot \sqrt{\sum p_T}} > 13;$$

- the combination of two untagged jets (j) and one b -tagged jet (b) with the highest $p_T^{j,b}$ satisfying $m_{jb} \in [120, 240]$ GeV ensures the selection of a topology consistent with a top quark decay.

5.5 Background Estimations

This section introduces data-driven background estimation methods utilised for the charged Higgs boson searches. First the measurement of the τ lepton mis-identification probability from electrons is explained in detail. This measurement was, in the process of this work, performed for the first time at ATLAS experiment, with data taken in 2010. Subsequently the usage of its results in the charged Higgs boson searches, with data taken in 2011, for the estimation of background contributions stemming from electrons mis-identified as τ leptons in a data-driven way, as well as further data-driven background estimation methods for other background contributions are described.

5.5.1 Measurement of the τ Lepton Mis-identification Probability from Electrons

A dedicated measurement of the mis-identification probability of τ leptons from electrons was performed with the first data taken in 2010, this work is documented in Reference [151]. Electrons are an important background for analyses involving hadronically decaying τ leptons, first and foremost the τ leptons with one associated track. Therefore, a dedicated cut-based electron veto algorithm is available, utilising on the following variables [278]:

- E_{\max}^{strip} : The maximum energy deposited in the strip layer of the electromagnetic calorimeter, not associated with that of the leading track, $p_{\text{T}}^{\text{Ltrk}}$.
- $E_{\text{EM}}/p^{\text{Ltrk}}$: The ratio of the energy deposited in the electromagnetic calorimeter, E_{EM} , and the momentum of the leading track, p^{Ltrk} .
- $E_{\text{Had}}/p^{\text{Ltrk}}$: The ratio of the energy deposited in the first layer of the hadronic calorimeter, E_{Had} , and the leading track momentum, p^{Ltrk} .
- $N_{\text{HT}}/N_{\text{LT}}$: The ratio of high-threshold hits to low-threshold hits in the TRT. This variable is only used within the acceptance region $|\eta| < 1.7$.

The distributions of these, by the cut-based electron veto algorithm utilised, variables are shown in Figure 5.7 after the full tag-and-probe selection, as described below. Generally a good agreement is observed between data and Monte Carlo, except for the ratio of high-threshold to low-threshold hits, where a significant shift to higher values is observed in data. This shift can mainly be attributed to electron candidates falling inside the TRT region with $|\eta| > 0.8$. The selection performed by the cut-based electron veto algorithm based on the variables described above are p_{T} and $|\eta|$ dependent [278]. A Boosted Decision Tree (BDT) based electron veto algorithm was equally considered and studied in this measurement.

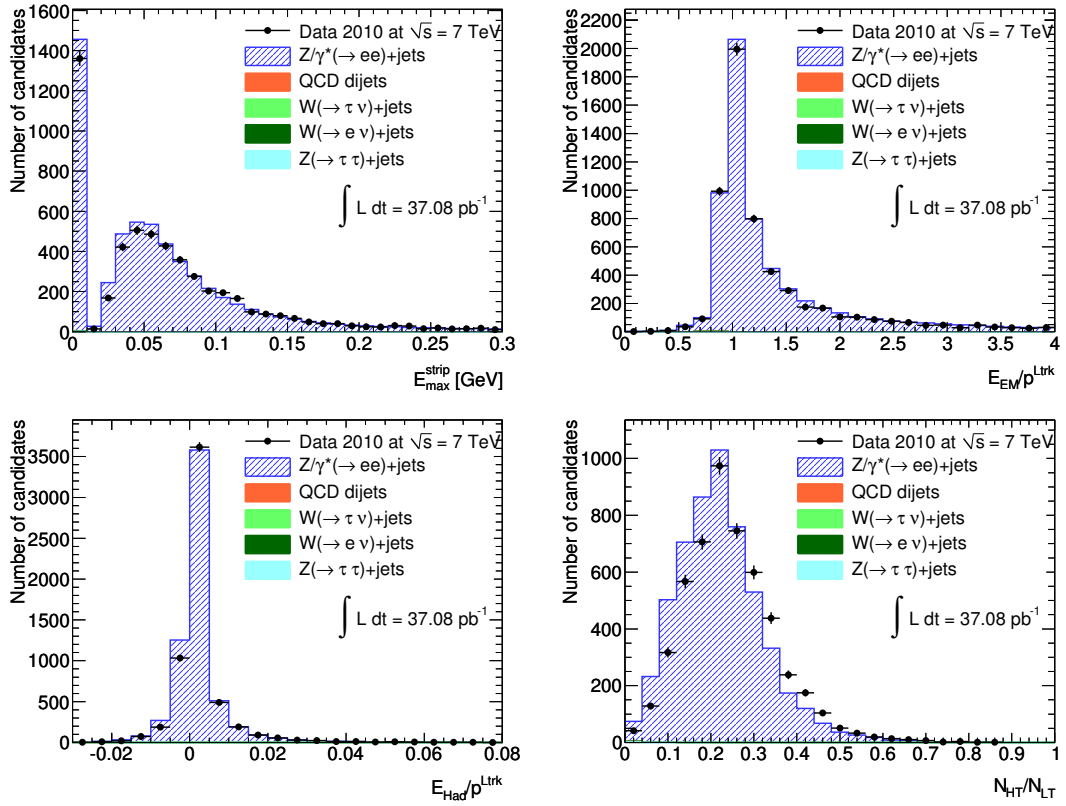


Figure 5.7: Variables utilised by the cut-based electron veto algorithm. The points represent the data and the shaded area the signal prediction from Monte Carlo simulations. Backgrounds investigated include QCD, as well as W boson events, but were found to be negligible. [151]

To measure the performance of the electron veto from data, a tag-and-probe method based on $Z \rightarrow ee$ events is developed. Events that pass the electron trigger requirements on Event-Filter level with a threshold of $E_T = 15$ GeV and medium electron identification criteria are selected. The electron candidate matched to the trigger is required to fulfil $p_T > 30$ GeV, to fall inside $|\eta| < 2.47$, excluding the transition region of the electromagnetic calorimeter, $1.37 < |\eta| < 1.52$, and not to be reconstructed in regions of the calorimeter which are known to be not fully operational. This “tag” electron further has to satisfy the tight electron identification criteria [279] and has to be isolated from the rest of the event. An isolation criterion [280], is calculated from the sum of the p_T of all tracks found in a cone of $\Delta R = 0.4$ around the tag electron, normalised to the p_T of the tag electron and required to have a value < 0.06 . As “probe” a reconstructed τ lepton candidate with $p_T > 15$ GeV and $|\eta| < 2.5$ is selected. It has to have exactly one associated track, as three-prong τ lepton candidates suffer from a background level which is too high for a reliable measurement of the electron mis-identification probability, it is estimated to be negligibly small. The p_T distribution of the probe at the τ energy scale and the invariant mass distribution of the tag-and-probe pair are displayed on the left- and right-hand side of Figure 5.8, respectively.

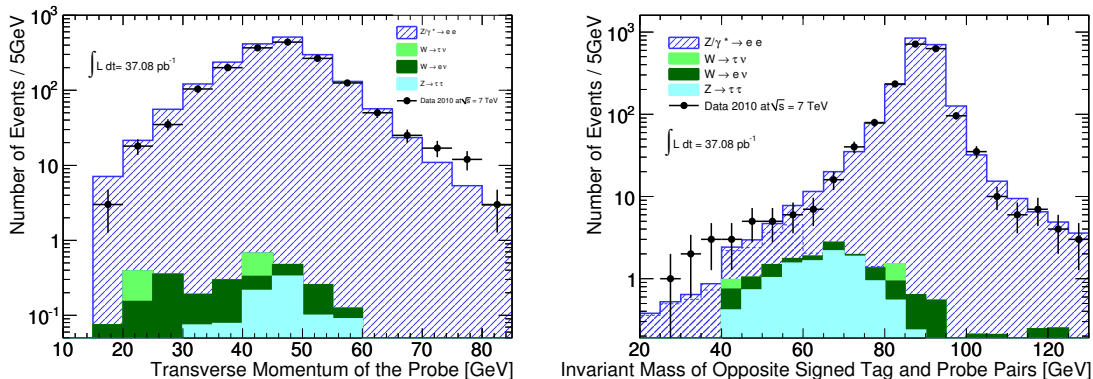


Figure 5.8: Distributions of p_T of the probe candidate (left-hand side) at the τ energy scale and the invariant mass distribution of the tag-and-probe pair (right-hand side), calculated at the electromagnetic scale. The points represent the data and the predictions from Monte Carlo simulation are displayed as shaded histograms. [151]

In case more than one pair of tag-and-probe objects is found in the event, the pair with the highest scalar sum of E_T is chosen. In addition, the invariant mass of the tag-and-probe pair, calculated using the energy at the electromagnetic scale, is required to fall inside the mass window $80 \text{ GeV} < m_{ee} < 100 \text{ GeV}$. To suppress remaining backgrounds, mainly from $W \rightarrow e\nu$ processes, $E_T^{\text{miss}} < 20 \text{ GeV}$ is required where the missing energy in the event is calculated from the vector sum of all calorimeter cells associated to clusters in the region $|\eta| < 4.5$, corrected for identified muons [281].

The probe candidates, satisfying the criteria above, are then subjected to the τ identification algorithms and to the electron veto algorithms in order to determine the mis-identification probability of electrons as hadronically decaying τ leptons. The mis-identification probability is defined as:

$$f_{\text{ID}} = \frac{\text{Number of probe candidates passing electron veto and } \tau \text{ ID}}{\text{Number of all selected probe candidates}}. \quad (5.2)$$

To assess the influence of backgrounds on the mis-identification probability, three control regions are selected, based on the charge product of the tag and the probe candidates and on the number of tracks associated to the probe candidate. The three regions are:

- Events with a negative charge product and three or more tracks associated to the probe candidate.
- Events with a positive or zero charge product and three or more tracks associated to the probe candidate.
- Events with a positive or zero charge product and one track associated to the probe candidate.

Since the available statistics in the control regions is not sufficient to correct the contribution of the backgrounds binned in p_{T} and $|\eta|$, an overall correction factor is calculated, integrated over p_{T} and $|\eta|$, and treated as a systematic uncertainty of the mis-identification probability. Additional sources of systematic uncertainties considered are the energy scale of the probe electron (1 % in the barrel region and 3 % in the end-cap region) and the choice of the signal mass window. The latter is broadened to $70 < m_{ee} < 110$ GeV, doubling the expected amount of background events. The effects of the variations on the mis-identification probability were taken into account as systematic uncertainties.

The mis-identification probabilities for the cut-based electron veto working point used in the H^{\pm} analyses with data taken in 2010 are displayed in Figure 5.9 as a function of p_{T} (left-hand side) and $|\eta|$ (right-hand side) of the probe candidate. The mis-identification probability is of the order of 1 % for probe candidates above a p_{T} of 20 GeV, independent of the τ -identification algorithm applied [151]. The region $15 < p_{\text{T}} < 20$ GeV of the probe candidate is dominated by background stemming from QCD processes, and due to a lack of statistics a data-driven background estimation is not possible. Therefore, the mis-identification probability determined in this p_{T} region is not considered to be reliable. The mis-identification probabilities for the looser electron veto algorithm working points have a typical mis-identification probability between 3 % and 5 %.

The mis-identification probabilities are potentially influenced by the amount of pile-up present in the event. Therefore, the mis-identification probability was studied as a function of the number of reconstructed vertices found in the event. The results of this study are displayed in Figure 5.10 for the tighter cut-based τ identification working point. In general, the

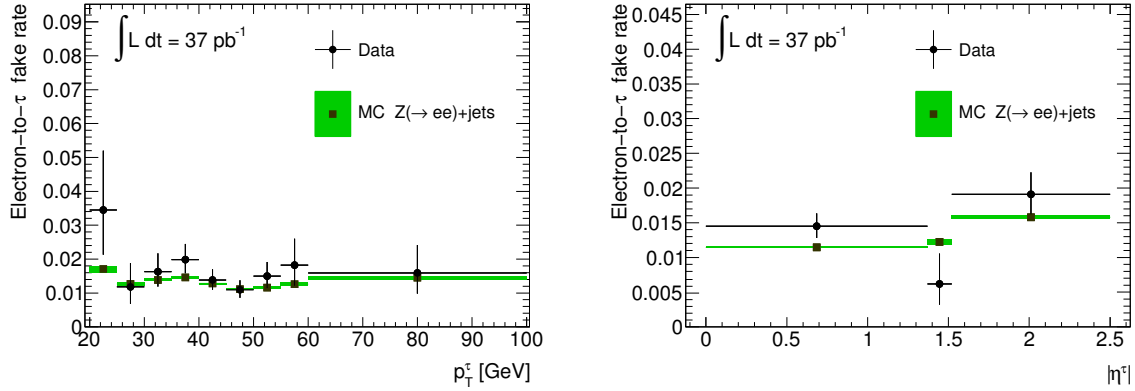


Figure 5.9: The mis-identification probabilities for probe objects passing the likelihood-based τ identification and the cut-based electron veto as well as the overlap removal with electrons parametrised by E_T and $|\eta|$, for the working point used in the H^\pm analyses with data taken in 2010 are shown. The error bars denote the binomial statistical uncertainty.

influence of pile-up on the mis-identification probability of electrons as τ leptons was found to be small. In the process of these studies mis-configurations of the cut-based as well as the BDT-based electron veto algorithms were found. The cut-based electron veto used a wrong $|\eta|$ range for the calorimeter transition region, and the BDT-based electron veto, due to not considering performance changes of the ID in the different η -regions, especially the lack of the TRT system at $\eta > 2.0$, in the training resulted in a significant efficiency degradation in the forward regions. These inefficiencies were promptly addressed for following versions of these algorithms. The BDT-based electron veto algorithm with its thus improved performance was utilised for the H^\pm analysis with the data taken 2011.

5.5.2 Backgrounds with Electrons and Jets Mis-identified as τ Leptons

About 51 % of the simulated $t\bar{t}$ events in the $\tau_{\text{had}} + \text{lepton}$ final state contain a reconstructed τ lepton matched to a, at the MC generator level, simulated hadronically decaying τ lepton. In the other events, the reconstructed τ lepton is hence called “mis-identified”. These mis-identified τ leptons originate from leptons, e or μ , in 3 % and hadronic objects, initiated by light quarks, b -quarks or gluons, in 46 % of all simulated events.

The background of electrons mis-identified as τ leptons is estimated selecting a $Z \rightarrow e^+e^-$ control region in the data [151], where either the electron or the positron are reconstructed as a hadronically decaying τ lepton. The measured mis-identification probabilities, as explained in detail in Section 5.5.1, with an average value of 0.2 % at the selected working point, are then applied to all simulated events in the $\tau_{\text{had}} + \text{lepton}$ analysis. Studies of Monte Carlo simulation show that the application of the mis-identification rates determined from $Z \rightarrow ee$ to $t\bar{t}$ events is valid, as the electron-to- τ mis-identification probabilities for $Z \rightarrow e^+e^-$ and $t\bar{t}$ events agree

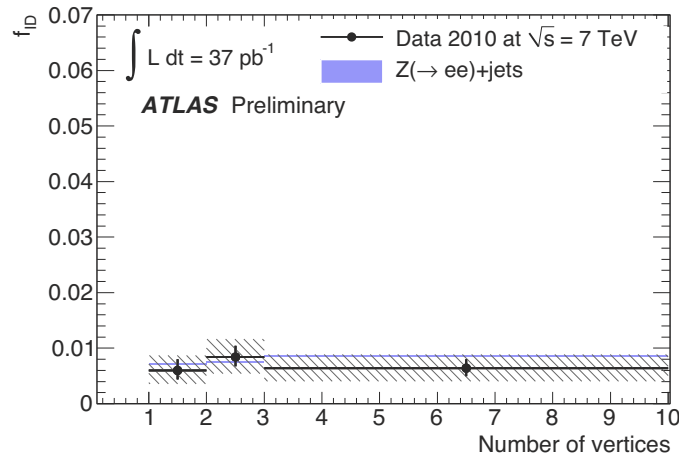


Figure 5.10: Mis-identification probability as a function of the number of primary vertices found in the event for the tighter cut-based τ identification working point. The points represent the data. The statistical uncertainty is represented by the vertical bars and the total uncertainty, calculated by adding the statistical and systematic uncertainties in quadrature, is displayed by the hatched areas. The square markers indicate the prediction from simulation and the shaded area represent the statistical uncertainty of the Monte Carlo sample used. [151]

well [175].

The majority of mis-identified τ leptons after the final event selection however originate from jets for which the mis-identification probability depends on the initial parton, i.e. light quark, heavy-flavour quark or gluon. All jet types occur in $t\bar{t}$ events, and it is not possible to accurately predict the fraction of each, potentially leading to a large systematic uncertainty on the jet $\rightarrow \tau$ lepton mis-identification probability. However, the influence of all jet types other than light-quark jets can effectively be eliminated by categorising all events in terms of the charge of the lepton relative to the τ lepton as opposite-sign (OS) or same-sign (SS) events. On the one hand all processes with gluon and b -quark jets produce positively and negatively charged mis-identified τ leptons at the same rate. While on the other hand the light-quark jet component in SS events represents both charge mis-reconstruction and quarks which fragment such that the leading charged particle does not have the same charge as the initial quark. Assigning a negative weight to the SS events therefore on average cancels the gluon and heavy-flavour-quark jet contributions from the OS events, leaving only the light-quark jets mis-identified as τ leptons.

The rate at which light-quark jets are mis-identified as τ candidates is derived using a region enriched with $W+>2$ jets events in the data, selected by requiring:

- exactly one electron or muon with E_T or p_T larger than 25 GeV;
- at least one τ lepton candidate;

- at least two jets in addition to the τ lepton candidate(s), none of them b -tagged;
- $E_T^{\text{miss}} > 40 \text{ GeV}$.

The leading process in this control region is $gq \rightarrow Wq'$. Hence, the final state quark mis-identified as a τ lepton candidate and the W boson usually have opposite charges. To reduce the contribution from events with a correctly reconstructed τ lepton, mostly originating from $Z + \text{jets}$ events, a requirement on the transverse mass, m_T , to be greater than 30 GeV is imposed. The $W + >2 \text{ jets}$ events are then classified as OS and SS events using the charges of the lepton and the τ lepton candidate. Figure 5.11 shows the m_T distribution for OS, SS and OS-SS events fulfilling the $W + >2 \text{ jets}$ selection, demonstrating the cancellation of heavy-flavour-quark and gluon contributions.

However, Figure 5.11 also suggests that simulation poorly models mis-identified τ lepton candidates. This motivates the use of data-driven methods to predict the background due to mis-identified τ leptons. In particular, the number of tracks associated to jets mis-identified as τ lepton candidates is found to be poorly modelled in simulation. Events in the data tend to have fewer τ lepton candidates with one or three tracks. To correct the τ lepton candidate selection efficiencies in simulation, τ track multiplicity scale factors are derived using OS-SS events fulfilling the $W + >2 \text{ jets}$ selection, and are then applied to all jets mis-identified as τ candidates in the simulation: 0.71 ± 0.03 for 1-track τ lepton candidates; 0.92 ± 0.03 for 3-track τ lepton candidates where the given errors are statistical only.

The probability for a light-quark jet to be mis-identified as a τ jet is measured in the data and binned in p_T^τ , the number of associated tracks N_{track}^τ (one or three), and the number of tracks found within $0.2 < \Delta R < 0.4$ of the τ lepton candidate $N_{\text{track}}^{\text{iso}}$. For each bin, the jet $\rightarrow \tau$ lepton mis-identification probability is defined as the number of objects passing the τ identification based on the likelihood criterion divided by the number prior to requiring identification. OS events are given a weight +1 and SS events are given a weight -1, in both the numerator and denominator of the jet $\rightarrow \tau$ lepton mis-identification probability. After OS-SS subtraction, the selected events mostly contain τ candidates from light-quark jets and, to a much lesser extent, electrons, muons, and correctly reconstructed hadronically decaying τ leptons. Figure 5.12 shows the measured values of the jet $\rightarrow \tau$ lepton mis-identification probability in $W + >2 \text{ jets}$ events selected from the data, after OS-SS subtraction. These are then used to scale all simulated events in the signal region. Events fulfilling the requirements listed in the beginning of this section, in which the selected reconstructed τ lepton originates from a jet (of any type), are weighted by the mis-identification probabilities. An additional weighting factor, +1 for OS events and -1 for SS events, is further assigned to perform the OS-SS subtraction. The results of the application of both methods are given in Table 6.1.

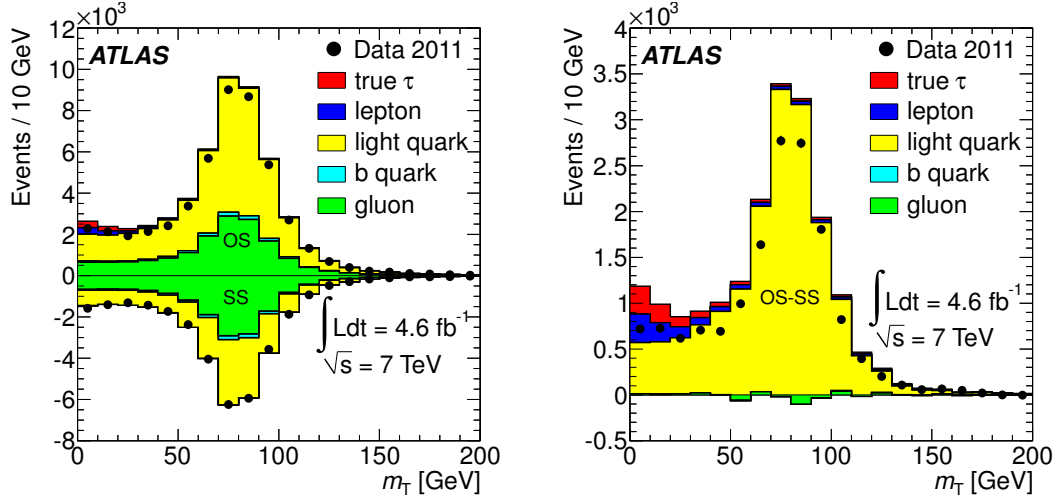


Figure 5.11: Distributions of m_T for events fulfilling the $W + >2$ jets selection, without the requirement $m_T > 30$ GeV. Each colour corresponds to a type of generator-level particle matched to a τ lepton candidate, the highest energy particle within a cone of radius $\Delta R = 0.2$ around the τ lepton candidate is considered. The SS events are given a weight of -1 , as shown in the left plot and in the right plot subtracted from the OS events. All simulated SM processes are considered. [173]

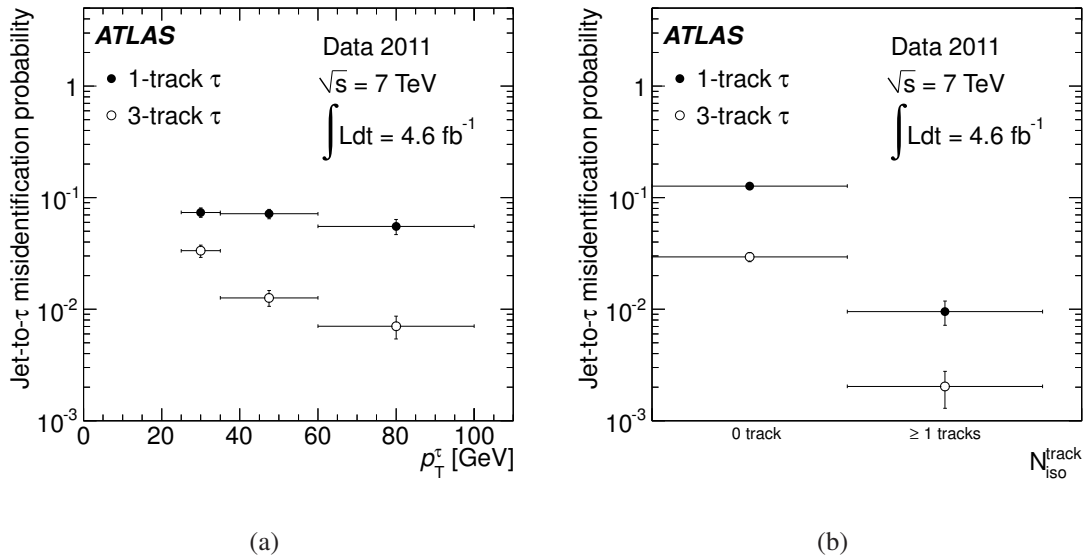


Figure 5.12: Probability for a light quark jet to be mis-identified as a 1-track or 3-track τ lepton, measured in a region enriched with OS-SS $W + >2$ jets events in the data, as a function of (a) p_T^τ and (b) the number of tracks $N_{\text{track}}^{\text{iso}}$ found within $0.2 < \Delta R < 0.4$ of the τ lepton. [173]

5.5.3 Embedding Method

The method consists of selecting a control sample of $t\bar{t}$, single-top and $W+jets$ events with a reconstructed muon and replacing the detector signature of this muon with that of a simulated τ lepton. Reconstruction algorithms are then re-applied to the new hybrid events, which are used afterwards to estimate the background arising from SM processes with correctly reconstructed hadronically decaying τ leptons. The complete event (except for the τ leptons) is thus taken directly from the data, including underlying event and pile-up, E_T^{miss} , b -quark and light-quark jets. In Figure 5.13 the prediction of the embedding method compared to Monte Carlo simulation for the m_T variable of correctly reconstructed τ leptons is shown.

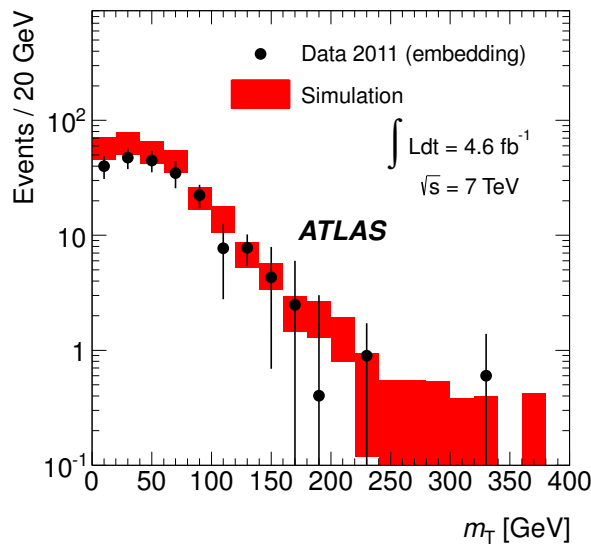


Figure 5.13: Comparison of the m_T distribution for correctly reconstructed hadronically decaying τ leptons predicted by the embedding method and by simulation. Combined statistical and systematic uncertainties are shown. [172]

5.5.4 Multi-Jet Background

The multi-jet background is estimated by adjusting its rate such that the E_T^{miss} distribution of the sum of the data-derived QCD-template and a template for all other simulated processes agree well with the measurement. To achieve this a control region is defined where the τ leptons must pass a looser τ identification, but fail the tighter τ identification [276] of the default selection. Furthermore the events of the control region are required not to contain any b -tagged jet. Assuming that the shapes of the E_T^{miss} and m_T distributions are the same in control and signal regions, the E_T^{miss} shape of the multi-jet background is measured in the control region, after subtracting the simulated background contributions from other processes. These amount to less than 1% of the observed events in the control region. Figure 5.14(a) compares the E_T^{miss}

shapes obtained with the $\tau_{\text{had}} + \text{jets}$ selection and in the control region, just before the final $E_{\text{T}}^{\text{miss}}$ requirement of the selection. The differences between the two distributions are taken into account as systematic uncertainty of this estimation method. A simultaneous fit is then performed on the $E_{\text{T}}^{\text{miss}}$ distribution of the selected data. The first fit-template is the multi-jet model obtained from the control region and the second template is the shape of the sum of the other processes, dominated by $t\bar{t}$ and $W + \text{jets}$, from Monte Carlo simulation. The fit result is shown in Figure 5.14(b).

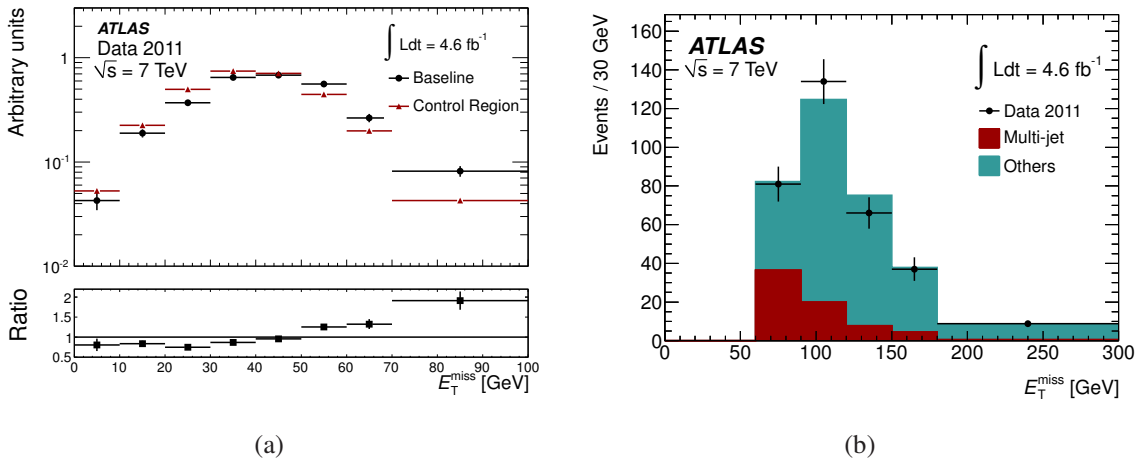


Figure 5.14: (a) Shape of $E_{\text{T}}^{\text{miss}}$ in the data control region after the baseline selection (before the $E_{\text{T}}^{\text{miss}}$ requirement) and after subtracting the simulated expectation from $t\bar{t}$, $W + \text{jets}$, and single top quark processes. (b) Fit of the $E_{\text{T}}^{\text{miss}}$ templates in the signal region to data, only statistical uncertainties are given. [172]

5.5.5 Backgrounds with Mis-identified Leptons

While the lepton identification provides a very pure sample of candidates, there is a non-negligible contribution from non-isolated leptons arising from the semi-leptonic decay of hadrons containing b -quarks or c -quarks from the decay-in-flight of π^\pm or K mesons and, in the case of mis-identified electron objects, from the reconstruction of π^0 mesons, photon conversions or shower fluctuations. All leptons from such mechanisms are referred to as “mis-identified” leptons, as opposed to truly isolated leptons, for example stemming from the prompt decay of W or Z bosons, which are hence referred to as “real” leptons. The data-driven estimation of the number of mis-identified leptons passing the lepton selections of Sections 5.3.1 and 5.3.2 is based on exploiting differences in the lepton identification between real and mis-identified electrons or muons. Two data samples are defined which differ only in the lepton identification criteria. The “tight” sample contains mostly events with real leptons and uses the same lepton selection as in the analysis. Whereas the “loose” sample contains mostly events with mis-identified leptons. This latter sample is obtained by loosening the

isolation and identification requirements for the leptons. For loose electrons, the isolation requirements have an efficiency of about 98 % for true isolated electrons, compared to 90 % in the tight sample. For loose muons, the isolation requirement is removed. By construction, the tight sample is therefore a subset of the loose sample.

Let N_r^L and N_m^L (N_r^T and N_m^T) be the number of events containing real and mis-identified leptons, respectively, passing a loose (tight) criterion. The numbers of events containing one loose or tight lepton are then given by:

$$N^L = N_m^L + N_r^L, \quad (5.3)$$

$$N^T = N_m^T + N_r^T. \quad (5.4)$$

Defining p_r and p_m as:

$$p_r = \frac{N_r^T}{N_r^L} \quad \text{and} \quad p_m = \frac{N_m^T}{N_m^L}, \quad (5.5)$$

the number of mis-identified leptons passing the tight selection, N_m^T , can be calculated:

$$N_m^T = \frac{p_m}{p_r - p_m} (p_r N^L - N^T). \quad (5.6)$$

The main ingredients of this data-driven method are thus the relative efficiencies p_r and p_m for a real or a mis-identified lepton, respectively, to be detected as a tight lepton. On the one hand the lepton identification efficiency p_r is measured using a tag-and-probe method on $Z \rightarrow \ell\ell$ data events with a dilepton invariant mass between 86 GeV and 96 GeV, where one lepton is required to fulfil tight selection criteria. The rate at which the other lepton passes the same tight selection criteria defines p_r . The average values of the electron and muon identification efficiencies are 80 % and 97 %, respectively. While on the other hand, a control sample with mis-identified leptons is selected by considering events in the data with exactly one lepton passing the loose criteria. To select events dominated by multi-jet production the measured E_T^{miss} is required to lie within 5 GeV and 20 GeV. Residual true leptons contribute at a level below 10 % and are subtracted from this sample utilising Monte Carlo simulation. After this subtraction, the rate at which a loose lepton passes tight selection criteria defines the mis-identification rate p_m . The average values of the electron and muon mis-identification probabilities are 18 % and 29 %, respectively. In the final parametrisation of p_r and p_m , dependencies on the pseudorapidity of the lepton, its distance ΔR to the nearest jet and the leading jet p_T in the event are taken into account [172].

Chapter 6

Direct Searches for the Charged Higgs Boson

6.1 Analysis of the $\tau_{\text{had}} + \text{Lepton}$ Channel

After employing the optimised selection detailed described in Section 5.4.1 the expected number of background events for the SM-only hypothesis and the observation in the data is given in Table 6.1. The total number of predicted events (signal+background) in the presence of a 130 GeV charged Higgs boson, assuming $\mathcal{B}(t \rightarrow bH^+) = 5\%$, is also shown.

The $\tau_{\text{had}} + \text{lepton}$ analysis relies on the theoretically calculated $t\bar{t}$ production cross-section $\sigma_{t\bar{t}} = 167^{+17}_{-18} \text{ pb}$ [179] for the background estimation. In the presence of a charged Higgs boson in the top quark decays, with a branching ratio $\mathcal{B}(t \rightarrow bH^+)$, the contributions of $t\bar{t} \rightarrow b\bar{b}W^+W^-$ events in the backgrounds with true or mis-identified hadronically decaying τ leptons are scaled according to this branching ratio. In this analysis the background with correctly reconstructed τ leptons is obtained with simulation. The data are found to be consistent with the expectation for the background-only hypothesis. The $E_{\text{T}}^{\text{miss}}$ distributions, after all selection cuts applied, are shown in Figure 6.1(a) and Figure 6.1(b) for the $\tau_{\text{had}} + e$ and the $\tau_{\text{had}} + \mu$ channels, respectively.

6.2 Analysis of the $\tau_{\text{lep}} + \text{Jets}$ Channel

Having selected a $\tau_{\text{lep}} + \text{jets}$ sample enriched in $t\bar{t}$ candidates, by employing the selection described in Section 5.4.2, jets must be assigned correctly to the decay products of each W boson (with a mass $m_W = 80.4 \text{ GeV}$) and top quark. In particular, the hadronic side of the event is identified by selecting the combination of one b -tagged jet (b) and two untagged jets (j) that minimises:

$$\chi^2 = \frac{(m_{jjb} - m_{\text{top}})^2}{\sigma_{\text{top}}^2} + \frac{(m_{jj} - m_W)^2}{\sigma_W^2}, \quad (6.1)$$

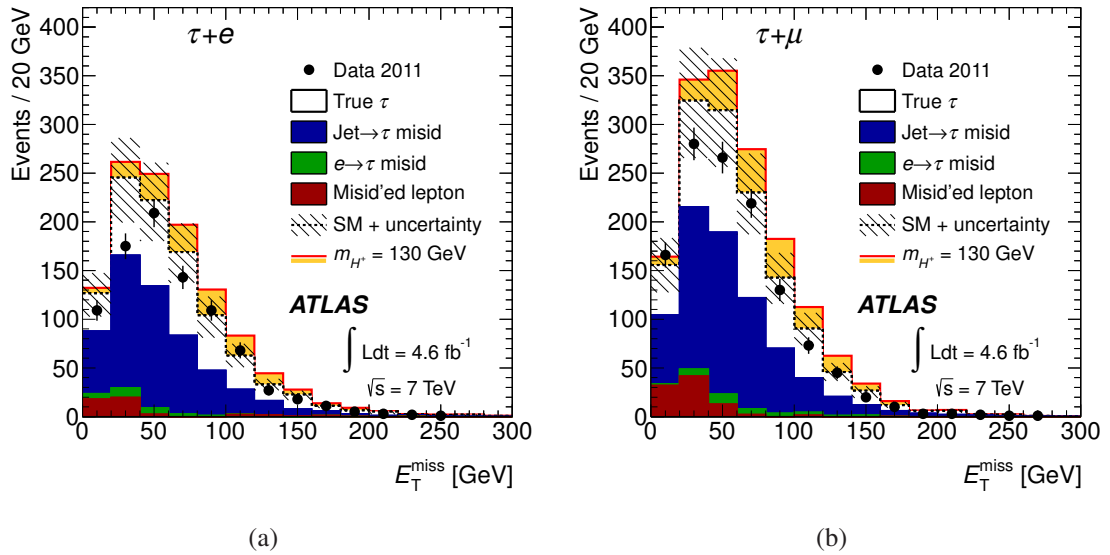


Figure 6.1: E_T^{miss} distribution after all selection cuts in the $\tau_{\text{had}} + \text{lepton}$ channel, for (a) $\tau + \text{electron}$ and (b) $\tau + \text{muon}$ final states. The dashed line corresponds to the SM-only hypothesis and the hatched area around it shows the total uncertainty for the SM backgrounds. The solid line shows the predicted contribution of signal+background in the presence of a 130 GeV charged Higgs boson with $\mathcal{B}(t \rightarrow bH^+) = 5\%$ and $\mathcal{B}(H^+ \rightarrow \tau\nu) = 100\%$. The contributions of $t\bar{t} \rightarrow b\bar{b}W^+W^-$ events in the backgrounds with true or mis-identified τ leptons are scaled down accordingly. [172]

Sample	Event yield ($\tau_{\text{had}} + \text{lepton}$)	
	$\tau_{\text{had}} + e$	$\tau_{\text{had}} + \mu$
True $\tau + \text{lepton}$	$430 \pm 14 \pm 59$	$570 \pm 15 \pm 75$
Mis-identified jet $\rightarrow \tau$	$510 \pm 23 \pm 86$	$660 \pm 26 \pm 110$
Mis-identified $e \rightarrow \tau$	$33 \pm 4 \pm 5$	$34 \pm 4 \pm 6$
Mis-identified leptons	$39 \pm 10 \pm 20$	$90 \pm 10 \pm 34$
All SM backgrounds	$1010 \pm 30 \pm 110$	$1360 \pm 30 \pm 140$
Data	880	1219
$t \rightarrow bH^+$ (130 GeV)	$220 \pm 6 \pm 29$	$310 \pm 7 \pm 39$
Signal+background	$1160 \pm 30 \pm 100$	$1570 \pm 30 \pm 130$

Table 6.1: Expected event yields after all selection cuts in the $\tau_{\text{had}} + \text{lepton}$ channel and comparison with 4.6 fb^{-1} of data. The numbers in the last two rows, obtained for a hypothetical H^+ signal with $m_{H^+} = 130 \text{ GeV}$, are obtained with $\mathcal{B}(t \rightarrow bH^+) = 5\%$ and $\mathcal{B}(H^+ \rightarrow \tau\nu) = 100\%$. All other rows assume $\mathcal{B}(t \rightarrow bW^+) = 100\%$. Both statistical and systematic uncertainties, explained detailed in Section 6.4, are shown, in this respective order. [172]

where $\sigma_{\text{top}} = 17 \text{ GeV}$ and $\sigma_W = 10 \text{ GeV}$ are the widths of the reconstructed top quark and W boson mass distributions, as measured in simulated $t\bar{t}$ events. Using information about the correctly identified combinations in the generated events, the jet assignment efficiency is found to be 72 %. Events with $\chi^2 > 5$ are rejected to select well-reconstructed hadronically decaying top quark candidates.

The analysis uses two variables that discriminate between leptons produced in $\tau \rightarrow \ell\nu_\ell\nu_\tau$ and leptons stemming directly from W boson decays. The first discriminating variable is the invariant mass $m_{b\ell}$ of the b -tagged jet and the charged lepton from the same top quark candidate, alternatively rewritten as $\cos \theta_\ell^*$ defined as:

$$\cos \theta_\ell^* = \frac{2m_{b\ell}^2}{m_{\text{top}}^2 - m_W^2} - 1 \simeq \frac{4 p^b \cdot p^\ell}{m_{\text{top}}^2 - m_W^2} - 1. \quad (6.2)$$

Both m_b^2 and m_ℓ^2 are neglected as small contribution, hence the approximation $m_{b\ell}^2 \simeq 2 p^b \cdot p^\ell$ is used, where p^b and p^ℓ are the four-momenta of the b -tagged jet and of the charged lepton, respectively. The presence of a charged Higgs boson in a leptonic top quark decay reduces the invariant product $p^b \cdot p^\ell$, compared to W -mediated top quark decays, resulting in $\cos \theta_\ell^*$ values closer to -1 .

The second discriminating variable is the charged Higgs transverse mass m_T^H [282], obtained

by fulfilling the constraint $(p^{\text{miss}} + p^\ell + p^b)^2 = m_{\text{top}}^2$ on the leptonic side of $\tau_{\text{lep}} + \text{jets}$ $t\bar{t}$ events. Note that more than one neutrino contributes to the missing four-momentum p^{miss} and its transverse component $p_{\text{T}}^{\text{miss}}$. By construction, m_{T}^H gives an event-by-event lower bound on the mass of the leptonically decaying charged W or Higgs boson produced in the top quark decay and can be written as:

$$(m_{\text{T}}^H)^2 = \left(\sqrt{m_{\text{top}}^2 + (p_{\text{T}}^\ell + p_{\text{T}}^b + p_{\text{T}}^{\text{miss}})^2} - p_{\text{T}}^b \right)^2 - (p_{\text{T}}^\ell + p_{\text{T}}^{\text{miss}})^2. \quad (6.3)$$

The $\cos \theta_\ell^*$ distribution measured in the data is shown in Figure 6.2(a) superimposed on the predicted background determined with the data-driven multi-jet background estimation and simulation for the other SM backgrounds. In the presence of a charged Higgs boson in the top quark decays, with a branching ratio $\mathcal{B}(t \rightarrow bH^+)$, the contribution of $t\bar{t} \rightarrow b\bar{b}W^+W^-$ events in the backgrounds are scaled according to this branching ratio. A control region enriched in $t\bar{t} \rightarrow b\bar{b}W^+W^-$ events is defined by requiring $-0.2 < \cos \theta_\ell^* < 1$. In the limit setting procedure, described later in Section 6.5, this sample is used to fit the branching ratio $\mathcal{B}(t \rightarrow bH^+)$ and the product of the cross-section $\sigma_{b\bar{b}WW}$, the luminosity, the selection efficiency and acceptance for $t\bar{t} \rightarrow b\bar{b}W^+W^-$, simultaneously with the likelihood for the signal estimation. This ensures that the final results, and in particular the upper limit on $\mathcal{B}(t \rightarrow bH^+)$, are independent of the assumed theoretical production cross-section for $t\bar{t}$. With a branching fraction $\mathcal{B}(t \rightarrow bH^+) = 5\%$, the signal contamination in the control region would range from 1.3 % for $m_{H^+} = 90\text{ GeV}$ to 0.4 % for $m_{H^+} = 160\text{ GeV}$. The signal region is defined by requiring $\cos \theta_\ell^* < -0.6$ and $m_{\text{T}}^W < 60\text{ GeV}$, with the definition:

$$m_{\text{T}}^W = \sqrt{2p_{\text{T}}^\ell E_{\text{T}}^{\text{miss}} (1 - \cos \Delta\phi_{\ell,\text{miss}})}. \quad (6.4)$$

This is done to suppress the background from events with a W boson decaying directly into an electron or muon along with the corresponding neutrino. For events in the signal region m_{T}^H is used as a discriminating variable in the search for charged Higgs bosons. The m_{T}^H distribution is shown in Figure 6.2(b).

Table 6.2 lists the contributions to the signal region of the SM processes and of $t\bar{t}$ events with at least one decay $t \rightarrow bH^+$, assuming $m_{H^+} = 130\text{ GeV}$ and $\mathcal{B}(t \rightarrow bH^+) = 5\%$. When including signal in the prediction, the simulated SM $t\bar{t}$ contribution is scaled according to this branching ratio. The data are consistent with the predicted SM background and no significant deviation in the m_{T}^H distribution is observed.

6.3 Analysis of the $\tau_{\text{had}} + \text{Jets}$ Channel

After the selection described in Section 5.4.3 the expected number of background events for the SM-only hypothesis and the observation in the data is shown in Table 6.3. The total number of

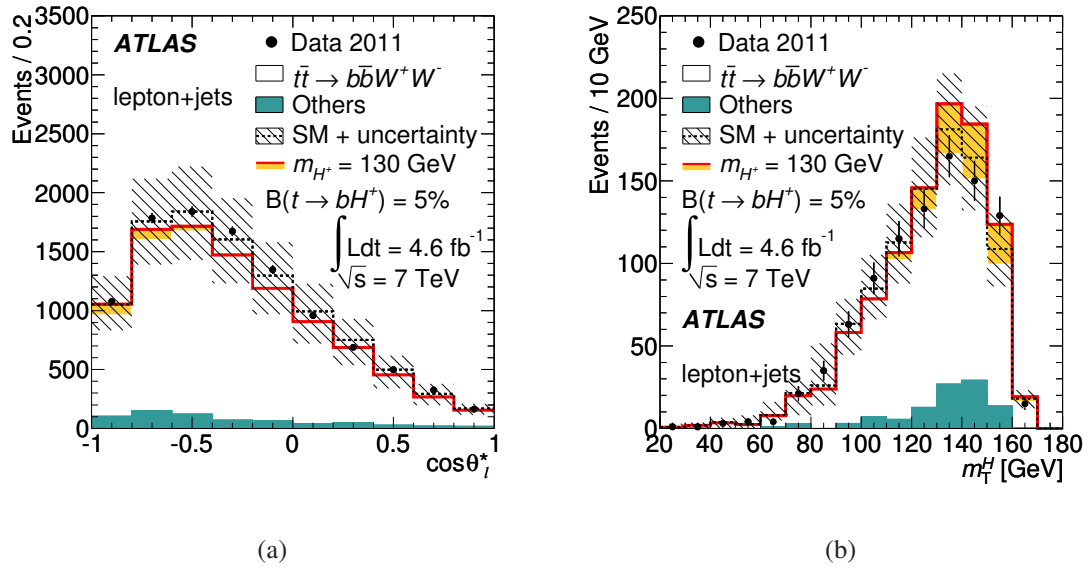


Figure 6.2: Distribution of (a) $\cos\theta_{\ell}^*$ and (b) m_T^H , in the signal region ($\cos\theta_{\ell}^* < -0.6$, $m_T^H < 60$ GeV) for the latter. The dashed line corresponds to the SM-only hypothesis and the hatched area around it shows the total uncertainty for the SM backgrounds, where “Others” refers to the contribution of all SM processes except $t\bar{t} \rightarrow b\bar{b}W^+W^-$. The solid line shows the predicted contribution of signal+background in the presence of a 130 GeV charged Higgs boson, assuming $\mathcal{B}(t \rightarrow bH^+) = 5\%$ and $\mathcal{B}(H^+ \rightarrow \tau\nu) = 100\%$. The light area below the solid line corresponds to the contribution of the H^+ signal, stacked on top of the scaled $t\bar{t} \rightarrow b\bar{b}W^+W^-$ background and other SM processes. [172]

Sample	Event yield ($\tau_{lep}+jets$)		
$t\bar{t}$	840	± 20	± 150
Single top quark	28	± 2	$^{+8}_{-6}$
$W+jets$	14	± 3	$^{+6}_{-3}$
$Z+jets$	2.1	± 0.7	$^{+1.2}_{-0.4}$
Diboson	0.5	± 0.1	± 0.2
Mis-identified leptons	55	± 10	± 20
All SM backgrounds	940	± 22	± 150
Data	933		
$t \rightarrow bH^+$ (130 GeV)	120	± 4	± 25
Signal+background	990	± 21	± 140

Table 6.2: Expected event yields in the signal region of the $\tau_{lep}+jets$ final state, and comparison with 4.6 fb^{-1} of data. A cross-section of 167 pb is assumed for the SM $t\bar{t}$ background. The numbers shown in the last two rows, for a hypothetical H^+ signal with $m_{H^+} = 130$ GeV, are obtained with $\mathcal{B}(t \rightarrow bH^+) = 5\%$. Both statistical and systematic uncertainties are shown, in this respective order. [172]

predicted events (signal+background) in the presence of a 130 GeV charged Higgs boson with $\mathcal{B}(t \rightarrow bH^+) = 5\%$ is also shown.

Sample	Event yield ($\tau_{\text{had}} + \text{jets}$)
True τ (embedding method)	$210 \pm 10 \pm 44$
Mis-identified jet $\rightarrow \tau$	$36 \pm 6 \pm 10$
Mis-identified $e \rightarrow \tau$	$3 \pm 1 \pm 1$
Multi-jet processes	$74 \pm 3 \pm 47$
All SM backgrounds	$330 \pm 12 \pm 65$
Data	355
$t \rightarrow bH^+$ (130 GeV)	$220 \pm 6 \pm 56$
Signal+background	$540 \pm 13 \pm 85$

Table 6.3: Expected event yields after all selection cuts in the $\tau_{\text{had}} + \text{jets}$ channel and comparison with 4.6 fb^{-1} of data. The numbers in the last two rows, obtained for a hypothetical H^+ signal with $m_{H^+} = 130 \text{ GeV}$, are obtained with $\mathcal{B}(t \rightarrow bH^+) = 5\%$ and $\mathcal{B}(H^+ \rightarrow \tau\nu) = 100\%$. The rows for the backgrounds with mis-identified objects assume $\mathcal{B}(t \rightarrow bW^+) = 100\%$. Both statistical and systematic uncertainties are given, in this respective order. [172]

On the one hand, the number of events with a correctly reconstructed τ lepton is derived from the number of embedded events and does not depend on the cross-section of the $t\bar{t} \rightarrow b\bar{b}W^+W^-$ process. On the other hand, the $\tau_{\text{had}} + \text{jets}$ analysis does rely on the theoretical inclusive $t\bar{t}$ production cross-section for the estimation of the background with electrons or jets mis-identified as τ leptons. In the presence of a charged Higgs boson in the top quark decays, with a branching ratio $\mathcal{B}(t \rightarrow bH^+)$, the contributions of $t\bar{t} \rightarrow b\bar{b}W^+W^-$ events in these backgrounds are scaled according to this branching ratio. The data are found to be consistent with the estimation of the SM background. The m_T distribution for the $\tau_{\text{had}} + \text{jets}$ channel, after all selection cuts are applied, is shown in Figure 6.3.

6.4 Systematic Uncertainties

6.4.1 Systematic Uncertainties of Detector Simulation

Systematic uncertainties arising from the simulation of pile-up and object reconstruction are considered. The latter arise from the simulation of the trigger, from the reconstruction and identification efficiencies, as well as from the energy or momentum scale and resolution for the

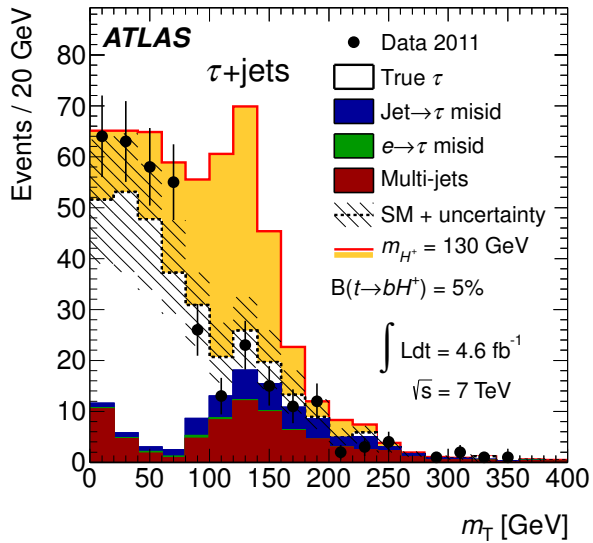


Figure 6.3: Distribution of m_T after all selection cuts in the $\tau_{\text{had}} + \text{jets}$ channel. The dashed line corresponds to the SM-only hypothesis and the hatched area around it shows the total uncertainty for the SM backgrounds. The solid line shows the predicted contribution of signal+background in the presence of a charged Higgs boson with $m_{H^+} = 130 \text{ GeV}$, assuming $\mathcal{B}(t \rightarrow bH^+) = 5\%$ and $\mathcal{B}(H^+ \rightarrow \tau\nu) = 100\%$. The contributions of $t\bar{t} \rightarrow b\bar{b}W^+W^-$ events in the backgrounds with mis-identified objects are scaled down accordingly. [172]

objects described in Section 5.3. To assess the impact of most sources of systematic uncertainty, the selection cuts for each analysis are re-applied after shifting a particular parameter by its ± 1 standard deviation uncertainty, as given in Table 6.4. The systematic uncertainties related to electrons and muons are discussed in Reference [228] and References [261, 283], respectively. The systematic uncertainties related to jets are discussed in Reference [267] and Reference [272] describes the b -tagging calibration. Systematic uncertainties related to τ leptons are taken from Reference [276]. Finally, for the reconstruction of E_T^{miss} and its uncertainties Reference [221] was consulted. All studies of systematic uncertainties have been updated with the full 4.6 fb^{-1} dataset collected in 2011. The dominant instrumental systematic uncertainties arise from the jet energy resolution (10–30 %, depending on p_T and η), the jet energy scale (up to 14 %, depending on p_T and η , to which a pile-up term of 2–7 % and a b -tagged jet term of 2.5 % are added in quadrature), as well as the b -tagging efficiency (5–17 %, depending on p_T and η) and mis-identification probability (12–21 %, depending on p_T and η). In comparison to these the systematic uncertainties arising from the reconstruction and identification of electrons and muons are small. All instrumental systematic uncertainties are propagated to the reconstructed E_T^{miss} .

6.4.2 Systematic Uncertainties of Generation of $t\bar{t}$ Events

To estimate the systematic uncertainties arising from the $t\bar{t}$ generation and the utilised parton shower model, the acceptance is computed for $t\bar{t}$ events produced with MC@NLO [161] interfaced to HERWIG/JIMMY [146] and PowHEG [183] interfaced to PYTHIA [145]. For the signal samples, which are generated with PYTHIA without higher-order corrections, no alternative generator is available. The systematic uncertainty for the signal samples is thus set to the relative difference in acceptance between $t\bar{t}$ events generated with MC@NLO interfaced to HERWIG/JIMMY and with ACERMC, which is a leading-order generator, interfaced to PYTHIA. The systematic uncertainties arising from initial state radiation and final state radiation are computed using $t\bar{t}$ samples generated with ACERMC interfaced to PYTHIA, where initial and final state radiation parameters are set to a range of values not excluded by the experimental data [292]. The largest relative differences with respect to the reference sample after full event selections are used as systematic uncertainties. The systematic uncertainties arising from the modelling of the $t\bar{t}$ event generation and the parton shower, as well as initial and final state radiation, are summarised in Table 6.5 separately for each analysis channel.

6.4.3 Systematic Uncertainties of Data-Driven Background Estimates

The systematic uncertainties arising from the data-driven methods, used to estimate backgrounds from various sources, are summarised in Table 6.6 for each of the three channels.

For backgrounds with mis-identified leptons, discussed in Section 5.5.5, the main systematic

Source of uncertainty	Treatment in analysis
Electron trigger efficiency	Up to 1.0%, depending on p_T , η and the data period.
Electron reco. efficiency	$\pm (0.6\text{--}1.1)\%$, depending on η .
Electron ID efficiency	$\pm (2.8\text{--}3.5)\%$, depending on E_T and η .
Electron energy scale	[284] $\pm (0.5\text{--}2.4)\%$, additional constant term, depending on p_T and η .
Electron energy resolution	[284] Up to 1%, depending on E and η .
Muon trigger efficiency	$\pm (0.5\text{--}6.0)\%$, depending on η , ϕ and the data period.
Muon reco efficiency	$\pm (0.4\text{--}0.8)\%$, depending on E , η , ϕ .
Muon ID efficiency	$\pm (0.3\text{--}1.2)\%$, depending on the data period.
Muon momentum scale and resolution	[285] Up to 1%, depending on p_T , η and the charge.
Jet energy resolution (JER)	[286] $\pm (10\text{--}30)\%$, depending on p_T and η .
Jet energy scale (JES)	[287] $\pm (2.5\text{--}14)\%$, depending on p_T and η , + pile-up term (2\text{--}7\%) in quadrature.
Jet reco efficiency	Randomly drop jets (2\%) from the events and symmetrise.
b -tagging efficiency	[288] $\pm (5\text{--}17)\%$, depending on p_T and η .
b -tagging mis-tag rate	[288] $\pm (12\text{--}21)\%$, depending on p_T and η .
b -tagged jet JES uncertainty	[289] Up to 2.5%, depending on p_T , added to the standard JES.
τ ID efficiency	[290] $\pm (4\text{--}7)\%$, depending on the number of tracks.
τ energy scale	[290] $\pm (2.5\text{--}5.0)\%$, depending on p_T , η and the number of tracks.
E_T^{miss} uncertainty	[291] Uncertainties from object scale and resolution, Soft Jets & Cell Out terms + 6.6\% flat pile-up contribution.

Table 6.4: Detector-related systematic uncertainties.

Source of uncertainty	Normalisation uncertainty
$\tau_{\text{lep}} + \text{jets}:$	
Generator and parton shower ($b\bar{b}WH^+$, signal region)	10 %
Generator and parton shower ($b\bar{b}W^+W^-$, signal region)	8 %
Generator and parton shower ($b\bar{b}WH^+$, control region)	7 %
Generator and parton shower ($b\bar{b}W^+W^-$, control region)	6 %
Initial and final state radiation (signal region)	8 %
Initial and final state radiation (control region)	13 %
$\tau_{\text{had}} + \text{lepton}:$	
Generator and parton shower ($b\bar{b}WH^+$)	2 %
Generator and parton shower ($b\bar{b}W^+W^-$)	5 %
Initial and final state radiation	13 %
$\tau_{\text{had}} + \text{jets}:$	
Generator and parton shower ($b\bar{b}WH^+$)	5 %
Generator and parton shower ($b\bar{b}W^+W^-$)	5 %
Initial and final state radiation	19 %

Table 6.5: Systematic uncertainties arising from the modelling of $t\bar{t} \rightarrow b\bar{b}W^+W^-$ and $t\bar{t} \rightarrow b\bar{b}WH^+$ events and the parton shower, as well as from initial and final state radiation. [172]

Source of uncertainty	Normalisation uncertainty	Shape uncertainty
$\tau_{\text{lep}} + \text{jets}$: lepton mis-identification		
Choice of control region	6 %	–
Z mass window	4 %	–
Jet energy scale	16 %	–
Jet energy resolution	7 %	–
Sample composition	31 %	–
$\tau_{\text{had}} + \text{lepton}$: jet $\rightarrow \tau$ mis-identification		
Statistics in control region	2 %	–
Jet composition	11 %	–
Object-related systematics	23 %	3 %
$\tau_{\text{had}} + \text{lepton}$: $e \rightarrow \tau$ mis-identification		
Mis-identification probability	20 %	–
$\tau_{\text{had}} + \text{lepton}$: lepton mis-identification		
Choice of control region	4 %	–
Z mass window	5 %	–
Jet energy scale	14 %	–
Jet energy resolution	4 %	–
Sample composition	39 %	–
$\tau_{\text{had}} + \text{jets}$: true τ		
Embedding parameters	6 %	3 %
Muon isolation	7 %	2 %
Parameters in normalisation	16 %	–
τ identification	5 %	–
τ energy scale	6 %	1 %
$\tau_{\text{had}} + \text{jets}$: jet $\rightarrow \tau$ mis-identification		
Statistics in control region	2 %	–
Jet composition	12 %	–
Purity in control region	6 %	1 %
Object-related systematics	21 %	2 %
$\tau_{\text{had}} + \text{jets}$: $e \rightarrow \tau$ mis-identification		
Mis-identification probability	22 %	–
$\tau_{\text{had}} + \text{jets}$: multi-jet estimate		
Fit-related uncertainties	32 %	–
$E_{\text{T}}^{\text{miss}}$ -shape in control region	16 %	–

Table 6.6: Dominant systematic uncertainties on the data-driven estimates. The shape uncertainty given is the relative shift of the mean value of the final discriminant distribution. A “–” in the second column indicates negligible shape uncertainties. [172]

uncertainties arise from the simulated samples used to subtract the true leptons in the determination of the mis-identification probabilities. These are sensitive to the instrumental systematic uncertainties and to the sample dependence, since mis-identification probabilities are calculated in a control region dominated by gluon-initiated events, but later used in a data sample with a higher fraction of quark-initiated events.

The dominant systematic uncertainties in the estimation of the multi-jet background in the $\tau_{\text{had}} + \text{jets}$ channel, discussed in Section 5.5.4, are the statistical uncertainty of the fit due to the limited size of the data control sample and uncertainties due to potential differences of the $E_{\text{T}}^{\text{miss}}$ shape in the signal and control regions. The dominant systematic uncertainties in estimating the contribution of events with electrons mis-identified as τ leptons in Section 5.5.2 arise from the subtraction of the multi-jet and electroweak backgrounds in the control region enriched with $Z \rightarrow ee$ events and from potential correlations in the selections of the tag-and-probe electrons. For the estimation of backgrounds with jets mis-identified as hadronically decaying τ leptons, also discussed in Section 5.5.2, the dominant systematic uncertainties on the mis-identification probability are the statistical uncertainty due to the limited control sample size and uncertainties due to the difference of the jet composition (gluon or quark-initiated) in the control and signal regions, which is estimated using simulation. Other uncertainties stem from the impurities arising from multi-jet background events and from true hadronic τ lepton decays in the control sample. The systematic uncertainties affecting the estimation of the background from correctly reconstructed τ leptons in the $\tau_{\text{had}} + \text{jets}$ channel, discussed in Section 5.5.3, consist of the potential bias introduced by the embedding method itself, uncertainties from the trigger efficiency measurement, uncertainties associated to simulated τ leptons (τ energy scale and identification efficiency) and uncertainties on the normalisation. They are dominated by the statistical uncertainty of the selected control sample and the $\tau + E_{\text{T}}^{\text{miss}}$ trigger efficiency uncertainties.

6.5 Results

No significant deviation from the SM prediction is observed in any of the investigated final states in 4.6 fb^{-1} of data. To test the compatibility of the data with background-only and signal+background hypotheses, a profile likelihood ratio [293] is used with m_{T}^H for $\tau_{\text{lep}} + \text{jets}$, $E_{\text{T}}^{\text{miss}}$ for $\tau_{\text{had}} + \text{lepton}$ and m_{T} for $\tau_{\text{had}} + \text{jets}$ as the discriminating variables [294]. The statistical analysis is based on a binned likelihood function for these distributions. The systematic uncertainties in shape and normalisation are incorporated. Assuming $\mathcal{B}(H^+ \rightarrow \tau\nu) = 100\%$, upper limits are extracted on the branching ratio $t \rightarrow bH^+$ as a function of m_{H^\pm} . Events featuring $t\bar{t} \rightarrow b\bar{b}H^+H^-$ are not considered in the following, as previous analyses suggest $\mathcal{B}(t \rightarrow bH^+) < 10\%$, thus the contribution from $t\bar{t} \rightarrow b\bar{b}H^+H^-$ is assumed as small. Thus this estimation of the upper limit on $\mathcal{B}(t \rightarrow bH^+)$ may be considered conservative.

With μ and n the number of expected and observed events in the signal region after the event

selection, the acceptances ϵ_W and ϵ_H for $t\bar{t} \rightarrow b\bar{b}W^+W^-$ and $t\bar{t} \rightarrow b\bar{b}H^\pm W^\mp$, derived from Monte Carlo simulations, the expected number of observed events is given by:

$$\mu = \mu_W \epsilon_W + \mu_H \epsilon_H + \mu_{\text{others}} = \mu_{\bar{t}\bar{t}} \left((1 - B)^2 \epsilon_W + 2B(1 - B) \epsilon_H \right) + \mu_{\text{others}},$$

where $B \equiv \mathcal{B}(t \rightarrow bH^+)$.

In the SM case, with no charged Higgs boson in the top quark decays, μ_W is the product of theoretical $t\bar{t}$ cross-section and the integrated luminosity. However in the presence of a charged Higgs boson in the top quark decays, μ_W is reduced by a factor $(1 - B)^2$. The simulated E_T^{miss} distribution is described with a probability density function $f_i(E_T^{\text{miss}})$. Expected and observed number of events in each bin, i , are thus $\mu_i = \mu f_i(E_T^{\text{miss}})$ and n_i . The resulting likelihood is given by:

$$\mathcal{L}(B) = \prod_i f_{\text{Poisson}}(n_i | \mu_i) \prod_j p(\tilde{\theta}_j | \theta_j).$$

Nuisance parameters, θ_j , are used to describe the effect of systematic uncertainties, with the Gaussian constraints, $p(\tilde{\theta}_j | \theta_j)$, relating each parameter to its nominal estimate, $\tilde{\theta}_j$.

A profile likelihood statistical analysis with B as the only parameter of interest is then performed. The test statistic is given by [293]:

$$q_B = -2 \log \frac{\mathcal{L}(B, \hat{\theta}_B)}{\mathcal{L}(\hat{B}, \hat{\theta})}, \quad 0 \leq \hat{B} \leq B,$$

with $\hat{\theta}_B$ the maximum likelihood estimators of the nuisance parameters for a fixed B , as well as $\hat{\theta}$ and \hat{B} the global maximum likelihood estimators of θ and B , respectively. The limit itself is derived using the CL_s criterion [295] based on a fully frequentist ensemble in which n_i and $\tilde{\theta}_j$ are randomised. These limits are based on the asymptotic distribution of the test statistic [293]. The combined limit is derived from the product of the individual likelihoods, and systematic uncertainties are treated as correlated, where appropriate. The exclusion limits for the individual channels, as well as the combined limit, are shown in Figure 6.4 in terms of $\mathcal{B}(t \rightarrow bH^+)$ with the usual assumption $\mathcal{B}(H^+ \rightarrow \tau\nu) = 100\%$.

In Figure 6.5, the combined limit on $\mathcal{B}(t \rightarrow bH^+) \times \mathcal{B}(H^+ \rightarrow \tau\nu)$ is interpreted in context of the m_h^{max} scenario [296] of the MSSM. By rejecting the signal hypothesis at the 95 % Confidence Level (C.L.) again utilising the CL_s procedure [295]. The following relative theoretical uncertainties on $\mathcal{B}(t \rightarrow bH^+)$ are considered and added linearly [88, 128]:

- 5 % for one-loop electroweak corrections missing from the calculations,
- 2 % for missing two-loop QCD corrections
- about 1 %, depending on $\tan\beta$, for Δ_b -induced uncertainties. Δ_b is a correction factor to the running b quark mass [297].

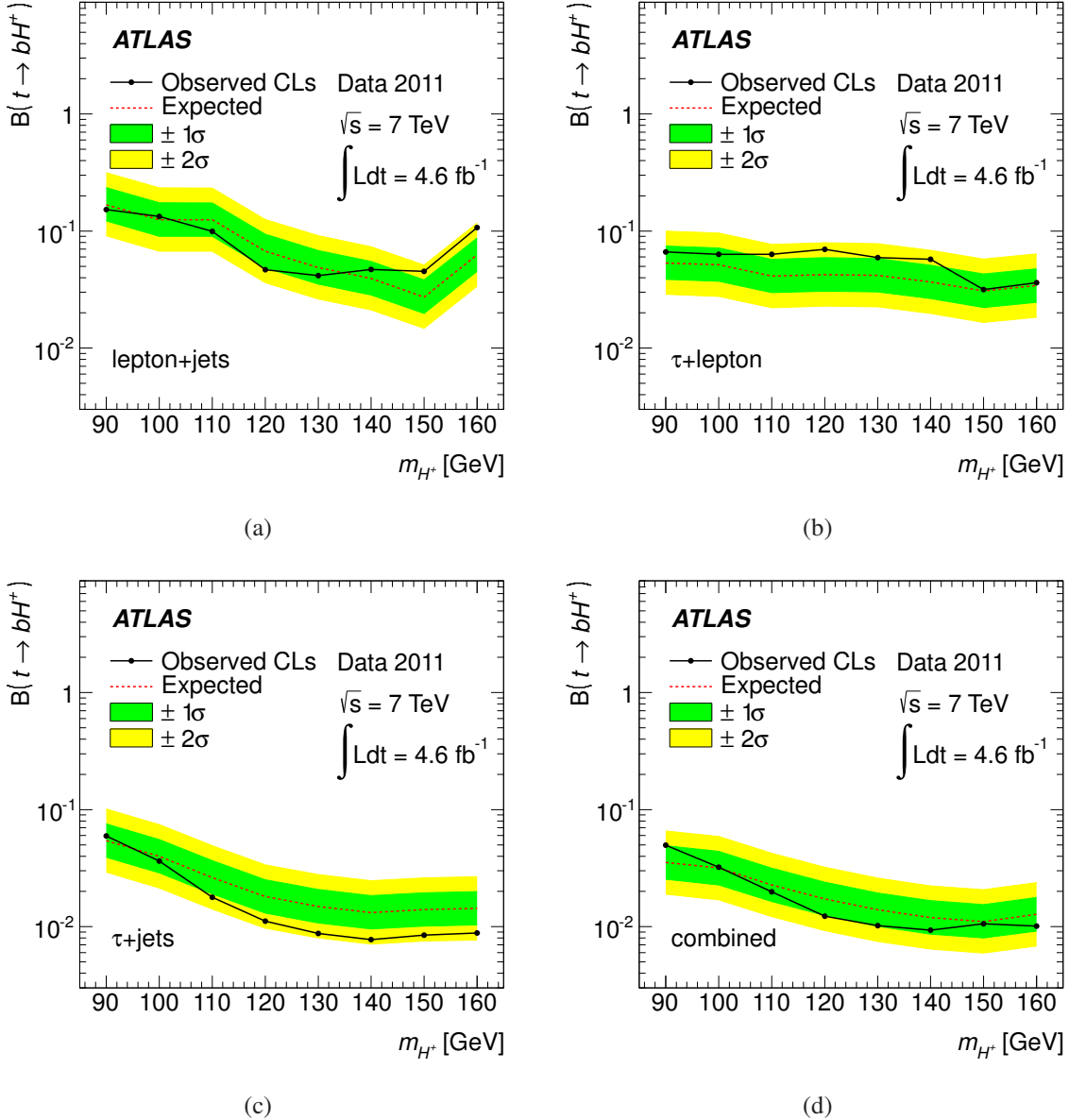


Figure 6.4: Expected and observed 95 % C.L. exclusion limits on $\mathcal{B}(t \rightarrow bH^+)$ for charged Higgs boson production from top quark decays as a function of m_{H^+} , assuming $\mathcal{B}(H^+ \rightarrow \tau\nu) = 100 \text{ \%}$. Shown are the results for: (a) $\tau_{\text{lep}} + \text{jets}$ channel; (b) $\tau_{\text{had}} + \text{lepton}$ channel; (c) $\tau_{\text{had}} + \text{jets}$ channel; (d) their combination. [172]

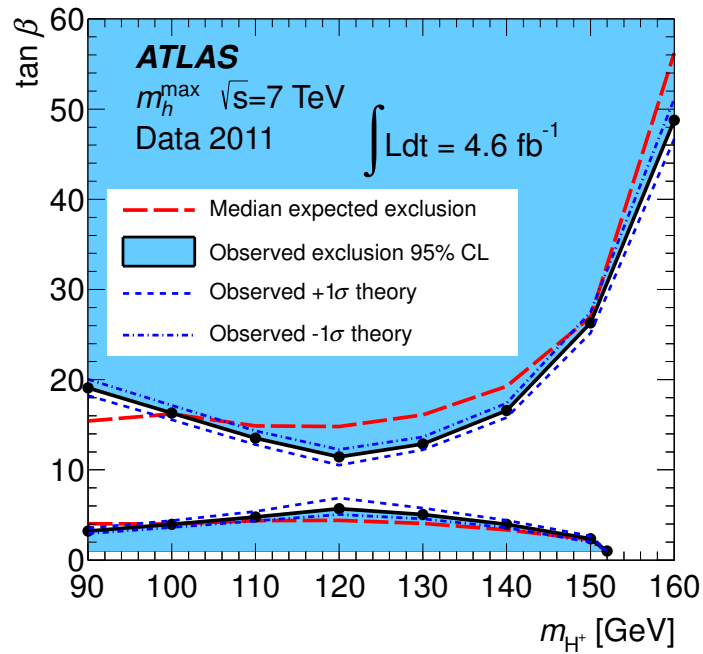


Figure 6.5: Combined 95 % C.L. exclusion limits on $\tan \beta$ as a function of m_{H^+} . The results are presented in the context of the m_h^{\max} scenario of the MSSM for the region $1 < \tan \beta < 60$ in which reliable theoretical predictions exist. The theoretical uncertainties described as in the text are included. [172]

A detailed discussion of the results and comparison to other current charged Higgs boson searches will be given in Chapter 8, as the ratio-method analysis, introduced in the following Chapter 7, is able to further improve the results of the direct searches.

Chapter 7

Indirect Search for the Charged Higgs Boson – The Ratio-Method

7.1 Ratio-Method: A Re-Analysis of the $\tau_{\text{had}} + \text{Lepton}$ Channel

The ratio-method [127, 173] is based on the idea that a light charged Higgs boson preferably decays into τ leptons. Thus, an excess compared to the SM $t\bar{t}$ decay should be an indicator if top quark decays are mediated via a charged Higgs and not a W boson. An advantage is that almost all systematic uncertainties not related to leptons (e or μ) or τ leptons cancel in first order, if choosing a ratio of event yields as the final discriminating variable.

For each of the four final states considered ($e + \tau_{\text{had}}$, $e + \mu$, $\mu + \tau_{\text{had}}$ and $\mu + e$), the difference of the opposite sign (OS) to the same sign (SS) event yield \mathcal{N} can be split into two contributions: $t\bar{t}$ events (where the top quark decays are mediated by both W and H^+) and all other SM processes, except $t\bar{t} \rightarrow b\bar{b}W^+W^-$. The contributions from $t\bar{t}$ events are expressed as a function of the cross-section, $\sigma_{t\bar{t}}$, the integrated luminosity, \mathcal{L} , the branching fraction, $B \equiv \mathcal{B}(t \rightarrow bH^+)$, as well as the selection efficiencies $\epsilon_{W^+W^-}$, $\epsilon_{H^+W^-}$, $\epsilon_{H^-W^+}$ and $\epsilon_{H^+H^-}$ for $t\bar{t} \rightarrow b\bar{b}W^+W^-$, $t\bar{t} \rightarrow b\bar{b}H^+W^-$, $t\bar{t} \rightarrow b\bar{b}H^-W^+$ and $t\bar{t} \rightarrow b\bar{b}H^+H^-$ events, respectively, in each of the four final states considered:

$$\mathcal{N} = \sigma_{t\bar{t}} \times \mathcal{L} \times \left[(1 - B)^2 \epsilon_{W^+W^-} + B(1 - B)(\epsilon_{H^+W^-} + \epsilon_{H^-W^+}) + B^2 \epsilon_{H^+H^-} \right] + \mathcal{N}_{\text{Others}} .$$

The event yield ratios are defined as:

$$R_e = \frac{\mathcal{N}(e + \tau_{\text{had}})}{\mathcal{N}(e + \mu)} \quad \text{and} \quad R_\mu = \frac{\mathcal{N}(\mu + \tau_{\text{had}})}{\mathcal{N}(\mu + e)} .$$

A variation of the event yields $\mathcal{N}(e + \tau_{\text{had}})$ and $\mathcal{N}(e + \mu)$, $\mathcal{N}(\mu + \tau_{\text{had}})$ and $\mathcal{N}(\mu + e)$ and their ratios as a function of $\mathcal{B}(t \rightarrow bH^+)$ for a charged Higgs boson mass of 130 GeV is shown in

Figure 7.1. The presence of $H^+ \rightarrow \tau\nu$ in a fraction of the top quark decays results in an increase of the number of $t\bar{t}$ events with a lepton and a hadronically decaying τ lepton in the final state, hence of the ratios R_e and R_μ . Note that the event yields for dilepton final states become smaller in the presence of a charged Higgs boson in top quark decays, despite the fact that a τ lepton decays into an electron or muon more often than a W boson. This results from the fact that electrons and muons produced in the decay chain $t \rightarrow bH^+ \rightarrow b\tau\nu \rightarrow b\ell + N\nu$ are, on average, softer than those stemming from $t \rightarrow bW \rightarrow b\ell + N\nu$.

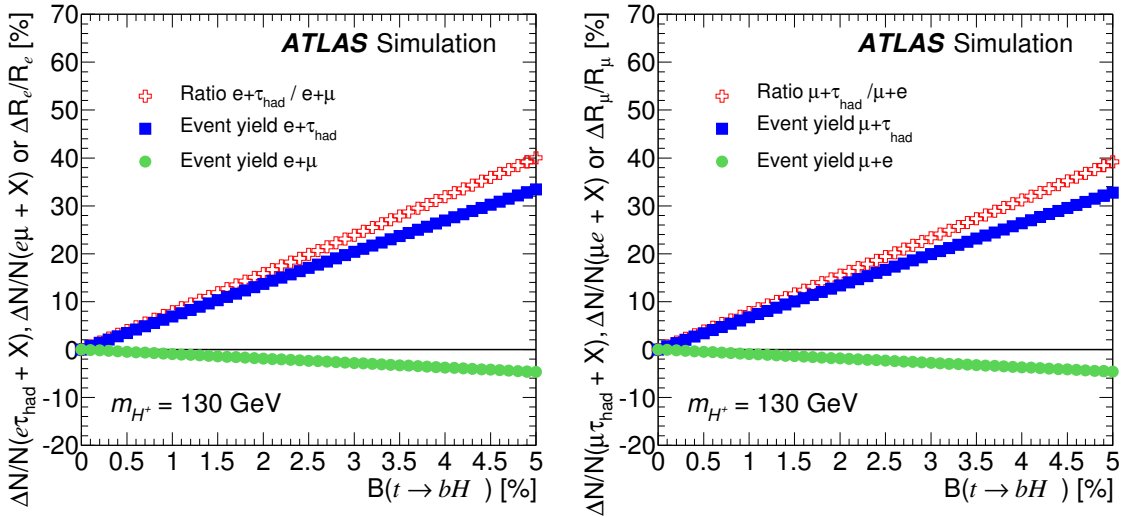


Figure 7.1: Relative variation with $\mathcal{B}(t \rightarrow bH^+)$ of the event yields $\mathcal{N}(e + \tau_{\text{had}})$, $\mathcal{N}(e + \mu)$ and their ratio in the left plot, as well as $\mathcal{N}(\mu + \tau_{\text{had}})$, $\mathcal{N}(\mu + e)$ and their ratio in the right plot, assuming the presence of a 130 GeV charged Higgs boson in the $t\bar{t}$ events. [173]

The sensitivity of this analysis to charged Higgs bosons is determined by the rate at which the ratios R_e and R_μ change with $\mathcal{B}(t \rightarrow bH^+)$, which in turn depends on the selection efficiencies $\epsilon_{H^+W^-}$, $\epsilon_{H^-W^+}$, $\epsilon_{H^+H^-}$ and on the charged Higgs boson mass. For $m_{H^+} = 150$ (160) GeV, the rate at which the ratios R_e and R_μ change with $\mathcal{B}(t \rightarrow bH^+)$ is found to be two (five) times smaller than for $m_{H^+} = 130$ GeV. The selection efficiencies $\epsilon_{H^+W^-}$, $\epsilon_{H^-W^+}$, $\epsilon_{H^+H^-}$ are reduced for m_{H^+} values in the vicinity of m_{top} , as the b -tagged jet arising from $t \rightarrow bH^+$ becomes softer as the mass difference $m_{\text{top}} - m_{H^+}$ decreases. Table 7.1 illustrates how the slopes s_e and s_μ of the ratios R_e and R_μ as a function of $\mathcal{B}(t \rightarrow bH^+)$ vary with m_{H^+} . The slopes obtained with $m_{H^+} = 130$ GeV, as shown in Figure 7.1, are used as the reference in Table 7.1.

7.2 Event Selection

This analysis uses events passing a single-lepton trigger with an E_T threshold of 20 GeV or 22 GeV for electrons and a p_T threshold of 18 GeV for muons, as given in Section 5.2.1. To

m_{H^+} (GeV)	90	100	110	120	130	140	150	160
s_e/s_e^{130}	1.12	0.96	1.15	1.06	1.00	0.81	0.52	0.22
s_μ/s_μ^{130}	1.04	1.04	1.06	1.04	1.00	0.81	0.47	0.16

Table 7.1: Variation with m_{H^+} of the slopes s_e and s_μ relative increase of the ratios R_e and R_μ with $\mathcal{B}(t \rightarrow bH^+)$. $m_{H^+} = 130$ GeV is used as the reference mass point. The relatively low value of the slope in the electron-triggered channel at 100 GeV is caused by a statistical fluctuation in the corresponding Monte Carlo signal sample. [174]

select a sample enriched in $t\bar{t}$ events, the following requirements are imposed:

- one charged lepton, ℓ (e, μ), having $E_T > 25$ GeV (e) or $p_T > 25$ GeV (μ) and matched to the corresponding trigger object;
- at least two jets with $p_T > 20$ GeV and within $|\eta| < 2.4$, exactly two of these b -tagged;
- either exactly one τ_{had} lepton with $p_T^\tau > 25$ GeV and $|\eta| < 2.3$ with no additional charged lepton, or exactly one additional charged lepton, ℓ' , with E_T or p_T above 25 GeV with a different flavour than the trigger-matched lepton;
- $E_T^{\text{miss}} > 40$ GeV.

At this stage, the selected events are classified into two categories according to the matched single-lepton trigger: an electron trigger or a muon trigger category. Each category contains $\tau_{\text{had}} + \text{lepton}$ and dilepton ($\ell\ell'$) events. The lepton appearing first in the final state name is, by convention, matched to the corresponding trigger object. The electron triggered category, therefore, consists of $e + \tau_{\text{had}}$ and $e + \mu$ events, while the muon triggered category contains $\mu + \tau_{\text{had}}$ and $\mu + e$ events. Events firing both, a single-electron and a single-muon trigger are assigned to both categories, and accounted for in the combined limit setting, as explained later in Section 7.5.

The analysis uses the generalised transverse mass [282], $m_{T2}^{H^+}$, which can help discriminate leptons produced in $H^+ \rightarrow \tau\nu$ decays from leptons stemming from W bosons. Here for the first time $m_{T2}^{H^+}$ is utilised with hadronically decaying τ leptons.

The method by which such a variable is obtained for a general event topology is rather simple: maximisation (or minimisation, depending on the nature of the constraints) of an unknown particle mass in the event, is subjected to the constraints that are imposed by the known particle masses and by assuming momentum conservation in the transverse plane. Here $t\bar{t} \rightarrow H^+ bW^- \bar{b}$, with subsequent decays $W^- \rightarrow \ell^- \bar{\nu}_\ell$ and $H^+ \rightarrow \tau_{\text{had}}^+ \nu$ are considered. Assuming that the top quarks and the W boson are on-shell, and the missing transverse momentum in the event stems entirely from neutrinos produced in the decays of the charged Higgs and W bosons. The fol-

lowing constraints are obtained for the particles in $t\bar{t} \rightarrow b\bar{b}W^-H^+ \rightarrow b\bar{b}(\ell^-\bar{\nu}_\ell)(\tau_{\text{had}}^+\nu)$:

$$\begin{aligned} (p^{H^+} + p^b)^2 &= m_{\text{top}}^2, \\ (p^{\ell^-} + p^{\bar{\nu}_\ell})^2 &= m_W^2, \\ (p^{\ell^-} + p^{\bar{\nu}_\ell} + p^{\bar{b}})^2 &= m_{\text{top}}^2, \\ (p^{\bar{\nu}_\ell})^2 &= 0, \\ \vec{p}_T^{H^+} - \vec{p}_T^{\tau_{\text{had}}^+} + \vec{p}_T^{\bar{\nu}_\ell} &= \vec{p}_T^{\text{miss}}. \end{aligned} \quad (7.1)$$

In these equations, p^{H^+} and $p^{\bar{\nu}_\ell}$ represent the unknown quantities in the event, while all other four-momenta are known. Hence, there are eight unknown variables and only six constraints, meaning that the system is under-constrained with two degrees of freedom. $m_{\text{T2}}^{H^+}$ is defined as the maximum of the invariant mass $(p^{H^+})^2$ subjected to the constraints of Equations (7.1):

$$(m_{\text{T2}}^{H^+})^2 = \max_{\{ \text{Equations (7.1)} \}} \left[(p^{H^+})^2 \right]. \quad (7.2)$$

By choosing the z -component of the H^+ momentum as one of the unconstrained degrees of freedom, half of the maximisation can be performed analytically using the result obtained for the transverse mass of a charged Higgs boson in semi-leptonic $t\bar{t}$ decays, as described in detail in Reference [298]. Doing this, one obtains:

$$m_{\text{T2}}^{H^+} = \max_{\vec{p}_T^{H^+}} \left[M_T^H \left(\vec{p}_T^{H^+} \right) \right], \quad (7.3)$$

where

$$(M_T^H)^2 = \left(\sqrt{m_{\text{top}}^2 + (\vec{p}_T^{H^+} + \vec{p}_T^b)^2} - p_T^b \right)^2 - (p_T^{H^+})^2. \quad (7.4)$$

Since $\vec{p}_T^{H^+}$ is constrained by Equation (7.1), there is effectively one remaining degree of freedom. The rest of the maximisation has to be done numerically. A program that computes the generalised transverse mass for dilepton $t\bar{t}$ events was written. Its input parameters are the two components of the missing transverse momentum, as well as the four-momenta of the two leptons and of the two b -tagged jets. By construction, the generalised transverse mass satisfies $m_{\text{T2}}^{H^+} \geq m_{H^+}$, where m_{H^+} is the true charged Higgs boson mass. It is this property that provides the potential for the generalised transverse mass $m_{\text{T2}}^{H^+}$ to discriminate between charged Higgs and W bosons.

In $\tau_{\text{had}} + \text{lepton}$ events, before computing the generalised transverse mass, each b -tagged jet must be assigned to the other visible decay product of each top quark candidate. This is done by selecting the combination that minimises the sum of the distances between each b -tagged jet and either the charged lepton or the hadronic τ lepton, $\Delta R(b_1, \ell) + \Delta R(b_2, \tau_{\text{had}})$. In simulated SM $t\bar{t}$ events, by using information about the correctly identified combinations in the generated

events, the efficiency of finding the correct association for the b -tagged jets is about 70 %. The hadronic τ lepton and its associated b -tagged jet are assigned to the “ H^+ -side” of the event, where $m_{T2}^{H^+}$ is computed. The charged lepton and its associated b -tagged jet are assigned to the “W-side” of the event, where the single-lepton trigger is fired.

In dilepton events, the b -tagged jet assignment is performed by selecting the combination that minimises the sum of the distances between each b -tagged jet and each charged lepton. The efficiency of finding the right assignment in simulated SM $t\bar{t}$ events is about 76 %. Similarly to the $\tau_{\text{had}} + \text{lepton}$ events, the “W-side” of the event is assigned to the lepton firing the trigger (the electron for $e + \mu$ events and the muon for $\mu + e$ events), and the other side of the event is used to compute $m_{T2}^{H^+}$, with the corresponding charged lepton instead of τ lepton in Equation 7.1.

At first order, this transverse mass is larger than the true charged Higgs boson mass m_{H^+} and smaller than the top quark mass, m_{top} , used in the constraints. For incorrect pairings of τ leptons or leptons with b -tagged jets, the numerical determination of $m_{T2}^{H^+}$ may fail. Therefore, only events with $m_{T2}^{H^+} > 0$ are kept in the following, the $m_{T2}^{H^+}$ distributions are shown in Figure 7.2.

The backgrounds due to mis-identified τ leptons are, estimated with the data-driven procedures as given in Section 5.5.2, mis-identified electrons and muons are estimated by the data-driven approach described in Section 5.5.5.

7.3 Measured Event Yield Ratios

The event yields in the $\tau_{\text{had}} + \text{lepton}$ and dilepton final states are summarised in Table 7.2 for the background-only hypothesis as well as in the presence of a 130 GeV charged Higgs boson in the top quark decay. The predicted values in the SM-only hypothesis and the measured values of the ratios R_e and R_μ are summarised in Table 7.3.

7.4 Systematic Uncertainties

7.4.1 Systematic Uncertainties of Detector Simulation

The systematic uncertainties arising from detector, pile-up and the object reconstruction in this analysis are the same for this analysis as described in Section 6.4.1.

7.4.2 Systematic Uncertainties of Generation of $t\bar{t}$ Events

Section 6.4.2 describes the systematic uncertainties also for this analysis arising from the generation of $t\bar{t}$ events. Further the $t\bar{t}$ cross-section used in this analysis is $\sigma_{t\bar{t}} = 167^{+17}_{-18} \text{ pb}$ [179]. Initial state radiation and final state radiation systematic uncertainties are dominated by the difference in modelling the numbers of tracks N_{track}^{τ} and $N_{\text{track}}^{\text{iso}}$ in the core and isolation regions of

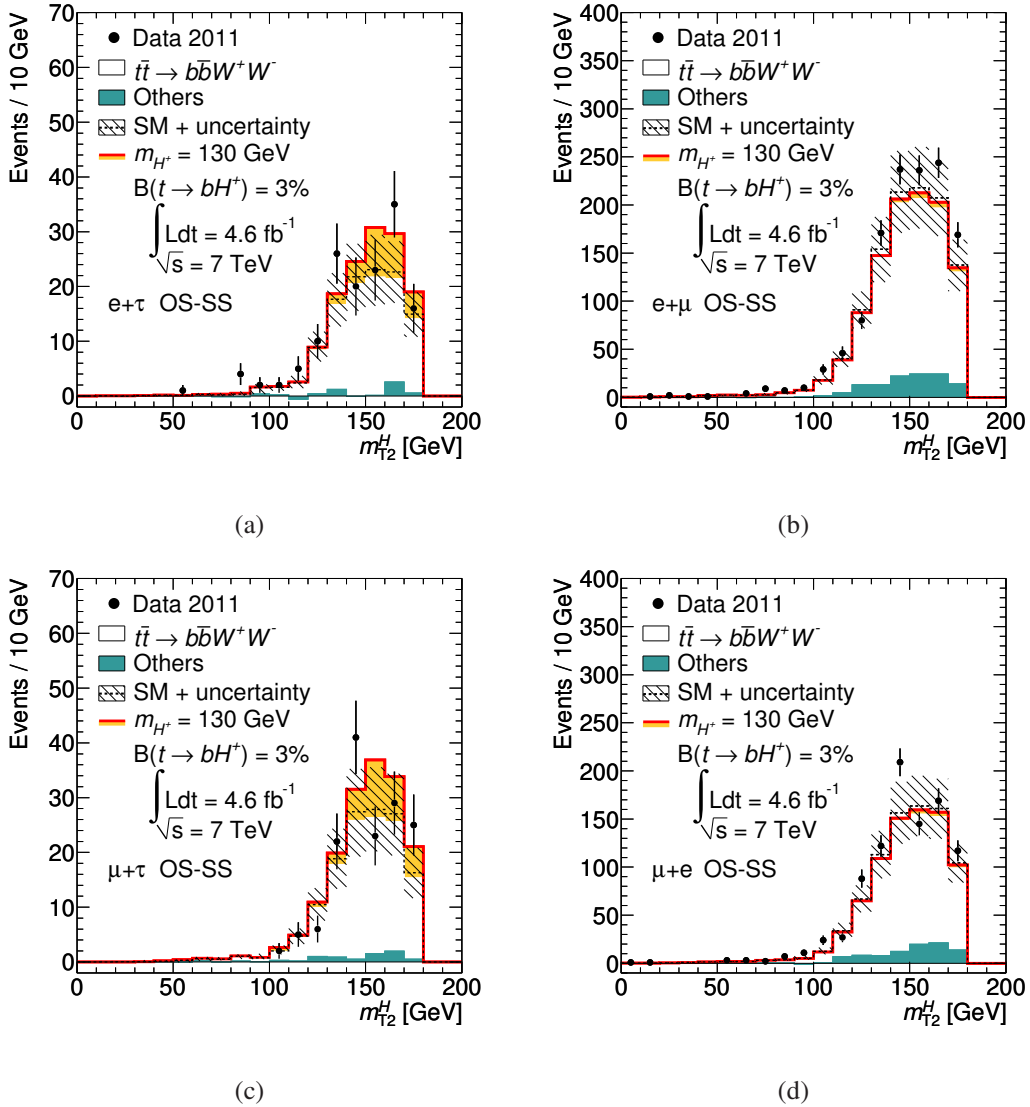


Figure 7.2: Distribution of m_{T2}^H in the signal region enriched in OS-SS $t\bar{t}$ events for (a) $e + \tau_{\text{had}}$ or (b) $e + \mu$ and (c) $\mu + \tau_{\text{had}}$ or (d) $\mu + e$ final state selections. The dashed line corresponds to the SM-only hypothesis and the hatched area around it shows the total uncertainty for the SM backgrounds, where “Others” refers to the contribution of all SM processes except $t\bar{t} \rightarrow b\bar{b}W^+W^-$. The solid line shows the predicted contribution of signal+background in the presence of a 130 GeV charged Higgs boson, assuming $\mathcal{B}(t \rightarrow bH^+) = 3\%$ and $\mathcal{B}(H^+ \rightarrow \tau\nu) = 100\%$. The yellow area below the solid line corresponds to the contribution of the H^+ signal, stacked on top of the scaled $t\bar{t} \rightarrow b\bar{b}W^+W^-$ background and other SM processes. [174]

Sample	OS–SS event yields			
	$e + \tau_{\text{had}}$		$e + \mu$	
Mis-identified electrons or muons	-0.8 ± 3.0		94 ± 37	
$W/Z+\text{jets}$ & diboson	2.1 ± 0.9		0.7 ± 0.4	
Single top quark	3.3 ± 0.8		24 ± 4	
$t\bar{t}$	111 ± 25		980 ± 200	
$\sum \text{SM}$	116 ± 25		1100 ± 210	
Data	144		1247	
$t\bar{t}$ with $t \rightarrow bH^+$ (130 GeV)	30 ± 4		27 ± 4	
Prediction with signal	139 ± 28		1070 ± 200	
Sample	$\mu + \tau_{\text{had}}$		$\mu + e$	
	0.2 ± 1.0		74 ± 37	
Mis-identified electrons or muons	2.6 ± 1.6		0.7 ± 0.4	
$W/Z+\text{jets}$ & diboson	4.6 ± 0.9		18 ± 3	
$t\bar{t}$	131 ± 28		740 ± 150	
$\sum \text{SM}$	138 ± 29		830 ± 160	
Data	153		929	
$t\bar{t}$ with $t \rightarrow bH^+$ (130 GeV)	35 ± 4		20 ± 3	
Prediction with signal	166 ± 32		810 ± 150	

Table 7.2: Expected opposite sign (OS) – same sign (SS) event yields after all selection cuts in $\tau_{\text{had}}+\text{lepton}$ and dilepton channels, compared with 4.6 fb^{-1} of ATLAS data. The numbers shown for a hypothetical 130 GeV H^+ signal correspond to $\mathcal{B}(t \rightarrow bH^+) = 3\%$. The contribution of $t\bar{t} \rightarrow b\bar{b}W^+W^-$ events to the background is scaled accordingly. Statistical and systematic uncertainties are combined. [173]

Ratio	R_e	R_μ
SM value	0.105 ± 0.012	0.166 ± 0.017
Measured value	$0.115 \pm 0.010 \text{ (stat)}$	$0.165 \pm 0.015 \text{ (stat)}$

Table 7.3: Predicted (in the SM-only hypothesis) and measured values of the event yield ratios R_e and R_μ . For the values of the ratios predicted using simulation, the statistical and systematic uncertainties are combined. [173]

the jets mis-identified as τ lepton candidates, respectively. The various simulated $t\bar{t}$ samples are reweighted so the N_{track}^{τ} and the $N_{\text{track}}^{\text{iso}}$ distributions match, where both variables are reweighted in a correlated way, before the systematic uncertainties on the $t\bar{t}$ generation, the parton shower model, as well as initial state radiation and final state radiation, are evaluated.

The signal samples are generated with PYTHIA, without higher-order corrections, as no alternative generator is available for the charged Higgs boson simulation. Hence, the systematic uncertainty is evaluated to be the relative difference in acceptance between $t\bar{t}$ events generated with MC@NLO interfaced to HERWIG/JIMMY and with ACERMC, which is also a leading-order generator, interfaced to PYTHIA. For the systematic uncertainty from initial state radiation and final state radiation the same simulated samples as for the SM $t\bar{t}$ events are used. In the evaluation of the systematic uncertainties for the signal samples only τ leptons matched to simulated hadronically decaying τ leptons in the generated events are considered.

7.4.3 Systematic Uncertainties of Data-Driven Background Estimates

Concerning the backgrounds with mis-identified leptons the largest systematic uncertainties arise from the sample dependence: the mis-identification probabilities are calculated in a control region dominated by gluon-initiated events, but they are then used in a data selection with a higher fraction of quark-initiated events. The total systematic uncertainty on the backgrounds with mis-identified leptons is 38 % for electron-triggered events and 49 % for muon-triggered events. This corresponds to the relative variation of the number of events with exactly one trigger-matched lepton and two jets, after having considered all systematic uncertainties. The requirement of having two b -tagged jets in the event does not have a significant impact on these systematic uncertainties and neither does the presence of a second lepton.

For the estimation of backgrounds with jets mis-identified as hadronically decaying τ leptons, the systematic uncertainty on the scale factors associated with the number of tracks is determined by varying the requirement on the jet multiplicity and the magnitude of the subtraction of τ candidates matched to a simulated electron, muon or τ lepton in the generated events. This uncertainty is 7 % for 1-track τ leptons and 11 % for 3-track τ leptons. In addition, systematic uncertainties on the jet $\rightarrow \tau$ lepton mis-identification probability arise from statistical uncertainties due to the limited control sample size, the differences between mis-identification probabilities computed in the region enriched with $W+ > 2$ jets events and the signal region as well as the small contamination from correctly reconstructed τ leptons (including those possibly stemming from $H^+ \rightarrow \tau\nu$) in the region enriched with $W+ > 2$ jets events.

Some of the systematic uncertainties above affect the $\tau_{\text{had}} + \text{lepton}$ and dilepton event yields in the same manner and, as a result, have a limited impact on R_e and R_μ . Systematic uncertainties arising from jets and E_T^{miss} are common to all reconstructed events in the simulation. Hence, they should cancel in the ratios R_e and R_μ . However, due to the use of data-driven background estimates and because of the removal of geometric overlaps between reconstructed objects,

some of these systematic uncertainties still do have a minor impact. In each category, the systematic uncertainties related to the trigger-matched electron or muon are the same for the $e + \tau_{\text{had}}$ and $e + \mu$ or $\mu + \tau_{\text{had}}$ and $\mu + e$ events. Thereby, they do not affect the predicted value of the ratios R_e and R_μ . Those systematic uncertainties stemming from the reconstructed muon or electron only affect event yields in the denominator and hence the ratio. Similarly, the systematic uncertainties caused by τ leptons and their mis-identification probabilities only affect the numerator of R_e and R_μ . Hence these systematic uncertainties do have an impact on the analysis. This is also the case for systematic uncertainties on the backgrounds with mis-identified leptons, which have a larger contribution in the dilepton events on the denominator of R_e and R_μ . Table 7.4 shows how these ratios, for the SM-only hypothesis, change when shifting a particular parameter by its ± 1 standard deviation uncertainty.

7.5 Results

7.5.1 Upper Limits obtained from Results of the Ratio-Method

No significant deviation from the SM predictions is observed for the event yield ratios R_e and R_μ , given in Table 7.3. With the assumption $\mathcal{B}(H^+ \rightarrow \tau\nu) = 100\%$, upper limits are extracted on the branching ratio, $B \equiv \mathcal{B}(t \rightarrow bH^+)$, as a function of the charged Higgs boson mass. Before deriving upper limits from the event yield ratios, the m_{T2}^H distributions of Figure 7.2 are used for the computation of limits, with the procedure described in Section 6.5, just as a reference. For this purpose, a probability density function $f_i(m_{\text{T2}}^H)$ is introduced, such that the expected and observed number of events in each bin, i , are, respectively, $\mu_i = \mu f_i(m_{\text{T2}}^H)$, where μ is the expected number of events in the signal region, and n_i . The resulting likelihood is given by:

$$\mathcal{L}(B) = \prod_i f_{\text{Poisson}}(n_i|\mu_i) \prod_j p(\tilde{\theta}_j|\theta_j). \quad (7.5)$$

Nuisance parameters, θ , are used to describe the effect of systematic uncertainties, and $p(\tilde{\theta}_j|\theta_j)$ are the Gaussian constraints relating each parameter to its nominal estimate, $\tilde{\theta}_j$. A profile likelihood statistical analysis is then performed with B as the only parameter of interest. The test statistic is given by [293]:

$$q_B = -2 \log \frac{\mathcal{L}(B, \hat{\theta}_B)}{\mathcal{L}(\hat{B}, \hat{\theta})}, \quad 0 \leq \hat{B} \leq B, \quad (7.6)$$

where $\hat{\theta}_B$ are the maximum likelihood estimators of the nuisance parameters for a fixed B , while $\hat{\theta}$ and \hat{B} are the global maximum likelihood estimators of θ and B . The limit itself is derived using the CL_s criterion [295] and asymptotic approximations [293]. For the calculation of the expected limits and the error bands the Asimov dataset [293] is employed. Using the m_{T2}^H

Systematic uncertainty	ΔR_e	ΔR_μ
Integrated luminosity	0.3 %	0.3 %
Electron trigger efficiency	0.1 %	n/a
Electron reconstruction and ID efficiencies	0.2 %	1.9 %
Electron energy resolution	0.1 %	<0.1 %
Electron energy scale	0.1 %	0.3 %
Muon trigger efficiency	n/a	0.1 %
Muon reconstruction and ID efficiencies	1.0 %	0.1 %
Muon momentum resolution	<0.1 %	<0.1 %
Muon momentum scale	0.1 %	<0.1 %
τ ID efficiency	3.9 %	3.9 %
τ energy scale	2.9 %	3.0 %
τ mis-ID (data-driven): number of associated tracks	2.1 %	2.1 %
τ mis-ID (data-driven): true τ contamination	0.2 %	0.2 %
τ mis-ID (data-driven): H^+ signal contamination	0.6 %	0.6 %
τ mis-ID (data-driven): event environment	1.3 %	1.2 %
τ mis-ID (data-driven): statistical uncertainties	3.3 %	3.2 %
τ mis-ID (data-driven): electron veto uncertainties	0.6 %	0.3 %
b -tagging	1.9 %	2.3 %
Jet vertex fraction	0.1 %	0.4 %
Jet energy resolution	0.4 %	<0.1 %
Jet energy scale	0.7 %	0.5 %
Jet reconstruction efficiency	0.1 %	0.4 %
E_T^{miss}	0.3 %	0.1 %
$t\bar{t}$: cross-section	0.7 %	0.6 %
$t\bar{t}$: generator and parton shower	5.7 %	4.4 %
$t\bar{t}$: initial state and final state radiation	3.6 %	3.7 %
Backgrounds with mis-identified leptons	3.5 %	4.3 %
Total (added in quadrature)	10.3 %	10.1 %

Table 7.4: Relative variation of the ratios, R_e and R_μ , in the SM-only hypothesis after shifting a particular parameter by its ± 1 standard deviation uncertainty. In this table only “ID” stands shorthand for identification. [173]

distributions of Figures 7.2, upper limits in the range 3.3 %–13.0 % and 2.4 %–14.0 % can be placed on $\mathcal{B}(t \rightarrow bH^+)$, for $e + \tau$ and $\mu + \tau$ events, respectively, illustrated in Figures 7.3(a) and 7.3(b).

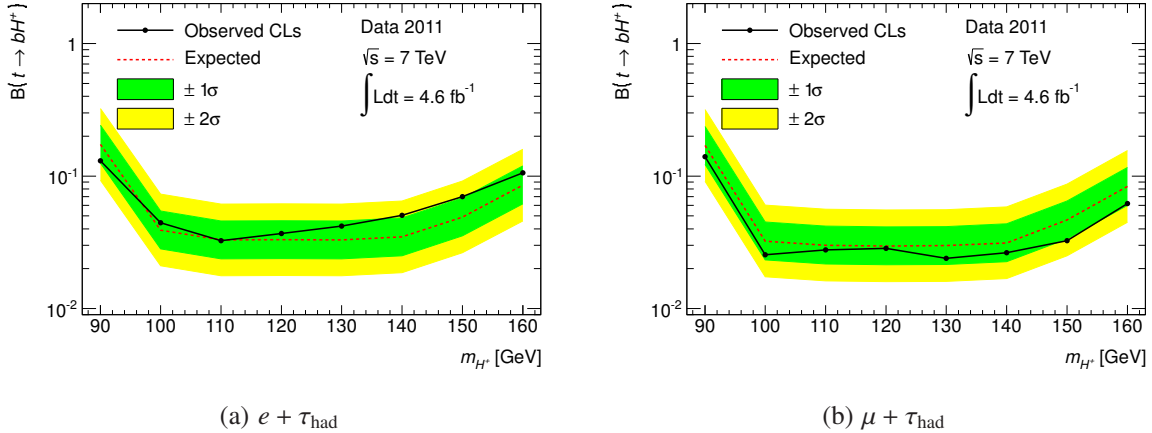


Figure 7.3: Upper limits on $\mathcal{B}(t \rightarrow bH^+)$ derived from the $m_{\text{T}2}^H$ distributions of (a) $e + \tau$ and (b) $\mu + \tau$ events, as a function of the charged Higgs boson mass, obtained for an integrated luminosity of 4.6 fb^{-1} and with the assumption $\mathcal{B}(H^+ \rightarrow \tau\nu) = 100\%$. All systematic uncertainties are included, as described in the text. The solid line in the figure is used to denote the observed 95 % C.L. upper limits, while the dashed line represents the expected exclusion limits. The outer edges of the green and yellow regions show the 1σ and 2σ error bands. [174]

To cancel out or reduce some systematic uncertainties, the study presented here uses the ratio of integrated event yields rather than the $m_{\text{T}2}^H$ distributions themselves. In this context the assumed underlying probability density function of the measured variables must be known to perform a profile likelihood statistical analysis.

The measured event yield ratios R_e and R_μ are the ratios of two Poisson distributed variables, the probability density function of which is unknown. However, the sampling variation of $\mathcal{N}_{\ell+\ell'}$ is restricted to the subset $\mathcal{N}_{\ell+\tau_{\text{had}}} + \mathcal{N}_{\ell+\ell'} (0 < \mathcal{N}_{\ell+\ell'} < \mathcal{N}_{\ell+\tau_{\text{had}}} + \mathcal{N}_{\ell+\ell'})$. This implies that the variable $\mathcal{N}_{\ell+\ell'}$ follows a binomial distribution, defined as:

$$f_{\text{Binomial}}(k, n, p) = \binom{n}{k} p^k (1-p)^{n-k}, \quad (7.7)$$

where the parameters k , n and p are:

$$k = \mathcal{N}_{\ell+\ell'},$$

$$n = \mathcal{N}_{\ell+\tau_{\text{had}}} + \mathcal{N}_{\ell+\ell'}, \quad (7.8)$$

$$p = \frac{\mathcal{N}_{\ell+\ell'}}{\mathcal{N}_{\ell+\tau_{\text{had}}} + \mathcal{N}_{\ell+\ell'}},$$

hence, $k = np$. In addition, the binomial parameter p can be rewritten as a monotonic function of the ratio, R_ℓ :

$$p = \frac{1}{1 + R_\ell}. \quad (7.9)$$

If both np and $np(1 - p)$ are greater than 5, a good approximation to the binomial distribution $f_{\text{Binomial}}(k, n, p)$ is given by the normal distribution:

$$f_{\text{Gauss}}(np, \sigma = \sqrt{np(1 - p)}). \quad (7.10)$$

Dividing by the parameter n yields that p is approximated by the normal distribution:

$$f_{\text{Gauss}}\left(p, \sigma = \sqrt{\frac{p(1 - p)}{n}}\right). \quad (7.11)$$

If the ratio R_e or R_μ is used for the computation of upper limits on the branching ratio, B , the resulting likelihood, introducing ρ and R , the expected and observed ratios, and n the sum of expected $\tau_{\text{had}} + \text{lepton}$ and dilepton events in a signal region, is given by:

$$\mathcal{L}(B) = f_{\text{Gauss}}(p(R_i) | p(\rho_i), \sigma(\rho_i, n_i)) \prod_j q(\tilde{\theta}_j | \theta_j), \quad (7.12)$$

where σ represents the second parameter of the normal distribution of Equation (7.11) and the index i this time indicates the category (electron or muon triggered). Similar to Equation (7.5), nuisance parameters are used to describe the effect of systematic uncertainties, and $q(\tilde{\theta}_j | \theta_j)$ are the Gaussian constraints relating each parameter to its nominal estimate, $\tilde{\theta}_j$.

Using the event yield ratios R_e and R_μ , upper limits in the range 4.5%–6.3% and 3.6%–4.7% can be placed on $\mathcal{B}(t \rightarrow bH^+)$ for charged Higgs boson masses in the range 90–140 GeV, in the electron and muon triggered category, respectively, illustrated in Figure 7.4. Note that the observed limits follow the trend of the expected limits. This results from the fact that the utilised limit setting method resembles a counting experiment and this behaviour is expected, as no shape information is utilised.

For higher charged Higgs boson masses, the loss of sensitivity, as predicted by Table 7.1, is clearly visible. It can be noted that the upper limits on $\mathcal{B}(t \rightarrow bH^+)$ obtained from the event yield ratios are significantly better than those derived from the m_{T2}^H distributions, except in the vicinity of the top quark mass, where more information is found in the shape of the generalised transverse mass distribution than in the event yield ratios. In addition, the differences between the expected upper limits in the electron and muon triggered categories are small, since the dominant systematic uncertainties arise from the τ leptons and are similar in both categories, as suggested by Table 7.4.

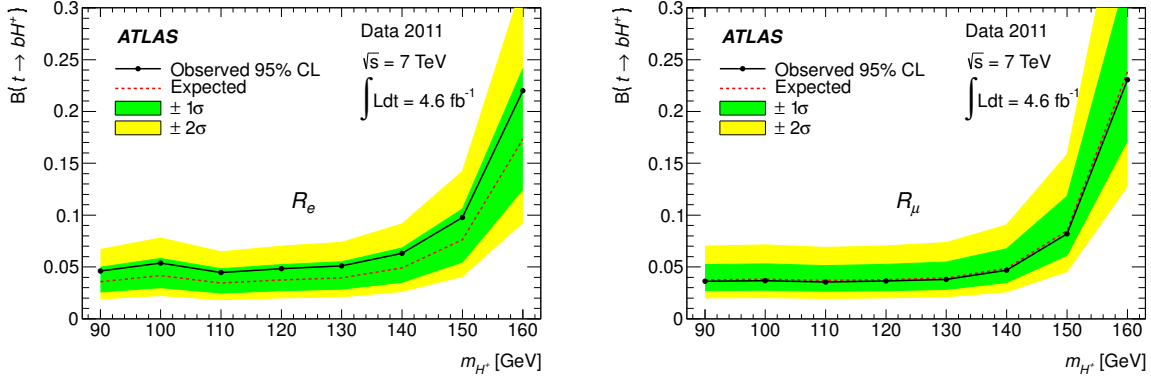


Figure 7.4: Upper limits on $\mathcal{B}(t \rightarrow bH^+)$ derived from the event yield ratios R_e left and R_μ right, as a function of the charged Higgs boson mass, obtained for an integrated luminosity of 4.6 fb^{-1} and with the assumption $\mathcal{B}(H^+ \rightarrow \tau\nu) = 100\%$. The solid line in the figure is used to denote the observed 95 % C.L. upper limits, while the dashed line represents the expected exclusion limits. The outer edges of the green and yellow regions show the 1σ and 2σ error bands. [173]

A combined upper limit for the electron and muon triggered categories is obtained utilising the same formalism with a global event yield ratio, $R_{e+\mu}$, defined as:

$$R_{e+\mu} = \frac{\mathcal{N}(e + \tau_{\text{had}}) + \mathcal{N}(\mu + \tau_{\text{had}})}{\mathcal{N}(e + \mu) + \mathcal{N}_{\text{OR}}(\mu + e)}, \quad (7.13)$$

where $\mathcal{N}_{\text{OR}}(\mu + e)$ is the event yield in the $\mu + e$ channel after removing the dilepton events that simultaneously fire a single-electron trigger and a single-muon trigger, as those are already accounted for in $\mathcal{N}(e + \mu)$. The fraction of dilepton events common to the $\mu + e$ and $e + \mu$ final states, after the event selection, is about 42 % in the data. Utilising this global event yield ratio, upper limits in the range 3.2 %–4.4 % can be placed on $\mathcal{B}(t \rightarrow bH^+)$ for charged Higgs boson masses in the range 90–140 GeV, as given in Figure 7.5 and Table 7.5.

The profiled values and constraints on systematic uncertainties (nuisance parameters) from an unconditional fit of the combined model to data are given in Table 7.6, assuming a charged Higgs boson mass of 130 GeV. No significant pulls or over-constraints of the nuisance parameters are observed.

In Figure 7.6, the limit on $\mathcal{B}(t \rightarrow bH^+) \times \mathcal{B}(H^+ \rightarrow \tau\nu)$ is interpreted in the context of the m_h^{max} scenario of the MSSM [296] and illustrated in the $m_{H^+} - \tan\beta$ plane. Note that no exclusion limit is shown for charged Higgs boson masses above 140 GeV, as no reliable calculations of $\mathcal{B}(t \rightarrow bH^+)$ exist for $\tan\beta$ values in this range. The following relative uncertainties on $\mathcal{B}(t \rightarrow bH^+)$ are considered and added linearly [88, 128]:

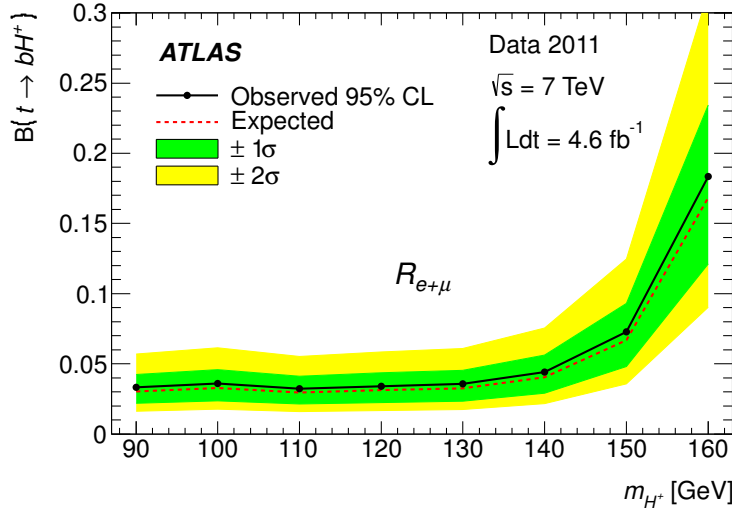


Figure 7.5: Upper limits on $\mathcal{B}(t \rightarrow bH^+)$ derived from the event yield ratio, $R_{e+μ}$, as a function of the charged Higgs boson mass, obtained for an integrated luminosity of 4.6 fb^{-1} , assuming $\mathcal{B}(H^+ \rightarrow τν) = 100 \text{ \%}$. The solid line in the figure is used to denote the observed 95 % C.L. upper limits, while the dashed line represents the expected exclusion limits. The outer edges of the green and yellow regions show the 1σ and 2σ error bands. [173]

- 5 % for one-loop electroweak corrections missing from the calculations,
- 2 % for missing two-loop QCD corrections
- about 1 %, depending on $\tan\beta$, for $Δ_b$ -induced uncertainties. $Δ_b$ is a correction factor to the running b quark mass [297].

7.5.2 Combination of Upper Limits obtained from Direct Searches for Charged Higgs Bosons in the $τ_{\text{had}} + \text{jets}$ final state and the Ratio-Method Results

In the direct searches for charged Higgs bosons presented in Section 6, upper limits on the branching ratio $\mathcal{B}(t \rightarrow bH^+)$ were derived using various distributions of discriminating variables in the $τ_{\text{had}} + \text{lepton}$, $τ_{\text{had}} + \text{jets}$ and $τ_{\text{lep}} + \text{jets}$ final states [172]. The most sensitive channel was found to be $τ_{\text{had}} + \text{jets}$, except for low values of m_{H^+} , as is evinced in Table 7.7.

A full orthogonality of the $τ_{\text{had}} + \text{jets}$ event selection to the selection of this analysis, as described in Section 7.2, is a result of a lepton veto imposed in $τ_{\text{had}} + \text{jets}$ event selection. The physics object definitions and the corresponding systematic uncertainties are the same in this analysis and the direct searches [172], thus a new set of combined upper limits on $\mathcal{B}(t \rightarrow bH^+)$ using both the transverse mass distribution, m_T , of $τ_{\text{had}} + \text{jets}$ events and the global event yield

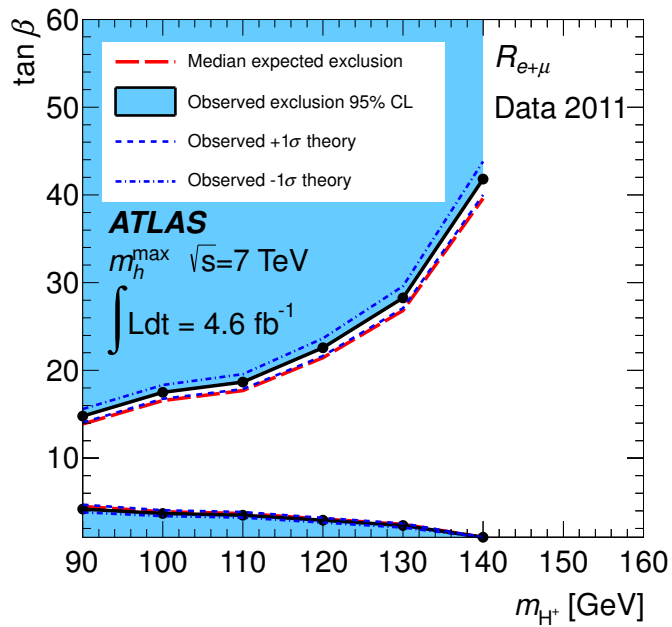


Figure 7.6: Limits for charged Higgs boson production from top quark decays in the $m_{H^+} - \tan \beta$ plane, derived using the ratio, $R_{e+\mu}$, in the context of the m_h^{\max} scenario of the MSSM, obtained for an integrated luminosity of 4.6 fb^{-1} . The 1σ band around the observed limit (blue dashed lines) shows the theoretical uncertainties. Values below $\tan \beta = 1$, where the calculations in the MSSM become non-perturbative, are not considered, as results become unphysical. [173]

m_{H^+} (GeV)	90	100	110	120	130	140	150	160
95 % C.L. observed								
(expected) limit on $\mathcal{B}(t \rightarrow bH^+)$ using the ratio $R_{e+\mu}$	3.3 % (3.1 %)	3.6 % (3.3 %)	3.2 % (3.0 %)	3.4 % (3.1 %)	3.6 % (3.3 %)	4.4 % (4.0 %)	7.3 % (6.7 %)	18.3 % (16.8 %)

Table 7.5: Observed (expected) 95 % C.L. upper limits on $\mathcal{B}(t \rightarrow bH^+)$ derived from the event yield ratio, $R_{e+\mu}$, as a function of the charged Higgs boson mass, obtained for an integrated luminosity of 4.6 fb^{-1} , assuming $\mathcal{B}(H^+ \rightarrow \tau\nu) = 100 \%$. [174]

ratio, $R_{e+\mu}$, is calculated. The results of this combination are summarised in Table 7.8 and illustrated in Figure 7.7.

With this new combination of the upper limits the charged Higgs bosons can be excluded for values of $\mathcal{B}(t \rightarrow bH^+)$ ranging from 0.8 % to 3.4 %, for m_{H^+} between 90 GeV and 160 GeV, assuming $\mathcal{B}(H^+ \rightarrow \tau\nu) = 100 \%$. In Figure 7.8, this combined limit on $\mathcal{B}(t \rightarrow bH^+) \times \mathcal{B}(H^+ \rightarrow \tau\nu)$ is interpreted in the context of the m_h^{\max} scenario of the MSSM and illustrated in the $m_{H^+} - \tan\beta$ plane.

Systematic uncertainty	Profiled value	Constraint
Integrated luminosity	0.001	1.000
Electron trigger efficiency	0.002	1.000
Electron reconstruction and ID efficiencies	0.007	1.000
Electron energy scale	0.001	1.000
Electron energy resolution	0.000	1.000
Muon trigger efficiency	0.000	1.000
Muon reconstruction and ID efficiencies	0.004	1.000
Muon momentum resolution (inner detector)	0.000	1.000
Muon momentum resolution (muon spectrometer)	0.000	1.000
Muon momentum scale	0.001	1.000
τ ID efficiency	0.003	0.998
τ energy scale	0.004	1.000
τ mis-ID (data-driven): number of associated tracks	0.001	1.000
τ mis-ID (data-driven): τ contamination	0.000	1.000
τ mis-ID (data-driven): H^+ signal contamination	0.001	1.000
τ mis-ID (data-driven): event environment	0.001	1.000
τ mis-ID (data-driven): statistical uncertainties	0.004	1.000
τ mis-ID (data-driven): electron veto uncertainties	0.001	1.000
b -tagging	0.061	0.998
Jet vertex fraction	-0.014	1.000
Jet energy resolution	0.000	1.000
Jet energy scale	0.001	0.995
Jet reconstruction efficiency	0.000	1.000
E_T^{miss} CellOut and SoftJets	0.001	1.000
E_T^{miss} pile-up contribution	0.001	1.000
$t\bar{t}$: cross-section	0.000	1.000
$t\bar{t}$: generator and parton shower	0.000	1.000
$t\bar{t}$: initial and final state radiation	0.000	1.000
Backgrounds with mis-identified leptons	0.003	0.999

Table 7.6: Profiled values and constraints on the systematic uncertainties from an unconditional fit of the combined model to data. The assumed charged Higgs boson mass is 130 GeV. In this table only “ID” stands shorthand for identification. [174]

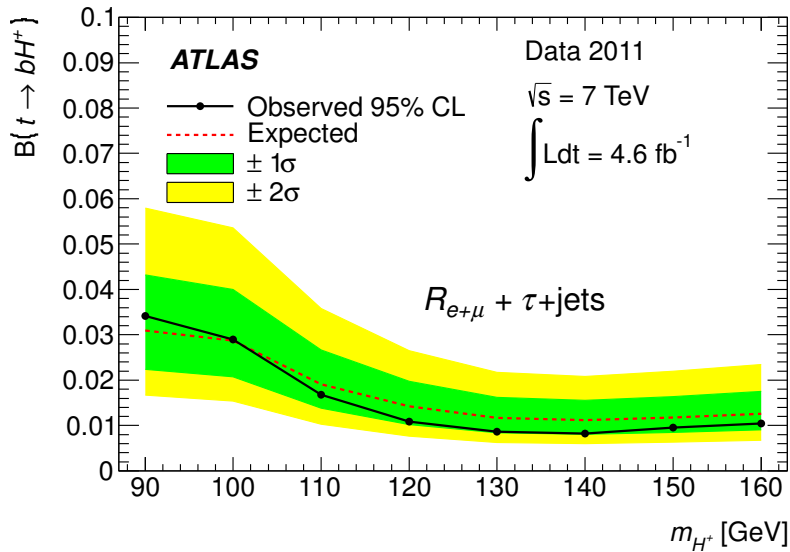


Figure 7.7: Upper limits on $\mathcal{B}(t \rightarrow bH^+)$ derived from the transverse mass distribution of $\tau_{\text{had}} + \text{jets}$ events in Section 6.5 and the event yield ratio, $R_{e+\mu}$, as a function of the charged Higgs boson mass, obtained for an integrated luminosity of 4.6 fb^{-1} and with the assumption $\mathcal{B}(H^+ \rightarrow \tau\nu) = 1$. The solid line in the figure is used to denote the observed 95 % C.L. upper limits, while the dashed line represents the expected exclusion limits. The green and yellow regions show the 1σ and 2σ error bands. [173]

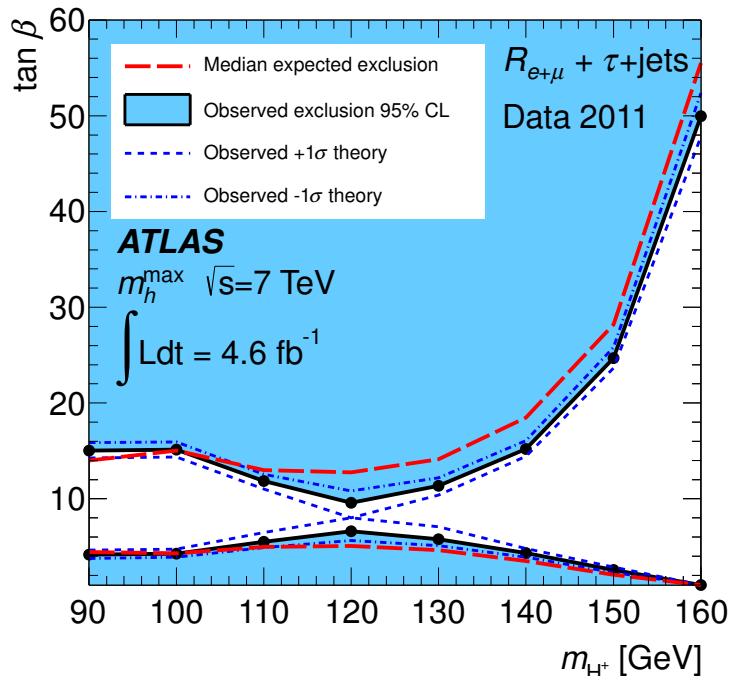


Figure 7.8: Limits for charged Higgs boson production from top quark decays in the m_{H^+} – $\tan\beta$ plane, derived using $\tau_{\text{had}} + \text{jets}$ events in Section 6.5 and the event yield ratio, $R_{e+\mu}$, in the context of the m_h^{max} scenario of the MSSM. The 1σ band around the observed limit (dashed lines) shows the theoretical uncertainties. Values below $\tan\beta = 1$, where the calculations in the MSSM become non-perturbative, are not considered, nor shown, as the results become unphysical. [173]

m_{H^+} (GeV)	90	100	110	120	130	140	150	160
95 % C.L. observed								
(expected) limit on	7.2 %	4.5 %	2.0 %	1.2 %	1.0 %	0.9 %	1.0 %	1.0 %
$\mathcal{B}(t \rightarrow bH^+)$ using	(5.3 %)	(4.6 %)	(2.5 %)	(1.9 %)	(1.5 %)	(1.3 %)	(1.3 %)	(1.3 %)
$\tau_{\text{had}} + \text{jets}$								

Table 7.7: Observed (expected) 95 % C.L. upper limits on $\mathcal{B}(t \rightarrow bH^+)$ derived from the m_T distribution of $\tau_{\text{had}} + \text{jets}$ events, described in Section 6.3, as a function of the charged Higgs boson mass, obtained for an integrated luminosity of 4.6 fb^{-1} and assuming $\mathcal{B}(H^+ \rightarrow \tau\nu) = 100 \%$. [172]

m_{H^+} (GeV)	90	100	110	120	130	140	150	160
95 % C.L. observed								
(expected) limit on	3.4 %	2.9 %	1.7 %	1.1 %	0.9 %	0.8 %	1.0 %	1.1 %
$\mathcal{B}(t \rightarrow bH^+)$ using	(3.1 %)	(2.8 %)	(1.9 %)	(1.4 %)	(1.2 %)	(1.1 %)	(1.2 %)	(1.2 %)
$R_{e+\mu}$ and $\tau_{\text{had}} + \text{jets}$								

Table 7.8: Observed (expected) 95 % C.L. upper limits on $\mathcal{B}(t \rightarrow bH^+)$ derived from the m_T distribution of $\tau_{\text{had}} + \text{jets}$ events, described in Section 6.3 and the event yield ratio, $R_{e+\mu}$, as a function of the charged Higgs boson mass, obtained for an integrated luminosity of 4.6 fb^{-1} and assuming that $\mathcal{B}(H^+ \rightarrow \tau\nu) = 100 \%$. [173]

Chapter 8

Comparison and Discussion of the Results

It was shown that in case of the $\tau_{\text{had}} + \text{lepton}$ channel the resulting limit was greatly improved by eliminating most of the systematic uncertainties. This was achieved by using the event yield ratio, $R_{e+\mu}$, as final discriminating variable, which intrinsically cancels the greatest contributing systematic uncertainties. These expressed as nuisance parameters have less space to be varied during limit setting, therefore the resulting limits are more stringent.

Direct searches similar to the ones described in the Chapter 6 were conducted by the CMS collaboration [299] at the LHC. The results are hardly comparable to the results presented in this work, as CMS has not yet analysed the full 2011 dataset in all charged Higgs boson searches. Only one analysis channel, the $\tau_{\text{had}} + \mu$, was updated with the full 2011 dataset of 4.9 fb^{-1} [300], which nevertheless yield a combined exclusion that, for charged Higgs masses below 110 GeV , are competitive with the ATLAS combined upper limits on $\mathcal{B}(t \rightarrow bH^+)$ obtained with the ratio-method analysis described in Chapter 7.

The direct comparison of the latest exclusion limits of both collaborations on $\mathcal{B}(t \rightarrow bH^+)$ is given in Figure 8.1. For a more complete comparison the limits obtained by the ATLAS direct searches, as described in Chapter 6, are also shown. The limits shown in Figure 8.1 are, for better comparison, transcribed and listed in Table 8.1.

For both experiments the most sensitive charged Higgs boson search channel proofs to be $\tau_{\text{had}} + \text{jets}$. It should be noted that CMS is able to achieve a similar sensitivity, considering the expected limits in the $\tau_{\text{had}} + \text{jets}$ channel, analysing merely half the integrated luminosity of data than ATLAS. Even though the ATLAS charged Higgs $\tau_{\text{had}} + \text{jets}$ analysis profits from lower $\tau + E_T^{\text{miss}}$ trigger thresholds than CMS and therefore should show a better sensitivity. To identify the sources for this not being the case is worth pursuing. The origins of the differing sensitivities of the $\tau_{\text{had}} + \text{jets}$ analyses of the two experiments shall be investigated in the following.

The most noteworthy difference is the assumed systematic uncertainties of the utilised data-driven multi-jet (QCD) background estimation techniques. While the ATLAS analysis relies on a template fit extracted from a control region, CMS utilises a p_T -binned factorisation technique, in detail discussed in Reference [301]. The E_T^{miss} shape fit, explained in Section 5.5.4, accounts

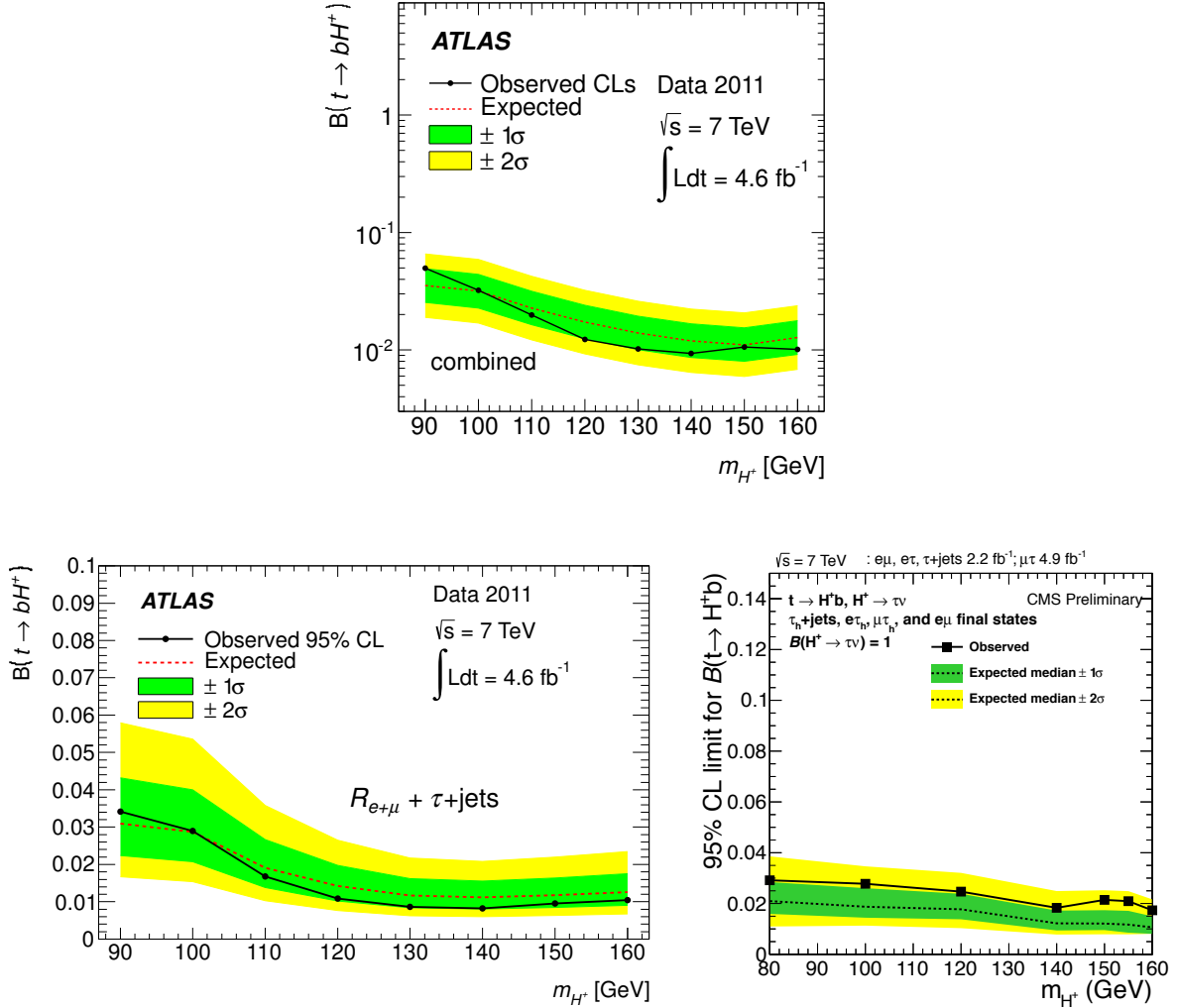


Figure 8.1: Top: For a better comparison the combined upper limits on $\mathcal{B}(t \rightarrow bH^+)$ of the direct searches as explained in Section 6.5 is given again. [172]

Left: Upper limits on $\mathcal{B}(t \rightarrow bH^+)$ derived from the transverse mass distribution of $\tau_{\text{had}} + \text{jets}$ events in Section 6.5 and the ratio-method event yield ratio, $R_{e+\mu}$, explained in Chapter 7, as a function of the charged Higgs boson mass, obtained for an integrated luminosity of 4.6 fb^{-1} and with the assumption $\mathcal{B}(H^+ \rightarrow \tau\nu) = 100\%$. The solid line in the figure is used to denote the observed 95 % C.L. upper limits, while the dashed line represents the expected exclusion limits. The green and yellow regions show the 1σ and 2σ error bands. [173]

Right: The combined limits with the results from the $e + \mu$, $e + \tau_{\text{had}}$, and $\tau_{\text{had}} + \text{jets}$ final states of the CMS collaboration are illustrated. [300]

for 32 % fit-related uncertainties and further 16 % uncertainty due to the E_T^{miss} -shape difference between control region and signal region. This shape fit method estimates $74 \pm 3 \pm 47$ multi-jet events, statistical and systematic uncertainties given in this respective order, while the CMS estimation yields $26 \pm 2 \pm 1$ QCD events [299]. It therefore seems that the CMS factorisation method, due to its relatively tiny systematic uncertainties, is superior to the here employed template shape fit method for estimation of the multi-jet background.

Further the embedding method, described in Section 5.5.3, utilised by both experiments for the estimation of backgrounds with correctly reconstructed τ leptons, again reveals differing systematic uncertainties estimated for the method. The τ embedding method estimates $210 \pm 10 \pm 44$ events with correctly reconstructed τ leptons, statistical and systematic uncertainties given in this respective order, and $78 \pm 3 \pm 11$ events, for ATLAS and CMS, respectively [172, 299].

An event selection specific difference is the $\Delta\phi(\tau, E_T^{\text{miss}}) < 160^\circ$ cut, which is applied as last step during the CMS event selection, and is not considered in the ATLAS search. This selection criterion is able to reduce the “multi-jets bump” in the m_T distribution, as can be evinced in Figure 8.2, and could thereby indeed significantly contribute to an improvement of the sensitivity, if utilising a shape aware limit setting procedure. It may therefore be a variable that the ATLAS analysis, in the $\tau_{\text{had}} + \text{jets}$ channel, could be studied and possibly also utilised to further improve the current results.

For better illustration proposes the physically more relevant $\mathcal{B}(t \rightarrow bH^+)$ limits are usually interpreted in the m_h^{max} scenario of the MSSM and presented in the $m_{H^+} - \tan\beta$ plane. A comparison in this manner of the ATLAS and CMS results is given in Figure 8.3. Note that unfortunately no such interpretation for the updated CMS results [300], therefore only the limits given in Reference [299] can be shown.

As almost the complete phase space of the m_h^{max} scenario is excluded by LHC results, new MSSM benchmark scenarios will need to be defined, for the presentation of results, in the near future. Potent candidates for successors are suggested for example in Reference [302]. The most important and universal results however will remain the limits set on $\mathcal{B}(t \rightarrow bH^+)$, as given in Table 8.1 and Figure 8.1, as these are interpretable in any thought of model and scenario.

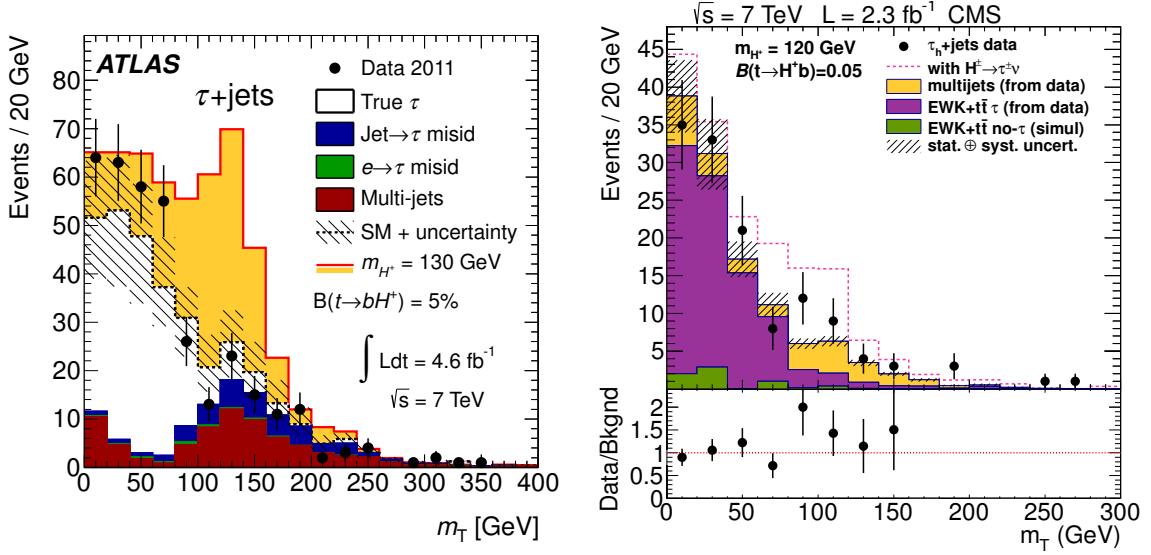


Figure 8.2: Left: Distribution of m_T after all selection cuts in the $\tau_{\text{had}} + \text{jets}$ channel. The dashed line corresponds to the SM-only hypothesis and the hatched area around it shows the total uncertainty for the SM backgrounds. The solid line shows the predicted contribution of signal+background in the presence of a charged Higgs boson with $m_{H^+} = 130$ GeV, assuming $\mathcal{B}(t \rightarrow bH^+) = 5\%$ and $\mathcal{B}(H^+ \rightarrow \tau\nu) = 100\%$. The contributions of $t\bar{t} \rightarrow b\bar{b}W^+W^-$ events in the backgrounds with mis-identified objects are scaled down accordingly. [172]

Right: The transverse mass of τ lepton and E_T^{miss} after full event selection for the $\tau_{\text{had}} + \text{jets}$ analysis. The expected event yield in the presence of the $t \rightarrow bH^+$, $H^+ \rightarrow \tau\nu$ decays is shown as the dashed line for $m_{H^+} = 120$ GeV and under the assumption that $\mathcal{B}(t \rightarrow bH^+) = 5\%$. The bottom panel shows the ratio of data over background along with the total uncertainties. The ratio is not shown for $m_T > 160$ GeV, where the expected total number of background events is 2.5 ± 0.3 while 5 events are observed. Statistical and systematic uncertainties are added in quadrature. [299]

m_{H^+} (GeV)	80	90	100	110	120	130	140	150	160
95 % CL observed									
(expected) limit	–	4.8 %	3.4 %	2.1 %	1.3 %	1.1 %	1.0 %	1.1 %	1.0 %
direct searches, Chapter 6	–	(4.2 %)	(3.5 %)	(2.5 %)	(1.9 %)	(1.5 %)	(1.3 %)	(1.2 %)	(1.3 %)
95 % CL observed									
(expected) limit	2.91 %	–	2.78 %	–	2.47 %	–	1.83 %	2.14 %	1.73 %
CMS direct searches, Reference [300]	(2.09) %	–	(1.87 %)	–	(1.77 %)	–	(1.22 %)	(1.21 %)	(1.06 %)
95 % CL observed									
(expected) limit on $\mathcal{B}(t \rightarrow bH^+)$ using $R_{e+\mu}$ and $\tau_{\text{had}+\text{jets}}$	–	3.4 %	2.9 %	1.7 %	1.1 %	0.9 %	0.8 %	1.0 %	1.1 %

Table 8.1: Observed (expected) 95 % CL upper limits on $\mathcal{B}(t \rightarrow bH^+)$ derived using $\tau_{\text{had}+\text{jets}}$ events and the ratio-method, explained in Chapter 7, event yield ratio $R_{e+\mu}$, as a function of the charged Higgs boson mass, obtained for an integrated luminosity of 4.6 fb^{-1} and assuming that $\mathcal{B}(H^+ \rightarrow \tau\nu) = 100 \%$. The combined exclusion limits resulting from the direct searches, presented in Chapter 6, the ratio-method event yield ratio, as described in Chapter 7 and the updated CMS results are given for a complete comparison. The “–” denotes charged Higgs boson mass points not available in the ATLAS or CMS results. [172, 173, 300]

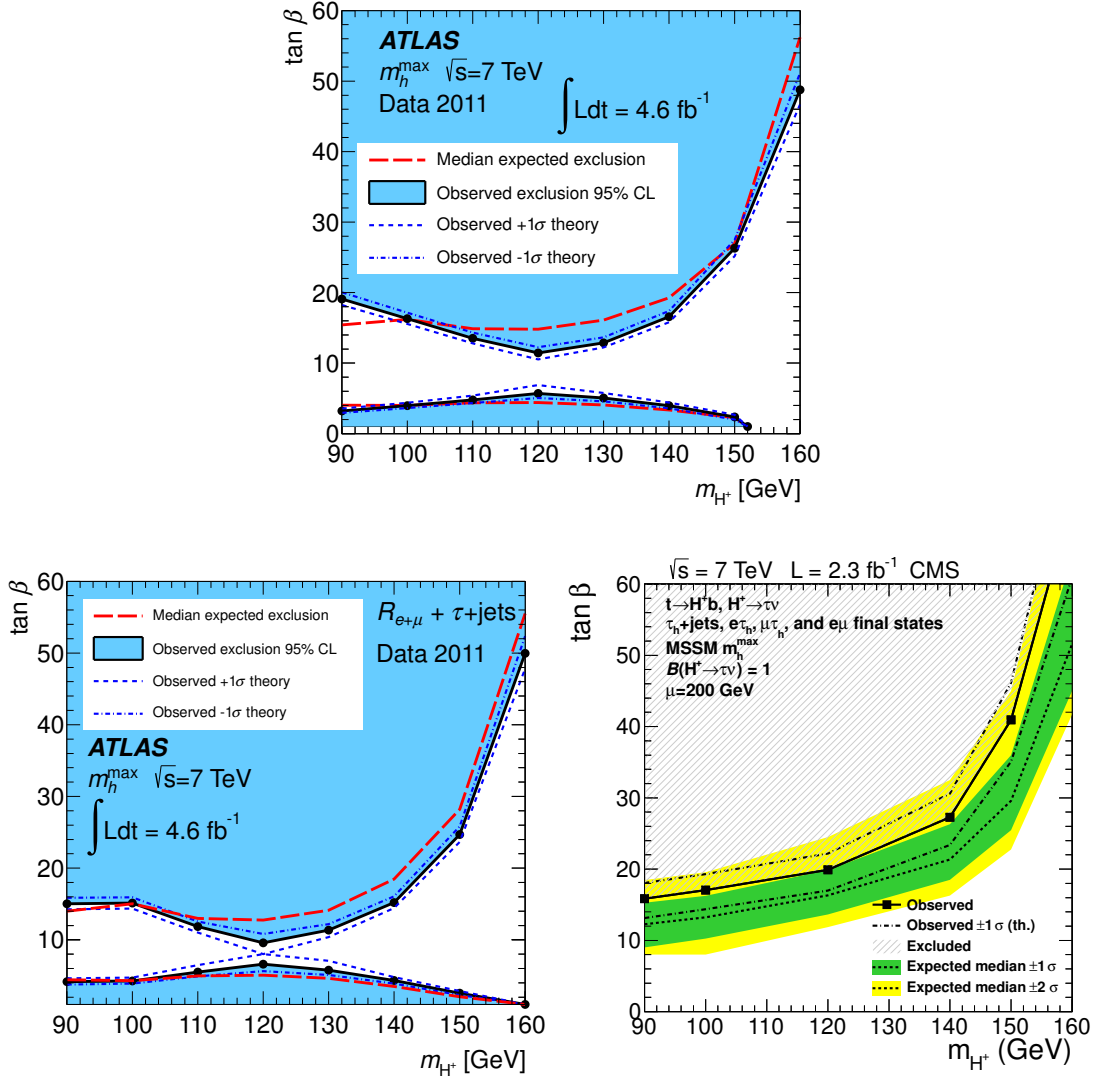


Figure 8.3: Top: For a better comparison the combined upper limits on $\mathcal{B}(t \rightarrow bH^+)$ of the direct searches, as explained in Section 6.5 is shown in the $m_{H^+} - \tan \beta$ plane. [172]

Left: Limits for charged Higgs boson production from top quark decays in the $m_{H^+} - \tan \beta$ plane, derived using the combined $\tau_{\text{had}} + \text{jets}$ analysis and the ratio-method, explained in Chapter 7, event yield ratio, $R_{e+\mu}$, results, in the context of the m_h^{\max} scenario of the MSSM. The $\pm 1\sigma$ band around the observed limit (dashed lines) shows the theoretical uncertainties. Values below $\tan \beta = 1$, where the calculations in the MSSM become non-perturbative, are not considered, nor shown, as the results become unphysical. [173]

Right: The exclusion region in the MSSM $m_{H^+} - \tan \beta$ parameter space obtained from the combined analysis for the MSSM m_h^{\max} scenario. The $\pm 1\sigma$ and $\pm 2\sigma$ bands around the expected limit are also shown. [299]

Chapter 9

Summary and Outlook

The observation of a charged Higgs boson would be an evidence for physics beyond the Standard Model. The measured branching ratio limits, $\mathcal{B}(t \rightarrow bH^+)$, obtained by the searches described in this work, are a very important source of knowledge and a valuable input for the discrimination of possible Standard Model extensions.

In this work the searches for light charged Higgs bosons with 4.6 fb^{-1} of data taken in 2011 at $\sqrt{s} = 7 \text{ TeV}$ by the ATLAS detector at the LHC were conducted. Direct searches [172] as well as an improved analysis of the $\tau_{\text{had}} + \text{lepton}$ channel based upon the measurement of possible violation of the lepton universality in $t\bar{t}$ events, the ratio-method [173] were performed. Charged Higgs bosons with τ leptons in the final state were in the focus of this thesis. The exclusion limits obtained on $\mathcal{B}(t \rightarrow bH^+)$ pose an improvement by over one order of magnitude compared to previous results, as for example by the LEP [118, 303] and Tevatron [124, 125] experiments.

The basis of this work was laid by the determination of the τ lepton mis-identification probability from electrons. It was the first time this measurement was performed in the ATLAS collaboration. A $Z \rightarrow ee$ tag-and-probe method was designed and implemented in order to achieve the task. This measurement utilised the first 37 pb^{-1} of pp collision data recorded at $\sqrt{s} = 7 \text{ TeV}$ in 2010 [151]. Its achievement was the determination of the mis-identification probabilities and scale factors as well as their systematic and statistical uncertainties, necessary for MC simulation to better reproduce data and therefore crucial to all analyses employing electron veto algorithms.

Based on the measured mis-identification probabilities a data-driven estimation method for the charged Higgs boson search was developed and implemented for the background contribution stemming from electrons mis-identified as hadronically decaying τ leptons [159].

New $\tau_{\text{had}} + E_{\text{T}}^{\text{miss}}$ trigger menu items were designed for the charged Higgs boson search. It was important to balance stable and sustainable rates, restricted by the readout bandwidth and based on predictions of the instantaneous luminosities for the 2012 data taking on the one hand with the goal to achieve highest efficiencies on the other. Special trigger items were designed for the $\tau + \text{jets}$ channel, the most sensitive charged Higgs boson search channel, and included

into the 2012 trigger menu of ATLAS after thorough validation.

An event selection optimisation was performed for the τ +lepton channel of the charged Higgs boson search, which helped to reduce all backgrounds, except for the kinematically indistinguishable $t\bar{t} \rightarrow b\bar{b}W^+W^-$ events. The remaining background contributions were successfully estimated with data-driven techniques.

The comparison of the three direct searches combined results and the ratio-method re-analysis of the $\tau_{\text{had}}+\text{lepton}$ channel combined with the $\tau_{\text{had}}+\text{jets}$ result, clearly indicates the future path of the light charged Higgs search with τ leptons in the final state. It is noteworthy to mention that these two analyses perfectly complement each other. The ratio-method is very efficient for lower charged Higgs masses, close to the W^\pm boson mass, whereas the direct $\tau+\text{jets}$ channel shows a great sensitivity for the higher mass regions close to the top quark mass. Utilising these two channels only, with hadronically decaying τ leptons in the final state, improved limits on $\mathcal{B}(t \rightarrow bH^+)$ were set. The two analyses could, with only minor adjustments, be applied on data taken in 2012 with $\sqrt{s} = 8$ TeV. Given that approximately four times the integrated luminosity of data taken 2011 were recorded in 2012, the limits on $\mathcal{B}(t \rightarrow bH^+)$ can be improved further. The gap in the $m_{H^+} - \tan\beta$ plane as can be seen in Figure 7.8, for the interpretation of the results in the m_h^{max} -scenario, would then most probably close. The most important, universal results however are the limits set on $\mathcal{B}(t \rightarrow bH^+)$, as these are interpretable in any thought of model and scenario.

With the amount of data collected in 2012 the gate opened for analyses searching for heavy charged Higgs bosons, $m_{H^\pm} > m_t$. The production cross section is strongly dependent on its mass, as discussed in Chapter 2. Here two decay channels are currently under investigation by ATLAS, $H^+ \rightarrow t\bar{b}$ [65] as the dominant contribution for the heavy H^\pm , and $H^+ \rightarrow \tau\nu$, with a branching ratio very sensitive to $\tan\beta$. A modified ratio-method could be utilised for the heavy charged Higgs boson search with a τ lepton in the final state.

Appendices

Appendix A

Monte Carlo Simulation Samples

A.1 Monte Carlo Simulation Samples for 2010 Analyses

A.1.1 Monte Carlo Simulation Samples for the Electron to τ Lepton Mis-identification Analysis

Sample	MC ID	Simulation and Reconstruction Tag	Generated Events	Cross Section [pb]	Generator Filter Efficiency
$Z \rightarrow ee$	106046	e574 s933 s946 r1831 r1700	4.695·10 ⁶	990	1
$\gamma^* \rightarrow ee$	108320	e574 s933 s946 r1831 r1700	995 854	1 296	1
$Z \rightarrow \tau\tau$	106052	e574 s934 s946 r1833 r1700	1.997·10 ⁶	990	1
$W \rightarrow e \nu$	106043	e574 s933 s946 r1831 r1700	6.98·10 ⁶	10 460	1
$W \rightarrow \tau\nu$	107054	e574 s934 s946 r1833 r1700	2.004·10 ⁶	10 460	1
J0	105009	e574 s934 s946 r1833 r1700	1.373·10 ⁶	9.9·10 ⁹	1
J1 electron-filtered	109271	e600 s934 s946 r1833 r1700	997 743	6.8·10 ⁸	1.2039·10 ⁻³
J2 electron-filtered	109272	e574 s934 s946 r1833 r1700	376 846	4.1·10 ⁷	5.9151·10 ⁻³
J3 electron-filtered	109273	e574 s934 s946 r1833 r1700	498 743	2.2·10 ⁶	1.5915·10 ⁻²
J4	105013	e574 s934 s946 r1833 r1700	2.8·10 ⁶	8.8·10 ⁴	1
J5	105014	e574 s934 s946 r1833 r1700	1.4·10 ⁶	2.3·10 ³	1

Table A.1: The $\sqrt{s} = 7$ TeV MC10-tune Monte Carlo samples used in the electron to τ mis-identification analysis. [152]

A.1.2 Monte Carlo Simulation Samples for the H^\pm Analysis

Table A.2: Table of Monte Carlo samples used for 2010 H^\pm analysis. (*) denotes that a k -factor is multiplied with the cross section of the ALPGEN samples in order to scale to the calculated NLO cross sections. [159, 160]

Sample	Generator	MC ID	Reconstruction Tag	Number of events	Cross-section [pb] ^(*)
$t\bar{t}$ (with $\geq 1\ell$, $\ell = e, \mu, \tau$)	MC@NLO & JIMMY	105200	e598 s933 s946 r1831 r1700 p406	997 333	89.7
Single top quark t -channel (with e)	MC@NLO & JIMMY	108340	e598 s933 s946 r1831 r1700 p406	199 935	7.152
Single top quark t -channel (with μ)	MC@NLO & JIMMY	108341	e598 s933 s946 r1831 r1700 p406	199 922	7.176
Single top quark t -channel (with τ)	MC@NLO & JIMMY	108342	e598 s933 s946 r1831 r1700 p406	197 921	7.128
Single top quark s -channel (with e)	MC@NLO & JIMMY	108343	e598 s933 s946 r1831 r1700 p406	8 995	0.4685
Single top quark s -channel (with μ)	MC@NLO & JIMMY	108344	e598 s933 s946 r1831 r1700 p406	9 991	0.4684
Single top quark s -channel (with τ)	MC@NLO & JIMMY	108345	e598 s933 s946 r1831 r1700 p406	9 997	0.4700
Single top quark Wt (inclusive)	MC@NLO & JIMMY	108346	e598 s933 s946 r1831 r1700 p406	299 794	14.581
$W \rightarrow ev$ (Np0)	ALPGEN & JIMMY	107680	e600 s933 s946 r1831 r1700 p406	1 382 306	6 913 * 1.20
$W \rightarrow ev$ (Np1)	ALPGEN & JIMMY	107681	e600 s933 s946 r1831 r1700 p406	641 361	1 293 * 1.20
$W \rightarrow ev$ (Np2)	ALPGEN & JIMMY	107682	e600 s933 s946 r1831 r1700 p406	750 788	377 * 1.20
$W \rightarrow ev$ (Np3)	ALPGEN & JIMMY	107683	e600 s933 s946 r1831 r1700 p406	199 928	101 * 1.20
$W \rightarrow ev$ (Np4)	ALPGEN & JIMMY	107684	e600 s933 s946 r1831 r1700 p406	51 963	25.3 * 1.20
$W \rightarrow ev$ (Np5)	ALPGEN & JIMMY	107685	e600 s933 s946 r1831 r1700 p406	13 933	6.9 * 1.20
$W \rightarrow \mu\nu$ (Np0)	ALPGEN & JIMMY	107690	e600 s933 s946 r1831 r1700 p406	1 374 816	6 935 * 1.20
$W \rightarrow \mu\nu$ (Np1)	ALPGEN & JIMMY	107691	e600 s933 s946 r1831 r1700 p406	640 867	1 281 * 1.20
$W \rightarrow \mu\nu$ (Np2)	ALPGEN & JIMMY	107692	e600 s933 s946 r1831 r1700 p406	751 718	375 * 1.20
$W \rightarrow \mu\nu$ (Np3)	ALPGEN & JIMMY	107693	e600 s933 s946 r1831 r1700 p406	203 910	101 * 1.20
$W \rightarrow \mu\nu$ (Np4)	ALPGEN & JIMMY	107694	e600 s933 s946 r1831 r1700 p406	51 969	25.7 * 1.20

Continued on next page

Table A.2 – continued from previous page

Sample	Generator	MC ID	Reconstruction Tag	Number of events	Cross-section [pb] ^(*)
$W \rightarrow \mu\nu$ (Np5)	ALPGEN & JIMMY	107695	e600 s933 s946 r1831 r1700 p406	13 994	7.0 * 1.20
$W \rightarrow \tau\nu$ (Np0)	ALPGEN & JIMMY	107700	e600 s933 s946 r1831 r1700 p406	3 389 440	6 836 * 1.20
$W \rightarrow \tau\nu$ (Np1)	ALPGEN & JIMMY	107701	e600 s933 s946 r1831 r1700 p406	638 809	1 277 * 1.20
$W \rightarrow \tau\nu$ (Np2)	ALPGEN & JIMMY	107702	e600 s933 s946 r1831 r1700 p406	188 443	377 * 1.20
$W \rightarrow \tau\nu$ (Np3)	ALPGEN & JIMMY	107703	e600 s933 s946 r1831 r1700 p406	201 912	101 * 1.20
$W \rightarrow \tau\nu$ (Np4)	ALPGEN & JIMMY	107704	e600 s933 s946 r1831 r1700 p406	51 969	25.7 * 1.20
$W \rightarrow \tau\nu$ (Np5)	ALPGEN & JIMMY	107705	e600 s933 s946 r1831 r1700 p406	3 996	7.0 * 1.20
$Z \rightarrow ee$ (Np0)	ALPGEN & JIMMY	107650	e600 s933 s946 r1831 r1700 p406	303 405	661.9 * 1.25
$Z \rightarrow ee$ (Np1)	ALPGEN & JIMMY	107651	e600 s933 s946 r1831 r1700 p406	63 484	133.3 * 1.25
$Z \rightarrow ee$ (Np2)	ALPGEN & JIMMY	107652	e600 s933 s946 r1831 r1700 p406	19 496	40.3 * 1.25
$Z \rightarrow ee$ (Np3)	ALPGEN & JIMMY	107653	e600 s933 s946 r1831 r1700 p406	5 500	11.2 * 1.25
$Z \rightarrow ee$ (Np4)	ALPGEN & JIMMY	107654	e600 s933 s946 r1831 r1700 p406	1 500	2.7 * 1.25
$Z \rightarrow ee$ (Np5)	ALPGEN & JIMMY	107655	e600 s933 s946 r1831 r1700 p406	500	0.8 * 1.25
$Z \rightarrow \mu\mu$ (Np0)	ALPGEN & JIMMY	107660	e600 s933 s946 r1831 r1700 p406	302 958	657.7 * 1.25
$Z \rightarrow \mu\mu$ (Np1)	ALPGEN & JIMMY	107661	e600 s933 s946 r1831 r1700 p406	62 981	132.8 * 1.25
$Z \rightarrow \mu\mu$ (Np2)	ALPGEN & JIMMY	107662	e600 s933 s946 r1831 r1700 p406	18 993	39.6 * 1.25
$Z \rightarrow \mu\mu$ (Np3)	ALPGEN & JIMMY	107663	e600 s933 s946 r1831 r1700 p406	5 497	11.1 * 1.25
$Z \rightarrow \mu\mu$ (Np4)	ALPGEN & JIMMY	107664	e600 s933 s946 r1831 r1700 p406	1 499	2.8 * 1.25
$Z \rightarrow \mu\mu$ (Np5)	ALPGEN & JIMMY	107665	e600 s933 s946 r1831 r1700 p406	500	0.8 * 1.25
$Z \rightarrow \tau\tau$ (Np0)	ALPGEN & JIMMY	107670	e600 s933 s946 r1831 r1700 p406	303 448	657.4 * 1.25

Continued on next page

Table A.2 – continued from previous page

Sample	Generator	MC ID	Reconstruction Tag	Number of events	Cross-section [pb] ^(*)
$Z \rightarrow \tau\tau$ (Np1)	ALPGEN & JIMMY	107671	e600 s933 s946 r1831 r1700 p406	63 483	133.0 * 1.25
$Z \rightarrow \tau\tau$ (Np2)	ALPGEN & JIMMY	107672	e600 s933 s946 r1831 r1700 p406	19 493	40.4 * 1.25
$Z \rightarrow \tau\tau$ (Np3)	ALPGEN & JIMMY	107673	e600 s933 s946 r1831 r1700 p406	5 496	11.0 * 1.25
$Z \rightarrow \tau\tau$ (Np4)	ALPGEN & JIMMY	107674	e600 s933 s946 r1831 r1700 p406	1 500	2.9 * 1.25
$Z \rightarrow \tau\tau$ (Np5)	ALPGEN & JIMMY	107675	e600 s933 s946 r1831 r1700 p406	500	0.7 * 1.25
J1 di-jet	PyTHIA	105010	e574 s934 s946 r1833 r1700 p406	7 384 565	$678 \cdot 10^9$
J2 di-jet	PyTHIA	105011	e574 s934 s946 r1833 r1700 p406	2 795 084	$41 \cdot 10^9$
J3 di-jet	PyTHIA	105012	e574 s934 s946 r1833 r1700 p406	2 792 379	$2.19 \cdot 10^9$
J4 di-jet	PyTHIA	105013	e574 s934 s946 r1833 r1700 p406	2 786 179	$8.77 \cdot 10^7$
JF17 (with jet filter)	PyTHIA	105802	e577 s933 s946 r1831 r1700 p406	39 692 090	$8.4878 \cdot 10^7$
J0 di-jet (with μ)	PyTHIA	109276	e574 s933 s946 r1831 r1700 p406	966 841	$7.821 \cdot 10^8$
J1 di-jet (with μ)	PyTHIA	109277	e574 s933 s946 r1831 r1700 p406	996 800	$8.16 \cdot 10^8$
J2 di-jet (with μ)	PyTHIA	109278	e574 s933 s946 r1831 r1700 p406	479 857	$5.4 \cdot 10^7$
J3 di-jet (with μ)	PyTHIA	109279	e574 s933 s946 r1831 r1700 p406	498 805	$1.3 \cdot 10^7$
J4 di-jet (with μ)	PyTHIA	109280	e574 s933 s946 r1831 r1700 p406	498 536	$1.936 \cdot 10^6$
B bbm15X	PyTHIA	108405	e574 s933 s946 r1831 r1700 p406	4 473 784	$7.39 \cdot 10^4$
B ccmu15X	PyTHIA	106059	e574 s933 s946 r1831 r1700 p406	1 498 247	$2.84 \cdot 10^4$

A.2 Monte Carlo Simulation Samples for 2011 Analyses

A.2.1 Monte Carlo Samples for H^\pm Ratio-Method Search Analysis

Process	Generator	Sample label(s)	Cross section (pb)
$t\bar{t}$ with at least one lepton ℓ	MC@NLO	105200	90.6
Single top quark t -channel (with ℓ)	ACERMC	117360–2	20.9
Single top quark s -channel (with ℓ)	MC@NLO	108343–5	1.5
Single top quark Wt (inclusive)	MC@NLO	108346	15.7
$W \rightarrow \ell\nu$	ALPGEN	107680–5 ($e\nu$)	
		107690–5 ($\mu\nu$)	3.1×10^4
		107700–5 ($\tau\nu$)	
$W + b\bar{b}$	ALPGEN	107280–3	1.3×10^2
$W(\ell\nu) + c\bar{c}$	ALPGEN	117284–7	3.6×10^2
$W + c$	ALPGEN	117293–7	1.1×10^3
$Z/\gamma^* \rightarrow \ell\ell, m(\ell\ell) > 10 \text{ GeV}$	ALPGEN	107650–5 + 116250–5 (ee)	
		107660–5 + 116260–5 ($\mu\mu$)	1.5×10^4
		107670–5 + 116270–5 ($\tau\tau$)	
		109300–3 (ee)	
$Z/\gamma^*(\ell\ell) + b\bar{b}, m(\ell\ell) > 30 \text{ GeV}$	ALPGEN	109305–8 ($\mu\mu$)	38.7
		109310–3 ($\tau\tau$)	
WW	HERWIG	105985	17.0
ZZ	HERWIG	105986	1.3
WZ	HERWIG	105987	5.5

Table A.3: Cross sections and dataset ID numbers for the main SM Monte Carlo samples. In this table, ℓ refers to the three lepton families e, μ and τ . [174]

m_{H^+} (GeV)	Sample label		
	$t\bar{t} \rightarrow b\bar{b}H^+W^-$	$t\bar{t} \rightarrow b\bar{b}H^-W^+$	$t\bar{t} \rightarrow b\bar{b}H^+H^-$
90	116970	128120	116980
100	116971	128121	116981
110	116972	128122	116982
120	116973	128123	116983
130	116974	109851	116984
140	116975	128125	116985
150	116976	109850	116986
160	116977	128127	116987

Table A.4: ATLAS simulation dataset ID numbers for the charged Higgs boson Monte Carlo samples.

List of Figures

2.1	Running of the strong gauge coupling	5
2.2	Higgs potential $V(\Phi)$	10
2.3	SM processes production cross-sections	12
2.4	SM Higgs boson branching ratios	15
2.5	Running of gauge couplings in SM and MSSM	18
2.6	Higgs mass one-loop quantum corrections	20
2.7	Feynman diagrams for charged Higgs boson production at the LHC	23
2.8	Production cross-section for the charged Higgs boson	23
2.9	Branching ratios of the charged Higgs boson	24
2.10	LEP charged Higgs $\mathcal{B}(H^+ \rightarrow \tau^+ \nu)$ limits	25
2.11	LEP charged Higgs production cross-section limits	26
2.12	CDF limits in the $m_{H^+} - \tan\beta$ plane	27
2.13	DØ upper limits on $\mathcal{B}(t \rightarrow H^+ b)$	27
2.14	CDF and ATLAS upper limits on $\mathcal{B}(t \rightarrow H^+ b)$ with $\mathcal{B}(H^+ \rightarrow c\bar{s})$	28
2.15	Penguin diagrams contributing to $b \rightarrow s\gamma$	29
2.16	BABAR $B \rightarrow D^{(*)}\tau\nu$ comparison of results and charged Higgs boson of type-II 2HDM predictions	30
2.17	Disagreement between BABAR measurement and charged Higgs boson of type-II 2HDM predictions	30
3.1	Flow chart of ATLAS simulation software	33
3.2	Pile-up in 2011 pp collision data in ATLAS	39
4.1	CERN accelerator complex	42
4.2	LHC and its pre-accelerator system, unscaled	42
4.3	LHC and its experiments	43
4.4	Cut-away view of the ATLAS detector, showing all subsystems	44
4.5	Layers of the ATLAS detector	44
4.6	Pseudorapidity, η , as a function of the polar angle, θ	45
4.7	Layout of the magnet system	46
4.8	Barrel and one end-cap toroid	46

4.9	Inner detector overview	47
4.10	Inner detector barrel detailed view	48
4.11	Inner detector setup	49
4.12	Calorimeter systems overview	51
4.13	Layers, cells and spacial dimensions of the electromagnetic calorimeter	51
4.14	Material of and in front of the electromagnetic calorimeter	53
4.15	ECAL ϕ non-uniformity	54
4.16	Electronic noise of EM calorimeter	55
4.17	Sampling and constant noise of EM calorimeter	56
4.18	Segmentation of the hadronic tile calorimeter	57
4.19	Schematic view of a hadronic calorimeter module	58
4.20	Cut-away view of the three end-cap calorimeters	58
4.21	Cumulative amount of material in λ	59
4.22	Forward calorimeter electrode structure	59
4.23	Muon spectrometer	60
4.24	Barrel muon a a cross-section view	61
4.25	cross-section view of the muon system in the bending plane	61
4.26	Position of the forward detectors	62
4.27	Block diagram of trigger and data acquisition systems	64
4.28	Architecture of the L1 calorimeter trigger	65
4.29	Block diagram of the L1 trigger	65
4.30	Trigger rates of ATLAS in 2011	66
4.31	LHC total integrated luminosity	68
4.32	LHC peak instantaneous luminosity	69
4.33	Peak interactions as a function of time	69
5.1	Example for leading-order Feynman diagram for light charged Higgs production	73
5.2	Pie chart of τ lepton decay modes	74
5.3	E_T^{miss} for different light charged Higgs signal masses	75
5.4	Trigger turn on curves	76
5.5	$\sum E_T$ distribution for the $\tau_{\text{had}} + \text{leptons}$ analysis	81
5.6	E_T^{miss} distribution for the $\tau_{\text{had}} + \text{leptons}$ analysis	81
5.7	Variables of τ lepton cut-based electron veto algorithm	85
5.8	Probe p_T and tag-and-probe pair invariant mass distribution	86
5.9	Electron to τ lepton mis-identification probabilities as a function of p_T^τ and $ \eta $	88
5.10	Mis-identification probability as a function of the number of primary vertices	89
5.11	m_T distribution for events fulfilling $W + >2$ jets selection	91
5.12	Light quark jet to τ lepton mis-identification probabilities as function of p_T^τ and $N_{\text{track}}^{\text{iso}}$	91

5.13	m_T distribution embedding method and MC simulation	92
5.14	E_T^{miss} distributions in control region and template fit in signal region	93
6.1	E_T^{miss} distributions of $\tau_{\text{had}} + \text{lepton}$ analysis	96
6.2	Distribution of $\cos \theta_\ell^*$ and m_T^H of $\tau_{\text{lep}} + \text{jets}$ analysis	99
6.3	m_T distribution of $\tau_{\text{had}} + \text{jets}$ analysis	102
6.4	Upper limits on $\mathcal{B}(t \rightarrow bH^+)$ of direct searches and combination	109
6.5	Combined upper limits in $m_{H^+} - \tan\beta$ plane of direct searches	110
7.1	Event yield ratios as function of charged Higgs mass	112
7.2	Distribution of m_{T2}^H in signal region enriched in OS–SS $t\bar{t}$ events	116
7.3	Upper limits on $\mathcal{B}(t \rightarrow bH^+)$ derived from the m_{T2}^H distributions	121
7.4	Upper limits on $\mathcal{B}(t \rightarrow bH^+)$ derived from the event yield ratios R_e and R_μ	123
7.5	Upper limits on $\mathcal{B}(t \rightarrow bH^+)$ derived from the event yield ratio, $R_{e+\mu}$	124
7.6	Limits for charged Higgs boson production from top quark decays in the $m_{H^+} - \tan\beta$ plane, derived using the ratio, $R_{e+\mu}$	125
7.7	Combined upper limits on $\mathcal{B}(t \rightarrow bH^+)$ of ratio-method and $\tau_{\text{had}} + \text{jets}$ analysis	128
7.8	Combined upper limits in $m_{H^+} - \tan\beta$ plane of ratio-method and $\tau_{\text{had}} + \text{jets}$ analysis results	129
8.1	Combined upper limits on $\mathcal{B}(t \rightarrow bH^+)$ of the ATLAS direct searches, ratio-method analyses and CMS combined upper limits	132
8.2	m_T distributions of ATLAS and CMS $\tau_{\text{had}} + \text{jets}$ analyses	134
8.3	Comparison of upper limits on $\mathcal{B}(t \rightarrow bH^+)$ ATLAS direct searches, ratio-method analyses and the CMS results in the $m_{H^+} - \tan\beta$ plane	136

List of Tables

2.1	Fermions ordered in electroweak multiplets, with quantum numbers	4
2.2	Gauge bosons of Standard Model	4
2.3	Fermions of Standard Model	6
2.4	MSSM super-multiplets	14
2.5	Particles of the MSSM	16
3.1	Table of Monte Carlo samples used for 2010 H^\pm analyses	36
3.2	Table of Monte Carlo samples used for 2011 H^\pm direct search analyses	38
4.1	Granularity of the electromagnetic calorimeter	52
4.2	Constant noise of EM calorimeter derived from collision data	56
4.3	Data Periods 2010	70
4.4	Data Periods 2011	71
5.1	Signal selection efficiency for the $\tau_{\text{had}} + \text{lepton}$ charged Higgs boson analysis	82
6.1	Expected event yields $\tau_{\text{had}} + \text{lepton}$ analysis	97
6.2	Expected event yields $\tau_{\text{lep}} + \text{jets}$ analysis	100
6.3	Expected event yields $\tau_{\text{had}} + \text{jets}$ analysis	101
6.4	Detector-related systematic uncertainties	104
6.5	Systematic uncertainties from modelling of $t\bar{t}$ events	105
6.6	Dominant systematic uncertainties on data-driven background estimates	106
7.1	Variation with m_{H^\pm} of the slopes relative increase of the ratios R_e and R_μ with $\mathcal{B}(t \rightarrow bH^\pm)$	113
7.2	Expected OS–SS event yields $\tau_{\text{had}} + \text{lepton}$ and dilepton channels	117
7.3	Predicted and measured event yield ratios R_e and R_μ	117
7.4	Effect of systematic uncertainties on event yield ratios R_e and R_μ	120
7.5	Observed and expected 95 % C.L. upper limits on $\mathcal{B}(t \rightarrow bH^\pm)$ derived from the event yield ratio, $R_{e+\mu}$	126
7.6	Profiled values and constraints on the systematic uncertainties from unconditional fit	127

7.7	Observed (expected) 95 % C.L. upper limits on $\mathcal{B}(t \rightarrow bH^+)$ derived from the m_T distribution of $\tau_{\text{had}} + \text{jets}$ events	130
7.8	Observed and expected 95 % C.L. upper limits on $\mathcal{B}(t \rightarrow bH^+)$ derived from the m_T distribution of $\tau_{\text{had}} + \text{jets}$ events and the event yield ratio, $R_{e+\mu}$	130
8.1	Comparison of upper limits on $\mathcal{B}(t \rightarrow bH^+)$ ATLAS and CMS	135
A.1	List of Monte Carlo samples used for 2010 the electron to τ mis-identification analysis	142
A.2	List of Monte Carlo samples used for 2010 H^\pm analysis	144
A.3	List of Monte Carlo samples used for 2011 H^\pm Ratio-Method search analysis	147
A.4	Charged Higgs boson Monte Carlo sample IDs	148

Bibliography

- [1] A. Einstein, *On the Method of Theoretical Physics*, *Philosophy of Science* **1** (1934) no. 2, 163–169.
- [2] S. L. Glashow, *Partial Symmetries of Weak Interactions*, *Nucl. Phys.* **22** (1961) 579–588.
- [3] A. Salam, *Weak and Electromagnetic Interactions*, Conf. Proc. **C680519** (1968) 367–377.
- [4] S. Weinberg, *A Model of Leptons*, *Phys. Rev. Lett.* **19** (1967) 1264–1266.
- [5] M. Bustamante, L. Cieri, and J. Ellis, *Beyond the Standard Model for Montaneros*, [arXiv:0911.4409 \[hep-ph\]](https://arxiv.org/abs/0911.4409).
- [6] E. Accomando, A. Akeroyd, E. Akhmetzyanova, J. Albert, A. Alves, et al., *Workshop on CP Studies and Non-Standard Higgs Physics*, [arXiv:hep-ph/0608079 \[hep-ph\]](https://arxiv.org/abs/hep-ph/0608079).
- [7] Y. Gol’fand and E. Likhtman, *Extension of the Algebra of Poincare Group Generators and Violation of P invariance*, *JETP Lett.* **13** (1971) 323–326.
- [8] J. Wess and B. Zumino, *Supergauge Transformations in Four-Dimensions*, *Nucl. Phys.* **B70** (1974) 39–50.
- [9] P. Fayet, *Supersymmetry and Weak, Electromagnetic and Strong Interactions*, *Phys. Lett.* **B64** (1976) 159.
- [10] P. Fayet, *Spontaneously Broken Supersymmetric Theories of Weak, Electromagnetic and Strong Interactions*, *Phys. Lett.* **B69** (1977) 489.
- [11] H. P. Nilles, *Supersymmetry, Supergravity and Particle Physics*, *Phys. Rept.* **110** (1984) 1–162.
- [12] H. E. Haber and G. L. Kane, *The Search for Supersymmetry: Probing Physics Beyond the Standard Model*, *Phys. Rept.* **117** (1985) 75–263.
- [13] L. Evans, *The Large Hadron Collider (LHC)*, *New J. Phys.* **9** (2007) 335.

- [14] L. Evans, (ed.) and P. Bryant, (ed.), *LHC Machine*, *JINST* **3** (2008) S08001.
- [15] H. E. Haber, G. L. Kane, and T. Sterling, *The Fermion Mass Scale and Possible Effects of Higgs Bosons on Experimental Observables*, *Nucl. Phys.* **B161** (1979) 493.
- [16] V. D. Barger, J. Hewett, and R. Phillips, *New constraints on the charged Higgs sector in two-Higgs-doublet models*, *Phys. Rev.* **D41** (1990) 3421–3441.
- [17] M. S. Carena and H. E. Haber, *Higgs boson theory and phenomenology*, *Prog. Part. Nucl. Phys.* **50** (2003) 63–152, [arXiv:hep-ph/0208209v3](https://arxiv.org/abs/hep-ph/0208209v3) [hep-ph].
- [18] J. F. Gunion and H. E. Haber, *Higgs Bosons in Supersymmetric Models (I)*, *Nucl. Phys.* **B272** (1986) 1–76.
- [19] J. F. Gunion, H. E. Haber, G. L. Kane, and S. Dawson, *The Higgs Hunter’s Guide*. Addison-Wesley, 1990. ISBN 0-201-50935-0.
- [20] J. F. Gunion, H. E. Haber, G. L. Kane, and S. Dawson, *Errata for "The Higgs Hunter’s Guide"*, [arXiv:hep-ph/9302272](https://arxiv.org/abs/hep-ph/9302272) [hep-ph].
- [21] ATLAS Collaboration, *Observation of a new particle in the search for the Standard Model Higgs boson with the ATLAS detector at the LHC*, *Phys. Lett.* **B716** (2012) 1–29, [arXiv:1207.7214](https://arxiv.org/abs/1207.7214) [hep-ex].
- [22] CMS Collaboration, *Observation of a new boson at a mass of 125 GeV with the CMS experiment at the LHC*, *Phys. Lett.* **B716** (2012) 30–61, [arXiv:1207.7235](https://arxiv.org/abs/1207.7235) [hep-ex].
- [23] see for example: S. Heinemeyer, O. Stål and G. Weiglein, *Interpreting the LHC Higgs Search Results in the MSSM*, *Phys. Lett.* **B710** (2012) 201–206, [arXiv:1112.3026](https://arxiv.org/abs/1112.3026) [hep-ph].
- [24] ATLAS Collaboration, *The ATLAS Experiment at the CERN Large Hadron Collider*, *JINST* **3** (2008) S08003.
- [25] Y. Nambu and G. Jona-Lasinio, *Dynamical Model of Elementary Particles Based on an Analogy with Superconductivity. I*, *Phys. Rev.* **122** (1961) 345–358.
- [26] Y. Nambu and G. Jona-Lasinio, *Dynamical Model of Elementary Particles Based on an Analogy with Superconductivity. II*, *Phys. Rev.* **124** (1961) 246–254.
- [27] M. Gell-Mann, *A Schematic Model of Baryons and Mesons*, *Phys. Lett.* **8** (1964) 214–215.
- [28] M. Gell-Mann, *The Symmetry group of vector and axial vector currents*, *Physics* **1** (1964) 63–75.

- [29] D. Gross and F. Wilczek, *Ultraviolet Behavior of Nonabelian Gauge Theories*, *Phys. Rev. Lett.* **30** (1973) 1343–1346.
- [30] H. D. Politzer, *Reliable Perturbative Results for Strong Interactions?*, *Phys. Rev. Lett.* **30** (1973) 1346–1349.
- [31] H. D. Politzer, *Asymptotic Freedom: An Approach to Strong Interactions*, *Phys. Rept.* **14** (1974) 129–180.
- [32] H. Fritzsch, M. Gell-Mann, and P. Minkowski, *Vectorlike Weak Currents and New Elementary Fermions*, *Phys. Lett.* **B59** (1975) 256.
- [33] S. Weinberg, *Phenomenological Lagrangians*, *Physica* **A96** (1979) 327.
- [34] J. Gasser and H. Leutwyler, *Chiral Perturbation Theory to One Loop*, *Annals Phys.* **158** (1984) 142.
- [35] J. Gasser and H. Leutwyler, *Chiral Perturbation Theory: Expansions in the Mass of the Strange Quark*, *Nucl. Phys.* **B250** (1985) 465.
- [36] J. Beringer et al., *Review of Particle Physics (RPP)*, *Phys. Rev.* **D86** (2012) 010001.
- [37] S. Bethke, *Determination of the QCD coupling α_s* , *J. Phys.* **G26** (2000) R27, [arXiv:hep-ex/0004021 \[hep-ex\]](https://arxiv.org/abs/hep-ex/0004021).
- [38] H. Yukawa, *On the interaction of elementary particles*, *Proc. Phys. Math. Soc. Jap.* **17** (1935) 48.
- [39] M. Herrero, *The Standard model*, [arXiv:hep-ph/9812242 \[hep-ph\]](https://arxiv.org/abs/hep-ph/9812242).
- [40] F. J. Yndurain, *Limits on the mass of the gluon*, *Phys. Lett.* **B345** (1995) 524–526.
- [41] B. Pontecorvo, *Mesonium and antimesonium*, *Sov. Phys. JETP* **6** (1957) 429.
- [42] B. Pontecorvo, *Inverse beta processes and nonconservation of lepton charge*, *Sov. Phys. JETP* **7** (1958) 172–173.
- [43] B. Pontecorvo, *Neutrino experiments and the problem of conservation of leptonic charge*, *Sov. Phys. JETP* **26** (1968) 984–988.
- [44] V. N. Gribov and B. Pontecorvo, *Neutrino astronomy and lepton charge*, *Phys. Lett.* **B28** (1969) 493.
- [45] J. F. Donoghue, E. Golowich, and B. R. Holstein, *Dynamics of the Standard Model*. Cambridge, Great Britain: University Press, 1992. ISBN 0-521-47652-6.

[46] K. Lande, E. Booth, J. Impeduglia, L. Lederman, and W. Chinowsky, *Observation of Long-Lived Neutral V Particles*, *Phys. Rev.* **103** (1956) 1901–1904.

[47] ARGUS Collaboration, H. Albrecht et al., *Observation of $B^0 - \bar{B}^0$ Mixing*, *Phys. Lett.* **B192** (1987) 245.

[48] CDF Collaboration, A. Abulencia et al., *Observation of $B_s^0 - \bar{B}_s^0$ Oscillations*, *Phys. Rev. Lett.* **97** (2006) 242003, [arXiv:hep-ex/0609040](https://arxiv.org/abs/hep-ex/0609040) [hep-ex].

[49] BABAR Collaboration, B. Aubert et al., *Evidence for $D^0 - \bar{D}^0$ Mixing*, *Phys. Rev. Lett.* **98** (2007) 211802, [arXiv:hep-ex/0703020](https://arxiv.org/abs/hep-ex/0703020) [hep-ex].

[50] Belle Collaboration, M. Staric et al., *Evidence for $D^0 - \bar{D}^0$ Mixing*, *Phys. Rev. Lett.* **98** (2007) 211803, [arXiv:hep-ex/0703036](https://arxiv.org/abs/hep-ex/0703036) [hep-ex].

[51] CDF Collaboration, T. Aaltonen et al., *Evidence for $D^0 - \bar{D}^0$ mixing using the CDF II Detector*, *Phys. Rev. Lett.* **100** (2008) 121802, [arXiv:0712.1567](https://arxiv.org/abs/0712.1567) [hep-ex].

[52] BABAR Collaboration, B. Aubert et al., *Measurement of $D^0 - \bar{D}^0$ mixing from a time-dependent amplitude analysis of $D^0 \rightarrow K^+ \pi^- \pi^0$ decays*, *Phys. Rev. Lett.* **103** (2009) 211801, [arXiv:0807.4544](https://arxiv.org/abs/0807.4544) [hep-ex].

[53] BABAR Collaboration, B. Aubert et al., *Measurement of $D^0 - \bar{D}^0$ Mixing using the Ratio of Lifetimes for the Decays $D^0 \rightarrow K^- \pi^+$ and $K^+ K^-$* , *Phys. Rev.* **D80** (2009) 071103, [arXiv:0908.0761](https://arxiv.org/abs/0908.0761) [hep-ex].

[54] LHCb Collaboration, R. Aaij et al., *Observation of $D^0 - \bar{D}^0$ oscillations*, *Phys. Rev. Lett.* **110** (2013) 101802, [arXiv:1211.1230](https://arxiv.org/abs/1211.1230) [hep-ex].

[55] F. Halzen and A. D. Martin, *Quarks and leptons: an introductory course in modern particle physics*. New York, USA: Wiley, 1984. ISBN 0-471-88741-2.

[56] D. Griffiths, *Introduction to elementary particles*. Weinheim, USA: Wiley-VCH, 2008. ISBN 0-471-60386-4.

[57] C. Burgess and G. Moore, *The Standard Model, A Primer*. Cambridge, Great Britain: University Press, 2007. ISBN 0-521-86036-9.

[58] F. Englert and R. Brout, *Broken symmetry and the mass of gauge vector mesons*, *Phys. Rev. Lett.* **13** (1964) 321–323.

[59] P. W. Higgs, *Broken symmetries, massless particles and gauge fields*, *Phys. Lett.* **12** (1964) 132–133.

- [60] P. W. Higgs, *Broken symmetries and the masses of gauge bosons*, *Phys. Rev. Lett.* **13** (1964) 508–509.
- [61] G. Guralnik, C. Hagen, and T. Kibble, *Global conservation laws and massless particles*, *Phys. Rev. Lett.* **13** (1964) 585–587.
- [62] P. W. Higgs, *Spontaneous symmetry breakdown without massless bosons*, *Phys. Rev.* **145** (1966) 1156–1163.
- [63] T. Kibble, *Symmetry breaking in non-Abelian gauge theories*, *Phys. Rev.* **155** (1967) 1554–1561.
- [64] J. Goldstone, A. Salam, and S. Weinberg, *Broken Symmetries*, *Phys. Rev.* **127** (1962) 965–970.
- [65] T. Goepfert, *Studies of Charged Higgs Boson Observability in the $H^+ \rightarrow t\bar{b}$ Decay at the ATLAS Experiment within the Minimal Supersymmetric Standard Model*. PhD thesis, TU, Dresden, 2010. Presented on 15 Dec 2010, [CERN-THESIS-2010-173](#).
- [66] W. Greiner and B. Müller, *Theoretische Physik, Band 8, Eichtheorie der schwachen Wechselwirkung*. Thun, Germany: Harri Deutsch, 1986. ISBN 3-87144-712-9.
- [67] S. Novaes, *Standard model: An Introduction*, [arXiv:hep-ph/0001283](#) [hep-ph].
- [68] T. van Ritbergen and R. G. Stuart, *Hadronic contributions to the muon lifetime*, *Phys. Lett.* **B437** (1998) 201–208, [arXiv:hep-ph/9802341](#) [hep-ph].
- [69] T. van Ritbergen and R. G. Stuart, *Complete two loop quantum electrodynamic contributions to the muon lifetime in the Fermi model*, *Phys. Rev. Lett.* **82** (1999) 488–491, [arXiv:hep-ph/9808283](#) [hep-ph].
- [70] T. van Ritbergen and R. G. Stuart, *On the precise determination of the Fermi coupling constant from the muon lifetime*, *Nucl. Phys.* **B564** (2000) 343–390, [arXiv:hep-ph/9904240](#) [hep-ph].
- [71] UA1 Collaboration, G. Arnison et al., *Experimental Observation of Isolated Large Transverse Energy Electrons with Associated Missing Energy at $\sqrt{s} = 540 \text{ GeV}$* , *Phys. Lett.* **B122** (1983) 103–116.
- [72] UA2 Collaboration, M. Banner et al., *Observation of Single Isolated Electrons of High Transverse Momentum in Events with Missing Transverse Energy at the CERN $\bar{p}p$ Collider*, *Phys. Lett.* **B122** (1983) 476–485.

[73] UA1 Collaboration, G. Arnison et al., *Experimental Observation of Lepton Pairs of Invariant Mass Around $95\text{ GeV}/c^2$ at the CERN SPS Collider*, *Phys. Lett.* **B126** (1983) 398–410.

[74] UA2 Collaboration, P. Bagnaia et al., *Evidence for $Z^0 \rightarrow e^+e^-$ at the CERN $\bar{p}p$ Collider*, *Phys. Lett.* **B129** (1983) 130–140.

[75] ATLAS Collaboration, *Measurements of the properties of the Higgs-like boson in the four lepton decay channel with the ATLAS detector using 25 fb^{-1} of proton-proton collision data*, [ATLAS-CONF-2013-013](#).

[76] ATLAS Collaboration, *Study of the spin of the Higgs-like boson in the two photon decay channel using 20.7 fb^{-1} of pp collisions collected at $\sqrt{s} = 8\text{ TeV}$ with the ATLAS detector*, [ATLAS-CONF-2013-029](#).

[77] ATLAS Collaboration, *Study of the spin properties of the Higgs-like particle in the $H \rightarrow WW^{(*)} \rightarrow e\bar{\nu}\mu\bar{\nu}$ channel with 21 fb^{-1} of $\sqrt{s} = 8\text{ TeV}$ data collected with the ATLAS detector*, [ATLAS-CONF-2013-031](#).

[78] CMS Collaboration, *Combination of standard model Higgs boson searches and measurements of the properties of the new boson with a mass near 125 GeV* , [CMS-PAS-HIG-12-045](#).

[79] CMS Collaboration, *Properties of the Higgs-like boson in the decay H to ZZ to $4l$ in pp collisions at $\sqrt{s} = 7$ and 8 TeV* , [CMS-PAS-HIG-13-002](#).

[80] CDF Collaboration, DØ Collaboration, T. Aaltonen et al., *Evidence for a particle produced in association with weak bosons and decaying to a bottom-antibottom quark pair in Higgs boson searches at the TeVatron*, *Phys. Rev. Lett.* **109** (2012) 071804, [arXiv:1207.6436 \[hep-ex\]](#).

[81] ATLAS Collaboration, *Combined coupling measurements of the Higgs-like boson with the ATLAS detector using up to 25 fb^{-1} of proton-proton collision data*, [ATLAS-CONF-2013-034](#).

[82] ATLAS Collaboration, *ATLAS high-level trigger, data-acquisition and controls. Technical Design Report*, [ATLAS-TDR-16](#); CERN-LHCC-2003-022.

[83] R. Haag, J. T. Łopuszanski, and M. Sohnius, *All Possible Generators of Supersymmetries of the S Matrix*, *Nucl. Phys.* **B88** (1975) 257.

[84] S. R. Coleman and J. Mandula, *All possible Symmetries of the S Matrix*, *Phys. Rev.* **159** (1967) 1251–1256.

- [85] H. Murayama, *Supersymmetry phenomenology*, [arXiv:hep-ph/0002232](https://arxiv.org/abs/hep-ph/0002232) [hep-ph].
- [86] S. P. Martin, *A Supersymmetry Primer*, [arXiv:hep-ph/9709356](https://arxiv.org/abs/hep-ph/9709356) [hep-ph].
- [87] A. Djouadi, *The Higgs sector of supersymmetric theories and the implications for high-energy colliders*, *Eur. Phys. J.* **C59** (2009) 389–426, [arXiv:0810.2439](https://arxiv.org/abs/0810.2439) [hep-ph].
- [88] LHC Higgs Cross Section Working Group, Dittmaier, S., Mariotti, C., Passarino, G., Tanaka, R. and others, *Handbook of LHC Higgs Cross Sections: 2. Differential Distributions*, CERN-2012-002, [arXiv:1201.3084](https://arxiv.org/abs/1201.3084) [hep-ph].
- [89] D. I. Kazakov, *Beyond the standard model (in search of supersymmetry)*, [arXiv:hep-ph/0012288](https://arxiv.org/abs/hep-ph/0012288) [hep-ph].
- [90] U. Amaldi, W. de Boer, and H. Fürstenau, *Comparison of grand unified theories with electroweak and strong coupling constants measured at LEP*, *Phys. Lett.* **B260** (1991) 447–455.
- [91] G. Bertone, D. Hooper, and J. Silk, *Particle dark matter: Evidence, candidates and constraints*, *Phys. Rept.* **405** (2005) 279–390, [arXiv:hep-ph/0404175](https://arxiv.org/abs/hep-ph/0404175) [hep-ph].
- [92] H. Goldberg, *Constraint on the Photino Mass from Cosmology*, *Phys. Rev. Lett.* **50** (1983) 1419.
- [93] J. R. Ellis, J. Hagelin, D. V. Nanopoulos, K. A. Olive, and M. Srednicki, *Supersymmetric Relics from the Big Bang*, *Nucl. Phys.* **B238** (1984) 453–476.
- [94] A. Djouadi, *The Anatomy of electro-weak symmetry breaking. II. The Higgs bosons in the minimal supersymmetric model*, *Phys. Rept.* **459** (2008) 1–241, [arXiv:hep-ph/0503173](https://arxiv.org/abs/hep-ph/0503173) [hep-ph].
- [95] G. R. Farrar and P. Fayet, *Phenomenology of the Production, Decay, and Detection of New Hadronic States Associated with Supersymmetry*, *Phys. Lett.* **B76** (1978) 575.
- [96] L. O’Raifeartaigh, *Spontaneous Symmetry Breaking for Chiral Scalar Superfields*, *Nucl. Phys.* **B96** (1975) 331.
- [97] K. A. Intriligator, N. Seiberg, and D. Shih, *Dynamical SUSY breaking in meta-stable vacua*, *JHEP* **04** (2006) 021, [arXiv:hep-th/0602239](https://arxiv.org/abs/hep-th/0602239) [hep-th].
- [98] L. F. Matos, *Some examples of F and D-term SUSY breaking models*, [arXiv:0910.0451](https://arxiv.org/abs/0910.0451) [hep-ph].

[99] G. Giudice and R. Rattazzi, *Theories with gauge mediated supersymmetry breaking*, *Phys. Rept.* **322** (1999) 419–499, [arXiv:hep-ph/9801271 \[hep-ph\]](https://arxiv.org/abs/hep-ph/9801271).

[100] E. Cremmer, B. Julia, J. Scherk, P. van Nieuwenhuizen, S. Ferrara, et al., *Super-Higgs Effect in Supergravity with General Scalar Interactions*, *Phys. Lett.* **B79** (1978) 231.

[101] W. Siegel and J. Gates, S. James, *Superfield Supergravity*, *Nucl. Phys.* **B147** (1979) 77.

[102] A. H. Chamseddine, R. L. Arnowitt, and P. Nath, *Locally Supersymmetric Grand Unification*, *Phys. Rev. Lett.* **49** (1982) 970.

[103] R. L. Arnowitt, A. H. Chamseddine, and P. Nath, *Masses of Superpartners of Quarks, Leptons, and Gauge Mesons in Supergravity Grand Unified Theories*, *Phys. Rev. Lett.* **50** (1983) 232–235.

[104] R. Barbieri, S. Ferrara, and C. A. Savoy, *Gauge Models with Spontaneously Broken Local Supersymmetry*, *Phys. Lett.* **B119** (1982) 343.

[105] J. Ellis, F. Luo, K. A. Olive, and P. Sandick, *The Higgs Mass beyond the CMSSM*, [arXiv:1212.4476 \[hep-ph\]](https://arxiv.org/abs/1212.4476).

[106] T. Lee, *A Theory of Spontaneous T Violation*, *Phys. Rev.* **D8** (1973) 1226.

[107] M. Perelstein, *Little Higgs models and their phenomenology*, *Prog. Part. Nucl. Phys.* **58** (2007) 247–291, [arXiv:hep-ph/0512128 \[hep-ph\]](https://arxiv.org/abs/hep-ph/0512128).

[108] J. F. Gunion, R. Vega, and J. Wudka, *Higgs triplets in the standard model*, *Phys. Rev.* **D42** (1990) 1673–1691.

[109] A. Carcamo Hernandez, R. Martinez, and J. A. Rodriguez, *Different kind of textures of Yukawa coupling matrices in the two Higgs doublet model type III*, *Eur. Phys. J.* **C50** (2007) 935–948, [arXiv:hep-ph/0606190 \[hep-ph\]](https://arxiv.org/abs/hep-ph/0606190).

[110] Y.-F. Zhou, *Texture of Yukawa coupling matrices in general two Higgs doublet model*, *J. Phys.* **G30** (2004) 783–792, [arXiv:hep-ph/0307240 \[hep-ph\]](https://arxiv.org/abs/hep-ph/0307240).

[111] M. Aoki, S. Kanemura, K. Tsumura, and K. Yagyu, *Models of Yukawa interaction in the two Higgs doublet model, and their collider phenomenology*, *Phys. Rev.* **D80** (2009) 015017, [arXiv:0902.4665 \[hep-ph\]](https://arxiv.org/abs/0902.4665).

[112] J. Diaz-Cruz, A. Diaz-Furlong, and J. Montes de Oca, *The General Two-Higgs doublet eXtensions of the SM: A Saucerful of secrets*, [arXiv:1010.0950v2 \[hep-ph\]](https://arxiv.org/abs/1010.0950v2).

[113] S. L. Glashow and S. Weinberg, *Natural Conservation Laws for Neutral Currents*, *Phys. Rev.* **D15** (1977) 1958.

[114] T. Cheng and M. Sher, *Mass-Matrix Ansatz and Flavor Nonconservation in Models with Multiple Higgs Doublets*, *Phys. Rev.* **D35** (1987) 3484.

[115] H. Fritzsch, *Calculating the Cabibbo Angle*, *Phys. Lett.* **B70** (1977) 436.

[116] J. F. Gunion and A. Turski, *Renormalization of Higgs Boson Mass Sum Rules and Screening*, *Phys. Rev.* **D39** (1989) 2701.

[117] ATLAS Collaboration, N. Andari, K. Assamagan, A. Bourgaux, M. Campanelli, G. Carrillo-Montoya, M. Escalier, M. Flechl, J. Huston, S. Muanza, B. Murray, B. Mellado, A. Nisati, J. Qian, D. Rebuzzi, M. Schram, M. Schumacher, R. Tanaka, T. Vickey, M. Warsinsky, and H. Zhang, *Higgs Production Cross Sections and Decay Branching Ratios*, [ATL-PHYS-INT-2010-030](#).

[118] The LEP working group for Higgs boson searches: ALEPH Collaboration, DELPHI Collaboration, L3 Collaboration and OPAL Collaboration, *Search for Charged Higgs bosons: Combined Results Using LEP Data*, submitted to *Eur. Phys. J. C* (2013) [CERN-PH-EP-2012-369](#); [LHWG-Note-2012-01](#); [ALEPH-2012-001-PHYSICS-2012-001](#); [DELPHI-2012-001-PHYS-953](#); [L3-Note-2835](#); [OPAL-PR433](#), [arXiv:1301.6065 \[hep-ex\]](#).

[119] ALEPH Collaboration, A. Heister et al., *Search for charged Higgs bosons in e^+e^- collisions at energies up to $\sqrt{s} = 209\text{ GeV}$* , *Phys. Lett.* **B543** (2002) 1–13, [arXiv:hep-ex/0207054 \[hep-ex\]](#).

[120] DELPHI Collaboration, P. Abreu et al., *Search for Charged Higgs Bosons in e^+e^- Collisions at $\sqrt{s} = 189\text{--}202\text{ GeV}$* , *Phys. Lett.* **B525** (2002) 17–28, [arXiv:hep-ex/0201023 \[hep-ex\]](#).

[121] L3 Collaboration, P. Achard et al., *Search for charged Higgs bosons at LEP*, *Phys. Lett.* **B575** (2003) 208–220, [arXiv:hep-ex/0309056 \[hep-ex\]](#).

[122] OPAL Collaboration, G. Abbiendi et al., *Search for Charged Higgs Bosons in e^+e^- Collisions at $\sqrt{s} = 189\text{--}209\text{ GeV}$* , *Eur. Phys. J.* **C72** (2012) 2076, [arXiv:0812.0267 \[hep-ex\]](#).

[123] CDF Collaboration, A. Abulencia et al., *Search for charged Higgs bosons from top quark decays in $p\bar{p}$ collisions at $\sqrt{s} = 1.96\text{ TeV}$* , *Phys. Rev. Lett.* **96** (2006) 042003, [arXiv:hep-ex/0510065 \[hep-ex\]](#).

[124] CDF Collaboration, T. Aaltonen et al., *Search for charged Higgs bosons in decays of top quarks in $p\bar{p}$ collisions at $\sqrt{s} = 1.96\text{ TeV}$* , *Phys. Rev. Lett.* **103** (2009) 101803, [arXiv:0907.1269 \[hep-ex\]](#).

[125] DØ Collaboration, V. Abazov et al., *Search for charged Higgs bosons in top quark decays*, *Phys. Lett.* **B682** (2009) 278–286, [arXiv:0908.1811 \[hep-ex\]](https://arxiv.org/abs/0908.1811).

[126] DØ Collaboration, V. Abazov et al., *Search for charged Higgs bosons in decays of top quarks*, *Phys. Rev.* **D80** (2009) 051107, [arXiv:0906.5326 \[hep-ex\]](https://arxiv.org/abs/0906.5326).

[127] DØ Collaboration, V. Abazov et al., *Combination of $t\bar{t}$ cross section measurements and constraints on the mass of the top quark and its decays into charged Higgs bosons*, *Phys. Rev.* **D80** (2009) 071102, [arXiv:0903.5525 \[hep-ex\]](https://arxiv.org/abs/0903.5525).

[128] S. Heinemeyer, W. Hollik, and G. Weiglein, *FeynHiggs: a program for the calculation of the masses of the neutral CP-even Higgs bosons in the MSSM*, *Comput. Phys. Commun.* **124** (2000) 76–89, [arXiv:hep-ph/9812320 \[hep-ph\]](https://arxiv.org/abs/hep-ph/9812320).

[129] J. Lee, M. Carena, J. Ellis, A. Pilaftsis, and C. Wagner, *CPsuperH2.0: an Improved Computational Tool for Higgs Phenomenology in the MSSM with Explicit CP Violation*, *Comput. Phys. Commun.* **180** (2009) 312–331, [arXiv:0712.2360 \[hep-ph\]](https://arxiv.org/abs/0712.2360).

[130] ATLAS Collaboration, *Search for a light charged Higgs boson in the decay channel $H^+ \rightarrow c\bar{s}$ in $t\bar{t}$ events using pp collisions at $\sqrt{s} = 7$ TeV with the ATLAS detector*, CERN-PH-EP-2012-338, [arXiv:1302.3694 \[hep-ex\]](https://arxiv.org/abs/1302.3694).

[131] O. Deschamps, S. Descotes-Genon, S. Monteil, V. Niess, S. T'Jampens, et al., *The Two Higgs Doublet of Type II facing flavour physics data*, *Phys. Rev.* **D82** (2010) 073012, [arXiv:0907.5135 \[hep-ph\]](https://arxiv.org/abs/0907.5135).

[132] J. R. Ellis, M. Gaillard, D. V. Nanopoulos, and S. Rudaz, *The Phenomenology of the Next Left-Handed Quarks*, *Nucl. Phys.* **B131** (1977) 285.

[133] UTfit Collaboration, M. Bona et al., *An Improved Standard Model Prediction of $\mathcal{B}(B \rightarrow \tau\nu)$ And Its Implications For New Physics*, *Phys. Lett.* **B687** (2010) 61–69, [arXiv:0908.3470 \[hep-ph\]](https://arxiv.org/abs/0908.3470).

[134] U. Haisch, $\bar{B} \rightarrow X_s \gamma$: Standard Model and Beyond, [arXiv:0805.2141 \[hep-ph\]](https://arxiv.org/abs/0805.2141).

[135] BABAR Collaboration, J. Lees et al., *Measurement of an Excess of $B \rightarrow D^{(*)}\tau\nu$ Decays and Implications for Charged Higgs Bosons*, [arXiv:1303.0571 \[hep-ex\]](https://arxiv.org/abs/1303.0571).

[136] D. Eriksson, F. Mahmoudi, and O. Stal, *Charged Higgs bosons in Minimal Supersymmetry: Updated constraints and experimental prospects*, *JHEP* **11** (2008) 035, [arXiv:0808.3551 \[hep-ph\]](https://arxiv.org/abs/0808.3551).

[137] Muon G-2 Collaboration, G. Bennett et al., *Final Report of the Muon E821 Anomalous Magnetic Moment Measurement at BNL*, *Phys. Rev.* **D73** (2006) 072003, [arXiv:hep-ex/0602035 \[hep-ex\]](https://arxiv.org/abs/hep-ex/0602035).

[138] J. P. Miller, E. de Rafael, and B. L. Roberts, *Muon (g-2): Experiment and theory*, *Rept. Prog. Phys.* **70** (2007) 795, [arXiv:hep-ph/0703049 \[hep-ph\]](https://arxiv.org/abs/hep-ph/0703049).

[139] WMAP Collaboration, E. Komatsu et al., *Five-Year Wilkinson Microwave Anisotropy Probe (WMAP) Observations: Cosmological Interpretation*, *Astrophys. J. Suppl.* **180** (2009) 330–376, [arXiv:0803.0547 \[astro-ph\]](https://arxiv.org/abs/0803.0547).

[140] Planck Collaboration, P. Ade et al., *Planck Intermediate Results. XI: The gas content of dark matter halos: the Sunyaev-Zeldovich-stellar mass relation for locally brightest galaxies*, [arXiv:1212.4131 \[astro-ph.CO\]](https://arxiv.org/abs/1212.4131).

[141] ATLAS Collaboration, *ATLAS Computing. Technical Design Report*, ATLAS-TDR-17; CERN-LHCC-2005-022.

[142] ATLAS Collaboration, *The ATLAS Simulation Infrastructure*, *Eur. Phys. J.* **C70** (2010) 823–874, [arXiv:1005.4568 \[physics.ins-det\]](https://arxiv.org/abs/1005.4568).

[143] P. M. Nadolsky, H.-L. Lai, Q.-H. Cao, J. Huston, J. Pumplin, et al., *Implications of CTEQ global analysis for collider observables*, *Phys. Rev.* **D78** (2008) 013004, [arXiv:0802.0007 \[hep-ph\]](https://arxiv.org/abs/0802.0007).

[144] J. Pumplin, D. Stump, J. Huston, H. Lai, P. M. Nadolsky, et al., *New generation of parton distributions with uncertainties from global QCD analysis*, *JHEP* **07** (2002) 012, [arXiv:hep-ph/0201195 \[hep-ph\]](https://arxiv.org/abs/hep-ph/0201195).

[145] T. Sjöstrand, S. Mrenna, and P. Z. Skands, *PYTHIA 6.4 Physics and Manual*, *JHEP* **05** (2006) 026, [arXiv:hep-ph/0603175 \[hep-ph\]](https://arxiv.org/abs/hep-ph/0603175).

[146] G. Corcella, I. Knowles, G. Marchesini, S. Moretti, K. Odagiri, et al., *HERWIG 6: An Event generator for hadron emission reactions with interfering gluons (including supersymmetric processes)*, *JHEP* **01** (2001) 010, [arXiv:hep-ph/0011363 \[hep-ph\]](https://arxiv.org/abs/hep-ph/0011363).

[147] M. L. Mangano, M. Moretti, F. Piccinini, R. Pittau, and A. D. Polosa, *ALPGEN, a generator for hard multiparton processes in hadronic collisions*, *JHEP* **07** (2003) 001, [arXiv:hep-ph/0206293 \[hep-ph\]](https://arxiv.org/abs/hep-ph/0206293).

[148] Z. Was and P. Golonka, *TAUOLA as tau Monte Carlo for future applications*, *Nucl. Phys. Proc. Suppl.* **144** (2005) 88, [arXiv:hep-ph/0411377 \[hep-ph\]](https://arxiv.org/abs/hep-ph/0411377).

[149] E. Barberio, B. van Eijk, and Z. Was, *PHOTOS: A Universal Monte Carlo for QED radiative corrections in decays*, *Comput. Phys. Commun.* **66** (1991) 115–128. CERN-TH-5857-90.

[150] GEANT4 Collaboration, S. Agostinelli et al., *GEANT4: A simulation toolkit*, *Nucl. Instrum. Meth. A* **506** (2003) 250.

[151] ATLAS Collaboration, *Measurement of the Mis-identification Probability of τ Leptons from Hadronic Jets and from Electrons*, [ATLAS-CONF-2011-113](#).

[152] ATLAS Collaboration, S. Bedikian, P. Czodrowski, S. Demers, J. Kraus, J. Kroseberg, W. Mader, X. Prudent, and A. Straessner, *Determination of the Electron-Tau Mis-identification Probability with a Tag-and-Probe Method*, [ATL-PHYS-INT-2011-069](#).

[153] C. Anastasiou, L. J. Dixon, K. Melnikov, and F. Petriello, *High precision QCD at hadron colliders: Electroweak gauge boson rapidity distributions at NNLO*, *Phys. Rev. D* **69** (2004) 094008, [arXiv:hep-ph/0312266 \[hep-ph\]](#).

[154] A. D. Martin, W. J. Stirling, R. S. Thorne, and G. Watt, *Parton distributions for the LHC*, *Eur. Phys. J. C* **63** (2009) 189–285, [arXiv:0901.0002 \[hep-ph\]](#).

[155] P. J. Rijken and W. L. van Neerven, *Order α_s^2 contributions to the Drell-Yan cross-section at fixed target energies*, *Phys. Rev. D* **51** (1995) 44–63, [arXiv:hep-ph/9408366 \[hep-ph\]](#).

[156] R. Hamberg, W. L. van Neerven, and T. Matsuura, *A Complete calculation of the order α_s^2 correction to the Drell-Yan K factor*, *Nucl. Phys. B* **359** (1991) 343–405.

[157] W. L. van Neerven and E. B. Zijlstra, *The $O(\alpha_s^2)$ corrected Drell-Yan K factor in the DIS and MS scheme*, *Nucl. Phys. B* **382** (1992) 11–62.

[158] *QCD Dijet in MC10 Production Round*, Available from the top monte carlo 2010 twiki web page: <https://twiki.cern.ch/twiki/bin/view/AtlasProtected/TopMC2010>.

[159] ATLAS Collaboration, *Data-driven estimation of the background to charged Higgs boson searches using hadronically-decaying τ final states in ATLAS*, [ATLAS-CONF-2011-051](#).

[160] ATLAS Collaboration, S. Arghir, S. Behar, V. Cavaliere, Y. Coadou, P. Czodrowski, M. Flechl, A. Kopp, A. McCarn, M. zur Nedden, M. Neubauer, A. Randle-Conde, Y. Rozen, S. Sekula, Y. Takahashi, M. Tomoto, T. Vickey, and S. Xella, *Data-driven estimation of the background to H^+ searches with hadronic-tau final states*, [ATL-PHYS-INT-2011-028](#).

[161] S. Frixione and B. R. Webber, *Matching NLO QCD computations and parton shower simulations*, *JHEP* **06** (2002) 029, [arXiv:hep-ph/0204244 \[hep-ph\]](#).

[162] J. M. Butterworth, J. R. Forshaw and M. H. Seymour, *Multiparton interactions in photoproduction at HERA*, *Z. Phys. C* **72** (1996) 637–646, [arXiv:hep-ph/9601371](https://arxiv.org/abs/hep-ph/9601371) [hep-ph].

[163] S. Frixione, E. Laenen, P. Motylinski, and B. R. Webber, *Single-top production in MC@NLO*, *JHEP* **03** (2006) 092, [arXiv:hep-ph/0512250](https://arxiv.org/abs/hep-ph/0512250) [hep-ph].

[164] ATLAS Collaboration, *Measurement of the top quark-pair production cross section with ATLAS in pp collisions at $\sqrt{s} = 7$ TeV*, *Eur. Phys. J. C* **71** (2011) 1577, [arXiv:1012.1792](https://arxiv.org/abs/1012.1792) [hep-ex].

[165] U. Langenfeld, S. Moch, and P. Uwer, *New results for $t\bar{t}$ production at hadron colliders*, [arXiv:0907.2527](https://arxiv.org/abs/0907.2527) [hep-ph].

[166] J. Alwall, S. Hoche, F. Krauss, N. Lavesson, L. Lonnblad, et al., *Comparative study of various algorithms for the merging of parton showers and matrix elements in hadronic collisions*, *Eur. Phys. J. C* **53** (2008) 473–500, [arXiv:0706.2569](https://arxiv.org/abs/0706.2569) [hep-ph].

[167] ATLAS Collaboration, *Expected Performance of the ATLAS Experiment – Detector, Trigger and Physics*, SLAC-R-980; CERN-OPEN-2008-020, [arXiv:0901.0512](https://arxiv.org/abs/0901.0512) [hep-ex].

[168] M. Smizanska, S. Baranov, J. Hrivnáč, and E. Kneringer, *Overview of Monte Carlo simulations for ATLAS B-physics in the period 1996-1999*, ATL-PHYS-2000-025.

[169] ATLAS Collaboration, C. Anastopoulos et al., *Physics analysis tools for beauty physics in ATLAS*, *J. Phys. Conf. Ser.* **119** (2008) 032003.

[170] ATLAS Collaboration, *ATLAS tunes of PYTHIA 6 and Pythia 8 for MC11*, ATL-PHYS-PUB-2011-009.

[171] ATLAS Collaboration, *New ATLAS event generator tunes to 2010 data*, ATL-PHYS-PUB-2011-008.

[172] ATLAS Collaboration, *Search for charged Higgs bosons decaying via $H^+ \rightarrow \tau\nu$ in top quark pair events using pp collision data at $\sqrt{s} = 7$ TeV with the ATLAS detector*, *JHEP* **06** (2012) 039, [arXiv:1204.2760](https://arxiv.org/abs/1204.2760) [hep-ex].

[173] ATLAS Collaboration, *Search for charged Higgs bosons through the violation of lepton universality in $t\bar{t}$ events using pp collision data at $\sqrt{s} = 7$ TeV with the ATLAS experiment*, *JHEP* **03** (2013) 076, [arXiv:1212.3572](https://arxiv.org/abs/1212.3572) [hep-ex].

[174] ATLAS Collaboration, K. Cranmer, P. Czodrowski, A. Ferrari, M. Flechl, J. Godfrey, J. Groth-Jensen, S. Hattrem Raddum, C. Isaksson, G. Lewis, A. Madsen, A. McCarn,

M. Neubauer, D. Pelikan, A. Read, A. Straessner, and M. zur Nedden, *Search for charged Higgs bosons through the apparent violation of lepton universality in $t\bar{t}$ events using pp collision data at $\sqrt{s} = 7$ TeV with the ATLAS experiment*, [ATL-PHYS-INT-2012-097](#).

[175] ATLAS Collaboration, S. Behar, C. Buszello, P. Czodrowski, A. Ferrari, M. Flechl, S. Hattrem Raddum, C. Isaksson, A. Madsen, A. McCarn, M. zur Nedden, M. Neubauer, N. Patel, D. Pelikan, A. Read, Y. Rozen, and A. Saavedra, *Search for a charged Higgs boson decaying via $H^+ \rightarrow \tau\nu + \text{lepton}$ in $t\bar{t}$ events using 4.6 fb^{-1} of pp collision data recorded at $\sqrt{s} = 7$ TeV with the ATLAS detector — Supporting Note*, [ATL-PHYS-INT-2012-046](#).

[176] ATLAS Collaboration, P. Assamagan, C. Bernius, P. Casado, V. Cavaliere, P. Czodrowski, D. Chakraborty, D. Greenwood, A. Ferrari, M. Flechl, S. Hattrem Raddum, A. Kopp, P. Mal, A. McCarn, M. Neubauer, N. Patel, A. Randle-Conde, A. L. Read, G. Rocha de Lima, A. Saavedra, M. Schumacher, and S. Sekula, *Search for charged Higgs bosons in the $\tau_{\text{had}} + \text{jets}$ final state in $t\bar{t}$ decays with 4.6 fb^{-1} of pp collision data recorded at $\sqrt{s} = 7$ TeV with the ATLAS Experiment — Supporting Note*, [ATL-PHYS-INT-2012-047](#).

[177] ATLAS Collaboration, L. Barak, A. Ferrari, M. Flechl, E. Gross, J. Groth-Jensen, S. Hattrem Raddum, and A. Read, *Search for a charged Higgs boson decaying via $H^+ \rightarrow \tau_{\text{lep}}\nu + \text{jets}$ in $t\bar{t}$ events using 4.6 fb^{-1} of pp collision data recorded at $\sqrt{s} = 7$ TeV with the ATLAS detector — Supporting Note*, [ATL-PHYS-INT-2012-045](#).

[178] B. P. Kersevan and E. Richter-Was, *The Monte Carlo event generator AcerMC version 2.0 with interfaces to PYTHIA 6.2 and HERWIG 6.5*, [arXiv:hep-ph/0405247 \[hep-ph\]](#).

[179] M. Aliev, H. Lacker, U. Langenfeld, S. Moch, P. Uwer, and M. Widermann, *HATHOR – HAdronic Top and Heavy quarks crOss section calculatoR*, *Comput. Phys. Commun.* **182** (2011) 1034, [arXiv:1007.1327 \[hep-ph\]](#).

[180] N. Kidonakis, *Next-to-next-to-leading-order collinear and soft gluon corrections for t -channel single top quark production*, *Phys. Rev.* **D83** (2011) 091503, [arXiv:1103.2792 \[hep-ph\]](#).

[181] N. Kidonakis, *NNLL resummation for s -channel single top quark production*, *Phys. Rev.* **D81** (2010) 054028, [arXiv:1001.5034 \[hep-ph\]](#).

[182] N. Kidonakis, *Two-loop soft anomalous dimensions for single top quark associated production with a W^- or H^-* , *Phys. Rev.* **D82** (2010) 054018, [arXiv:1005.4451 \[hep-ph\]](#).

[183] S. Frixione, P. Nason, and C. Oleari, *Matching NLO QCD computations with Parton Shower simulations: the POWHEG method*, *JHEP* **11** (2007) 070, [arXiv:0709.2092 \[hep-ph\]](https://arxiv.org/abs/0709.2092).

[184] R. Gavin, Y. Li, F. Petriello, and S. Quackenbush, *W physics at the LHC with FEWZ 2.1*, [arXiv:1201.5896 \[hep-ph\]](https://arxiv.org/abs/1201.5896).

[185] R. Gavin, Y. Li, F. Petriello, and S. Quackenbush, *FEWZ 2.0: A code for hadronic Z production at next-to-next-to-leading order*, *Comput. Phys. Commun.* **182** (2011) 2388, [arXiv:1011.3540 \[hep-ph\]](https://arxiv.org/abs/1011.3540).

[186] J. M. Campbell, R. Ellis, and C. Williams, *Vector boson pair production at the LHC*, *JHEP* **07** (2011) 018, [arXiv:1105.0020 \[hep-ph\]](https://arxiv.org/abs/1105.0020).

[187] ATLAS Collaboration, *Luminosity Determination in pp Collisions at $\sqrt{s} = 7$ TeV using the ATLAS Detector in 2011*, [ATLAS-CONF-2011-116](https://cds.cern.ch/record/1312116).

[188] *The Extended Pileup Reweighting*,
<https://twiki.cern.ch/twiki/bin/view/AtlasProtected/ExtendedPileupReweighting>.

[189] *Design study of a 22 to 130 GeV e^+e^- colliding beam machine (LEP)*. Pink book. CERN, Geneva, 1979. [CERN-ISR-LEP-79-33; ISR-LEP-79-33](https://cds.cern.ch/record/1312116).

[190] R. R. Wilson, *The TeVatron*, *Phys. Today* **30N10** (1977) 23–30 [FERMILAB-TM-0763](https://cds.cern.ch/record/1312116).

[191] *Tevatron Luminosity*, <http://www.fnal.gov/pub/now/tevlum.html>.

[192] *The accelerator complex*,
<http://public.web.cern.ch/public/Objects/Research/AccComplex0700829.gif>.

[193] V. Duvivier, *CERN Accelerator Complex (operating and approved projets). Chaine des accelerateurs du CERN (en fonctionnement et avec les projets approuves)*, [LHC-PHO-2001-190](https://cds.cern.ch/record/1312116). AC Collection. Legacy of AC. Pictures from 1992 to 2002.

[194] CMS Collaboration, *The CMS experiment at the CERN Large Hadron Collider*, *JINST* **3** (2008) S08004.

[195] ALICE Collaboration, *The ALICE experiment at the CERN Large Hadron Collider*, *JINST* **3** (2008) S08002.

[196] LHCb Collaboration, *The LHCb Detector at the CERN Large Hadron Collider*, *JINST* **3** (2008) S08005.

[197] LHCf Collaboration, *The LHCf detector at the CERN Large Hadron Collider*, *JINST* **3** (2008) S08006.

[198] TOTEM Collaboration, *The TOTEM experiment at the CERN Large Hadron Collider*, **JINST** **3** (2008) S08007.

[199] MoEDAL Collaboration, *Technical Design Report of the MoEDAL Experiment*, **CERN-LHCC-2009-006; MoEDAL-TDR-001**.

[200] O. S. Bruening, R. Cappi, R. Garoby, O. Groebner, W. Herr, T. P. R. Linnecar, R. Ostojic, K. Potter, L. Rossi, F. Ruggiero, K. Schindl, G. R. Stevenson, L. Tavian, T. Taylor, E. Tsesmelis, E. Weisse, and F. Zimmermann, *LHC Luminosity and energy upgrade: A Feasibility Study*, **LHC-Project-Report-626; CERN-LHC-Project-Report-626**.

[201] F. Gianotti, M. Mangano, T. Virdee, S. Abdullin, G. Azuelos, et al., *Physics potential and experimental challenges of the LHC luminosity upgrade*, **Eur. Phys. J.** **C39** (2005) 293–333, [arXiv:hep-ph/0204087](https://arxiv.org/abs/hep-ph/0204087) [hep-ph].

[202] ATLAS Collaboration, CMS Collaboration, K. Jakobs, *Physics at the LHC and sLHC*, **Nucl. Instrum. Meth.** **A636** (2011) S1–S7.

[203] ATLAS Collaboration, CERN, The LHC experiments Committee, LHCC, *Letter of Intent for the Phase-I Upgrade of the ATLAS Experiment*, **CERN-LHCC-2011-012; LHCC-I-020**.

[204] ATLAS Collaboration, CERN, The LHC experiments Committee, LHCC, *Letter of Intent for the Phase-II Upgrade of the ATLAS Experiment*, **CERN-LHCC-2012-022; LHCC-I-023**.

[205] CMS Collaboration, *CMS Technical Design Report for the Phase 1 Upgrade of the Hadron Calorimeter*, **CERN-LHCC-2012-015; CMS-TDR-10**.

[206] CMS Collaboration, *CMS Technical Design Report for the Pixel Detector Upgrade*, **CERN-LHCC-2012-016, CMS-TDR-11**.

[207] *Joint LHC Machine – Experiments Workshops*, <http://ts-dep.web.cern.ch/ts-dep/groups/lea/int/workshops/LHC.jpg>.

[208] *ATLAS Photos*, <http://www.atlas.ch/photos/full-detector-cgi.html>.

[209] J. Pequenao and P. Schaffner, *An computer generated image representing how ATLAS detects particles*, **CERN-EX-1301009**.

[210] *Plot of pseudorapidity vs polar angle*, <http://commons.wikimedia.org/wiki/File:Pseudorapidity.svg>.

- [211] *ATLAS Magnet System – Design Parameters*, <http://atlas-magnet.web.cern.ch/atlas-magnet/docs/design/pars/>.
- [212] M. Alekса, F. Bergsma, P. Giudici, A. Kehrli, M. Losasso, et al., *Measurement of the ATLAS solenoid magnetic field*, **JINST** **3** (2008) P04003.
- [213] *ATLAS Photos*, <http://www.atlas.ch/photos/magnets-barrel.html>.
- [214] *ATLAS Photos*, <http://www.atlas.ch/photos/full-detector-photos.html>.
- [215] ATLAS Collaboration, *ATLAS pixel detector: Technical design report*, **ATLAS-TDR-11; CERN-LHCC-98-013**.
- [216] ATLAS Collaboration, V. A. Mitsou, *ATLAS silicon microstrip tracker: Operation and performance*, [arXiv:1110.1983](https://arxiv.org/abs/1110.1983) [physics.ins-det].
- [217] ATLAS Collaboration, A. Ovcharova, *Track-Based Alignment of the Inner Detector of ATLAS*, **EPJ Web Conf.** **28** (2012) 12052, [arXiv:1201.4961](https://arxiv.org/abs/1201.4961) [physics.ins-det].
- [218] ATLAS Collaboration, *Particle Identification Performance of the ATLAS Transition Radiation Tracker*, **ATLAS-CONF-2011-128**.
- [219] D. Froidevaux and P. Sphicas, *General-Purpose Detectors for the Large Hadron Collider*, **Annu. Rev. Nucl. Part. Sci.** **56** (2006) 375–440.
- [220] ATLAS Collaboration, *Performance of Missing Transverse Momentum Reconstruction in ATLAS with 2011 Proton-Proton Collisions at $\sqrt{s} = 7$ TeV*, **ATLAS-CONF-2012-101**.
- [221] ATLAS Collaboration, *Performance of Missing Transverse Momentum Reconstruction in pp Collisions at $\sqrt{s} = 7$ TeV with ATLAS*, **Eur. Phys. J.** **C72** (2012) 1844, [arXiv:1108.5602](https://arxiv.org/abs/1108.5602) [hep-ex].
- [222] ATLAS Collaboration, *Performance of the ATLAS electromagnetic calorimeter for $\pi^0 \rightarrow \gamma\gamma$ and $\eta \rightarrow \gamma\gamma$ events*, **ATLAS-CONF-2010-006**.
- [223] ATLAS Collaboration, *Expected photon performance in the ATLAS experiment*, **ATL-PHYS-PUB-2011-007**.
- [224] ATLAS Collaboration, *Measurements of the photon identification efficiency with the ATLAS detector using 4.9fb^{-1} of pp collision data collected in 2011*, **ATLAS-CONF-2012-123**.
- [225] ATLAS Electromagnetic Barrel Calorimeter Collaboration, *Energy linearity and resolution of the ATLAS electromagnetic barrel calorimeter in an electron test-beam*, **Nucl. Instrum. Meth.** **A568** (2006) 601–623, [arXiv:physics/0608012](https://arxiv.org/abs/physics/0608012) [physics].

[226] J. Colas, L. Di Ciacio, M. Gouanere, R. Lafaye, S. Laplace, et al., *Response Uniformity of the ATLAS Liquid Argon Electromagnetic Calorimeter*, *Nucl. Instrum. Meth.* **A582** (2007) 429–455, [arXiv:0709.1094 \[physics.ins-det\]](https://arxiv.org/abs/0709.1094).

[227] ATLAS Collaboration, *Measurement of the response of the ATLAS liquid argon barrel calorimeter to electrons at the 2004 combined test-beam*, *Nucl. Instrum. Meth.* **A614** (2010) 400–432.

[228] ATLAS Collaboration, *Electron performance measurements with the ATLAS detector using the 2010 LHC pp collision data*, *Eur. Phys. J.* **C72** (2012) 1909, [arXiv:1110.3174 \[hep-ex\]](https://arxiv.org/abs/1110.3174).

[229] ATLAS Collaboration, *ATLAS Detector and Physics Performance. Technical Design Report*, ATLAS-TDR-14; CERN-LHCC-99-014 and ATLAS-TDR-15; CERN-LHCC-99-015.

[230] ATLAS Collaboration, *Performance of the ATLAS electromagnetic calorimeter end-cap module 0*, *Nucl. Instrum. Meth.* **A500** (2003) 178–201.

[231] ATLAS Collaboration, *Performance of the ATLAS electromagnetic calorimeter barrel module 0*, *Nucl. Instrum. Meth.* **A500** (2003) 202–231.

[232] ATLAS Collaboration, *Readiness of the ATLAS Liquid Argon Calorimeter for LHC Collisions*, *Eur. Phys. J.* **C70** (2010) 723–753, [arXiv:0912.2642 \[physics.ins-det\]](https://arxiv.org/abs/0912.2642).

[233] L. Hervas, *I15 intervention – Talk given about the status of the preparation for the FEB recovery intervention*, <https://indico.cern.ch/getFile.py/access?contribId=5&resId=1&materialId=slides&confId=144584>.

[234] *Electronic logbook for the ATLAS experiment*, ATLAS elog entry [159064].

[235] O. Simard, *Recovery of LAr FEBs – On behalf of the LAr Run Coordinators and Operations Team*, <https://indico.cern.ch/getFile.py/access?resId=0&materialId=slides&contribId=6&sessionId=1&subContId=0&confId=131306>.

[236] A. Falou, *LARG Calorimeter FEBs Summary of mini-USB cables in situ exchange (Atlas cavern)*, <https://indico.cern.ch/getFile.py/access?contribId=3&resId=1&materialId=slides&confId=141690>.

[237] ATLAS Tile Calorimeter Collaboration, N. Shalanda et al., *Radioactive source control and electronics for the ATLAS tile calorimeter cesium calibration system*, *Nucl. Instrum. Meth.* **A508** (2003) 276–286.

[238] ATLAS Collaboration, *ATLAS liquid argon calorimeter: Technical design report*, [ATLAS-TDR-2; CERN-LHCC-96-041; CERN/LHCC 96-41](#).

[239] F. Anulli, G. Ciapetti, D. De Pedis, A. Di Girolamo, C. Luci, et al., *The Level-1 Trigger Muon Barrel System of the ATLAS experiment at CERN*, [JINST 4 \(2009\) P04010](#).

[240] V. Cindro, D. Dobos, I. Dolenc, H. Frais-Kölbl, et al., *The ATLAS beam conditions monitor*, [JINST 3 \(2008\) P02004](#).

[241] S. van der Meer, *Calibration of the Effective Beam Height in the ISR*, [CERN-ISR-PO-68-31](#).

[242] B. Macek, *Measurement of Luminosity in ATLAS Spectrometer with Beam Conditions Monitor*. PhD thesis, Ljubljana U., Ljubljana, 2011. Presented 18 Nov 2011, [CERN-THESIS-2011-197](#).

[243] ATLAS Collaboration, *Improved Luminosity Determination in pp Collisions at $\sqrt{s} = 7$ TeV using the ATLAS Detector at the LHC*, [ATLAS-CONF-2012-080](#).

[244] S. Arfaoui, *The ATLAS liquid argon calorimeter high-voltage system: commissioning, optimisation, and LHC relative luminosity measurement*. PhD thesis, Marseille U., Luminy I U., Geneva, 2011. Presented 14 Oct 2011, [CERN-THESIS-2011-146](#).

[245] S. Maettig, *Luminosity Measurements with the ATLAS Detector*. PhD thesis, Hamburg U., 2012. Presented 06 Aug 2012, [CERN-THESIS-2012-249](#).

[246] R. G. Newton, *Optical theorem and beyond*, [American Journal of Physics 44 \(1976\) 639–642](#).

[247] ATLAS Collaboration, D. Caforio, *The ATLAS Forward Detectors - LUCID, ALFA and AFP: Past, Present and Future*, [ATL-LUM-SLIDE-2013-054](#).

[248] ATLAS Collaboration, *Performance of the ATLAS Trigger System in 2010*, [Eur. Phys. J. C72 \(2012\) 1849, arXiv:1110.1530 \[hep-ex\]](#).

[249] ATLAS Collaboration, B. A. Petersen, *The ATLAS Trigger Performance and Evolution*, [ATL-DAQ-PROC-2012-071](#).

[250] *Trigger Operation Public Results*, <https://twiki.cern.ch/twiki/bin/view/AtlasPublic/TriggerOperationPublicResults>.

[251] *CERN releases analysis of LHC incident*, <http://press.web.cern.ch/press-releases/2008/10/cern-releases-analysis-lhc-incident>.

[252] ATLAS Collaboration, *Luminosity Determination in pp Collisions at $\sqrt{s} = 7$ TeV Using the ATLAS Detector at the LHC*, *Eur. Phys. J.* **C71** (2011) 1630, [arXiv:1101.2185 \[hep-ex\]](https://arxiv.org/abs/1101.2185).

[253] ATLAS Collaboration, *Improved luminosity determination in pp collisions at $\sqrt{s} = 7$ TeV using the ATLAS detector at the LHC*, [arXiv:1302.4393 \[hep-ex\]](https://arxiv.org/abs/1302.4393).

[254] *ATLAS Public Luminosity Results*,
<https://twiki.cern.ch/twiki/bin/view/AtlasPublic/LuminosityPublicResults>.

[255] *LHC Luminosity 2010–2013*,
http://lpc.web.cern.ch/lpc/lumiplots_2010.htm,
http://lpc.web.cern.ch/lpc/lumiplots_2011.htm,
http://lpc.web.cern.ch/lpc/lumiplots_2012.htm,
http://lpc.web.cern.ch/lpc/lumiplots_2013.htm.

[256] *COMA Portal*, https://atlas-tagservices.cern.ch/tagservices/RunBrowser/runBrowserReport/rBR_Period_Report.php.

[257] R. Brun and F. Rademakers, *ROOT: An object oriented data analysis framework*, *Nucl. Instrum. Meth.* **A389** (1997) 81–86.

[258] *Tau Decay Pie Chart*, created by Felix Friedrich.

[259] ATLAS Collaboration, *Data-Quality Requirements and Event Cleaning for Jets and Missing Transverse Energy Reconstruction with the ATLAS Detector in pp Collisions at a Center-of-Mass Energy of $\sqrt{s} = 7$ TeV*, [ATLAS-CONF-2010-038](https://cds.cern.ch/record/720003).

[260] ATLAS Collaboration, W. Lampl, S. Laplace, D. Lelas, P. Loch, H. Ma, et al., *Calorimeter clustering algorithms: Description and performance*, [ATL-LARG-PUB-2008-002](https://cds.cern.ch/record/800000).

[261] ATLAS Collaboration, *Muon reconstruction efficiency in reprocessed 2010 LHC pp collision data recorded with the ATLAS detector*, [ATLAS-CONF-2011-063](https://cds.cern.ch/record/1000000).

[262] *ATLAS Muon Combined Performance – Guidelines for Analyses of 2011 Data in Release 17*, <https://twiki.cern.ch/twiki/bin/viewauth/AtlasProtected/MCPAnalysisGuidelinesRel17MC11a>.

[263] *ATLAS EgammaAnalysis Package*, <http://atlas-sw.cern.ch/cgi-bin/viewcvs-atlas.cgi/offline/Reconstruction/egamma/egammaAnalysis/>.

[264] M. Cacciari, G. P. Salam, and G. Soyez, *The anti- k_t jet clustering algorithm*, *JHEP* **04** (2008) 063, [arXiv:0802.1189 \[hep-ph\]](https://arxiv.org/abs/0802.1189).

[265] M. Cacciari and G. P. Salam, *Dispelling the N^3 myth for the k_t jet-finder*, *Phys. Lett.* **B641** (2006) 57, [arXiv:hep-ph/0512210](https://arxiv.org/abs/hep-ph/0512210) [hep-ph].

[266] ATLAS Collaboration, *Jet energy measurement with the ATLAS detector in pp collisions at $\sqrt{s} = 7$ TeV*, [arXiv:1112.6426](https://arxiv.org/abs/1112.6426) [hep-ex].

[267] ATLAS Collaboration, *Validating the measurement of jet energies with the ATLAS detector using Z +jet events from pp collisions at $\sqrt{s} = 7$ TeV*, [ATLAS-CONF-2011-159](#).

[268] DØ Collaboration, V. Abazov et al., *Measurement of the $p\bar{p} \rightarrow t\bar{t}$ production cross section at $\sqrt{s} = 1.96$ TeV in the fully hadronic decay channel*, *Phys. Rev.* **D76** (2007) 072007, [arXiv:hep-ex/0612040](https://arxiv.org/abs/hep-ex/0612040) [hep-ex].

[269] ATLAS Collaboration, D. W. Miller, A. Schwartzman, and D. Su, *Pile-up jet energy scale corrections using the jet-vertex fraction method*, [ATL-PHYS-INT-2009-090](#).

[270] *Jet-vertex fraction scaling factors for $t\bar{t}$ analyses in: TopJetUtils*, <https://svnweb.cern.ch/trac/atlasoff/browser/PhysicsAnalysis/TopPhys/TopPhysUtils/TopJetUtils/tags/TopJetUtils-00-00-04>.

[271] ATLAS Collaboration, *Measuring the b -tag efficiency in a top-pair sample with 4.7 fb^{-1} of data from the ATLAS detector*, [ATLAS-CONF-2012-097](#).

[272] ATLAS Collaboration, *Commissioning of the ATLAS high-performance b -tagging algorithms in the 7 TeV collision data*, [ATLAS-CONF-2011-102](#).

[273] ATLAS Collaboration, *b -jet tagging efficiency calibration using the System8 method*, [ATLAS-CONF-2011-143](#).

[274] ATLAS Collaboration, *Measurement of the b -tag efficiency in a sample of jets containing muons with 5 fb^{-1} of data from the ATLAS detector*, [ATLAS-CONF-2012-043](#).

[275] ATLAS Collaboration, *b -jet tagging calibration on c -jets containing D^{*+} mesons*, [ATLAS-CONF-2012-039](#).

[276] ATLAS Collaboration, *Performance of the Reconstruction and Identification of Hadronic Tau Decays with ATLAS*, [ATLAS-CONF-2011-152](#).

[277] ATLAS Collaboration, *Performance of the Reconstruction and Identification of Hadronic Tau Decays in ATLAS with 2011 Data*, [ATLAS-CONF-2012-142](#).

[278] ATLAS Collaboration, Z. Czyczula and M. Dam, *Cut-based electron veto algorithm for the track-seeded part of tauRec*, [ATL-PHYS-INT-2009-023](#).

[279] ATLAS Collaboration, *Expected electron performance in the ATLAS experiment*, [ATL-PHYS-PUB-2011-006](#).

[280] ATLAS Collaboration, *Observation of $Z \rightarrow \tau_{\text{had}}\tau_{\text{lep}}$ Decays with the ATLAS detector*, [ATLAS-CONF-2011-010](#).

[281] ATLAS Collaboration, *Performance of the ATLAS Detector using First Collision Data*, [JHEP 09 \(2010\) 056](#), [arXiv:1005.5254 \[hep-ex\]](#).

[282] E. Gross and O. Vitells, *Transverse mass observables for charged Higgs boson searches at hadron colliders*, [Phys. Rev. D81 \(2010\) 055010](#), [arXiv:0907.5367 \[hep-ph\]](#).

[283] ATLAS Collaboration, *ATLAS Muon Momentum Resolution in the First Pass Reconstruction of the 2010 pp Collision Data at $\sqrt{s} = 7$ TeV*, [ATLAS-CONF-2011-046](#).

[284] *The Energy Rescaler Tool*,
<https://twiki.cern.ch/twiki/bin/view/AtlasProtected/EnergyRescaler>.

[285] *Muon Scale Factors for 2011 analyses: EPS and Beyond*,
<https://twiki.cern.ch/twiki/bin/view/AtlasProtected/TopCommonScales>.

[286] *Jet Energy Resolution Provider*,
<https://twiki.cern.ch/twiki/bin/view/Main/JetEnergyResolutionProvider>.

[287] *Using the Multijet Jet Energy Scale Uncertainty Provider for Top*, <https://twiki.cern.ch/twiki/bin/view/AtlasProtected/MultijetJESUncertaintyProviderTop>.

[288] *Flavour Tagging – Scale Factors and Calibrations for EPS and Beyond*, <https://twiki.cern.ch/twiki/bin/view/AtlasProtected/Analysis16>.

[289] *Top Jet Liaison – b -tagged Jet Energy Uncertainty*, <https://twiki.cern.ch/twiki/bin/view/AtlasProtected/TopJetLiaison>.

[290] *Tau Systematics for Winter 2012*,
<https://twiki.cern.ch/twiki/bin/viewauth/AtlasProtected/TauSystematicsWinterConf2012>.

[291] *Top Missing transverse mass Liaison recommendations for EPS*, https://twiki.cern.ch/twiki/bin/view/AtlasProtected/TopETmissLiaison_EPS#Recommendations_for_Calculating.

[292] P. Skands, *Tuning Monte Carlo generators: The Perugia tunes*, [Phys. Rev. D82 \(2010\) 074018](#).

[293] G. Cowan, K. Cranmer, E. Gross, and O. Vitells, *Asymptotic formulae for likelihood-based tests of new physics*, *Eur. Phys. J.* **C71** (2011) 1554, [arXiv:1007.1727 \[physics.data-an\]](https://arxiv.org/abs/1007.1727).

[294] ATLAS Collaboration, M. Flechl, S. Hattrem Raddum, and A. Read, *Combined limits for $H^\pm \rightarrow \tau^\pm + \nu$ in $t\bar{t}$ decays with 4.6fb^{-1} of pp collision data recorded at $\sqrt{s} = 7$ TeV with the ATLAS experiment — Supporting Note*, **ATL-PHYS-INT-2012-044**.

[295] A. L. Read, *Presentation of search results: The CL_s technique*, *J. Phys.* **G28** (2002) 2693.

[296] M. S. Carena, S. Heinemeyer, C. Wagner, and G. Weiglein, *Suggestions for benchmark scenarios for MSSM Higgs boson searches at hadron colliders*, *Eur. Phys. J.* **C26** (2003) 601–607, [arXiv:hep-ph/0202167 \[hep-ph\]](https://arxiv.org/abs/hep-ph/0202167).

[297] M. Carena, D. Garcia, U. Nierste, and C. E. M. Wagner, *Effective lagrangian for the $t\bar{b}H^+$ interaction in the MSSM and charged Higgs phenomenology*, *Nucl. Phys.* **B577** (2000) 88, [arXiv:hep-ph/9912516 \[hep-ph\]](https://arxiv.org/abs/hep-ph/9912516).

[298] E. Gross and O. Vitells, *A Method for Deriving Transverse Masses Using Lagrange Multipliers*, [arXiv:0801.1459 \[physics\]](https://arxiv.org/abs/0801.1459).

[299] CMS Collaboration, *Search for a light charged Higgs boson in top quark decays in pp collisions at $\sqrt{s} = 7$ TeV*, *JHEP* **07** (2012) 143, [arXiv:1205.5736 \[hep-ex\]](https://arxiv.org/abs/1205.5736).

[300] CMS Collaboration, *Updated search for a light charged Higgs boson in top quark decays in pp collisions at $\sqrt{s} = 7$ TeV*, **CMS-PAS-HIG-12-052**.

[301] A. Attikis, *Search for light charged Higgs bosons with the $H^+ \rightarrow \tau + \nu$ decay in the fully hadronic final state*. PhD thesis, Cyprus University, 2012.
[CERN-THESIS-2012-174; CMS-TS-2012-033](https://cds.cern.ch/record/1402033).

[302] M. Carena, S. Heinemeyer, O. Stål, C. E. M. Wagner, and G. Weiglein, *MSSM Higgs Boson Searches at the LHC: Benchmark Scenarios after the Discovery of a Higgs-like Particle*, [arXiv:1302.7033 \[hep-ex\]](https://arxiv.org/abs/1302.7033).

[303] LEP Higgs Working Group for Higgs boson searches, ALEPH, DELPHI, L3, Opal collaborations, *Search for Charged Higgs bosons: Preliminary Combined Results Using LEP data Collected at Energies up to 209 GeV*, [arXiv:hep-ex/0107031 \[hep-ex\]](https://arxiv.org/abs/hep-ex/0107031).

Acknowledgements

At this point I want to thank all without whom the completion of this thesis might not have been possible!

First of all I would like to thank THE LOVE OF MY LIFE – Anne, who understands and supports my passion for physics and thus was able to accept all the (from time to time very very) late evenings in the office, especially when a conference note or paper was on the verge of being finished. I am truly in dept to her for all love and patience!

I want to thank Arno Straessner my “Doktorvater” – who has allowed me to join his group, always had an open ear and time for me, when I was in need of advice and guidance – I am deeply thankful to You forever! I also want to thank Michael Kobel, my Diploma adviser, who was the one to introduce me to the ATLAS and the “Institut für Kern- und Teilchenphysik” family of the TU Dresden, and Heiko Lacker, who was so kind to share many experiences and helpful advices with me. At the IKTP I especially want to thank the coffee people and team – thank You all for the inspiring, sometimes very practical problem solving, most of the time entertaining and rare silent, but always inspiring coffee breaks – I will surely miss them and You guys! Further at the IKTP I also wanted to thank all the helpful people, who always took the time, when I approached them concerning a problem or idea, especially: Thomas Goepfert, Andreas Petzold, Marcus Morgenstern, Felix Friedrich, Peter Steinbach and last but not at all least Christian Rudolph and I will never forget Rainer Schwierz, who has accompanied me throughout my whole studies at Dresden and was the greatest, caring and skillful (always smiling) admin an institute can dream of, also I want to thank my CERN companions (two were already mentioned above), especially Konrad Jende (and his “Tatze”) for providing us with a place to sleep during the first month and being a great colleague. The same amount of thanks should go to Uwe Kriesten. I want to further thank the Graduiertenkolleg – the many great people I met thanks to it – especially Martin zur Nedden and the students from DESY Zeuthen, of whom I want to especially mention Christoph Wasicki, a great help to the charged Higgs group (when they needed it most) and a dear colleague! Thank I also want all the advisers on the way of my Ph.D. studies here in Dresden: Wolfgang Mader, Martin zur Nedden and Xavier Prudent, and all the advisers and supporters from the ATLAS collaboration: Martin Flechl, Stephen Sekula, Arnaud Ferrari, Eilam Gross and Jacob Groth-Jensen, further Chris(topher) Collins-Tooth, Stan Lai, Olga Igonkina, Soshi Tsuno and Stefania Xella. The fellow Ph.D.

students, whom I really enjoyed working with during this exciting time: Susie (Sourpouhi) Bedikian, Jana Kraus, Allison McCarn, Liron Barak, Silje Hattrem Raddum, Cathrin Bernius, Jennifer Godfrey, Anna Kopp, Alexander Madsen, Daniel Pelikan and Charlie Isaksson. I also want to thank the LAr group of ATLAS for the wonderful time as shifter and expert – it was a truly great experience.

Finally I want to thank my parents for their never-ending support and believe in me, no matter which path I chose.

Versicherung

Hiermit versichere ich, dass ich die vorliegende Arbeit ohne unzulässige Hilfe Dritter und ohne Benutzung anderer als der angegebenen Hilfsmittel angefertigt habe; die aus fremden Quellen direkt oder indirekt übernommenen Gedanken sind als solche kenntlich gemacht. Die Arbeit wurde bisher weder im Inland noch im Ausland in gleicher oder ähnlicher Form einer anderen Prüfungsbehörde vorgelegt.

Die Bildzitate der Erstveröffentlichungen stammen aus Exemplaren der in der Bibliographie aufgeführten Werke. Trotz intensiver Bemühungen konnten unter Umständen nicht sämtliche Inhaber von Rechten an den in diesem Band wiedergegebenen Bildzitate ermittelt werden. Bei berechtigten Copyright-Ansprüchen bitte ich die Betreffenden, sich an den Autor zu wenden.

Die vorliegende Dissertation wurde angefertigt unter der wissenschaftlichen Betreuung von Jun.-Prof. Dr. Arno Straessner (Institut für Kern- und Teilchenphysik, TU Dresden).

Es haben keine früheren erfolglosen Promotionsverfahren stattgefunden.

Hiermit erkenne ich die Promotionsordnung der Fakultät Mathematik und Naturwissenschaften der Technischen Universität Dresden vom 23.02.2011 an.

Patrick Czodrowski, Diplom-Physiker

